CRANFIELD UNIVERSITY

TAIB ISKANDAR MOHAMAD

DEVELOPMENT OF A SPARK PLUG FUEL INJECTOR FOR DIRECT INJECTION OF METHANE IN SPARK IGNITION ENGINE

SCHOOL OF ENGINEERING

PhD THESIS

CRANFIELD UNIVERSITY

SCHOOL OF ENGINEERING

PhD THESIS

Academic Year 2005-2006

TAIB ISKANDAR MOHAMAD

DEVELOPMENT OF A SPARK PLUG FUEL INJECTOR FOR DIRECT INJECTION OF NATURAL GAS IN SPARK IGNITION ENGINE

Supervisors: Dr. Matthew Harrison & Professor Douglas Greenhalgh

July 2006

This thesis is submitted in partial fulfilment of the requirements for the degree of
Doctor of Philosophy

ABSTRACT

The use of methane in spark ignition engines is mainly due to its cleaner emissions and relatively low price. However, when methane replaces gasoline in the externally mixing carburettor or port injection engine, power is reduced and upper speed is limited. These are because the burning velocity of methane is slower than of gasoline, and some air is displaced in the intake manifold in order to compensate the low density methane. The problem can be mitigated when fuel is directly injected into the combustion chamber after the intake valve closes. This results in an increased volumetric efficiency, a higher absolute heating value of mixture and a faster burning rate.

The work presented in this thesis aims to develop a conversion system that enables methane to be directly injected into the combustion chamber of a spark ignition engine without modifying the original structure of the engine. The system, named as Spark Plug Fuel Injector (SPFI) combines a fuel injector with a spark plug. A fuel path is drawn along the periphery of the spark plug body to deliver the injected fuel to the combustion chamber. The system was installed and tested on a Ricardo E6 single cylinder engine with compression ratio of 10.5:1. Cylinder pressures were taken as the main indicator of the engine performance and selected indicated performance were presented. A set of port injected data for the engine running on methane was also taken in order to provide a comparison of performance with SPFI direct injection.

Results show that the indicated performance of the SPFI methane direct injection at the tested speed was lower than the optimised methane port injection operation. This was mainly due to the quality of air-fuel mixing, which is a result of spatial and temporal limitation of direct injection operation. Flow visualization using the PLIF method shows that even though sufficient gas jet penetration from SPFI injection nozzle was achieved, the cone angle was very narrow. The conclusion from imaging experiments implies poor mixing, hence the performance suffers drawback. However, with direct injection, volumetric efficiency is increased ands combustion duration is faster. These two factors are desirable for engine performance improvement. SPFI has proven to be a practical and low cost conversion to methane. Even though the performance is lower than port injection, its benefits are significant. As the SPFI design is simple and requires no modification to the original structure of the converted engine.

ACKNOWLEDGMENTS

In the name of God, The Most Gracious, The Most Merciful. By His will, this thesis has been completed as another episode of knowledge seeking and contribution.

The author wishes to express a greatest gratitude to the academic supervisor for this project, Dr. Matthew Harrison and Professor Douglas Greenhalgh for their warmth, continuous guidance and support, priceless knowledge and expertise, and kindly understanding. Secondly, author's deepest appreciation to Dr. Mark Jermy, the initial supervisor for this project, for his ideas, understanding, support, availability and generosity for providing assistance both in author's academic and private life.

To my mother and father whose supplications and encouragements have given me strength to complete this work. To my family whose support during this course of studies has given me comfort. To my parents in-law and siblings in-law, thank you for your support.

My dearest gratitude to the beloved wife, Ira for standing by my side and giving me continuous support throughout this course of study and the hardship of life due to it. Your sacrifice is priceless. To my children, Balqis, Naufal, Nadiyah and Safiyah, you are my source of inspirations.

A special thank to Dr. Glenn Sherwood, Tim Lee, Brian Scully, Richard Kennewell, Alan Hutching, and all others for providing technical supports during the experiment works.

To Andreas, Eudoxios, Anni, Edouard, Fatiha, Alessio, Andy and Adam, I thank you all for the friendship and helps during my studies.

TABLE OF CONTENTS

LIST OF FIGURES

NOMENCLATURE

ABDC	After bottom dead centre
AC	Alternating current
AFR	Air-fuel ratio
ATDC	After top dead centre
BDC	Bottom dead centre
BMEP	Brake mean effective pressure
BTDC	Before top dead centre
CA	Crank angle
CCD	Charge Coupled Device
CH_4	Methane
CI	Compression ignition
CNG	Compressed natural gas
CO	Carbon monoxide
CO_2	Carbon dioxide
CR	Compression ratio
CVPI	Closed valve port injection
DAQ	Data acquisition
DC	Direct current
DI	Direct injection
DISI	Direct injection spark ignition
ECU	Engine control unit
EGR	Exhaust gas Recirculation
EVC	Exhaust valve close
EVO	Exhaust valve open
GDI	Gasoline direct injection
GFI	Gaseous fuel injection
HC	Hydrocarbons
HCHO	Formaldehyde
IC	Internal combustion
IMEP	Indicated mean effective pressure
IVC	Inlet valve close
IVO	Inlet valve open
LEV	Low emission vehicle
LIF	Laser induced fluorescent
LNG	Liquefied natural gas
LPG	Liquefied petroleum gas
MBF	Mass burnt fraction
MBT	Minimum spark advance for best torque
Mosfet	Metal Oxide Semiconductor Field Effect Transistor
Nd-YAG	Neodymium-doped yttrium aluminum garnet
NG	Natural gas
NGV	Natural gas vehicle
NMOG	Non methane organic gasses
NO_x	Nitrous oxide
OBD	On-board diagnostics
OVPI	Open valve port injection
PFI	Port fuel injection

PI	Port injection
PIV	Particle imaging velocimetry
PLIF	Planar laser induced fluorescent
PM	Particulate matters
ROHR	rate of heat release
RON	Research octane number
rpm	Revolution per minute
SI	Spark ignition
SPFI	Spark plug fuel injector
TDC	Top dead centre
WOT	Wide open throttle

Note:

In addition, the definitions of all symbols used in the equations are given in the text.

Chapter 1

INTRODUCTION

1.1 Overview

The increasing concerns over energy security and the emission of pollutant gases have triggered greater efforts to develop alternatives to conventional fuels for road vehicles. In the presence of these concerns, automotive engine technology is challenged by the increasing divergence between higher power output, better fuel economy and lower pollutant emission requirements [Stan, 2002]. Several alternatives to gasoline and diesel fuels have been studied on current internal combustion (IC) engines. These include natural gas (NG), which is predominantly methane, liquefied petroleum gas (LPG), hydrogen, as well as ethanol and methanol. They are used either as supplement or replacement to gasoline in spark ignition (SI) engines. For compression ignition (CI) engines, dual fuel operation with diesel fuel providing pilot ignition source has been successful for heavy-duty applications. CI engines have also benefited from the use of various alternative fuels of vegetable origins as diesel replacement.

Natural gas use has various advantages over conventional fuels mainly due to its potential for higher thermal efficiency (due to higher octane value that allows the use of higher compression ratios), and lower CO_2 emission (due to lower carbon-to-hydrogen ratio) [Shiga et. al. 2002]. From the supply point of view, natural gas has the advantage of energy diversification and the total reserves have been estimated in the same order as petroleum but with only 60% of its production rate [Vuorenkoski, 2004]. LPG has been another promising alternative fuel mainly due to its relatively high energy density, high octane rating and low pollutant emissions. It can be stored as liquid at moderate pressure, which gives it major advantage over most other alternative fuels. Methanol on the other hand has a very high octane rating but low heating value and stoichiometric air fuel ratio (AFR). Thus it leads to higher volumetric fuel consumption when compared to gasoline. Hydrogen fuel for electrically driven fuel cell cars, seen as the future replacement to IC engine technology, is undergoing relatively slower research and development and is expected to be in large scale production at some distance of time. IC engines is therefore will remain the key power source in the 21st century until fuel cell vehicles become widespread [Morita, 2003]

1.1.1 Emissions reductions

Possibly the toughest challenge in automotive technology, from the perspective of car manufacturers, is to meet the enforced emission limits without compromising users requirement for efficiency and performance. The main strategies to reduce pollutant emissions have been to improve engine management systems, mixture formation systems and emission after-treatment equipment. Several methods have been applied on newly designed engines in the attempt to control tailpipe emissions. These include rapid feedback engine management systems with on-board diagnostics, new combustion chamber geometry, multi-valve technology, catalytic converter, exhaust gas recirculation (EGR) technique, adaptive valve operations, lean burn strategy and direct injection spark ignition technology (DISI). The use of cleaner alternative fuels however, has been a more straightforward, cheap and effective solution for engines already in the marketplace.

Tougher emission laws that are being gradually imposed worldwide have steered manufacturers to improve the current vehicle engine and fuel technologies. The emission standards defines limits for carbon monoxide (CO), hydrocarbons (HC), nitric oxides (NO_x), particulate matters (PM), non methane organic gases (NMOG) and formaldehyde (HCHO) in terms of mass per distance traveled. Limits are categorized for vehicle age, capacity and type of fuel used. Over the last decade, the enforcement has become more stringent as numbers of road vehicles grow exponentially. Among the most recent and highly rated standards are the European Union's Euro 4 and California Low Emission Vehicles II emission standards (LEV II) as shown in Table 1(a) and Table 1(b).

European Union emission regulations for new light duty vehicles (cars and light commercial vehicles) are specified in the Directive 70/220/EEC. This basis

Directive was amended a number of times, some of the most important amendments including:

- Euro 1 standards (also known as EC 93): Directives 91/441/EEC (passenger cars only) or 93/59/EEC (passenger cars and light trucks)
- Euro 2 standards (EC 96): Directives 94/12/EC or 96/69/EC
- Euro 3/4 standards (2000/2005): Directive 98/69/EC, further amendments in 2002/80/EC
- Euro 5 standards (2008): Proposed regulation *[COM(2005) 683]* published in December 2005

European emission standards are sets of requirements defining the acceptable limits for exhaust emissions of new vehicles sold in European Union (EU) member states. The standards are defined in a series of European Union Directives staging the progressive introduction of increasingly stringent standards. Currently, emissions of NO_x, HC, CO, and particulate matters are regulated for most vehicle types, including cars, lorries, trains, tractors and similar machinery, barges, but excluding seagoing ships and airplanes. For each vehicle type, different standards apply. Compliance is determined by running the engine over standardized test cycles. Noncompliant vehicles cannot be sold in the EU, but new standards do not apply to vehicles already on the roads. No uses of specific technologies are mandated to meet the standards, though available technology is considered when setting the standards.

The California LEV II emission standards (Table 1(b)), was made effective from the year 2004 and will run until 2010. The standards were first adopted in November 1998. Under the LEV II regulations, the light-duty truck and medium-duty vehicle categories of below 8500 lbs (3855 kg) gross weight are reclassified and have to meet passenger car requirements. Under the LEV II standard, NO_x and PM standards for all emission categories are significantly tightened. The same standards apply to both gasoline and diesel vehicles. If the trends of emission limits are projected to the far future, probably only fuel cell powered vehicles will be able to meet the regulations.

EU Emission Standards for Passenger Cars (Category M), g/km

Tier	Year	CO	HC	HC+NO_x	NO_x	PM
Diesel						
Euro 1†	1992.07	2.72 (3.16)	-	0.97 (1.13)	-	0.14 (0.18)
Euro 2, IDI	1996.01	1.0	-	0.7	-	0.08
Euro 2, DI	1996.01^a	1.0	-	0.9	-	0.10
Euro 3	2000.01	0.64	-	0.56	0.50	0.05
Euro 4	2005.01	0.50	-	0.30	0.25	0.025
Petrol (Gasoline)						
Euro 1†	1992.07	2.72 (3.16)	-	0.97 (1.13)	-	-
Euro 2	1996.01	2.2	-	0.5	-	-
Euro 3	2000.01	2.30	0.20	-	0.15	-
Euro 4	2005.01	1.0	0.10	-	0.08	-

† Values in brackets are conformity of production (COP) limits.

a - until 1999.09.30 (after that date DI engines must meet the IDI limits)

Table 1(a) EU emission standards (Source: European Environment Agency)

California Emission Standards for Light-Duty Vehicles, FTP 75, g/mi

Category	50,000 miles/5 years					100,000 miles/10 years				
	NMOG^a	CO	NO_x	PM	HCHO	NMOG^a	CO	NO_x	PM	HCHO
Passenger cars										
Tier 1	0.25	3.4	0.4	0.08	-	0.31	4.2	0.6	-	-
TLEV	0.125	3.4	0.4	-	0.015	0.156	4.2	0.6	0.08	0.018
LEV	0.075	3.4	0.2	-	0.015	0.090	4.2	0.3	0.08	0.018
ULEV	0.040	1.7	0.2	-	0.008	0.055	2.1	0.3	0.04	0.011
ULEV	0.040	1.7	0.2	-	0.008	0.055	2.1	0.3	0.04	0.011

a - NMHC for all Tier 1 standards

Abbreviations:

NMOG - non-methane organic gases

HCHO - formaldehyde

California LEV II Emission Standards, Passenger Cars & LDVs <8500 lbs, g/mi

Category	50,000 miles/5 years					120,000 miles/11 years				
	NMOG	CO	NO_x	PM	HCHO	NMOG	CO	NO_x	PM	HCHO
LEV	0.075	3.4	0.05	-	0.015	0.090	4.2	0.07	0.01	0.018
ULEV	0.040	1.7	0.05	-	0.008	0.055	2.1	0.07	0.01	0.011
SULEV	-	-	-	-	-	0.010	1.0	0.02	0.01	0.004

Table 1(b) California emission standards (Source: California Environmental Protection Agency)

In the LEV regulations and starting from the Euro 3 stage, vehicles must be equipped with an onboard diagnostic system for emission control. In these regulations, the inclusion of on-board diagnostic (OBD) instruments on new cars became mandatory. OBD detects any malfunction in engines that may cause abnormality in combustion which lead to increase in pollutant emission by continuously monitoring signals from various sensors and actuators.

The use of methane (i.e. natural gas) in IC engines has a significant effects regarding reduction of pollutant emissions. Its use reduces reactive hydrocarbon emission, and in addition, particulate production from engines using methane is negligible. Because of its gaseous status, methane does not need to vaporize, thus the needs for fuel enrichment during cold start can be significantly reduced. This results in reduction of CO emission. Another advantage using gaseous fuel is the elimination of oil contamination by unburned fuel during cold operation, which extends lubrication oil change interval and increases engine life [Unich, 1993].

1.1.2 Fuel economy and performance

The balance between lower fuel consumption and higher performance is found with higher thermal efficiency. It is a vital consideration from the perspective of vehicle users. Road transportation has been one of the world major energy consumers and environmental pollutants since the beginning of the 20th century. The advancement of its technology has undoubtedly contributed to the global socioeconomic growth. The transportation sector is almost totally dependent on petroleum as the source of energy. The ability to freely and inexpensively move goods and people is a fundamental link in the economic chain. Today, there are approximately 600 million cars in the world, from which 80% are passenger cars [MacLean, 2003] and will surpass one billion sometime around year 2030. If driving habits remain unchanged, cars will have to become nearly three times more energy-efficient by 2030 to maintain present energy consumption. If energy use trends were projected to year 2100, transportation would then have to be twenty times more energy-efficient, which roughly equals to 400-mpg cars [Ove Sviden, 1992].

Several methods have been adopted to improve thermal efficiency in existing naturally aspirated spark ignition engines including advanced combustion cylinder shape, stratified charge and lean combustion as well as direct fuel injection. Optimising cylinder shape by understanding the fluid flow inside it can improve air-fuel mixing whilst minimising heat loss, which is crucial to better combustion. This is achieved by properly positioning of the spark plug, intake valve and fuel injector, in the case of direct injection. The piston crown is shaped accordingly taking into account the fluid motions in order to achieve optimised mixing and turbulent intensity for subsequently better combustion. In addition, fuel injection timing must be properly tuned for the same reason.

Lean burn engines offer higher thermal efficiencies than stoichiometric engines and lower emissions of NO_x and particulate than diesel engines [Reynolds, 2003]. Unfortunately, the problem associated with lean combustion is high cycle-to-cycle variation as well as reduced flame initiation and propagation rates. The most practical approach to improve engine stability under this condition is to reduce the combustion duration through enhanced in-cylinder mean flow and turbulence combined with stratification of local mixture near spark plug at ignition time [Iwamoto, 1997 & Arcoumanis, 1998]. Direct injection spark ignition of gaseous fuel has been considered to be the most promising solution for achieving this aim due to its ability to control both the fluid mechanics and mixture strength at spark plug independent of the in-cylinder pre-injection flow motion [Kim, 2000].

Direct fuel injection has the potential for increased volumetric efficiency, thus thermal efficiency of spark ignition engine because engine output performance is proportional to mass of air induced per cycle [Heywood, 1988] whereas friction losses remain constant for a given engine swept volume and speed. DI increases the amount of air intake, thus the absolute heating value of mixture [Stan, 2002] in every cycle by injection fuel after the intake valve closes, eliminating the problem of air displacement by fuel in the port of manifold injection engines. Direct injection of natural gas combines two advantages. One is the improved performance and better fuel economy of properly tailored direct injection method, and two, is the low emission of polluting gases from natural gas combustion. The concept of stratified charge combustion is achievable through direct fuel injection. In the case of natural gas use in stratified charge spark ignition engine, specific fuel consumption equivalent to those of diesel engines over a broad range of load, speed and output power is of high potential while significantly reducing emission of harmful pollutant gases [Goto, 1999, Rubas, 1998].

1.1.3 Natural gas vehicles (NGV)

According to the statistics by the International Association for Natural Gas Vehicles [IANGV, 2006], there are nearly five millions NGVs in operation worldwide with long establishment record in Europe, North America and South America. In Europe, Italy has about 382,000 NGV with 509 refueling stations. Russia has 41,780 NGV with 213 stations. Argentina has largest number of NGV in the total of 1,459,236 and converting over 5,000 vehicles monthly with over 1400 stations. Canada has 36,000 vehicles converted to NG. In the USA, about 130,000 vehicles are fuelled with NG supported by more than a thousand private and public refueling stations. The numbers are increasing with mounting interest from other countries like India (204,000 NGV) and Malaysia (14,900 NGV). Most NGV are fuel converted and dual fuel types.

Natural gas is often stored compressed at ambient temperature as compressed natural gas (CNG) in these vehicles but it requires more storage space. NG can also be stored cryogenically at ambient pressure as liquefied natural gas (LNG) in heavy-duty vehicles. For the same energy content, the emission from NG combustion have significantly less harmful combustion products such as CO_2 and NO_x than gasoline and diesel engines [Bradley, 1996].

NGV can be categorized into three types, (1) fuel converted, (2) dual fuel operation and (3) dedicatedly developed engine. Most NGV are of type (1) and (2) while type (3) available mainly for heavy duty vehicles. It is well known that when a port injection gasoline engine is converted to NG, with the fuel injected in the intake manifold, torque is reduced and upper speed is limited. These are due to reduction of volumetric efficiency and the relatively lower turbulent flame speed of NG-air combustion [Ishii, 1994]. The problems can be mitigated by direct injection which increases volumetric efficiency and improves mixing as a result of turbulence induced by high pressure injection.

This project aims to improve engine performance when converting port injection gasoline engines to methane operation by use of a low cost direct injection strategy. Methane is injected at pressure to an appropriate air-fuel ratio. This can be stoichiometric at high load or lean at low speed and low load for low emissions [Shiga et al. 2002]. The turbulence induced by the jet aids mixing and boosts the burning velocity, assisting complete combustion. In this thesis, the conversion is achieved by the use of spark plug fuel injector (SPFI) system. SPFI is a physical combination of fuel injector and market-available spark plug in a single body through a simple machining process. Methane is directly delivered from the injection nozzle to the combustion chamber through a fuel path attached and drawn in the spark plug body. The design allows any SI engine to be converted to NG direct injection without any modification of the original engine structure. This provides a very attractive alternative for simple and low cost conversion to NG for any SI engine.

1.2 Objectives

This study was undertaken to develop a low-cost conversion from gasoline port injection to natural gas direct injection without any modification to the engine structure. This allows any car to benefit from the low emission and relatively low cost NG and source of power by installing the system. Methane was used in place of NG. The objectives of the work are:

1.2.1 To understand the fundamentals of methane use and its effect when used as replacement for gasoline in internal combustion. This was done by practicality studies and applying a simple engine model simulation using AVL Boost computer code.

1.2.2 To develop a direct injection of methane in SI engine by combining spark plug and fuel injector for direct conversion from port injection gasoline engine to methane direct injection. The design was carried out taking into account the fundamental spatial and operational limitation of port injection SI engines.

1.2.3 To determine the optimum operating parameters of this conversion system by single cylinder engine experiments, data analyses followed by design and operational optimization processes.

1.2.4 To visualize and understand the injection and mixing of methane direct injection effect on the engine performance. This was done by laser-induced fluorescent (LIF) imaging of fuel spray method into confined chamber.

1.3 Methodology

The work was approached with simulation study, theory and experiment by these following steps.

1.3.1 Literature review, technology update and preliminary practicality calculation of methane combustion in direct injection spark ignition engine

The existing automotive spark ignition engines technologies were reviewed. The potential of direct injection methods were taken into perspective and the operational characteristics were studied. The hydrocarbon-air combustion was reviewed with concentration on the methane-air reaction. These include understanding of methane thermo chemical properties, stoichiometry effects, fuel-air mixture formation processes, combustion reaction, combustion turbulence and turbulence flame speed. A disk-shaped combustion chamber filled with stoichiometric mixture of methane and air was studied to determine the reliability of ignition and completeness of combustion at given physical parameters. The chamber is a representation of the Ricardo E6 gasoline head combustion chamber that was later used in the actual experiments.

1.3.2 Computer simulation of methane and gasoline-fuelled engine

Computer simulation using AVL Boost v4.0 code was used to model a single cylinder and a 4-cylinder engines which has 0.5 litres and 2.0 litres capacity respectively. The single cylinder model was developed based on the Ricardo E6 engine that will be used later in the experiments. Fuel delivery by port injection and direct injection was applied on the same operational and physical parameters of the models. The overall performance was investigated at optimal ignition setting. The results were used to ideally conclude the effect of performance when the same engine undergone PI-to-DI conversion.

1.3.3 Design and fabrication of spark plug fuel injector (SPFI)

The SPFI design was based on the idea of combining a spark plug and fuel injector in one component without changing the spark plug hole in the engine. The main considerations of the SPFI design were, first, to ensure that solenoid valve is capable of injecting high pressure methane at engine speed up to 6000 rpm and, second, the injection nozzle at cylinder wall not to exceed the quenching distance of methane-air combustion in order to avoid penetration of flame into fuel path. Three designs were made before SPFI could operate on the Ricardo E6 engine with reliability and consistency.

1.3.4 Design and fabrication of SPFI system

The SPFI system consists of fuel delivery, injection and ignition controls. A gasoline fuel injector was selected as a base component. Ignition control was achieved based on the available ignition system on the Ricardo E6 engine. The fuel injection system was developed by the combination of a crank angle encoder, a pulse generator, a pulse gate (MOSFET) and a power supply unit. Methane was delivered to the injector from a 200 bar bottle at a specified injection pressure controlled by a pressure regulator. Air fuel ratio was predetermined from theoretical calculation and verified by a fuel flow meter, an air flow meter and a lambda sensor attached to the exhaust manifold.

1.3.5 Engine experiment

Engine experiments were undertaken to achieve two goals. One was to check the operation of SPFI for design improvement and second, to measure the performance of complete SPFI methane DI system in various configurations. In order to provide the basis of comparison, the Ricardo E6 engine was first run in port injection mode. Data from the best performance of port injection at various settings were set as the baseline case. In the direct injection mode, the optimal injection location and ignition timing for best torque were determined from performance data. Then, the effects of injection pressure, fuel path length, load condition, air-fuel ratio and engine speed on the indicated performance of the engine were investigated and discussed.

1.3.6 SPFI design evaluation and optimisation

Design evaluation was done mainly from the engine tests where an SPFI system capable of operating continuously under harsh combustion environment with high reliability was the key factor. Design optimisation was based on ability of the SPFI system to produce combustion steadiness, appropriate cylinder pressure and engine torque that were continuously measured. Fuel delivery process and charge mixture control capability (i.e. control of air-fuel ratio to be within acceptable range) were other parameter that indicate the effectiveness of the design. These processes undergone three major steps before successful SPFI system was achieved which will be discussed in Chapter 5.

1.3.7 SPFI spray imaging

The images of fuel spray development in a confined and pressurised chamber were captured using high speed camera and planar laser-induced fluorescent (PLIF) method. Methane were doped with acetone and injected into the chamber at pressures tested in the Ricardo E6 engine. By changing the chamber pressure that match cylinder pressures during compression stroke and applying fuel injection at various pressures, the captured images provide fundamental understanding of spray shape and hence fuel-air mixing and then related to the measured engine performance.

1.3.8 Data analysis and discussion of results

The combination of engine data, flow visualization data, pre-calculated theoretical values and computer simulation output were compared and analyzed. The feasibility of SPFI system as a low cost tool for conversion to methane direct injection in SI engines is discussed. The findings were concluded and recommendation for future works presented.

Chapter 2

LITERATURE REVIEW

2.1 Introduction

This chapter starts by discussing the properties of natural gas/methane and its potential for automotive fuel applications. Properties of methane are compared with those of gasoline to give the idea of its potential as gasoline substitute in IC engines. Then a brief study on the combustion and turbulence of methane-air combustion in IC engine is presented. Combustion completeness and ignition reliability can be estimated by calculating turbulent flame speed and turbulent Reynolds number for a given cylinder geometry. A review of the previous works on natural gas engines and related technology advancement is also presented. Finally the discussion is focused on the potential of direct injection spark ignition technologies in automotive engines.

2.2 Natural gas

Natural gas occurs in reservoirs beneath the surface of the earth and is a naturally available fuel at the oil field. It is tapped either by itself or along with crude oil from underground. The annual worldwide production was almost 2 billion tonnes of oil equivalent or t.o.e ($1000m^3$ = 0.85 t.o.e) in the last 5 years of the 20th century. This figure corresponds to 60% of crude oil production. Natural gas reserve is estimated about 150 billion t.o.e, but is more evenly distributed than petroleum worldwide making it better in terms of security of supply [Guibert, 1999].

Natural gas mainly consist of methane, CH_4, which occupies 80-95% of the composition. Other constituents include nitrogen (0-4%), ethane (4%) and propane (1-2%). Variation of methane percentage in natural gas depends on the location it is extracted. For example, methane accounts for 85 to 90% of natural gas extracted from Ourengoi (Russia) and Kerteh (Malaysia) but in Uch (Pakistan) the percentage is 28% with propane and butane contents account for 7.4% and 0.6% respectively. The natural gas extracted from wells in Uch, Pakistan contains 25.2% nitrogen [Guibet, 1999]. Before it is distributed, natural gas usually undergoes some processing. The heavier hydrocarbons (propane and butane) and non-hydrocarbon gases, such as hydrogen sulphide are removed.

Natural gas is a colourless and odourless gas. At room temperature, methane is a gas less dense than air. It melts at –183°C and boils at –164°C. It is not very soluble in water. Methane is combustible, and mixtures of about 5 to 15 percent in air are explosive. Methane is not toxic when inhaled, but it can produce suffocation by reducing the concentration of oxygen inhaled. A trace amount of smelly organic sulphur compounds such as *tertiary*-butyl mercaptan, ($(CH_3)_3CSH$) and dimethyl sulphide, ($CH_3–S–CH_3$) is added to give commercial natural gas a detectable odour. This is done to make gas leaks readily detectible. An undetected gas leak could result in an explosion or asphyxiation.

2.3 Methane properties

Methane is the simplest form of hydrocarbon and is classified in the alkanes group. It is represented by a chemical formula of CH_4. Each methane molecule consists of one carbon atom and four hydrogen atoms. As a principal component of natural gas, methane is a significant alternative fuel in automotive engines. However, methane is a greenhouse gas with a global warming potential of 23 over 100 years [Source: World Meteorological Organization, 2005]. Global warming potential is an index used to approximate the warming effect of an instantaneous release of a unit mass (1kg) of a greenhouse gas in atmosphere, relative to that of carbon dioxide. The index takes into account the lifetime of the gas and describes the relative effectiveness of the gas in contributing to global warming. Releasing methane to atmosphere therefore has negative impact on global warming. Table 2.1 shows some of the properties of methane at conditions stated. It is important to compare some related properties of methane with the ones of conventional fuels in order to understand the potential of using this fuel in IC engines. Table 2.2 shows the comparisons of methane and gasoline properties [Bradley, 1996 and Goodger, 1982].

CH_4	Molecular weight	16.043 g/mol
	Flammability limits in air (STP conditions)	5.0-15.0 vol%
Solid phase	Melting point	-182.5 °C
	Latent heat of fusion (1.013bar, at triple point)	58.68 kJ/kg
Liquid phase	Liquid density (1.013bar at boiling point)	422.62 kg/m^3
	Liquid/gas equivalent (1.013bar and 15 °C)	630 vol/vol
	Boiling point (1.013 bar)	-161.5 °C
	Latent heat of vaporization (1.013bar boiling point)	512 kJ/kg
Critical point	Critical temperature	-82.4 °C
	Critical pressure	46.4 bar
Gaseous phase	Gas density (1.013bar at boiling point)	1.819 kg/m^3
	Gas density (1.013bar and 15 °C)	0.679 kg/m^3
	Compressibility Factor (Z) (1.013bar and 15 °C)	0.998
	Specific gravity (air = 1) (1.013 bar and 21 °C)	0.554
	Specific volume (1.013 bar and 21 °C)	1.48 m^3/kg
	Heat capacity at const. pressure, c_p (1 bar & 25 °C)	0.035 kJ/(mol.K)
	Heat capacity at const. volume, c_v (1 bar & 25 °C)	0.027 kJ/(mol.K)
	Ratio of specific heats ($\gamma = c_p/c_v$) (1 bar & 25 °C)	1.305454
	Viscosity (1.013bar and 0 °C)	11.05 μPa.s
	Thermal conductivity (1.013 bar and 0 °C)	32.81 mW/(m.K)
Misc.	Solubility in water (1.013 bar and 2 °C)	0.054 vol/vol
	Auto ignition temperature	595 °C

Table 2.1 Properties of methane (Source: Goodger, 1982)

Properties	Methane	Gasoline
Enthalpy of reaction (lower heating value), MJ/kg	50.0	44.3
Specific gravity at 15°C	0.424	0.72-0.78
Inhaled energy at stoich. mixture with air, MJ/kmole	76.25	83.6
Laminar burning velocity, m/s	0.43	0.5
Octane number	120	90-100
Adiabatic flame temperature, K	2776	2895
Stoichiometric air-fuel ratio	17.2	14.7
Auto ignition temperature, K	530	813
Minimum ignition energy, mJ	0.28	0.30
Flammability limits in air (Equivalent ratio)	0.50-1.68 5-16% vol. fuel	~0.6-4.0 ~1-6% vol. fuel

Table 2.2 Thermo-chemical properties comparison [Bradley, 1996, and Goodger, 1982]

2.3.1 Calorific value and stoichiometry

Calorific value refers to the amount of energy released when a unit mass of fuel reacts with oxygen in a combustion process. High hydrogen-to-carbon (H/C) ratio hydrocarbons tend towards high calorific values, obviously important for a fuel. The net specific energy of methane is 50 MJ/kg which is higher compared to 43 MJ/kg for gasoline.

Stoichiometric air-fuel ratio (AFR) indicates the minimum amount of air required to completely react with fuel to form only carbon dioxide and water as combustion products. Mass stoichiometric AFR for methane and gasoline are 17.2 and 14.7 respectively. The net calorific values for stoichiometric mixtures of methane and gasoline are fairly close; 2.75 MJ/kg and 2.78 MJ/kg respectively.

It is the energy that has been inhaled into the cylinder at the instant the inlet valve closes, along with cycle efficiency, which determines the power developed by the engine. At any given temperature and pressure at this instant, the volume is fixed. This means molar energies of air-fuel mixture of different fuels are the appropriate comparators for potential power developed by the engine [Bradley, 1996].

The high H/C hydrocarbons tend to have lower density. At normal ambient temperatures and pressures methane is at gaseous state therefore its lower density causes disadvantage to gasoline in terms of volumetric stoichiometric AFR. At 20°C and 1atm, with densities of 750 kg/m^3 and 0.679 kg/m^3 for gasoline and methane respectively, stoichiometric AFR mixture on volume or molar basis can be compared. As a result, the specific energy density for methane-air mixture is 3.24 MJ/m^3 compared to 3.62 MJ/m^3 for gasoline–air mixture [Simms, 1994]. In molar basis, the inhaled energy for stoichiometric mixtures with air is 76.25 MJ/mole for methane and 83.6 MJ/mole for iso-octane [Bradley, 1996]. This shows that the molar-based inhaled energy of methane for the same engine size is 11% less than of gasoline. For this basis alone, it is expected that operating the same engine with methane will cause 11% reduction in power output.

2.3.2 Specific heat capacity

Gasoline is a volatile liquid and mixing with air in the intake process produces a significant cooling effect. The cooling effect is associated with its latent heat of vaporization which increasing charge density and thus energy density. Methane, like other gaseous fuels, is usually stored at high pressure on-board the vehicle before being delivered to the intake manifold or cylinder at a pressure near ambient. Even though along the fuel delivery path, considerable pressure drop and charge cooling happen, during mixing with air, the charge cooling effect is minimal. Therefore methane has no advantage in this regard compared to gasoline.

2.3.3 Flammability and ignitability

Flammability of fuels is vital for engine performance and emission control. Burning of an ignited fuel mixture must take place in a very short time. Laminar burning velocity is the key factor here. Methane has a slower burning velocity of 0.43 m/s compared to 0.5 m/s for gasoline. However, it has been reported that the stoichiometric ratio of methane and air has a burning velocity of 0.36 m/s [Bosschaart, 2004]. This indicates that for the same turbulent intensity and equivalent mixture, gasoline will burn more rapidly than methane. For this reason, ignition must be advanced earlier with methane to ensure completion of combustion before exhaust valve open. However, the more ignition is advanced; the more combustion energy is transformed into negative work due to bigger fraction of combustion duration within compression stroke.

Even though it requires less ignition energy than gasoline per unit mass of mixture, in the spark ignition engine operations, about 50% more voltage must be supplied to spark plug to establish spark jump due to low conductivity of natural gas-air mixture [Goodger, 2000], fluctuation of spark plug local mixture strength as well as advanced ignition timing where gas temperature is low. The similar findings were also reported by Thomas [1991] and in Knowles [1984]. This however can be mitigated by using a closer distance between spark plug electrodes or enhanced the stability of mixture stoichiometry at the vicinity of spark plug electrodes. Special spark plugs have been used as well as other ignition devices to ensure successful ignition with natural gas/methane especially at weak mixtures [Beck, 1991]. The reluctance to ignite extends the ignition delay period in which flame kernel grows around the spark possibly requiring further spark advance, which in turn reduces gas temperature at ignition and hence reliability of ignition.

The flammability limits for fuels are important measures for operational and emission control. Lean limits are determined by the flammability limits and as these limits are approached, engine torque fluctuations become significant due to misfiring and thus result in higher unburned hydrocarbon emissions. The flammability ranges for methane and gasoline are $0.5 \leq \phi \leq 1.68$ and $0.57 \leq \phi \leq 4.0$ respectively, where ϕ is equivalence ratio. The limits indicate that leaner mixture of methane and air can maintain combustion once ignited. However, at equivalence ratio greater than 1.68:1, methane is less likely to maintain combustion; giving gasoline an advantage of burning a richer and higher heating value mixture up to equivalent ratio of 4.0 for better potential power.

The combined factors of charge displacement due to the less dense methane and slower flame speed result in 15% reduction of a same engine power when replacing gasoline. From this figure, 10% of the reduction is due to lower volumetric efficiency and 5% is due to slower burning velocity [Jones & Evan, 1985].

2.3.4 Knock resistance

Spark ignition engine efficiency is closely related to its compression ratio. Increasing compression ratio results in higher thermal efficiency and increased power. Methane has a higher research octane number (RON) of 120 which allows a practical compression ratio of 16:1. The RON for gasoline between 90 and 100 limits its operation to compression ratio of 10-11:1. Compression ratio can be increased by 60% when methane replaces gasoline with octane number of 90 before auto-ignition occurs. The octane property gives methane a significant advantage over gasoline for the potential of increased engine efficiency.

2.3.5 Mixture preparation

Fuel-air mixing is one of the most vital parameters in IC engine operation. Gasoline mixtures are produced either by carburetion or fuel injection. In carburetion, fuel is sucked into the air stream, where atomization and vaporization are controlled to an extent by the air flow. In fuel injection, the velocity of the spray determines air entrainment which causes evaporation and mixing. As methane is a gas, mixing with air should be easy but due to difference in densities, methane and air mixing is more difficult to achieve than might be expected [Thomas, 1991]. The overall mixing process in a gaseous jet is slower than fast evaporating liquid spray hence the burning rate is initially lower with gas injection [Abraham, 1995].

Mixture homogeneity is important in lean burn operation for emission control to avoid any rich or near-stoichiometry pockets in the charge which would burn at high combustion temperatures causing unacceptable NO_x levels. For emission control using stoichiometric AFR and a three-way catalytic converter, the control of AFR is important and seems to indicate the need to use fuel injection in methane operation [Simms, 1994].

2.3.6 Emissions from methane IC engines

The main constituents of polluting engine emission are carbon monoxide (CO), nitric oxide (NO_x), particulate matters and unburned hydrocarbon (UHC). Characteristics of methane and gasoline have some effects on the levels of these emissions.

2.3.6.1 Carbon Monoxide

CO formation during combustion is due to [Heywood, 1988];

1. Incomplete combustion – due to rich AFR where not enough oxygen is present and flame quenching at crevice volumes and/or due to poor mixing of charge and/or poor combustion efficiency in lean mixture.

2. Co-existence of CO_2 and CO at elevated high temperature even though with O_2 presence due to dissociation. As exhaust valve open, because further oxidation process is slow, CO concentration is frozen as temperature drops.

In gasoline engines, CO emissions vary from 0.2% at lean mixture to about 10% at equivalence ratios in the region of 1.4. At stoichiometric AFR, CO emission is typically 0.7%. H/C ratios of gaseous fuels however, have little effect on CO concentration. Emission of CO from methane combustion is less than from gasoline only for mixtures with equivalent ratio above 1.15 [Heywood, 1988].

2.3.6.2 Nitric oxide

NO_x emission is governed by temperature and duration of high pressure in the cylinder during combustion. The formation rate is increased with temperature. Thus high flame temperature produces high NO_x, peak concentration occurs at AFRs slightly rich of stoichiometric. AFR that are richer and leaner than this tend to produce lower combustion temperature, thus reduced NO_x concentrations. The adiabatic flame temperature of methane is less than the one of gasoline and this reduces the potential of NO_x formation in the combustion products [Evans, 1997, Jaaskelainen, 1993]. However, it has been reported that in some actual applications, the combustion temperature of methane is higher than of gasoline, resulting in more NO_x being released [Simms, 1994]. This was probably due to the absence of charge cooling as in the case of liquid fuel injection, and also due to the effect of operating at higher compression ratio. Therefore, for stoichiometric methane operation exhaust gas after-treatment or exhaust gas recirculation are desirable. Most engines fuelled with NG/methane operate at lean mixture to mitigate the NO_x problem.

2.3.6.3 Unburned hydrocarbons

Unburned hydrocarbons presence in the exhaust gas is due to various reasons [Heywood, 1988].

1. Incomplete combustion due to insufficient air at rich mixture or localized rich mixture in lean or stoichiometric charge.
2. Slow burning rate or over-retarded ignition with combustion not fully completed when the exhaust valve opens.
3. Crevice volume in cylinder that quenches flame from burning the available air-fuel mixture near cylinder wall and cavities.
4. Lean mixture near combustible mixture lean limits causes poor mixing and misfiring.

In addition to these, the emission of soot particles with size between 10 and 500 nm are considered significant for gas direct injection engines.

2.4 Combustion mechanism for methane

Methane, the simplest form of hydrocarbon which is by far is one of the best studied classes of compounds for which reliable and detailed chemical kinetic models for combustion exist [Simmie, 2003]. Combustion of hydrocarbons can be represented by the following equation.

$$C_\alpha H_\beta O_\gamma N_\delta + a_s(O_2 + 3.76N_2) \rightarrow n_1CO_2 + n_2H_2O + n_3N_2 \qquad \text{(Equation 2.1)}$$

This equation can be solved by atom conservation where $\alpha = n_1$, $\beta = 2n_2$, $\gamma + 2a_s = 2n_1 + n_2$ and $\delta + (2 \times 3.76 \times a_s) = 2n_3$. In methane-air reaction, where $\alpha = 1$ and $\beta = 4$, complete combustion of produces only a single molecule of CO_2 and two molecules of H_2O.

$$CH_4 + 2\,O_2 \rightarrow CO_2 + 2\,H_2O \qquad \text{(Equation 2.2)}$$

However, several steps are involved in this process. Methane forms a methyl radical (CH_3), which reacts with oxygen forming formaldehyde (HCHO or H_2CO). The formaldehyde gives a formyl radical (HCO), which then forms carbon monoxide. The process is called oxidative pyrolysis:

$$CH_4 + O_2 \rightarrow CO + H_2 + H_2O \qquad \text{(Equation 2.3)}$$

Following oxidative pyrolysis, the H_2 oxidizes, forming H_2O, replenishing the active species, and releasing heat. This occurs very quickly, usually in less than a millisecond.

$$H_2 + \frac{1}{2} O_2 \rightarrow H_2O \qquad \text{(Equation 2.4)}$$

Finally, the CO oxidizes, forming CO_2 and releasing more heat. This process is generally slower than the other chemical steps, and typically requires a few to several milliseconds to occur.

$$CO + \frac{1}{2} O_2 \rightarrow CO_2 \qquad \text{(Equation 2.5)}$$

The strength of the carbon-hydrogen covalent bond in methane is among the strongest in all hydrocarbons, which is proportional to the energy released when the bonds are broken.

The combustion duration of methane in an IC engine is longer than that of gasoline due to its lower flame speed. However, this can be improved by directly injecting methane into combustion chamber which intensifies turbulence and speeds up mixing with air [Abraham, 1994].

2.5 Turbulence in internal combustion engines

Flow and combustion in SI engines are highly turbulent in nature. Turbulent flow can be envisioned as a mean fluid flow upon which are superimposed vortices of various sizes randomly dispersed in the flow. The vortices begin to appear above critical value, about 2300, of the mean flow Reynolds number, Re [Ferguson, 2001]. This can be described by the following equations.

$$\mathrm{Re} = \frac{\overline{U}_p b}{\nu} \qquad \text{(Equation 2.6)}$$

where piston mean velocity, $\bar{U}_p$ is calculated by multiplying engine speed, *N*, in rev/min with piston stroke, *s*.

$$\overline{U}_p = 2Ns \qquad \text{(Equation 2.7)}$$

Flows that are statically periodic, as in the case with intermittent IC engines, are treated using ensemble averaging. The ensemble velocity is given by

$$\overline{U}(x,\theta) = \frac{1}{n}\sum_{j=1}^{n} U(x,\theta,j) \qquad \text{(Equation 2.8)}$$

where *n* is the number of cycles averaged, *x* is the position within flow, *j* is the individual cycle building up to *n* and θ varies from 0 to 4π for a four-stroke engine. To define the instantaneous turbulence within a cycle, one writes

$$U(x,\theta,j) = \overline{U}(x,\theta) + u'(x,\theta,j) \qquad \text{(Equation 2.9)}$$

where *u'* is turbulent fluctuation (difference between ensemble average and instantaneous velocity). To quantify the magnitude of turbulent fluctuations, a root mean square is determined by ensemble averaging.

$$u_t(x,\theta) = \left[\frac{1}{n}\sum_{j=1}^{n} u'^2(x,\theta,j)\right]^{1/2} \qquad \text{(Equation 2.10)}$$

One of the most important conclusions reached is that the magnitude of the fluctuating component increases with engine speed. The magnitude of turbulent velocity when piston is at top dead center, $u_{t,tdc}$ is in the order of one half mean piston speed [Liou et al, 1984].

$$u_{t,tdc} \approx \frac{1}{2}\overline{U}_p \qquad \text{(Equation 2.11)}$$

Turbulent velocity is also affected by fluid motion in the cylinder, by which increasing swirl on a same cylinder shape, increasing swirl results in increase in turbulent velocity. In order to fully characterize a turbulent flow, one also needs to specify the size distribution of the random vortices that make up the turbulence. These sizes are [Ferguson and Kirkpatrick, 2001]:

1. The characteristic length, *L*, of the enclosure that represent the largest possible eddy size that confining geometry of the walls will allow, such as cylinder bore or clearance height.
2. The integral scale, *l*, that represents the largest turbulent vortex size, quantified as the distance where the correlation between the velocities of two points goes to zero.
3. The Taylor microscale, λ, which is useful in estimating the mean strain rate of the turbulence.
4. The Kolmogorov microscale, η, which is the smallest size viscous damping will allow.

For a cylindrical combustion chamber, near TDC, the characteristic length is roughly equal to the clearance height, *h*; whereas near BDC, it should be roughly equal to cylinder bore, *b*. Dimensional analysis of simple turbulent flows leads to following relationship between the four scales.

$$\frac{\lambda}{l} = \left(\frac{15}{C_\lambda}\right)^{1/2} \mathrm{Re}_t^{-1/2} \qquad \text{(Equation 2.12)}$$

$$\frac{\eta}{l} = \left(C_\eta\right)^{-1/4} \mathrm{Re}_t^{-3/4} \qquad \text{(Equation 2.13)}$$

$$l = C_l L \qquad \text{(Equation 2.14)}$$

where the constants C_l, C_λ and C_η are numbers unique to flow of interest and whose order of magnitude is unity [Reynolds, 1974]. The turbulent Reynolds number, Re_t is based on the integral scale, turbulent velocity and kinematic viscosity of fluid, v.

Kinematic viscosity is a measure of a fluid's resistance to gravity flow: the lower the kinematic viscosity, the easier and faster the fluid will flow. This correlation is described in the following equation.

$$\mathrm{Re}_t = \frac{u_t l}{v} \quad \text{(Equation 2.15)}$$

Since the turbulence in the engine increases with piston speed, and the integral scales are independent of engine speed, as the engine speed goes up, the micro scales of turbulence will go down. This can be shown as the increase in flame wrinkling increase as engine speed increases [Smith, 1982]. Mattavi [1980] produced a correlation between turbulent flame speed, u_t laminar burning speed, u_l, and turbulent intensity, u_T by the following equation, where C is a constant for a given engine at a given engine speed.

$$u_t = u_l + Cu_T \quad \text{(Equation 2.16)}$$

Completion of combustion is determined mainly by the burning velocity. The laminar flame velocity is the key parameter in this regard. Turbulent burning velocity, u_t is proportional to laminar flame velocity, u_l, in the order of, $u_l^{0.6}$ [Bradley, 1992]. In comparison with the flame velocity of gasoline, at high cylinder pressure near the occurrence of spark ignition, the burning velocity of methane is significantly less [Bradley, 1996]. Based on the correlation described by Bradley, taking the laminar flame speed of methane and gasoline as 0.43 m/s and 0.50 m/s respectively, the turbulent flame speed can be deducted to 0.60 m/s and 0.66 m/s respectively. However, these numbers do not account the effect of turbulent flow in the cylinder which further enhances the turbulent flame speed. When the turbulent intensity is taken into account, using correlation in Equation 2.15, the turbulent flame speed is a function of engine speed. For example at 1500 rpm, with the calculated turbulent Reynolds number, Re_t is approximately 2000. Consider as piston nearing the TDC with cylinder mixture at 25°C and 7 bar, the kinematic viscosity is 16 x 10^{-6} m^2/s. The resulting theoretical turbulent flame speed is 1.77 m/s.

Turbulent flame speed is directly proportioned to the mass burnt fraction and rate of heat release where it increases as combustion reaches about 50% of mass burnt and decrease afterwards until flame quenches [Jones & Evan 1985]. In their experiment, the maximum ratios of turbulent to laminar burning velocity (u_t/u_l) of stoichiometric mixture of methane and air were measured to be in the order of 10, 12.5 and 18.5 at engine speeds of 1500, 2000 and 3000 rpm which correspond to 4 m/s, 5 m/s and 7.4 m/s respectively. These figures can be taken as the basis for determining the degree of combustion completeness, required spark adjustment and limitation to engine speed when methane is utilized as gasoline replacement in a same engine.

2.6 Control of Emissions

In these days, the main strategy for emission control is to treat the engine exhaust gas before reaching the atmosphere. The task is done by utilizing a three-way catalytic converter. The system controls CO, HC and NO_x emissions by the oxidation and reduction processes in the platinum/rhodium catalyst. However, it cannot control the emission of CO_2, which can be controlled by controlling fuel consumption. All these require a precise and accurate control of AFR especially during transient operations. The control is usually achieved by means of metered fuel injection coupled with continuous feedback measurement of oxygen concentration in the exhaust gas by lambda sensor.

Two types of exhaust gas sensor are in common use; EGO and UEGO. The EGO (Exhaust Gas Oxygen) sensor, another name for lambda sensor, operating like a switch, measures the equivalence ratio but does not indicate the actual AFR. While UEGO (Universal Exhaust Gas Oxygen) sensor responds to the actual AFR, therefore provides more meaningful and accurate information especially when operating with multiple fuels in a same engine. However, this sensor is significantly more expensive and therefore less common in production cars.

The EGO sensor monitors the AFR by mean of partial pressure of oxygen which produces output voltage based on electrochemical reaction. The difference of partial pressure of oxygen in the exhaust gas with the partial oxygen pressure in the atmosphere is proportional to the AFR of the reactant. However, this sensor has some weakness concerning time delay of reaction due to the distant locations of sensor at the exhaust manifold and the combustion chamber and also time delay due to two crank rotations for every cycle which elapses fuel input and mixture output.

Another measure to improve engine emission is by lean burn where the engine is run at a very high air-fuel ratio especially at part and low loads. Methane has the advantage over gasoline in this sense due to its wider range of flammability at lean mixtures. In a study done by Shiga et. al. [2002] concerning direct injection of natural gas in an SI engine, by properly adjusting the locations of spark plug and fuel injector, the combustion limits of natural gas-air were extended to an equivalence ratio of 0.02. However, combustion efficiency is reduced as the lean limit is approached due to thicker quenching layer near cylinder wall. The lean burn strategy has always been paired with fuel stratification and has proved not only to reduce emission, but also to shorten combustion duration by 10% and to increase thermal efficiency at the given mixture conditions [Reynolds & Evans, 2003].

2.7 Review on the existing natural gas/methane engine systems

A brief review of natural gas/methane engine technologies is necessary before presenting the project explored in this thesis. Engines operating with natural gas can be classified into three main categories: 1. dual fuel operation [Ahmed, 1997, Ben, 1999, Pirouzpanah, 1999, Papagiannakis, 2003, 2004], 2. fuel converted [Ishii, 1994, Hassaneen, 1998, Aslam, 2006, Roethlisberger, 2002] and 3. specially developed [Iwamoto, 1997, Cox, 2000, Kalam, 2005]. Most NG engines are either the first or the second type. Limited works have been done on the specially developed NG engine. The majority of NG engines are spark ignited type but compression ignition engines also benefit from the use of NG in bi-fuel operations with diesel providing pilot combustion [Chen, 2001, Ishida, 2003, Papagiannakis, 2003, 2004]. Pilot combustion for NG-fuelled compression ignition engine is necessary due to high auto ignition of natural gas compared to diesel. The use of NG in diesel engine is mainly because of its cleaner emission advantage.

In a natural gas engine, the operation can be described from Figure 2.1 as the following.

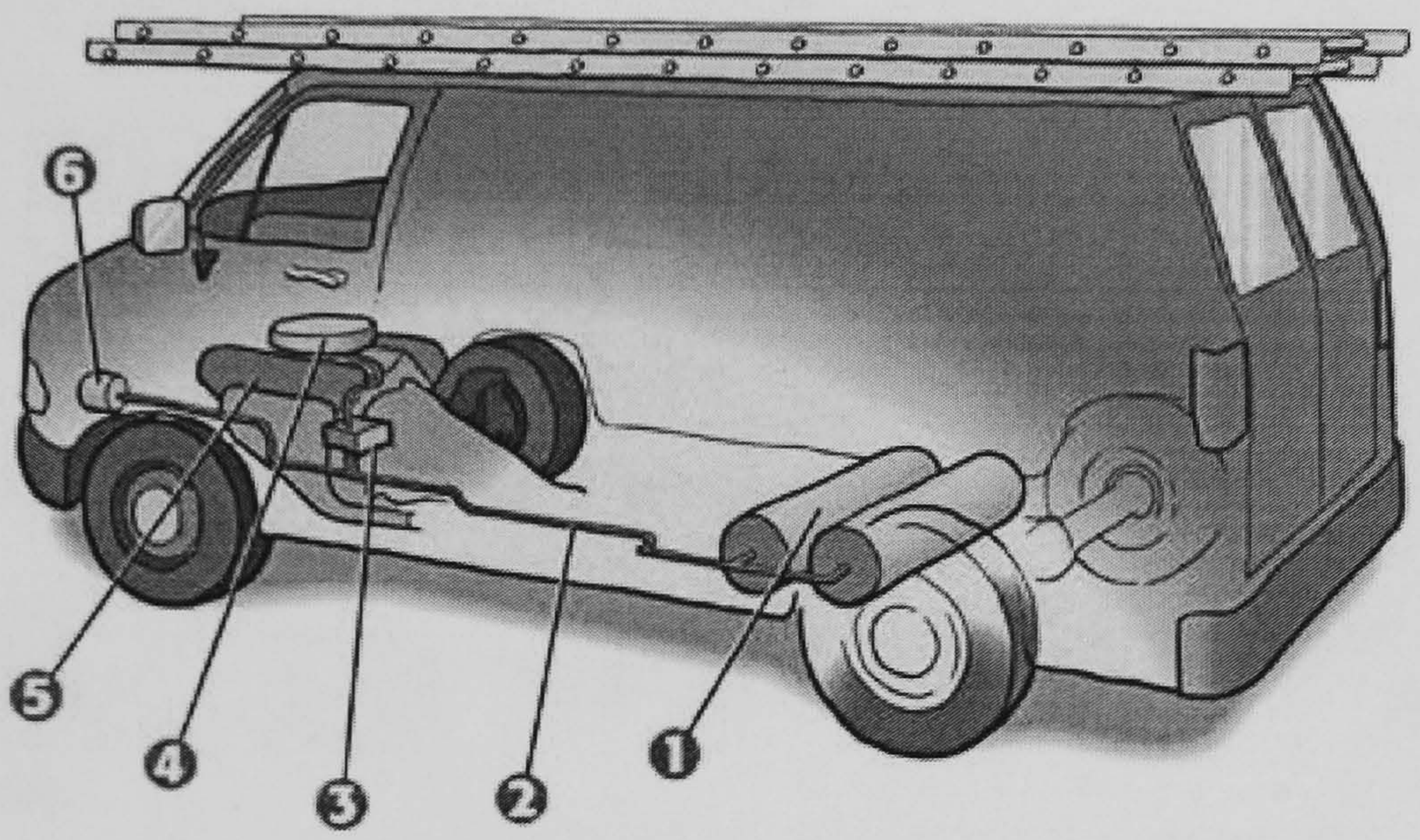

Figure 2.1 Port injection natural gas engine operations [IANGV, 2006]

1. NGVs burn natural gas that is compressed and stored in cylinders.
2. When the engine is started, natural gas flows into a fuel line.
3. The gas then enters a regulator where its pressure is reduced.
4. The natural gas feeds into the engine through a fuel delivery system where it's combined with air. The fuel/air mixture is adjusted to burn most efficiently and with the least possible emissions.

The tanks used to store natural gas can withstand crashes and heat far better than most gasoline tanks can. In the event of a crash, natural gas disperses into the air, whereas gasoline pools on the ground, creating a fire hazard.

In dual fuel engines, natural gas is used either as an alternative to the conventional fuel or as a fuel supplement on a simultaneous two fuels operation. Figure 2.2 shows an example of a dual-fuel natural gas engine used in a Volvo production car. It is a five-cylinder 2.4 litre Bi-Fuel engine for its Volvo S80, V70 and

S60 models with separate fuel systems, one for methane and another for gasoline. The engine automatically switches to the back-up petrol power should the car's gas supply run out. Typically, a tank of methane will give a range of 250-300 km, and the reserve gasoline tank provides an additional range of about 350 km [Volvocar, 2004].

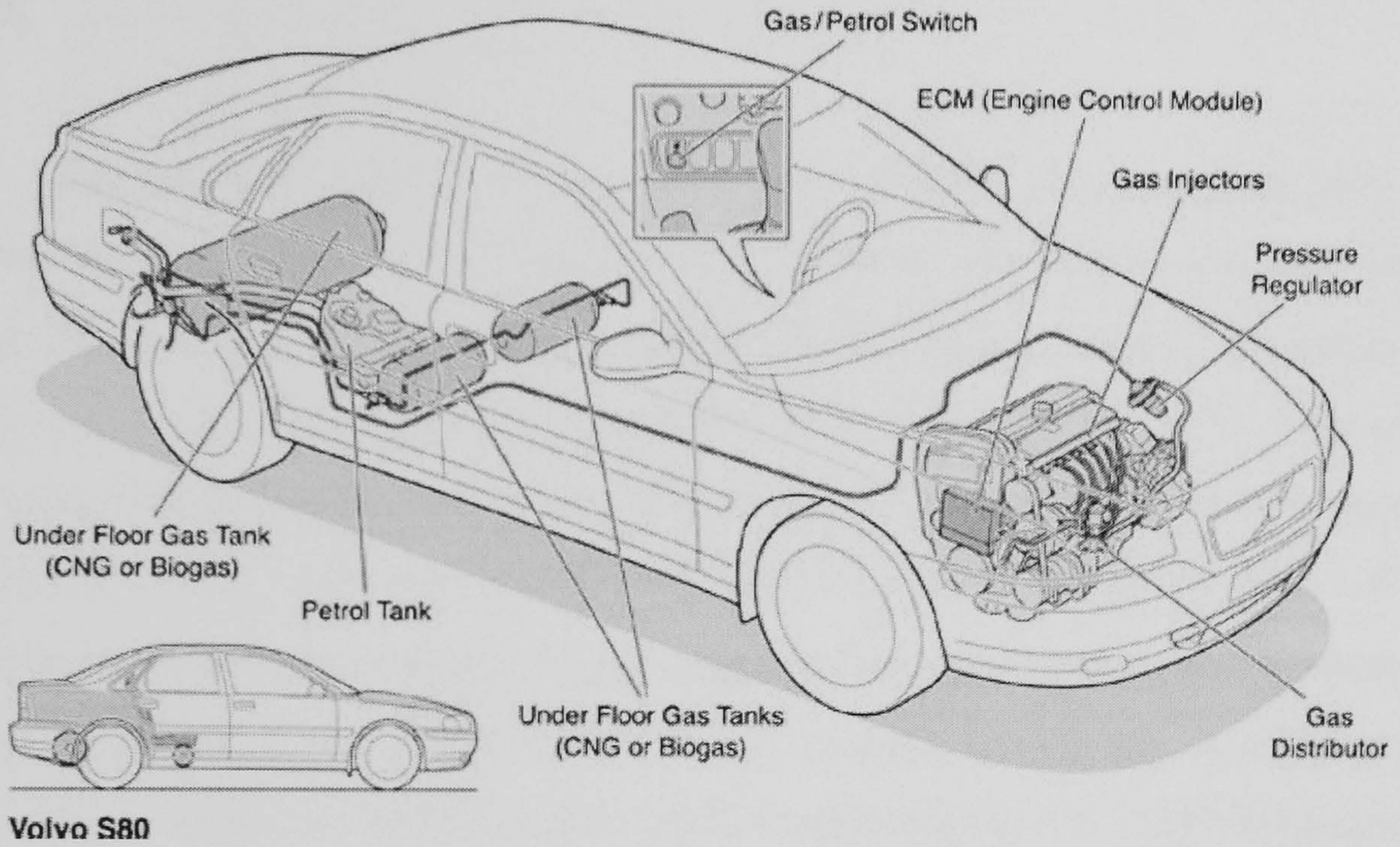

Figure 2.2 Volvo Bi-Fuel systems [Greencar Congress, 2004]

Another common type of dual fuel NG engines is the diesel/NG compression ignition engine. The interest in utilizing NG as partial supplement in diesel engine with diesel providing pilot ignition is mainly due to its advantage of reducing soot particles and NOx. The high auto ignition of NG is a significant advantage since the compression ratio of conventional diesel engine can be maintained. This dual fuel operation results in lower peak pressure compared to the original single fuel operation, thus reducing stress on the engine structure. Combustion duration at high load becomes shorter, but longer at part load than normal diesel operation. Brake power is slightly reduced but vast improvement was found in the reduction of particulate and NO_x emissions [Papagiannakis, 2004].

Fuel converted NG engines are achieved through a proper fuel conversion kits which may include a new ECU for fuel control. The performance of this type of engine is reported by many sources. When a gasoline engine is converted with natural gas utilizing the same but retrofitted fuel system, BMEP is reduced by 16% but

BSFC improved by 18%. In addition a 2.9% higher fuel conversion efficiency and lower emissions of CO_2 (20%), CO (80%), UHC (50%) but 33% higher NO_x were discovered [Aslam, 2006]. Similar results on performance reduction due to fuel conversion were reported by other sources including Jones and Evans [1985], Unich [1993], Jaaskelainen & Wallace [1993], Evans and Blaszczyk [1997], and Hayashida [1999].

Bespoke NG engines have gained more interest because they allow the optimization of engine design for NG characteristics. This type of engine usually taking the advantage of natural gas properties of high octane rating to operate at high compression ratio. The problem of displaced air in the intake manifold experienced with port fuel injection can be eliminated with closed valve direct fuel injection [Mohamad, 2003, Mohamad, 2005]. Several but only a small numbers of NG dedicated engines have been developed especially for heavy duty vehicles where fuel storage space has little limitation. Proton, a Malaysia-based car manufacturer is developing a dedicated direct injection CNG engine for the 1.6 – 2.0 litre passenger car application using the air-assisted Orbital direct fuel injection [Proton, 2006]. Most NG dedicated engined are designed for heavy duty vehicles. These include the 4.3 litre 3156 DING (Direct Injection Natural Gas) engine developed by Caterpillar with power and efficiency equal or better than that of diesel engine [Cox, 2000].

2.7.1 Fuel delivery systems

The way fuel is delivered to combustion chamber in natural gas engine is either by carburetion, indirect fuel injection or direct fuel injection.

2.7.1.1 Carburetors

Carburetors which were initially designed for gasoline fuel can be used for NG vehicles. The concept of carburetor is to release fuel into air flow by mean of pressure differentials. A carburetor basically consists of an open pipe, the carburetor's "throat" or "barrel", through which the air passes into the inlet manifold of the engine. The pipe is in the form of a venturi - it narrows in section and then widens again, causing the airflow to increase in speed in the narrowest part. Below the venturi is a butterfly valve or throttle - a rotating disc that can be turned end-on to the airflow, so as to hardly restrict the flow at all, or can be rotated so that it almost completely blocks the flow of air. This valve controls the flow of air through the carburetor throat and thus the quantity of air/fuel mixture the system will deliver, thereby regulating engine power and speed. Fuel is introduced into the air stream through small holes at the narrowest part of the venturi. Fuel flow in response to a particular pressure drop in the venturi is adjusted by choosing small brass screws with finely calibrated holes, referred to as *jets*, into the fuel path. The carburetion method however is difficult to implement in an engine dedicated to NG because of its limitations during transient operation and its intake system pressure reduction [Guibet, 1999].

2.7.1.2 Indirect injection

The application of indirect fuel injection rather than carburetion has provided improvements in exhaust emissions and vehicle performance. This system introduces fuel at certain higher-than-ambient pressure, which provides more accurate control of fuel quantity injected. In addition, the absence of a venturi as in carburetor reduces intake system pressure reduction. There are mainly two type of indirect injection; single point and multipoint. The single point injection method uses an ECU-controlled fuel injector to introduce fuel into a mixer within the intake system. One common natural gas engine system utilizing this method is referred to Gaseous Fuel Injection (GFI), which functions by introducing the expanded fuel to 7 bar into the intake manifold from a single injector nozzle [Carter, 1992]. In the multipoint injection method, fuel is injected into each intake manifold, where the numbers of fuel injector depends on the number of engine cylinder. This method has several advantages over single point injection including minimizing the risk of intake flashback and improving fuel distribution between cylinders [Guibet, 1999]. The drawback of carburetor and indirect injection for the natural gas fueled engine is the displacement of air in the intake system due to low density natural gas compared to liquid fuels. Therefore, volumetric efficiency is reduced and power is restricted. In order to mitigate this problem, direct fuel injection is preferred where gaseous fuel is injected after intake valve closes and optimal amount of air has been induced to the cylinder.

2.7.1.3 Direct injection

When converting a port (indirect) injection engine to direct injection, volumetric efficiency increases by the factor of 9 – 12% [Wyszynski et. al., 2002]. Direct injection has been adopted for its potential of increasing thermal efficiency and reducing pollutant emissions. Direct injection allows the intrinsic advantages of natural gas and stratified charge combustion to be combined while taking advantage of fuel that is supplied at high pressure. The engine could operate with lean mixture without intake losses – two conditions that promote high efficiency. Fuel stratification and throttleless operation are two methods of performance and fuel economy improvements that can be achieved by the direct injection method. However, due to the fact that fuel-air mixing only occurs inside the engine cylinder, controlling the injected fuel mass requires a high degree of precision. In addition, this engine requires precise construction, careful maintenance and adjustment of the injection system. The fuel injector itself is design to operate at high fuel pressure (up to 150bar) and could withstand harsh conditions inside the combustion chamber. Table 2.3 summarizes the comparison of these fuel delivery systems in terms of advantages and disadvantages of various factors [Guibet, 1999].

	Carburetor		Single point injection		Multipoint injection	Direct injection
	Mechanical	Variable electronic	Continuous	Sequential		
Cost	++	+	+	-	-	--
Transient operation	--	-	-	+	+	++
Distribution b/w cylinder	--	--	--	--	++	++
Intake pressure reduction	--	--	-	-	+	++
Flashback risk	--	--	--	--	+	++

Table 2.3 Comparison of various NGV engine fuelling systems (+ advantage, - disadvantage) [Guibet, 1999]

2.7.2 Fuel storage

Fuel storage in NGV has been its drawback due to higher space required for achieving acceptable driving distance. NG can be stored pressurized at ambient pressure, known as compressed natural gas (CNG) or non-pressurized at cryogenic temperature known as liquefied natural gas (LNG). CNG is preferred in a smaller vehicle because it avoids the additional energy required for liquefaction of NG as with LNG. LNG is feasible for high loads large vehicles with centralized fuelling stations. The CNG storage space and safety requirement have prevented wide application in passenger cars.

The optimal storage pressure is 200 bar where below this pressure, the amount of energy stored is too small, and above this pressure, storage wall thickness must be increased which will results in excessive weight increase [Guibet, 1999]. The tank must be able to withstand up to 600 bar in the case of accidental exposure to fire. These constraints results in maximum capacities in the order of only 0.15m^3 of natural gas per kilogram of reservoir. The most common material for NG tank onboard vehicle is steel and its shape is restricted to cylindrical. However, with the advancement of other materials technology such as bare aluminum, aluminum wound with fiberglass or resin composites of glass or carbon fiber, the tank storage capacity can be increased by a factor of four for the same weight. These materials can also be shaped into other than cylindrical without losing the strength, making accommodating to car structure more feasible.

2.7.3 Improvement measures

A numbers of disadvantages are found with natural gas engines, which are mainly low power compared to gasoline engine. Throttling loss and part load operation, unsteady combustion and high NO$_x$ emissions associated with lean burn combustion are other problems reported [Evans, 1997, Goto, 1999, Goto, 2001, Huang, 2003, Zeng, 2006].

Natural gas operation in spark ignition engines suffers from low efficiency at part load due to throttling loss. Throttling is required at light loads with engines that use homogeneous mixture. To reduce load, the fuel rate must be decreased. Eventually, the mixture becomes so lean that the lean limit is reached. At lean limit, combustion is no longer possible and the engine misfires. In order to achieve unthrottled operation over the entire engine operating range, the engine must operate at air-fuel equivalence ratios well below the lean limit ($\phi \sim 0.60$) of a homogeneous natural gas-air charge. To achieve this equivalence ratio, the fuel-air charge must be stratified so that an ignitable mixture will be achieved near the spark plug at the time of ignition. Stratified charge can be formed with a carefully design direct injection combustion chamber. A novel means of forming charge stratification was developed by Kubesh [2002] with a divided chamber engine configuration of fuel injected prechamber (FIPC) system which successfully increased engine efficiency at part loads by 17% compared to the direct fuel injection method on the same engine. In addition, this method also results in stable engine operation over the entire load conditions and subsequently reduces the amount of NO_x emissions.

Another measure to improve natural gas combustion and performance is to introduce hydrogen in the combustion process which increases the specific inhaled energy of cylinder charge [Akansu, 2004]. Shudo [2000] conducted a study on methane DI stratified charge engine with hydrogen pre-mixing in four cylinder engine with a compression ratio of 13:1. Fuel injection was at 100 bar and injected towards the spark plug. With hydrogen pre-mixing, the combustion system achieved lower exhaust emission and higher thermal efficiency due to higher flame propagation velocity. Increasing the amount of hydrogen pre-mixing stabilizes the combustion as well as reduces CO and HC emissions, but increases NO_x emission. However, NO_x can be maintained at low level by retarding ignition timing without significantly deteriorating the improved thermal efficiency.

High total unburnt hydrocarbon (UHC) emissions at part load and high NO_x emissions at high loads remain the problem with direct injection natural gas engines. Goto [2001] investigated the effects of exhaust gas recirculation (EGR) combined with throttling to reduce the UHC and NO_x emissions from a direct injection natural gas engine at light and high loads. Combustion at light loads was improved and UHC emissions were greatly reduced by throttling even though pumping loss existed. With throttling at part and low loads, combustion became steadier compared to that in the absence of throttling. The brake thermal efficiency was improved with improvement of combustion which is heightened as driving loads become lighter. At medium and high load conditions, NO_x was greatly reduced with appropriate EGR level, about 25%, without combustion deterioration. This result was supported by the other findings by Ishida [2003], in which significant reductions of NOx as well as smoke were found with EGR application and natural gas preheating.

2.8 Direct injection concepts

Two main characteristics of direct injection are internal mixture formation and closed valve injection. Mixture formation is vital in direct injection because the available time for air-fuel mixing is relatively short compared to indirect port injection or carburetion.

2.8.1 Internal mixture formation in direct injection spark ignition engines

In spark ignition engines, air and fuel mixing takes place in the cylinder but a premixing process occurs to a certain degrees depending on type of fuel delivery. In a carburetor system, fuel vaporizes and mixes in the air stream prior to entering the combustion chamber. In a port injection system, fuel is injected and the velocity of fuel jet determines atomization and evaporation of fuel in air. In the direct injection method, fuel is directly injected into the combustion chamber as intake valve closes. The turbulence induced by the gas jet and the jet penetration determine the degree of mixing. In general, the mixing process in the direct injection method is restricted to a much shorter time. Furthermore, unlike the carburetion and port injection where mixing starts before air and fuel enter the combustion chamber, the mixing in direct injection mode can only happen in confined cylinder geometry.

The concepts of homogenous and stratified mixture formation are very important when discussing the direct injection in spark ignition engines because they form the basis of a better control of fuel mixture than the one experienced with port fuel injection. In addition, charge stratification can increase thermal efficiency and have the potential of reducing pollutant emissions. However, with direct injection operation, the degree of mixing and mixture uniformity is vital for reliable combustion. A combination of direct injection, high squish, high swirl and optimized piston crown shape can produced fast mixing and a high degree of mixture uniformity, thus turbulent intensity, molecular diffusion and chemical kinetics, which are the main contributors to the establishment and propagation of a turbulent flame [Risi, 1997]. Mixture formation in direct injection engines can be classified into homogeneous and stratified charge based on the injection strategies. The concepts of these mixture formations are determined by the engine operation and fuel economy requirements.

2.8.1.1 Early injection, homogeneous-charge operation

The homogeneous mixture operating mode in the direct injection engine is designed to meet the requirement of medium-to-high engine loads. Depending on the overall air-fuel ratio, the mixture can be homogeneous-stoichiometric or homogeneous lean. Early injection makes it possible to achieve a volumetric efficiency that is higher than port fuel injection, and slightly increased compression ratio operation which contributes to better fuel economy. It also benefits from better emission during cold start and transient operation [Zhao, 2002].

2.8.1.2 Late injection, stratified-charge operation

This operation is mainly to achieve lean burn and unthrottled operations by injecting fuel late during compression stroke. Fuel stratification is achieved by injection strategy such that the air-fuel ratio around the spark gaps yield stable ignition and flame propagation, whereas areas farther from the point of ignition is leaner or devoid of fuel. The advantage of charge stratification includes significant reduction in pumping work associated with throttling, reduced heat loss, reduced chemical dissociation from lower cycle temperatures and increases specific heat ratio for the cycle, which provide incremental gains in thermal efficiency [Zhao, 2002].

2.8.2 Potential for direct fuel injection in spark ignition engine

Direct injection in spark ignition engines could achieve a number of desirable effects. Even though most literature on direct injection methods are for liquid gasoline fuel, it offers a similar degree in benefits when applied to methane combustion due to similar combustion behaviors. Perhaps, when a direct injection method is applied to a gaseous fuel like methane, more achievement in terms of specific power output can be realized due to significant improvement in volumetric efficiency. The advantages of direct injection methods can be summarized as follows [Stan, 2002]

1. Increased thermal efficiency and lower specific fuel consumption

   At part load, avoiding fresh charge throttling results in charge stratification and burned gas in distinct zones. This ideal structure consists of stoichiometric mixture cloud with spark contact, enveloped by fresh air and burned gas that form a barrier against chemical reactions near chamber wall thus avoiding intense heat transfer to the wall during combustion. Thermal efficiency is bettered by increasing compression ratio, as well as turbo charging and supercharging. Knock can be avoided in such cases by different effects: mixture formation just before or during ignition; mixture concentration in central zone of combustion chamber; out of crevice; of mixture cooling by fuel vaporization during injection.

2. Higher torque due to increase in absolute heating value of mixture

   This is achieved by higher scavenging intensity. The more fresh air is captured, the more fuel can be injected. One the other hand, more captured air generally leads to greater scavenging losses. However, fresh air losses without fuel inclusion have no disadvantages in terms of pollutant emissions, leading to only a slight disturbance of thermal efficiency. Such enforced cylinder filling with air forms the basis for efficient downsizing, which involves supercharging of turbo-charging, inter-cooling, and also adapted valve control.

3. Decrease pollutant emission

Pollutant emission reduction is achieved mainly by the lean burn strategy, which is usually coupled with unthrottled operation. The lean mixture formation however needs a careful calibration of injection timing with respect to ignition timing, as well as proper shape of fuel spray and injection duration.

4. Improved acceleration behavior

Intensive scavenging and unthrottled operation results in a high charge of fresh air at every load. Thus, inertial effects of the air flow during acceleration can be partially avoided. On the other hand, the possible real-time adaptation of the fuel injection rate to the air flow behavior allows an adaptable correlation of mixture formation and combustion. Such dynamic response on torque demand is well known from advanced car diesel engines with direct injection.

The success of a direct injection method depends mainly on the effectiveness of mixture formation and control. This is achieved with precise fuel injection and better engine management system.

Chapter 3

PRELIMINARY INVESTIGATIONS

3.1 Introduction

This chapter discusses some preliminary studies that were undertaken to predict the conditions for successful combustion of methane in IC engine and to estimate the performance change under direct injection engine operation. Calculation and prediction studies of this sort are vital preparation for any large scale engine test programme such as that described in Chapter 5. They also aided the design of the SPFI described in Chapter 4. Combustion in the SI engine is extremely short in duration and highly turbulent in nature. Combustion effectiveness depends on many factors which, among others, include air-fuel mixture formation, turbulent intensity and turbulent burning speed. Spark ignition, which is the energy source for flame initiation, requires certain mixture conditions to successfully maintain the combustion process. The first part of this chapter will discuss combustion completeness and ignition reliability in a disk-shape cylinder with similar dimensions to the gasoline head combustion cylinder Ricardo E6 engine. The combustion and ignition studies are based on estimation of turbulent flame speed and turbulent number respectively.

The second part of the chapter discusses the fuel injection requirement for operation under direct injection on the Ricardo E6 engine. This mainly involves estimation of minimum injection pressures for various engine speeds. By studying the cam profile of this engine with respect to piston movement, and setting the injection duration limits based on close-valve fuel injection operation, minimum required methane injection pressure can be estimated.

The third part of the chapter discusses the results from computer simulation using AVL Boost v.40 code. The code was used to model a single engine operating on gasoline port injection, methane port injection and methane direct injection. By comparing the results of the first two methods, the effect of fuel type on port injection engine operation can be described. On the other hand, by comparing results from methane port injection with the ones from methane direct injection, improvement of performance via direct injection method can be used as the benchmark for the outcomes of this project. The engine models use the dimensions of a single-cylinder Ricardo E6 engine's combustion chamber, intake and exhaust piping geometries and its cam profile in order to provide fair basis for performance comparison with the engine test data.

3.2 Combustion completeness and ignition reliability

One of the fundamental aspects in the combustion of IC engines is completion of combustion. This means every unit mass of fuel inside the cylinder reacted with oxygen to form combustion product and no unburned fuel is wasted through the exhaust. However, total completeness cannot be achieved in practice in a real engine due to many factors such as poor air-fuel mixing, localised inadequate oxygen, flame quenching at cylinder wall leaving a small volume of unreacted mixture and expansion process during combustion and power stroke which reduce the pressure and temperature near piston wall thus slows down and retards flame propagation [Pulkrabek, 1997]. Combustion completeness can be predicted however by estimating turbulent flame speed.

3.2.1 Turbulent flame speed

Completion of combustion is closely related to the flame velocity. The laminar flame velocity is the key parameter in this regard. Turbulent burning velocity, u_t is proportional to laminar flame velocity, u_l, in the order of, $u_l^{0.6}$ [Bradley, 1992]. In comparison with the flame velocity of gasoline, at high cylinder pressure near the occurrence of spark ignition, the burning velocity of methane is significantly less [Bradley, 1996].

Based on the correlation described by Bradley, taking the laminar flame speed of methane and gasoline as 0.43 m/s and 0.50 m/s respectively, the turbulent flame speed can be deducted to 0.60 m/s and 0.66 m/s respectively. However, these values do not take into account the turbulent intensity induced by the moving piston. In the correlations described by Equation 3.1 and 3.2, $\bar{U}_p$ is the piston mean speed and N is engine speed (rpm). For the dimensions of the Ricardo E6 engine use in this work, shown in Table 3.1 and Figure 3.1, when piston is at TDC, turbulent flame speeds are calculated to be 1.85 m/s, 3.70 m/s and 11.10 m/s at 1000, 2000 and 6000 rev/min engine speeds respectively.

Table 3.1 Dimensions of the Ricardo E6 engine

CR = compression ratio = 10.5

B = bore = 76.2 mm

S = stroke = 111.125 mm

r = connecting rod length = 241.27 mm

a = crank offset = 55.5625 mm

s = piston position

θ = crank angle

V_c = clearance volume = 5.334 x 10^{-5} m^3

V_d = displacement volume = 5.07 x 10^{-4} m^3

Hc = clearance height = 0.011697 m

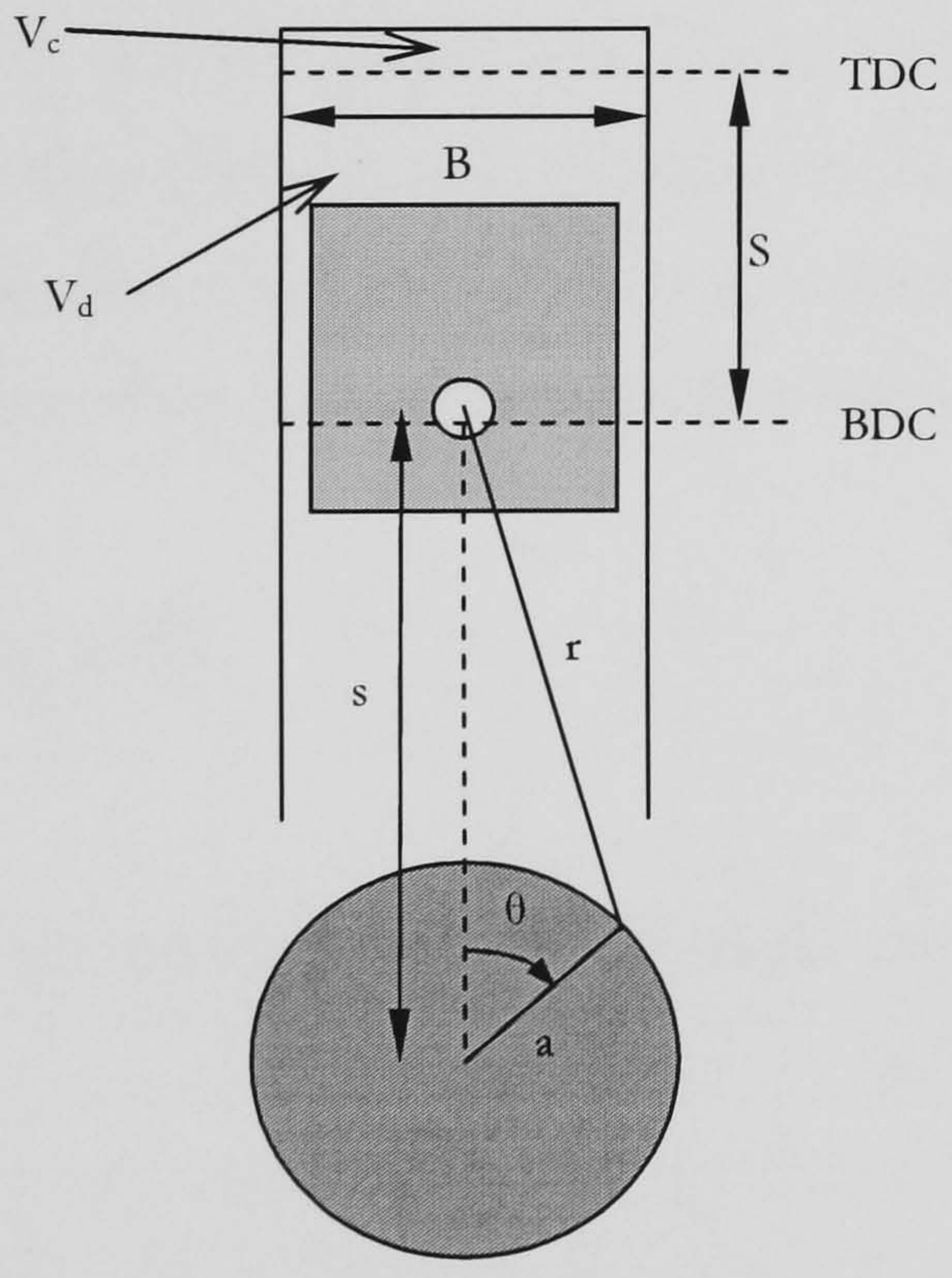

Figure 3.1 Piston and cylinder geometry of reciprocating engine

$$u_{t,tdc} \approx \frac{1}{2}\overline{U}_p \quad \text{(Equation 3.1)}$$

$$\overline{U}_p = 4aN \quad \text{(Equation 3.2)}$$

At 2000 rpm, the duration of expansion or power stroke is 15.0 milliseconds. Assume that this is the time allowed for completion of combustion. The instantaneous cylinder height at the end of combustion is 0.02736 m and half of cylinder bore is 0.0381 m. By taking the turbulent flame speed of 3.70 m/s, the calculated distance traveled by turbulent flame is 0.0555 m, which is sufficient to completely burn the entire cylinder air-fuel charge.

3.2.2 Turbulent Reynolds number

Turbulent Reynolds number, Re_t is estimated by the correlation described in Equation 3.3, where u_t is turbulent flame speed and l is the characteristics length taken as the clearance height, h_c. The engine bore is 0.0762 m and stroke is 0.111 m. With compression ratio of 10.5:1, the clearance height is 0.011m. Considering the condition during compression stroke just before spark ignition (25°BTDC) with temperature and pressure of air and methane at 300K and 7 bar, kinematic viscosity , ν, of stoichiometric air-methane mixture is estimated to be 16 x 10^{-6} m^2/s. Figure 3.2 shows the calculated turbulent Reynolds number at various engine speeds. The experiment with the Ricardo E6 engine will be limited to 2000 rpm only.

$$\mathrm{Re}_t = \frac{u_t l}{\nu} \qquad \text{(Equation 3.3)}$$

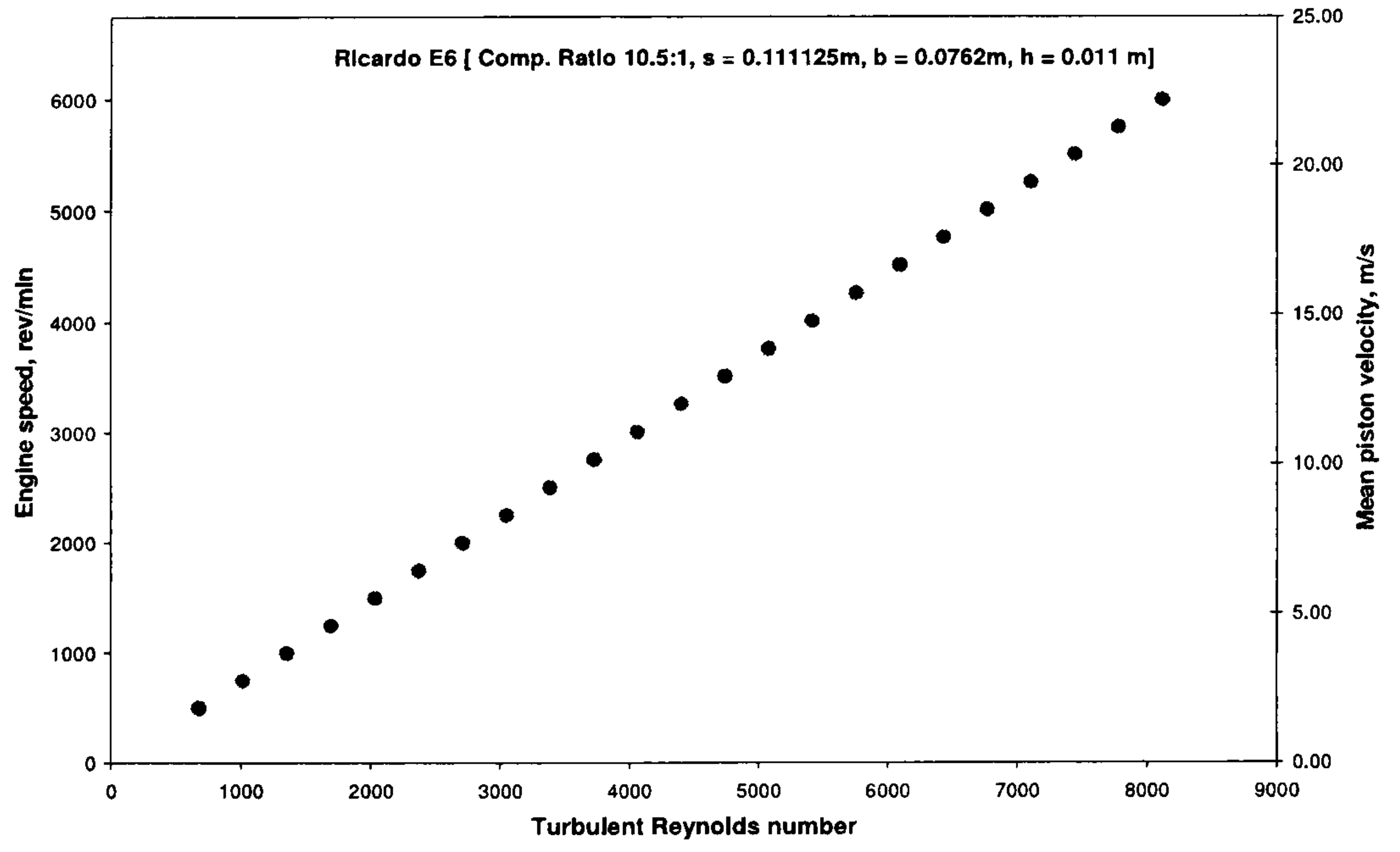

Figure 3.2 Calculated turbulent Reynolds number for flow in Ricardo E6 engine

In relation to the calculated turbulent Reynolds number, reliability of ignition of a homogeneous mixture can be evaluated based on a study of ignition limits for methane-air mixture shown in Figure 3.3 [Soriano, 1982]. In this work, mixture stoichiometry is set to a lambda value of 0.9, 1.0 and 1.1. According the calculated turbulent Reynolds numbers shown in Figure 3.1, which was based on the averaged turbulent flame speed at TDC and BDC, reliable ignition can be achieved for engine speed up to 6000 rev/min, which is a typical approximate of upper speed limit in automotive engine applications.

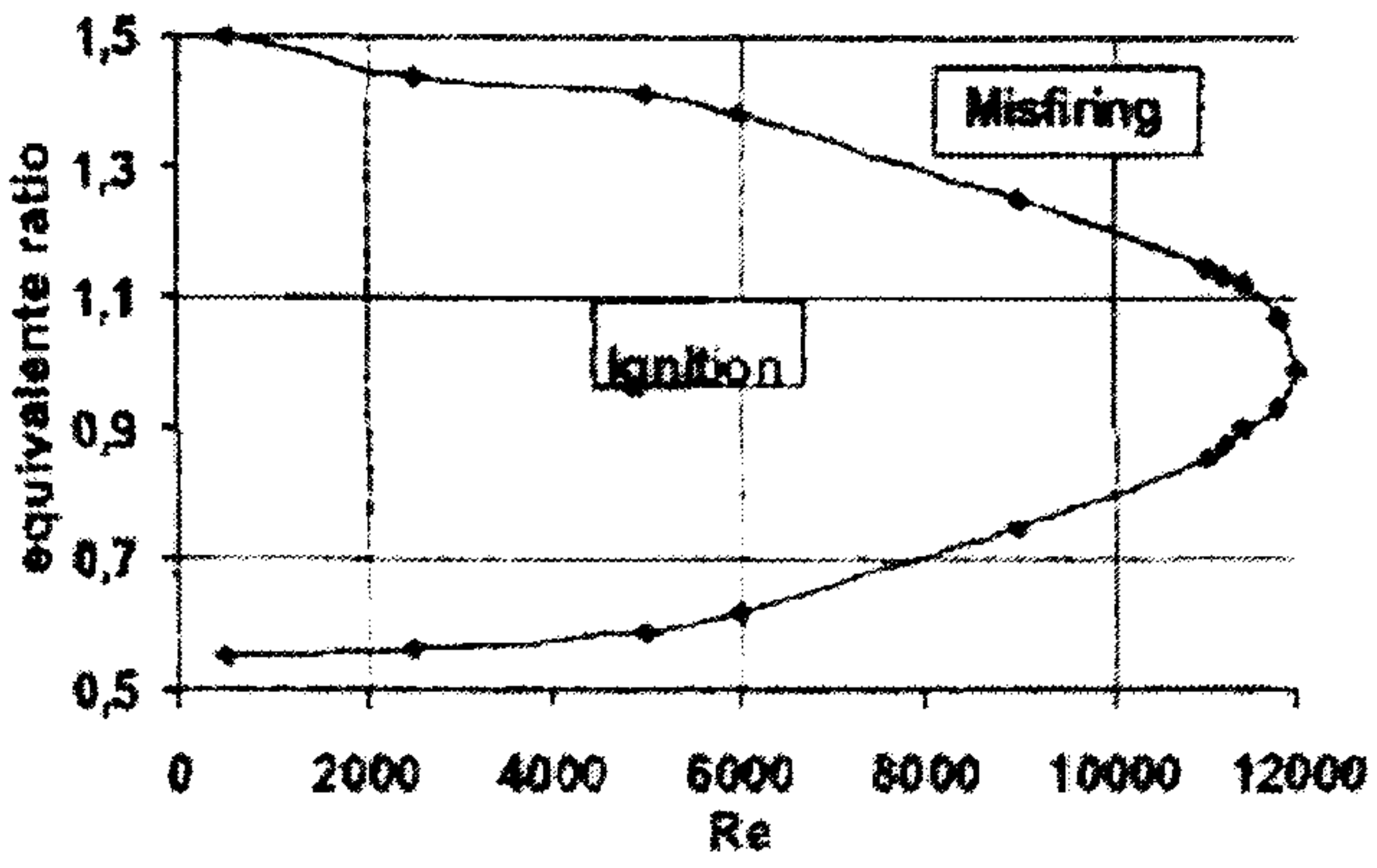

Figure 3.3 Influence of the flow Reynolds number on ignition for methane-air mixture [Soriano, 1982]

The calculated turbulent flame speed and turbulent Reynolds number indicate that complete combustion and reliable ignition are achievable at engine speed up to 6000 rev/min. In this work, the engine will only be run up to 1700 rev/min. This is because a spacer plate installation between the cylinder head and the crank case for optical access and placement of pressure transducer requires an addition of disk plate on top of the piston. This affects the dynamic harmony of the operations where harsh vibration occurs at engine speeds above 1800 rpm. At these speeds, result from Soriano [1982] indicates that combustion should be accomplished between equivalent ratio of 0.6 and 1.4 which correspond to lambda value of 1.67 and 0.714 respectively. These theoretical studies on the ideal operation provide useful information on the feasibility of engine operation with methane and strongly encouraged the design of an SPFI and the undertaking of an engine test programme.

3.3 Ricardo E6 engine

The Ricardo E6 engine is a 0.507 litre single cylinder engine with compression ratio set at 10.5:1 for this project. The bore and stroke are 76.2mm and

111.125mm respectively. Figure 4.4 shows the piston position and cam profiles. The horizontal axis represents crank angle where 0° corresponds to TDC at the start of the intake stroke and 360° refers to TDC at the end of compression stroke. The right-hand-side vertical axis indicates valve lift while the left-hand-side vertical axis is the piston position where position 0 indicates piston at BDC. Ideally the direct injection operation is characterised by fuel injection during intake valve close. However, because the duration between intake valve fully closes and ignition initiation is relatively short, proper injection advancement must be made in order to allow sufficient mixing of methane and air but not to sacrifice the gained volumetric efficiency from close valve operation.

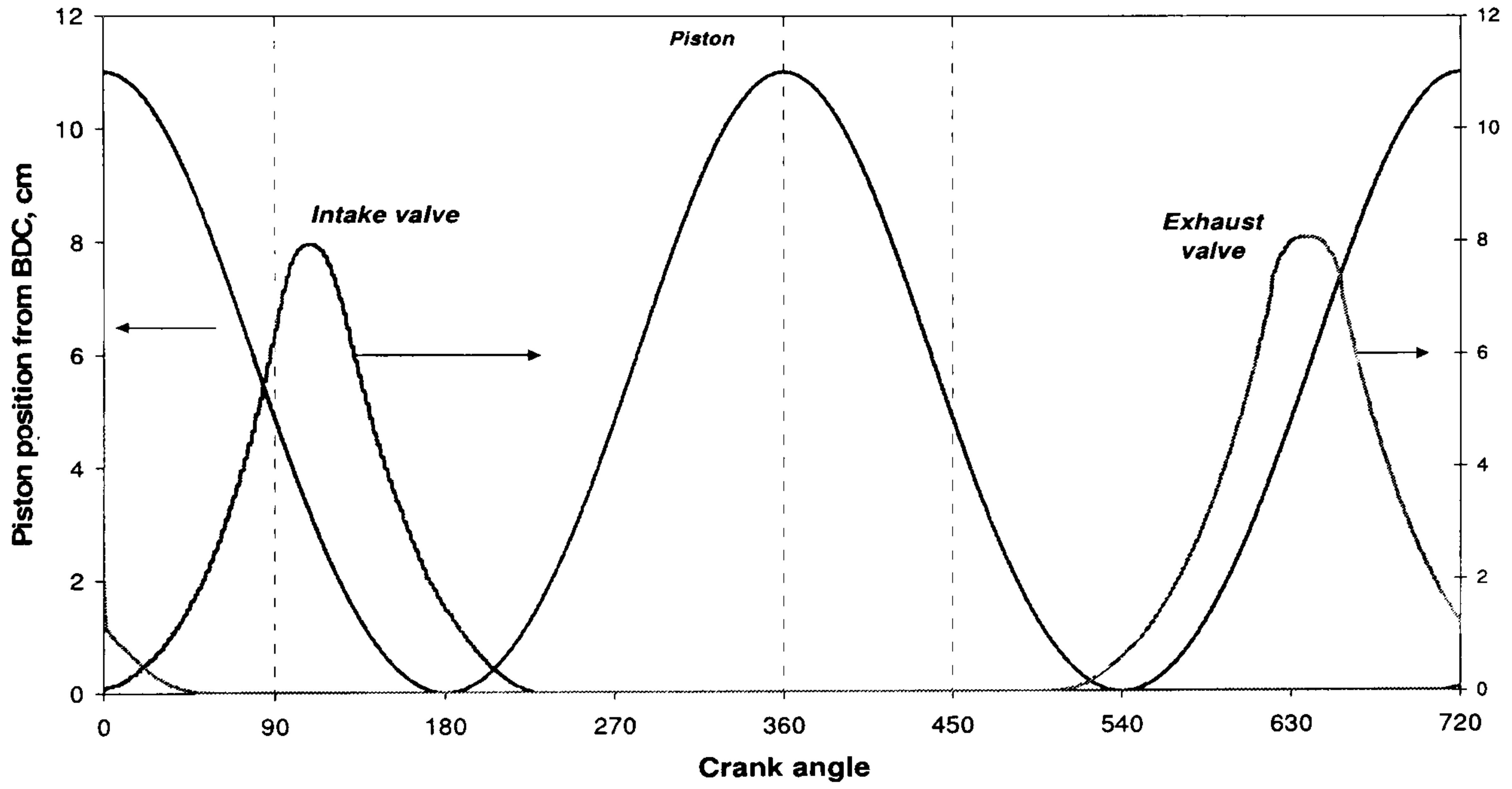

Figure 3.4 Piston position and cam profile for Ricardo E6 engine with gasoline cylinder head at 10.5:1 compression ratio

3.4 Methane injection pressures for direct injection method

One of the most important parameters dictating fuel delivery to the combustion cylinder under direct injection is the time limit for fuel injection. The time limit is idealised and described as the time starting from inlet valve fully closed to the time of the fully retarded spark (i.e. end of compression stroke). The limits imply the duration required to form a homogeneous mixture where air and fuel must be sufficiently mixed throughout cylinder before ignition takes place.

A simple calculation predicts the required injection pressure based on a fuel injector with a single 0.5 mm diameter nozzle operating on Ricardo E6 engine running with stoichiometric mixture at speeds up to 6000 rev/min. The effective cross sectional area of the injection nozzle is assumed to be 60% of actual value. Required methane mass per cycle is given by the following equation where V_{cyl} is cylinder total volume, ρ_{air} is air density, η_v is volumetric efficiency, and *AFR* is the air-fuel ratio of methane-air mixture.

$$m_{CH_4} = \frac{V_{cyl}\rho_{air}\eta_v}{AFR} \quad \text{(Equation 3.4)}$$

The effective fuel injector nozzle area, A_{eff} is related with the methane injection duration, $\Delta t_{injector}$, by the following equations where d_{inj} is the fuel injector nozzle diameter. Methane density, ρ_{CH4} was calculated based on the injection pressure.

$$A_{eff} = 0.6\pi\frac{d_{inj}^2}{4} \quad \text{(Equation 3.5)}$$

$$\Delta t_{injector} = \frac{m_{CH4}}{A_{eff}\sqrt{2\rho_{CH4}\Delta P}} \quad \text{(Equation 3.6)}$$

Pressure differential ΔP is the difference between injection pressure and cylinder pressure. Allowed injection duration Δt_{inj}, is estimated by is the duration of valve close during compression stroke, $\Delta t_{\theta,IVC}$, where $\theta_{TDC,comp}$ is TDC crank angle at the end of compression stroke (360° CA) and θ_{IVC} is the crank angle where inlet valve closes (214° CA). $\Delta\theta/\Delta t$ represents the crank angle travelled per unit time at a given speed.

$$\Delta t_{inj} = \Delta t_{\theta,IVC} = \frac{\theta_{TDC,comp} - \theta_{IVC}}{(\Delta\theta/\Delta t)} \quad \text{(Equation 3.7)}$$

For the Ricardo E6 engine with the cam profile shown in Figure 3.4, with *N* is engine speed in rev/min, this equation can be reduced to

$$\Delta t_{inj} = \frac{146}{6N}$$ (Equation 3.8)

For simplicity, the fuel injection is assumed to be a step function where the effects of needle lift and return on the instantaneous methane mass flow rate are neglected. This means the mass flow rate at the given nozzle diameter is of full calculated values at the time of injector needle lift and maintains its full values until nozzle is closed. Figure 3.5 shows the analogy used for calculating the mass flow rate of this estimation. The time between intake valve close and end of compression stroke (146° CA) are 24.33, 12.17, 8.11, 6.08, 4.87 and 4.06 milliseconds for 1000, 2000, 3000, 4000, 5000 and 6000 rev/min respectively. Figure 4.6 shows the ideal injection duration for various methane injection pressures at three different volumetric efficiencies.

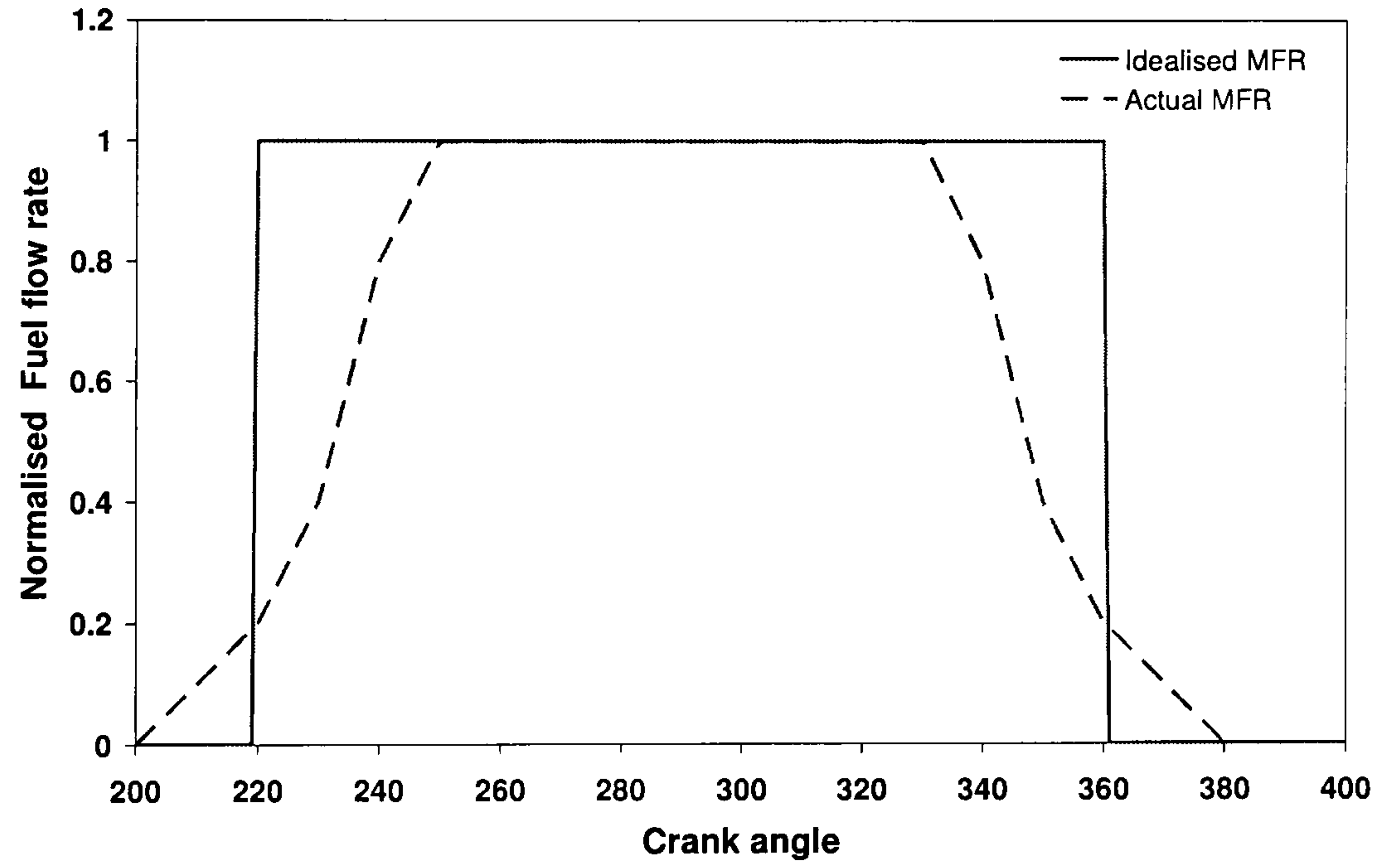

Figure 3.5 Effect of mass flow rate from the fuel injector needle lift behavior.

Since the engine will be run up to 1700 rev/min during the experiment, the direct methane injection should be done at pressure greater than 50 bars for sufficient fuel delivery. For injection pressure of 150 bars, the operation of engine is increased to 5000 rev/min. In the case of engine running up to 6000 rev/min, it is calculated that injection pressure should be in the excess of 150 bars. The FSI injector used in the experiment (see Chapter 4) was tested and worked up to 200 bar injection pressure. The volumetric efficiencies used to get the injection duration were based on the typical values for the Ricardo E6 performance from previous experimental works [Simms, 1994].

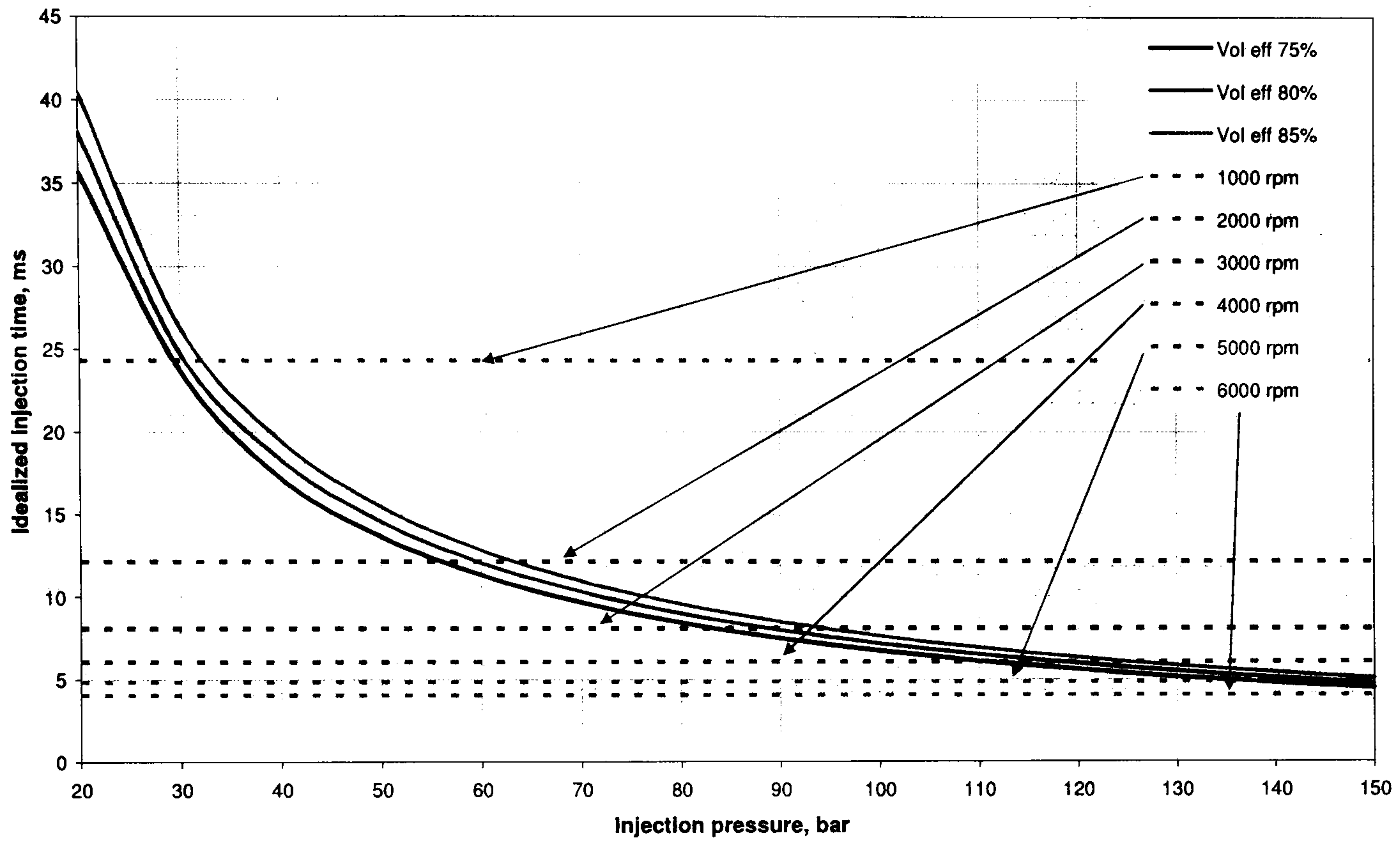

Figure 3.6 Injection durations of methane at various pressures and volumetric efficiencies on Ricardo E6 engine

3.5 Simulation studies

Simulation studies of the effects of methane use in spark ignition engines as gasoline substitute were undertaken using AVL Boost version 4.0 software. These had two objectives: first to simulate the operation and compare the performance of port injection engine running on gasoline and methane; second to simulate the operation and compare the performance of engine running on methane port injection and methane direct injection.

First, the port injection performance of the two fuels on a single cylinder engine was compared. The parameters of the engine were kept close to the parameters of the Ricardo E6 to be used in the engine experiment. Properties of methane were assumed to be the representative of natural gas. This study gives some comparison based on near-perfect combustion for each case based on the model input of 'perfect mixing' of air-fuel mixture in the combustion chamber. The engine operations are limited within the speeds covered in the physical experiments.

3.5.1 AVL Boost v4.0

AVL Boost is a one dimensional code for internal combustion engine modelling that accounts for wall friction, heat transfer, and energy losses in restrictions, volumes and pressure pulses. AVL Boost consists of three modules in the simulation: the pre-processor, the main program and the post processor.

The Pre-processor allows a graphical user interface by selecting the required elements from a displayed menu. The physical dimensions of each component are specified. Fluidic and thermodynamic properties are assigned to each component of the model. One-dimensional structure along the fluid flow is then build up and will be solve by the main program. The Main Calculation Program provides optimised solution algorithms for all elements. The flow in the pipe is treated as one dimensional. Pressures, temperatures and flow velocities obtained form the solution of the gas dynamic equation represent mean values over the cross section of the pipes. The Post Processor provides the following modes for the analysis of the calculated results: message analysis, transient analysis, traces analysis, series analysis and acoustic analysis. Further information can be found in the reference, AVL Boost User's Guide [2002].

One of the most important aspects in AVL Boost modelling is the determination of combustion model by heat release approach. The approach is done by specifying the rate of heat release, which is normally determined from cylinder pressure history. The direct input for the heat release curve is done using the approximation of Vibe Function. Vibe Function is presented in Equation 3.9 where x is mass fraction burnt, Q is total fuel heat input, θ is crank angle, θ_o is crank angle at start of combustion, $\Delta\theta_c$ is combustion duration, m and a are shape parameters (a = 6.9 for complete combustion).

$$\frac{dx}{d\theta} = \frac{a}{\Delta\theta_c}(m+1)y^m e^{-ay(m+1)} \qquad \text{(Equation 3.9)}$$

$$dx = \frac{dQ}{Q} \qquad \text{(Equation 3.10)}$$

$$y = \frac{\theta - \theta_o}{\Delta\theta_c} \qquad \text{(Equation 3.11)}$$

The integral of the vibe function gives the fraction of fuel mass that was burned since the start of combustion.

$$x = \int \frac{dx}{d\theta} d\theta = 1 - e^{-ay(m+1)} \qquad \text{(Equation 3.12)}$$

Therefore, other than specifying the physical parameters of the engine in the model, determination of rate of heat release and mass burnt fraction from the Vibe function is another important input to the model developed. In this regard, the AVL Boost pre-processing module requires input for combustion duration, $\Delta\theta_c$ and the shape parameters (*a* and *m*) for each fuel and fuel delivery system. The values can be obtained and adapted from experimental data.

3.5.2 Simulation of Ricardo Single Cylinder engine

The simulation of a single cylinder research engine used in the experimental part of the research was performed. The results represent the ideal operation of the engine. The results can be compared with the ones from engine testing in Chapter 5 and a two-way verification can be achieved.

3.5.3 Engine parameters

The basic parameters of the disk-shaped combustion chamber are listed in Table 3.2. The intake and exhaust valve lifts are adopted from the measured valve geometry and valve lift behaviour of the gasoline cylinder head valves for Ricardo

E6 engine. In the model, the geometry and dimensions of intake air path are specified from measurement of the air intake system in the same engine.

Parameter	Dimensions
Bore	76.2mm
Stroke	111.125mm
Connecting rod	241.27mm
Crank radius	43 mm
Swept volume	0.507 litre
No of valve	1 intake and 1 exhaust for each cylinder
Valve diameter	Intake 31.5mm / Exhaust 27 mm
Fuel type	Port injection and direct injection
Air intake	Naturally aspirated

Table 3.2 Single-cylinder model engine parameters

3.5.4 Operating parameters

Table 3.3 shows the operating parameters of the modelling. In the port injection fuel system, both gasoline and methane were used.

Fuel system	Port Injection & Direct Injection
Compression ratios	10.5
Inhaled air	1 bar @ 293.15K
Combustion start	MBT
Mixture stoichiometry	Stoichiometric air-fuel ratio
Engine speed	1100 rpm

Table 3.3 Single-cylinder engine operating parameters

3.5.5 Description of models

The models were developed based on the measured physical dimensions and profiles of the Ricardo E6 intake and exhaust systems, cylinder and camshaft-valves lifts. The difference between port injection model and direct injection model is the absence of fuel injector element in the direct injection model. Direct fuel injection is determined by specifying the evaporation rate of methane, which value is 512 kJ/kg.

3.5.5.1 Port injection

The port injection model consists of the following elements as in Table 3.4 and shown in Figure 3.7.

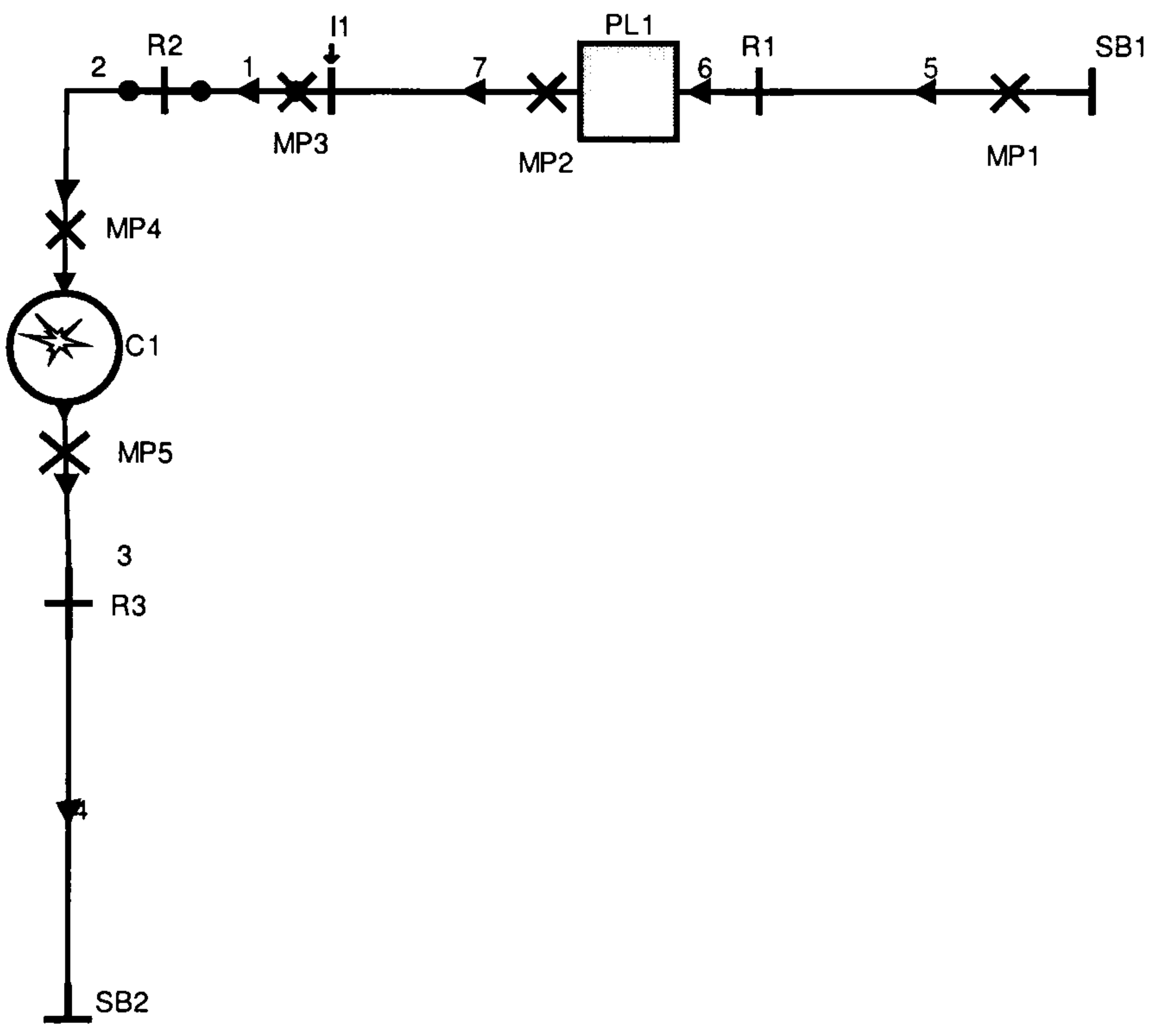

Figure 3.7 Model representation of port injection on Ricardo E6

3.5.5.2 Methane direct injection

In the direct injection model, fuel injector is taken out, but overall pipes lengths are kept the same. The elements are listed in Table 3.5 and shown in Figure 3.8.

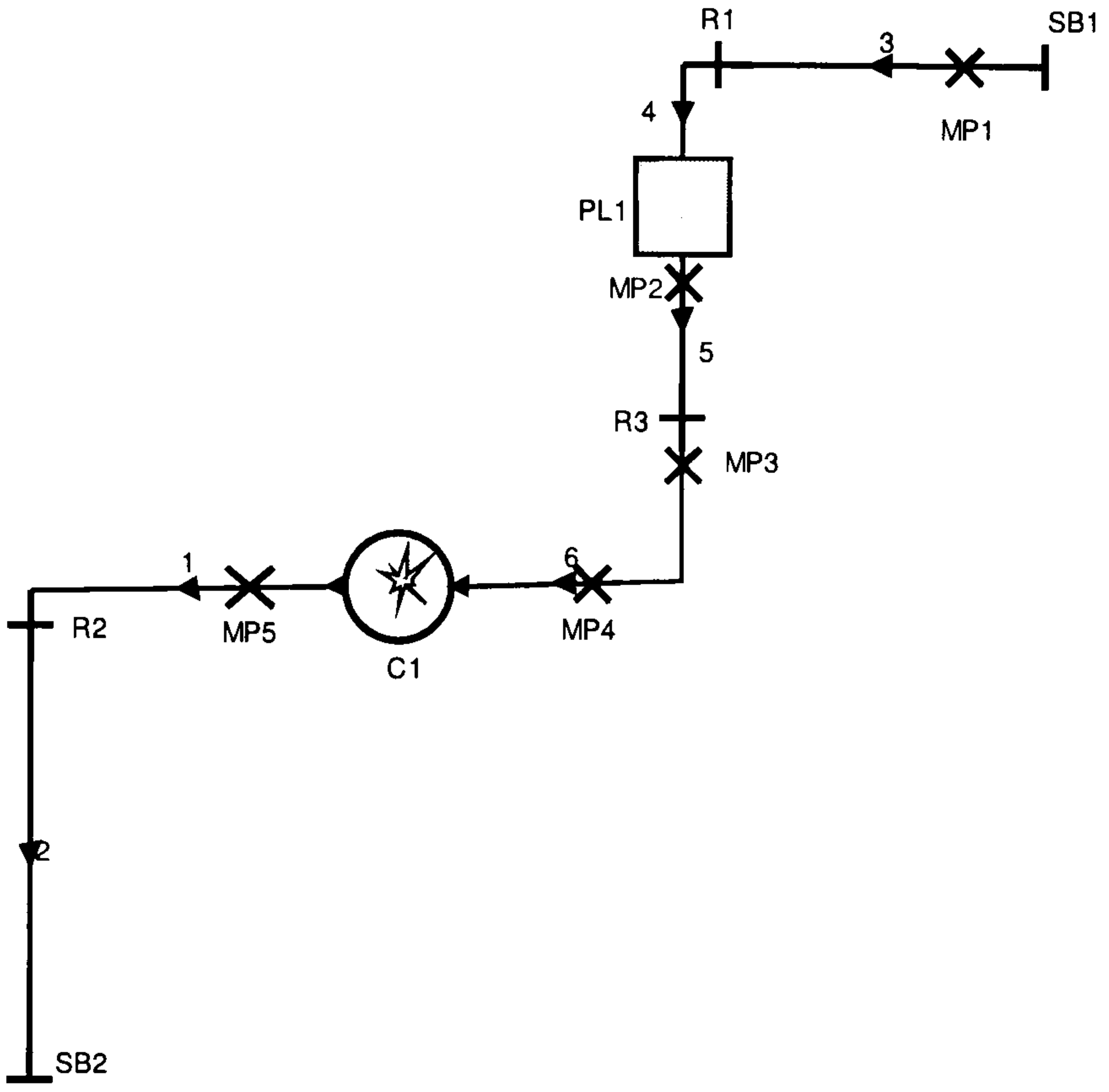

Figure 3.8 Model representation of methane direct injection in Ricardo E6 engine

3.5.6 Simulation methods

The model must be first closely matched the geometry, conditions and basic performance of the actual Ricardo E6 engine. This was done by confirming the simulation result with the motorised cylinder pressures of the actual engine. The volumetric efficiency at wide open throttle must be closely matched. This was done by adjusting the flow coefficient in each pipe, restrictions and plenum prior to the cylinder. Engine models were run without fuel and the compared with the intake manifold and peak cylinder pressure data from preliminary engine experiment. Once the volumetric efficiency and peak cylinder pressure at WOT matched the result from engine experiments, the models were saved and tested by varying other parameters.

As mentioned in the previous section, one of the most important inputs to the models is the Vibe function which indicates the mass burnt fraction of fuel-air mixture. It is important to note that specifying the Vibe function is very complex in nature because combustion behaviour depends on so many factors including engine breathing characteristic, fuel type, fuel stoichiometry, cylinder geometry, ignition timing and compression ratio. In order to simplify the modelling, the input parameters for Vibe function were adapted from the available literature. Input parameters (combustion durations, shape parameters and start of combustion) for Vibe functions with respect to different fuels and fuel delivery systems were derived from experimental data [Jones & Evans, 1985; Abraham, 1995; Evans & Blaszczyk, 1997] and from AVL Boost v.4.0 library. Table 3.4 shows the Vibe function parameters used for the simulation. These values are based on the facts that:

- Combustion duration of methane is about 2 to 10° CA longer than of gasoline
- Ignition delay of methane is in the order of 50% longer than of gasoline requiring a more advanced ignition
- Combustion duration is shorter with direct injection compared to port injection

Fuel system	Shape parameters		Combustion duration, °CA	Combustion starts, °CA BTDC
	m	*a*	$\Delta\theta_c$	θ_o
Gasoline port injection (GPI)	1.6	6.9	47	5
Methane port injection (CH_4 PI)	1.6	6.9	53	10
Methane direct injection (CH_4 DI)	1.6	6.9	50	7

Table 3.4 Input parameters for Vibe functions

3.5.7 Results

Table 3.5 shows the result of AVL Boost simulation where selected engine performance are presented.

	IMEP, bar	Thermal efficiency, η_{th}	ISFC, g/kWh	Volumetric efficiency, η_v	Fuel per cycle, g	Peak pressure, bar	Indicated torque, Nm	Indicated power, kW
GPI	9.80	32.59	253.93	84.10	0.0350	50.38	39.52	4.55
CH_4 PI	8.32	31.72	226.98	76.03	0.0266	47.52	33.54	3.86
CH_4 DI	8.342	30.36	237.12	85.04	0.0279	47.67	33.65	3.88

Table 3.5 AVL Boost simulation results

The results show that when methane is used in a port injection engine, volumetric efficiency is reduced by 9.6% compared to gasoline port injection. This reduction has caused the fuel heating value per cycle decrement of 13% (from 0.0350 g/cycle to 0.0266 g/cycle → 1.5 kJ/cycle to 1.3 kJ/cycle) when the heating value of gasoline and methane are taken to be 44 MJ/kg and 50 MJ/kg respectively. As a direct result indicated power and torque are decreased by 15%. Indicated mean effective pressure (IMEP) was reduced from 9.80 bar to 8.32 bar. Thermal efficiency is reduced from 32.59% to 31.72%, but the specific fuel consumption is improved by 11%. The peak pressure was reduced from 50.38 bar to 47.38 bar.

The reduction of engine performance with methane port injection is partially recovered with direct injection. The most noticeable improvement is the volumetric efficiency increase to 85.04%, which is even better than gasoline port injection. As a result, the fuel mass per cycle is increased to 0.0279g, therefore increasing the heating value to 1.4 kJ/cycle. This improvement resulted in power and torque recovery by 0.52% and 0.33% respectively. However, the downside of direct injection is the reduction fuel economy advantage gained from fuel conversion. This is shown by thermal efficiency reduction from 31.72% to 30.36% and ISFC increased from 226.98 g/kWh to 237.12 g/kWh.

The AVL Boost modelling, which is based on the ideal operation of the engine has shown that direct injection method can mitigate some of the fundamental performance lost when methane replaces gasoline in a spark ignition engine. It is therefore providing a benchmark for the potential improvement of an engine converted to methane direct injection such as the one that will be explored in the full scale engine experiment described in Chapter 5.

3.6 Discussion and conclusion

Ignition reliability and combustion completeness

The preliminary investigations on the combustion, ignition and engine performance has been presented. Even though the engine with similar settings has been run successfully with natural gas previously [Simms, 1994], the estimating calculations for turbulent speed and turbulent Reynolds number were done to verify the feasibility of methane operation. The values obtained from the above-mentioned calculations indicate that reliable ignition and combustion completeness can be achieved with high probability within the operating conditions set for the physical experiments.

Methane injection pressure

Determination of injection requirements for direct fuel injection method is highly critical because it significantly effects the mixture formation. In the port injection mode, the space and time allowed for air-fuel mixing is greater due to injection happening in the intake manifold while intake valve is opened and mixing can continue until spark plug ignites. But because methane has a relatively low density, some air must be displaced in the mixing process which reduces the amount of intake air, thus decreases volumetric efficiency and charge energy. On the other hand, in direct injection mode of fuel delivery, air-fuel mixing time is limited to the duration of intake valve close in order to preserve the gained volumetric efficiency. The volumetric efficiency is gained due to closed valve injection where maximum air had been induced during intake stroke before fuel injection takes place. However, the mixing time for gas jet with air, thus the combustion rate are slower than the ones of vapour spray with air as described by Abraham et. al. [1995] making it more difficult to achieve adequate mixture in the direct injection mode.

Calculation for the injection gas pressure was carried out based on the limitation of close valve injection and engine speed range in the physical experiment. Behaviour of the fuel injector was assumed to be ideal. It was found that for engine speed up to 2000 rpm, a minimum methane pressure of 60 bar is required for volumetric efficiency of 80%. Higher injection pressures are required for faster running engine, where at 6000 rpm, injection pressure in the excess of 150 bar is mandatory. However, the actual close-valve injection with the limitations described will require higher injection pressure because of the fuel injection behaviour described in [Yuan, 1990] as shown in Figure 3.9. The actual valve lift, and therefore mass flow rate do not follow the ideal input function where there will be valve lift delay with respect to input current time and also exponential increase and decrease of mass flow rate at both ends of injection process. Since the experiment with the Ricardo E6 engine will be limited to 1700 rpm, it was decided that injection pressure of 60 bar will be applied on the SPFI direct injection. If stable ignition and combustion achieved from this pressure setting, further experimental investigation will be carried out but if the injection pressure do not suffice the requirement, a higher injection pressure will be used.

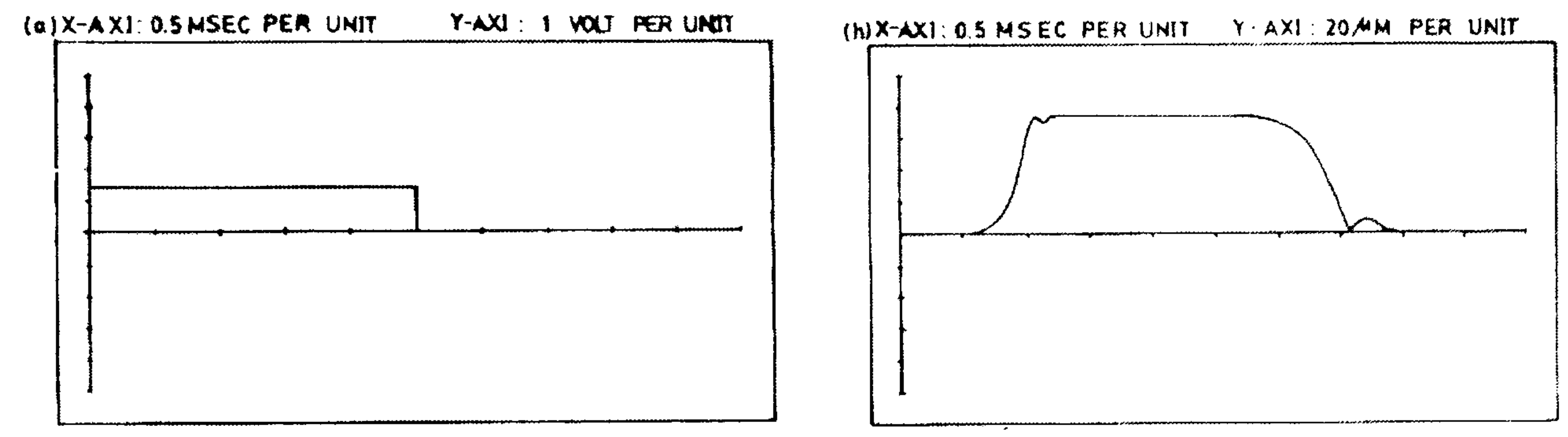

Figure 3.9 Input function/electric current (left) and actual valve lift (right) of a solenoid actuator [Yuan, 1990]

AVL Boost Simulation

The most important initial investigation is the use of AVL Boost v.4.0 as a simulation tool for modelling Ricardo E6 engine operations with different fuels and fuel systems. The effect of replacing gasoline with methane in the port injection single cylinder engine was measured. Volumetric efficiency was reduced by 9.6%, decreasing charge energy and therefore output power was decreased by 15%. However, with methane, the specific fuel consumption was 11% superior due to higher methane specific heating value which offset the charge energy loss from lower volumetric efficiency. The lost volumetric efficiency was recovered and even better than gasoline port injection when direct injection method was utilised in methane operation. The average volumetric efficiency of CH_4 DI is 1.1% higher than the one of G PI. Thus it results in higher charge density compared with CH_4 PI, which is the basis of performance improvement.

Chapter 4

DEVELOPMENT OF SPARK PLUG FUEL INJECTOR (SPFI)

4.1 Introduction

The main goal of this work is to develop a novel fuel injector that enables conversion from gasoline operation to methane direct injection without any modification to the original engine structure. The conversion can be achieved by a combination of a fuel injector with a spark plug without changing the spark plug threaded section that attaches it to the engine body. The objectives of this system development can be summarised as follows:

1. To design a combined spark plug and fuel injector for directly injecting gaseous fuel into combustion cylinder at the pressures found with methane fuel.

2. To identify or develop a solenoid that provides enough force to operate a fuel injector needle against the high closing force that results from gas pressure, spring force and gravitational effect.

3. To operate the injector over an extremely short time interval for completion of fuel delivery during each engine cycle at engine speed up to 6000 rpm.

4. To produce a reliable and durable injector for continuous high pressure and temperature operating conditions.

The final injector design was completed after fabricating, testing, modifying and validating four different prototypes on a Ricardo E6 engine. These prototypes can be classified as initial design, SPFI first prototype, SPFI second prototype and final SPFI.

4.2 Design considerations

Direct fuel injection in IC engines is subject to more demanding constraints than port fuel injection due to the direct exposure of the injector nozzle to the combustion chamber and limited time for air-fuel mixing. The fuel injector must be able to withstand high cylinder pressure and temperature, as well as delivering highly accurate metering of fuel for precise cylinder air-fuel ratio. Based on the simplified theoretical calculation and results from AVL Boost simulations shown in Chapter 3, there are three main constraints that the injection system must satisfy for successfully operating with methane direct injection.

1. The fuel injector must be able to operate at methane pressure of at least 20 bar and up to 100 bar for complete fuel delivery.
2. The fuel injector should withstand up to 80 bar peak cylinder pressure and 1500K peak cylinder gas temperature without deteriorating its performance.
3. The injection nozzle at the surface of the combustion cylinder must not exceed the quenching distance of methane-air combustion of 2.0 mm [Goodger, 1982, Potter, 1956] to avoid backfiring to the solenoid valve, yet be big enough to avoid substantial pressure lost in the fuel path.

4.3 Conceptual design

It was first envisioned that the all components in the combined fuel injector and spark plug would be developed from scratch. SPFI consists of a spark plug, fuel path and injection nozzle integrated in a single body. Fuel delivery is controlled by a solenoid-operated needle-lift valve. Figure 4.1 shows the conceptual design schematic.

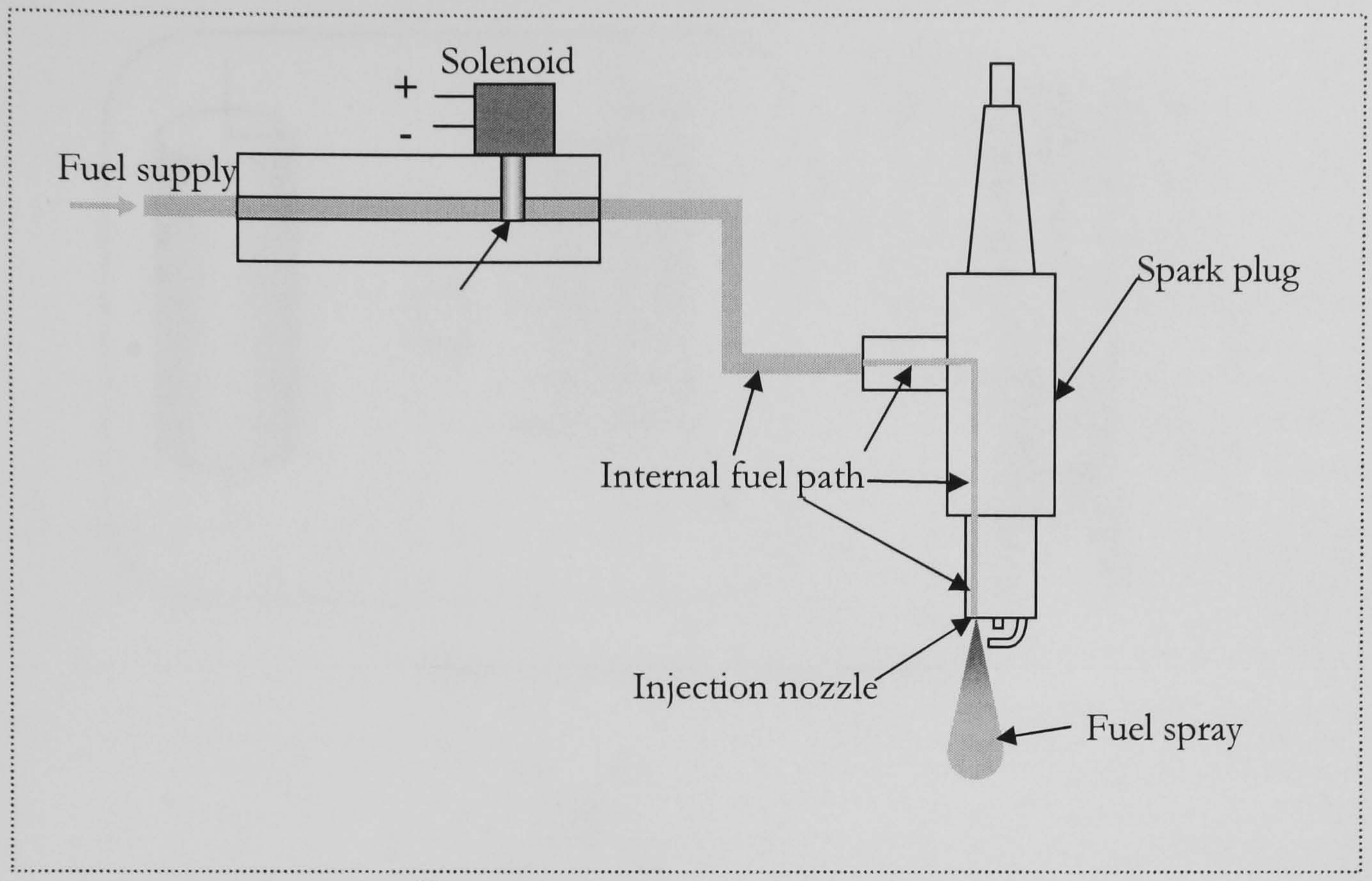

Figure 4.1 Conceptual design of SPFI

4.4 Design processes and stages

4.4.1 Solenoid valve

In Figure 4.2, the schematic of an initial design for the solenoid valve is shown. The solenoid was made from windings of enamelled copper wire of 0.33 mm diameter. The valve was a carbon steel ball that closed the fuel path by blocking a narrow path. A spring with a spring constant of 9.35 N/mm was inserted between the plunger ball and its retainer and compressed at a distance of 0.672 mm to provide closing force from 80 bar peak cylinder pressure on the 1 mm diameter nozzle hole. Figure 4.3 shows the detail dimensions of the solenoid-ball plunger system.

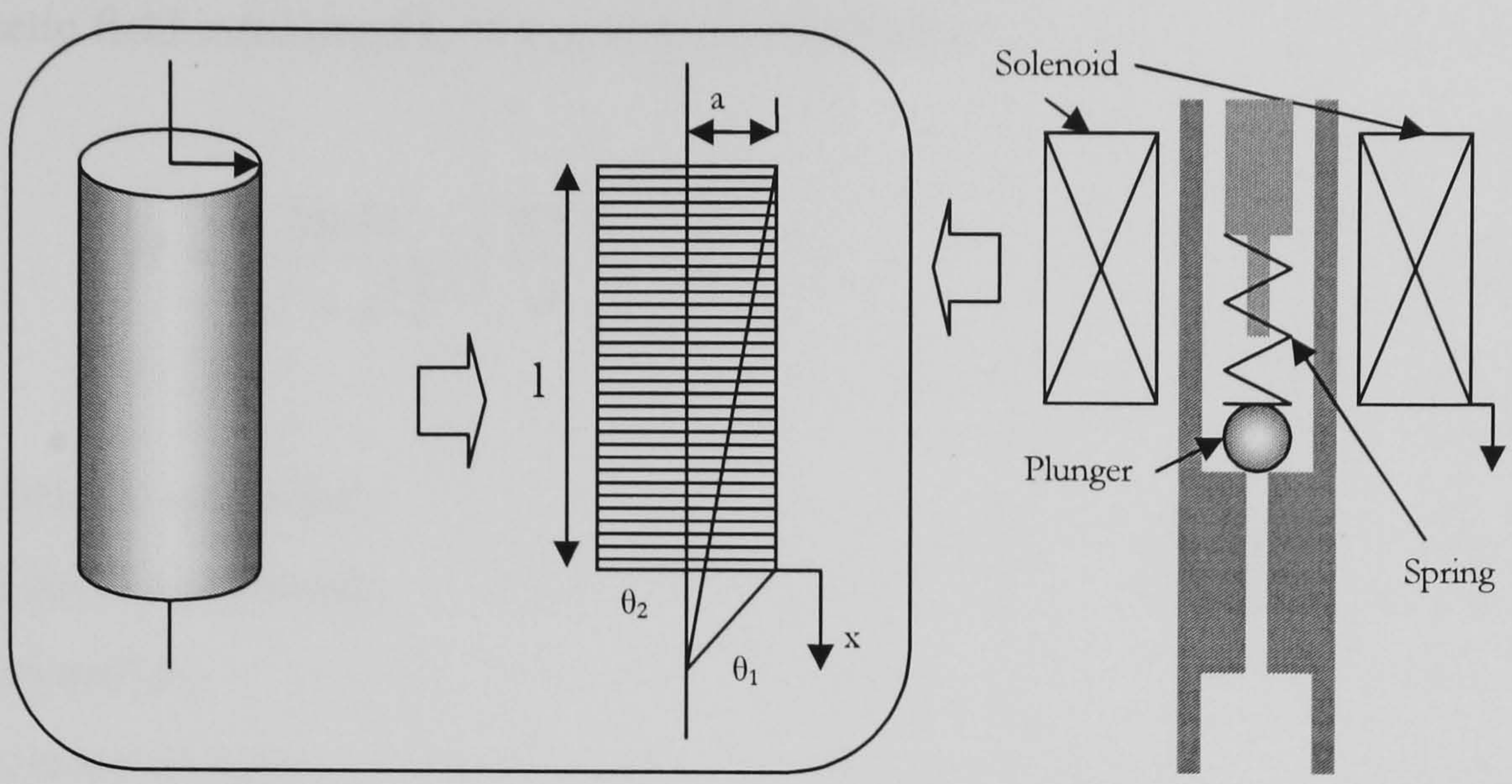

Figure 4.2 Schematic of solenoid valve

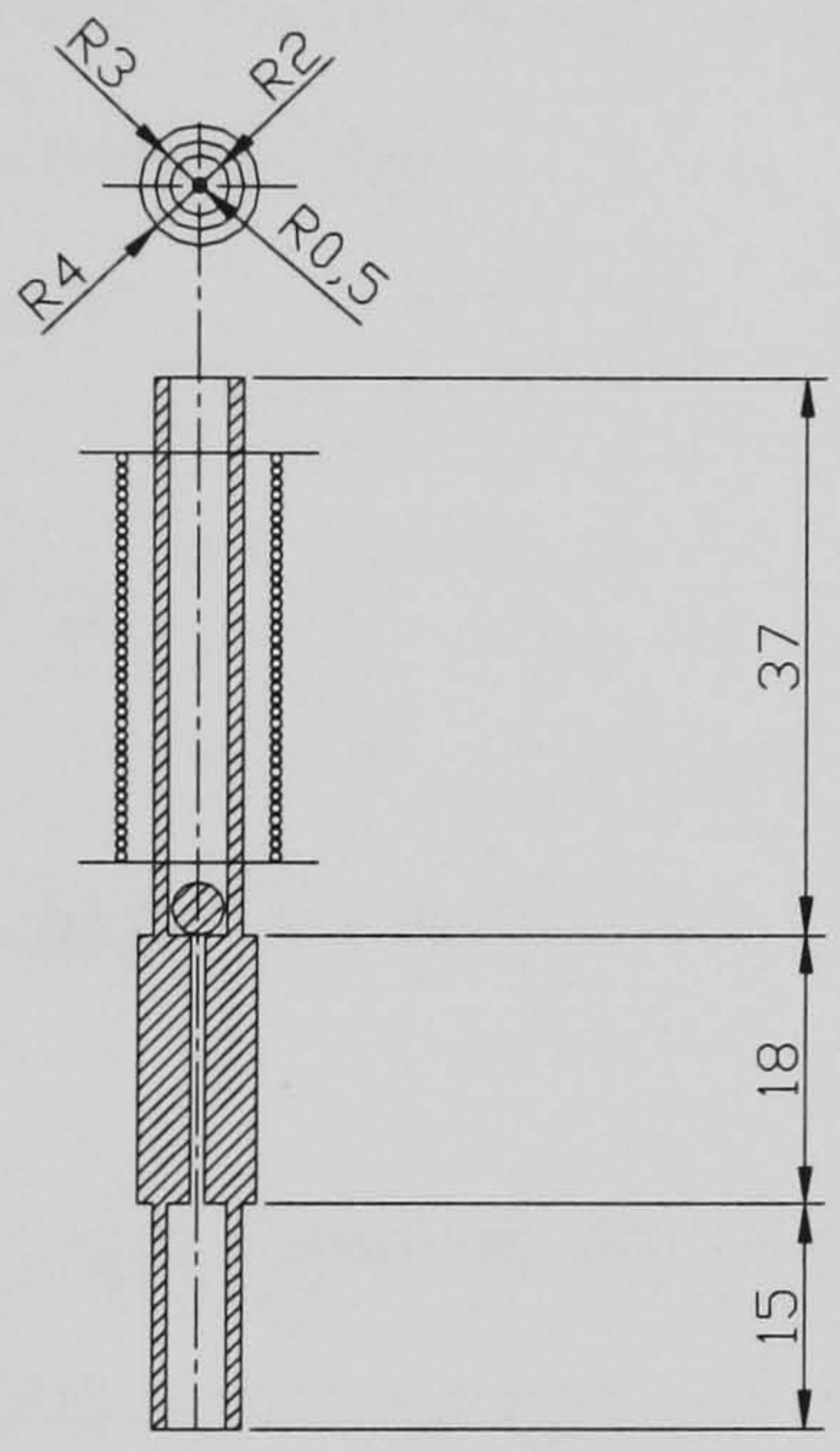

Figure 4.3 Detail design of solenoid valve (all dimensions in mm)

The solenoid force is determined by the magnetic energy produced by the winding solenoid coils. Magnetic energy, E is defined as

$$E = \frac{1}{2} L I^2 \quad \text{[Joule]} \qquad \text{Equation (4.1)}$$

Magnetic field, B is defined as

$$B = \frac{4\pi I N}{10000c} \quad \text{[Tesla]} \qquad \text{Equation (4.2)}$$

Magnetic field intensity, H, of a solenoid is defined as

$$H = \frac{2\pi n I a^2}{\left(x^2 + a^2\right)^{1.5}}\left(\frac{250}{\pi}\right) \quad [\mathrm{A.m^{-1}}]$$ Equation (4.3)

a = solenoid radius [m]

L = inductance [henry]

I = current [A]

n = number of turns

l = solenoid length [m]

N = n/l= number of turns per unit length [# turns/m]

x = plunger distance from solenoid end [m]

c = speed of light = 3.0 x 10^8 m/s

Equation (4.3) can be rewritten as

$$H = 2\pi N I\left(\cos\theta_1 - \cos\theta_2\right) \quad [\mathrm{A.m^{-1}}]$$ Equation (4.4)

θ_1 and θ_2 are defined as the angle between the solenoid symmetrical axis and a straight line drawn from the point x_i of solenoid end to the bottom end and top end of solenoid periphery respectively, as shown in Figure 3.2. The force on the plunger is calculated using the following correlation.

$$F = -\frac{d}{dx}\left(\frac{\mu_c - \mu_p}{8\pi}\right)H^2 V \quad [\mathrm{N}]$$ Equation (4.5)

μ_p = relative permeability of plunger

μ_c = relative permeability of medium

V = plunger volume

In order to calculate relative permeability, the following equation in used.

$$\mu = \frac{B}{B_o}$$ Equation (4.6)

$$B_o = \mu_o H$$ Equation (4.7)

B = induction

B_o = induction in free space, called the field in SI

μ_o = permeability of free space = $4\pi \times 10^{-7}$ H/m

Figure 3.4 shows the first tested fuel line. Figure 3.5 show the same device with the developed solenoid around it.

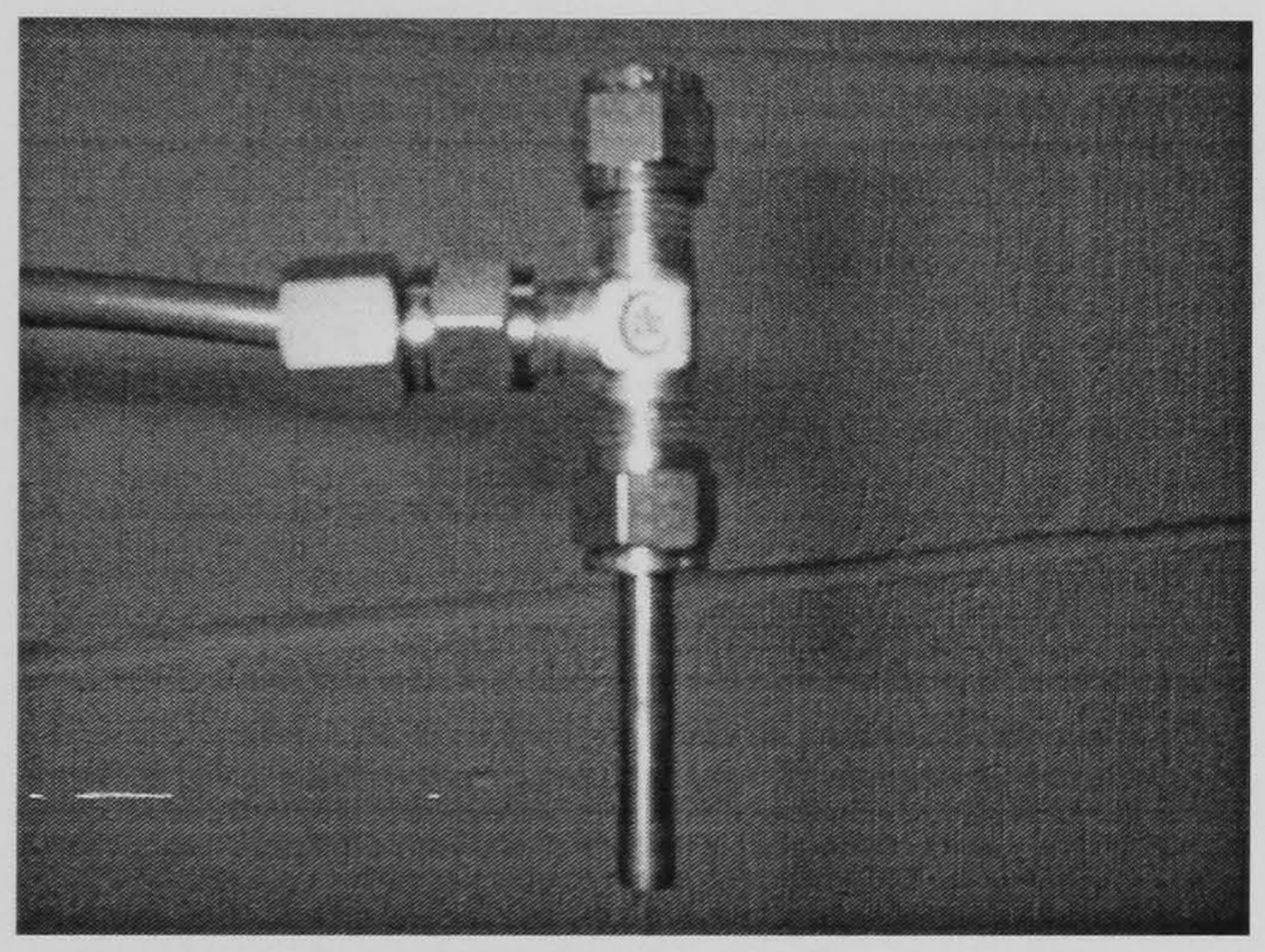

Figure 4.4 Fuel line and valve

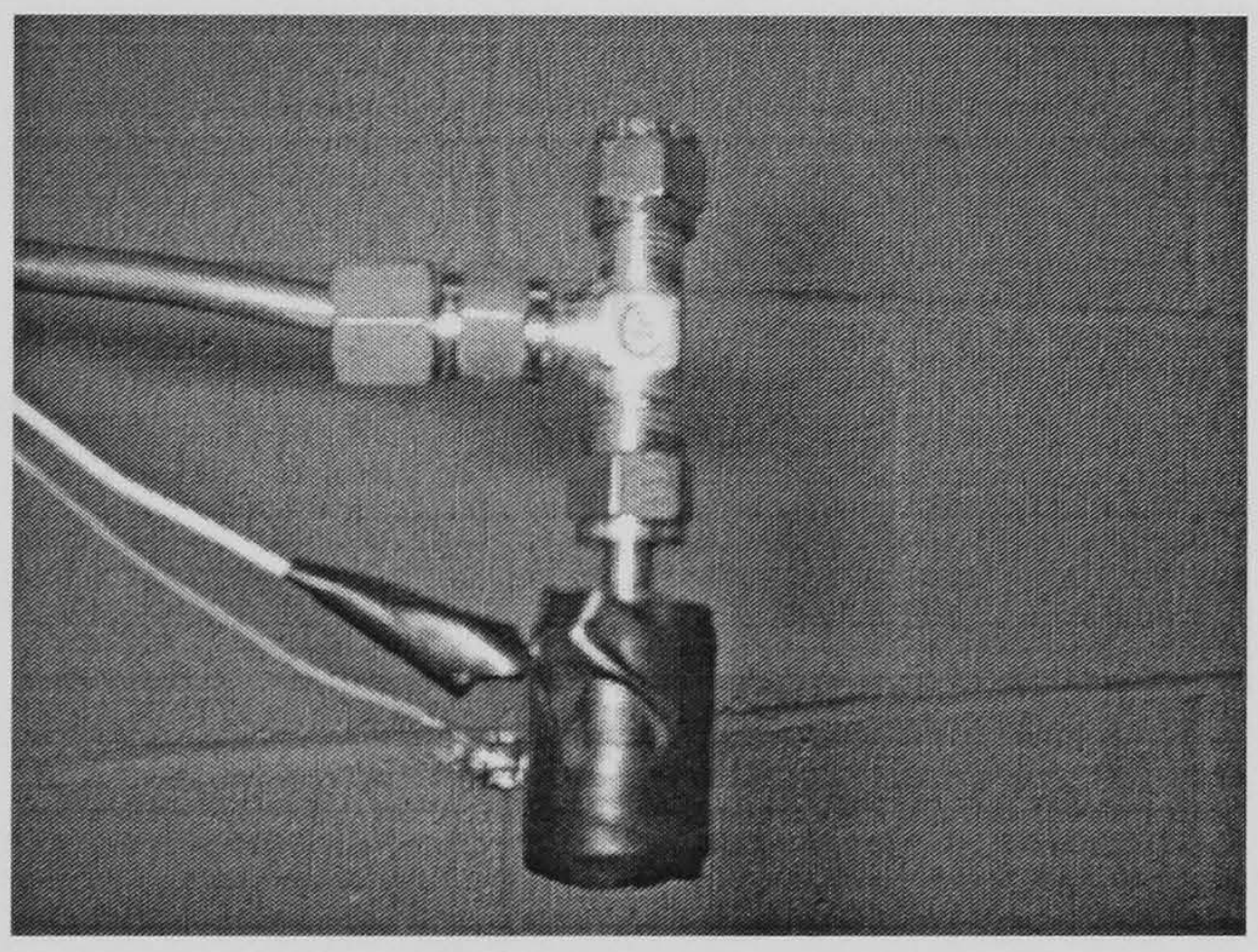

Figure 4.5 Fuel line, valve and solenoid

The calculation on the solenoid force on the plunger can be made based on Equations 4.1 to 4.7. The solenoid was made from 7 layers serial winding of a 0.33 mm diameter enamelled copper wire. The wire was wound on a solenoid casing of 4.25 mm diameter (a = 2.125mm) and 3 cm long (l = 30mm). Seven layers of solenoids connected in series gives N = 3571 turns/m. The permeability of the plunger was 1.01 W/A.m. The plunger was 3mm in diameter and with its mass of 0.00011 kg, the force due to gravity was 0.0011N. The force resulted from the spring with 9.35N/mm spring constant, compressed by 0.672mm is 6.28N and force due to methane pressure of 20 bar on the cross-sectional area of the ball was 2.39N. So the total force that solenoid must provide to open the valve is approximately 8.68N. A theoretical calculation of solenoid force developed at distance along its symmetrical axis starting from $x = 0$ (solenoid end as in Figure 4.2) is shown in Figure 4.6. Based on input current between 1.1 and 5.0 amperes the result indicates that this solenoid must operate with at least 3.0 amperes.

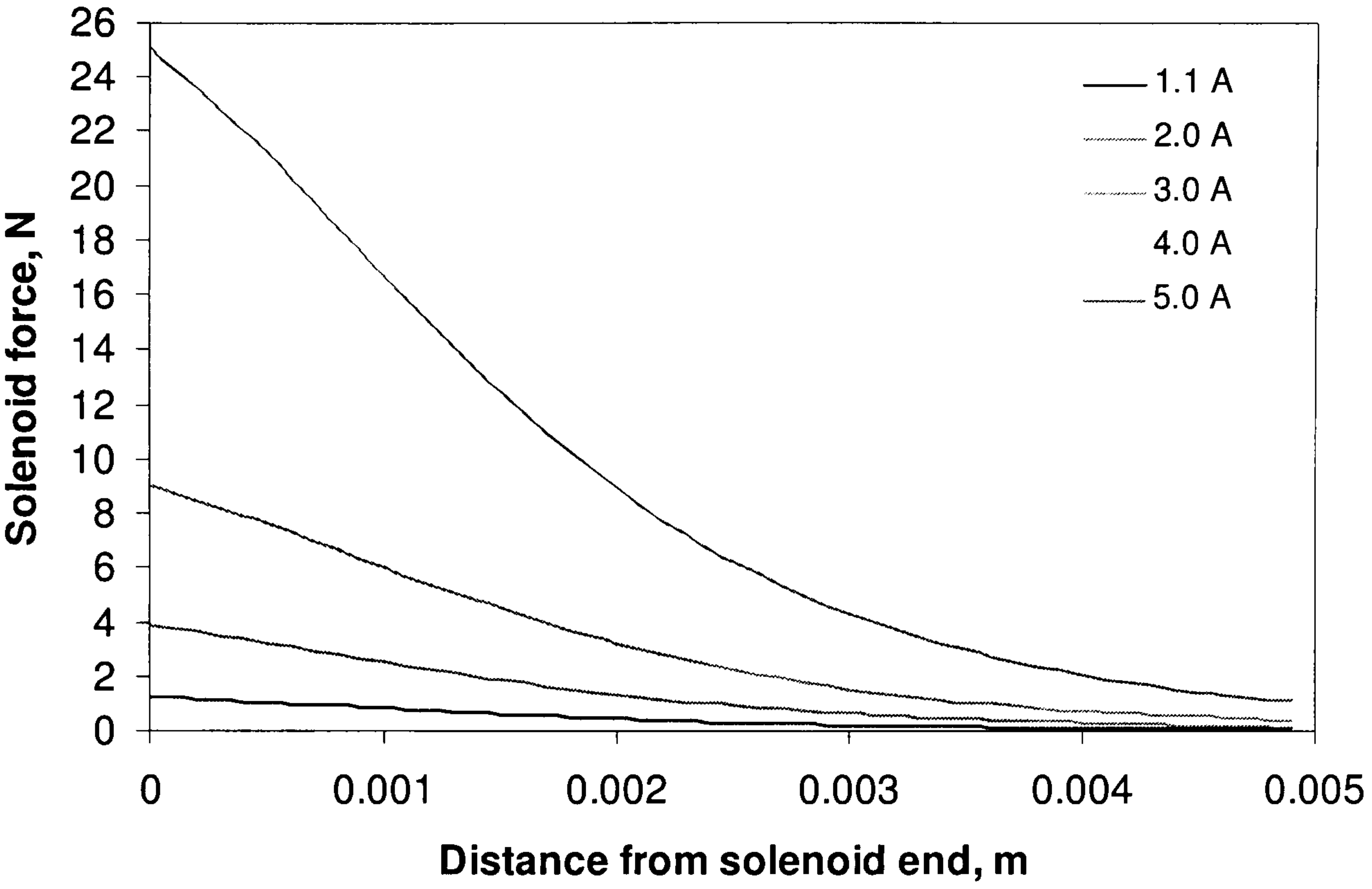

Figure 4.6 Theoretical value of solenoid force along symmetrical axis at various input current

An experiment was carried out to demonstrate the operation of the newly developed solenoid as shown in Figure 4.7. The solenoid was operated by a driver circuit, shown in Figure 4.8 which consists of a power supply unit capable of delivering up to 12 volts and 5 amperes, a pulse generator to generate high frequency signal and a field effect transistor (Mosfet) that acted as a gate to the supply power at frequency set by a pulse generator. A pressure transducer was placed 2mm from injection nozzle (Figure 4.10), opposing the outlet flow. Its output voltage was amplified and sent to the data acquisition system. Unfortunately, the solenoid valve was not capable of operating because if the input current was increased to more than 1.4 amperes, the enamel on the copper started to melt and consequently destroyed the solenoid. It was initially thought that the failure was due to fabrication fault but this was proven wrong when two more prototypes failed due to the same cause.

The next step was to repeat the calculation and experiment with a different plunger. Because the input current was limited to 1.4 amperes, another way to increase solenoid effect was to increase plunger volume. Figure 4.9 shows the new plunger which was a 3mm diameter and 6mm long cylinder-shape carbon steel. This increased the volume of plunger by 300% compared to the spherical ball. With the same material, increasing of plunger volume should increase the magnetic effect on it, because magnetic force is directly proportional to plunger volume. However, the new plunger failed to work as well and this was concluded due to: 1. limited magnetic force developed by the solenoid as a result of restricted current input and 2. relatively lower-than-theoretical magnetic permeability value of plunger material which resulted in low magnetic effect on it.

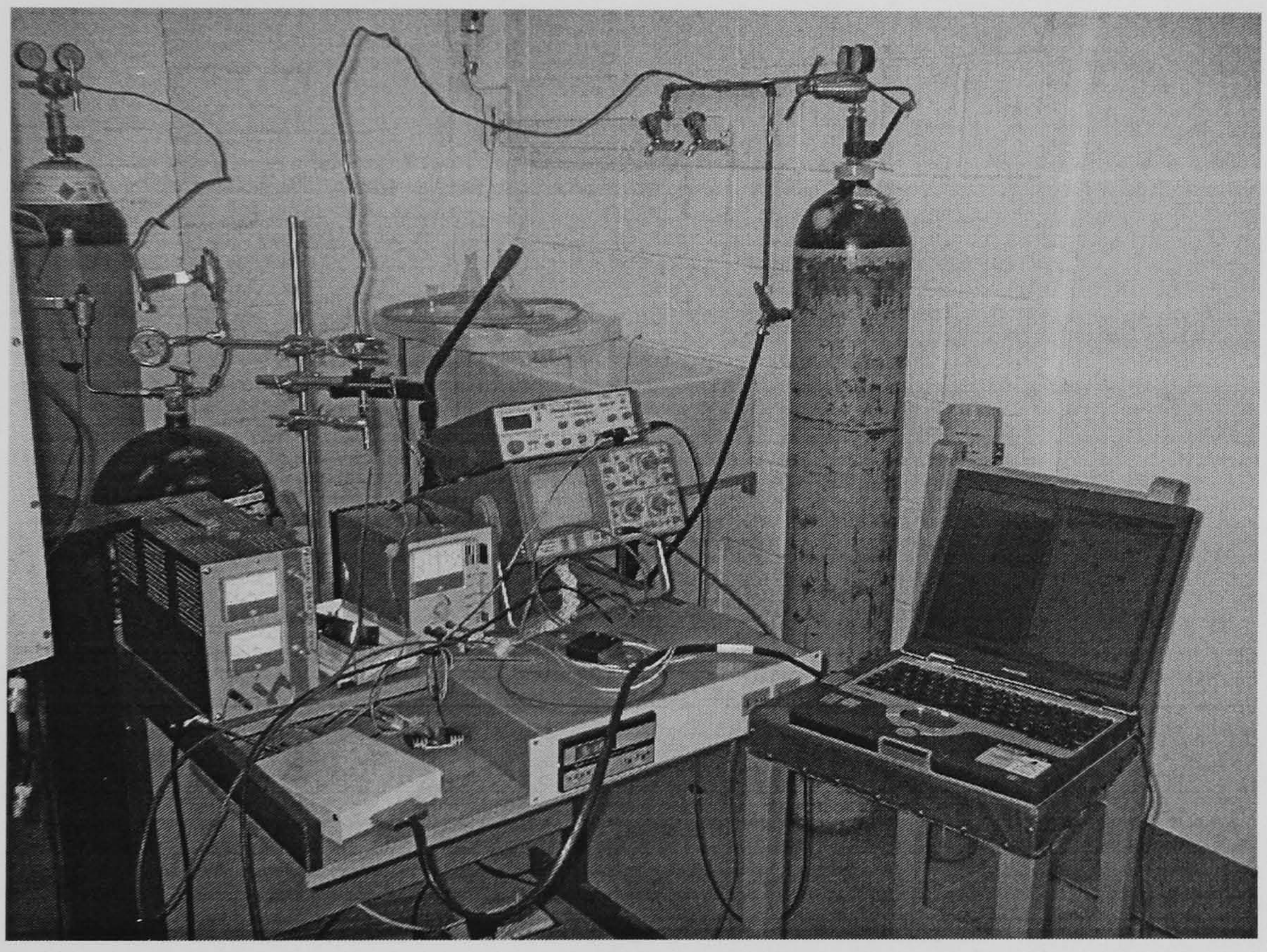

Figure 4.7 Arrangement for solenoid operational testing

The next step was to use a standard off-the-shelf solenoid to operate the plunger valve system. The solenoid selected was the OMVL Dream XXXI shown in Figure 4.10. It is a solenoid valve use for natural gas port injection system which operates at pressures lower than the SPFI operating pressure. One of the solenoid was taken out from its casing and placed around the plunger-type injection nozzle developed. The same experiment was performed and results showed that the OMVL

Dream XXXI injector valve can operate only up to 6 bar. It was concluded that it was not suitable for this application.

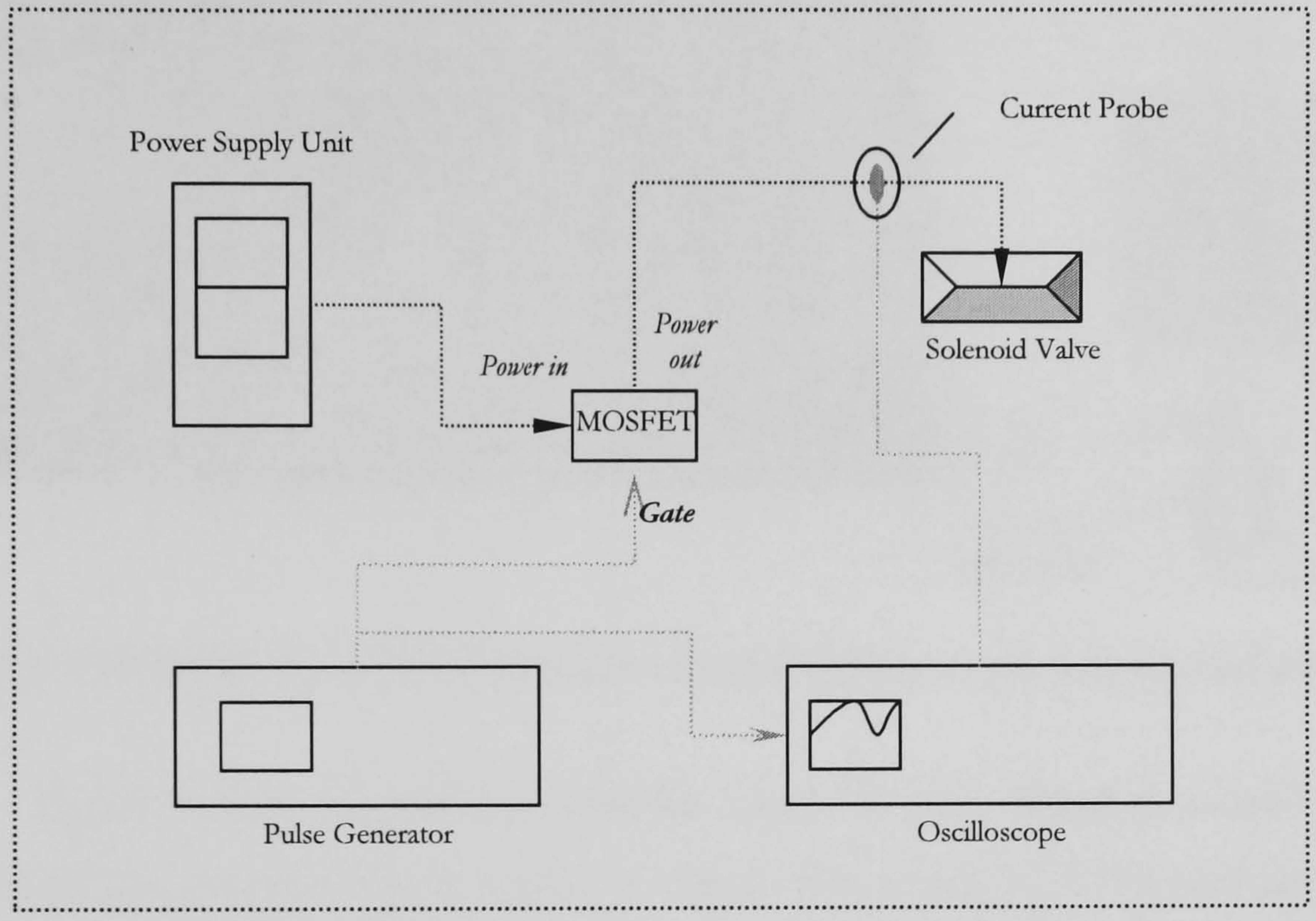

Figure 4.8 Schematic of solenoid driver circuit

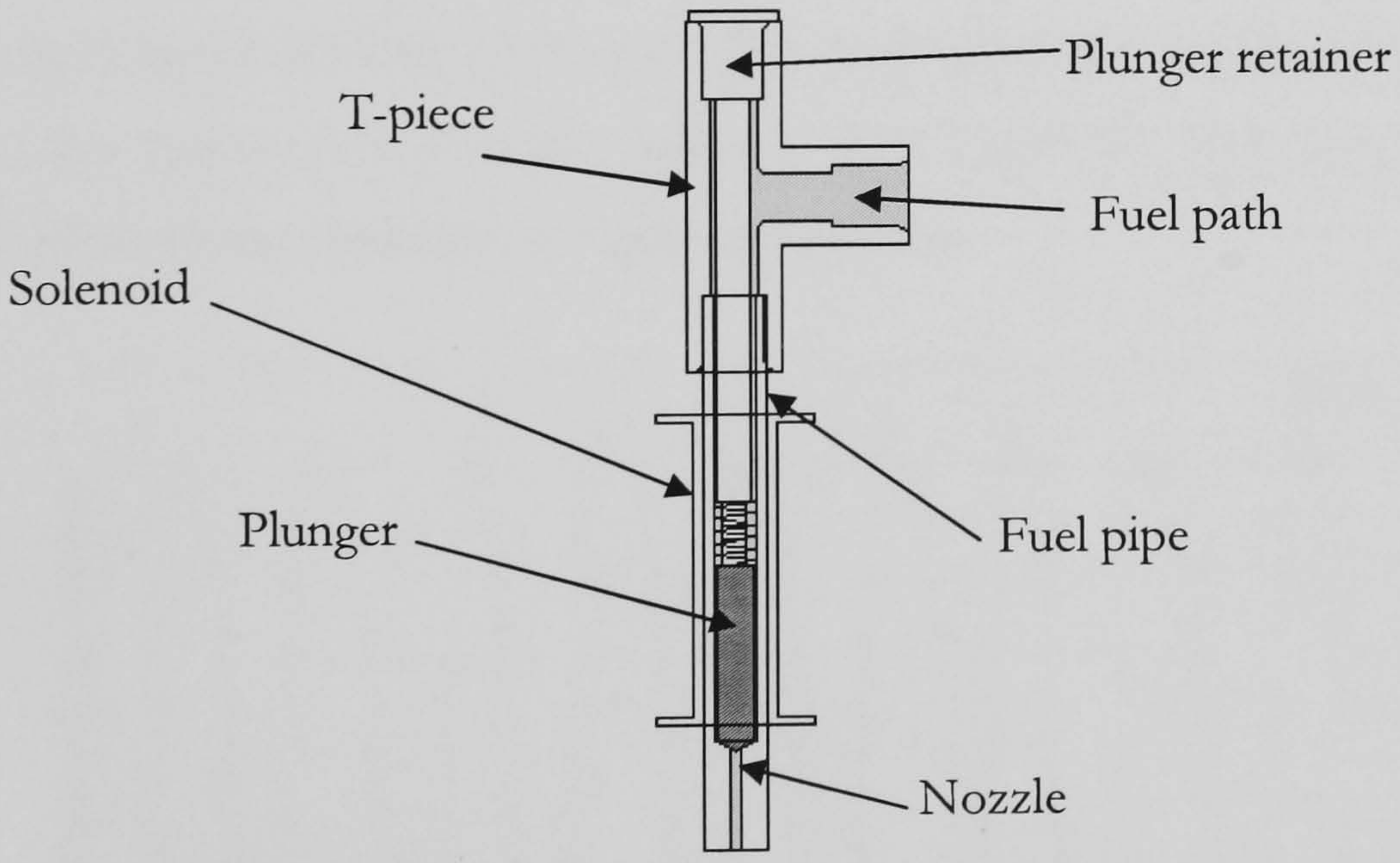

Figure 4.9 Cylindrical plunger valve system

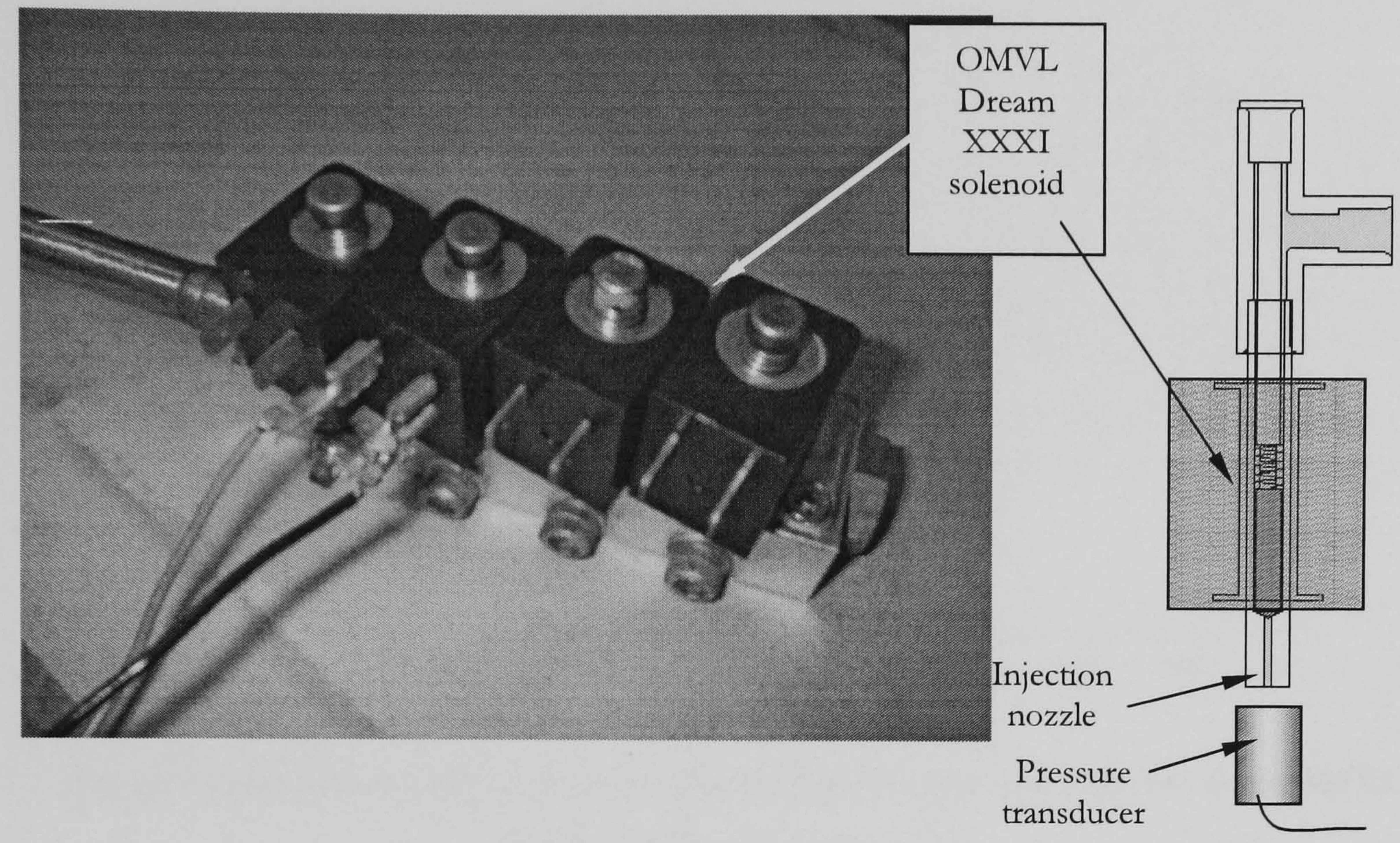

Figure 4.10 OMVL Dream XXXI solenoid valve (left) and pressure measurement set up

Figure 4.11(a), (b) and (c) show the result of valve lifting measured as the normalised gas pressure rise at nozzle outlet at various injection frequencies and 6 bar injection pressure. The 50Hz, 70Hz, and 90Hz frequencies are of the maximum limits of engine speed; 3000, 4200, 5400 and 6600 rev/min respectively. In all figures, the pressure rise was normalised and plotted against time for duration of 0.2 seconds. Ideally, input signal of 50Hz, 70Hz and 90Hz should produce 10, 14 and 18 spikes of pressure rise respectively over the duration of 0.2 seconds. However, the curves indicate deteriorating operation at higher frequencies.

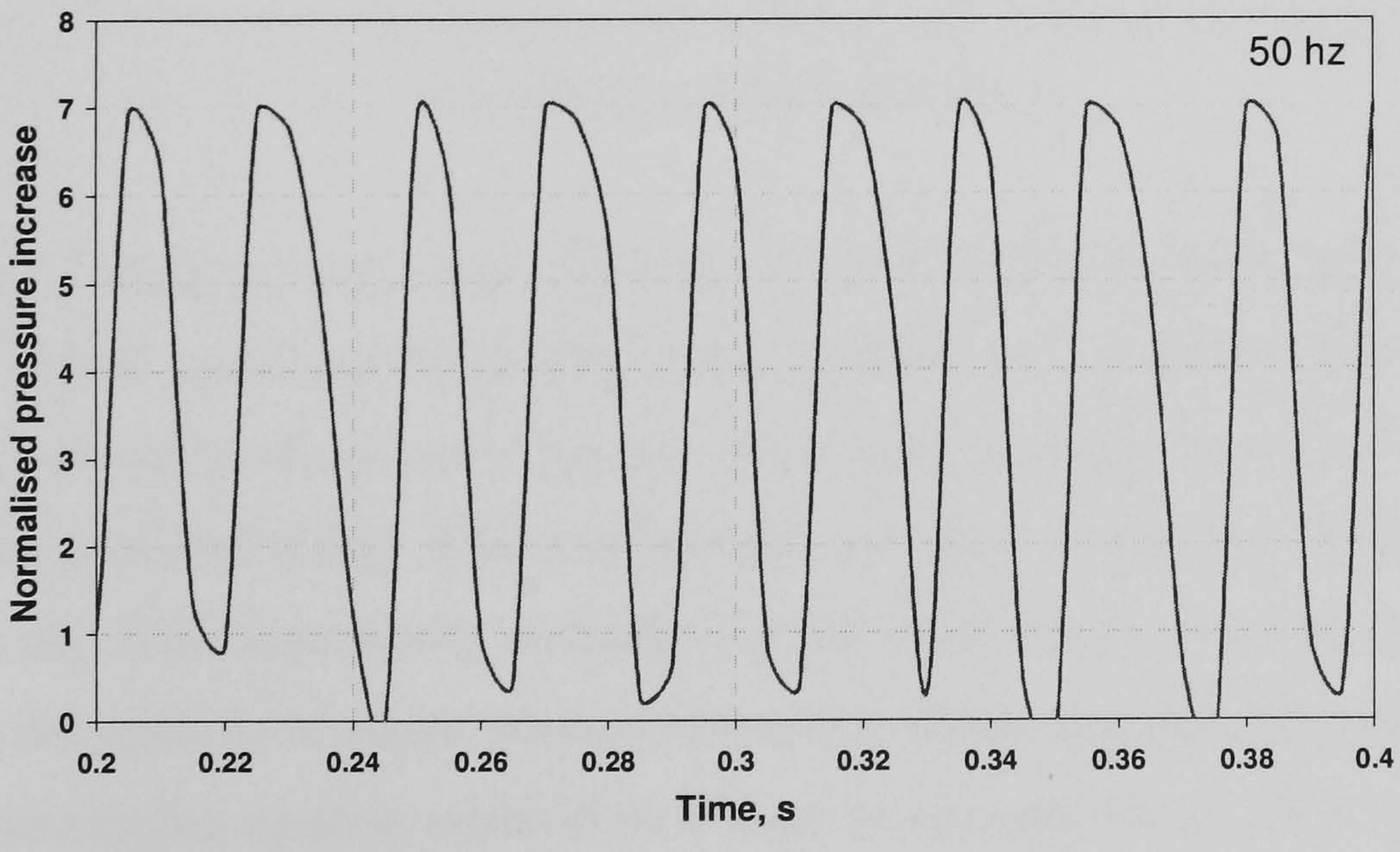

Figure 4.11 (a) Pressure rise at nozzle outlet for injection pressure of 6 bar using OMVL Dream XXXI solenoid at 50 Hz

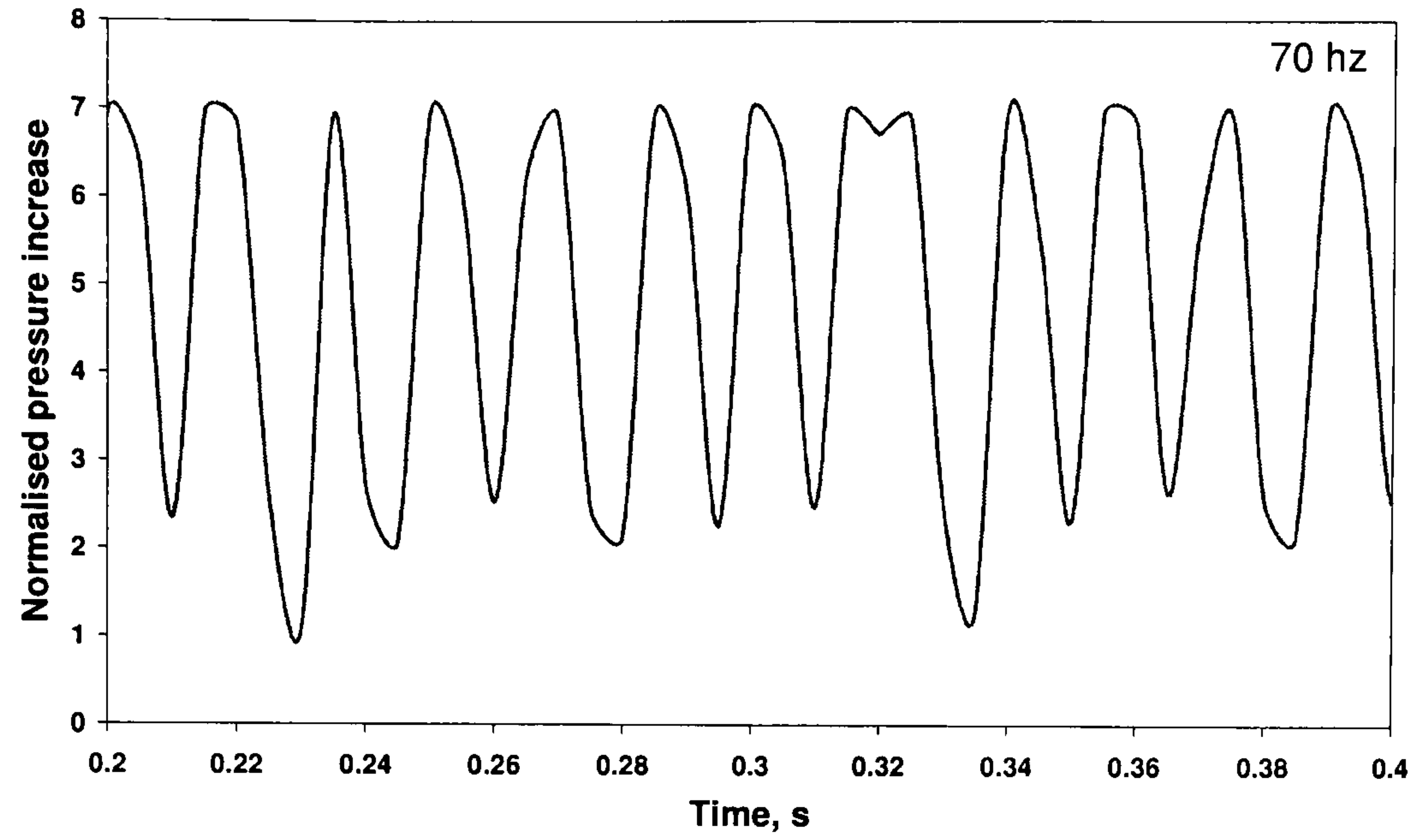

Figure 4.11(b) Pressure rise at nozzle outlet for injection pressure of 6 bar using OMVL Dream XXXI solenoid at 70 Hz

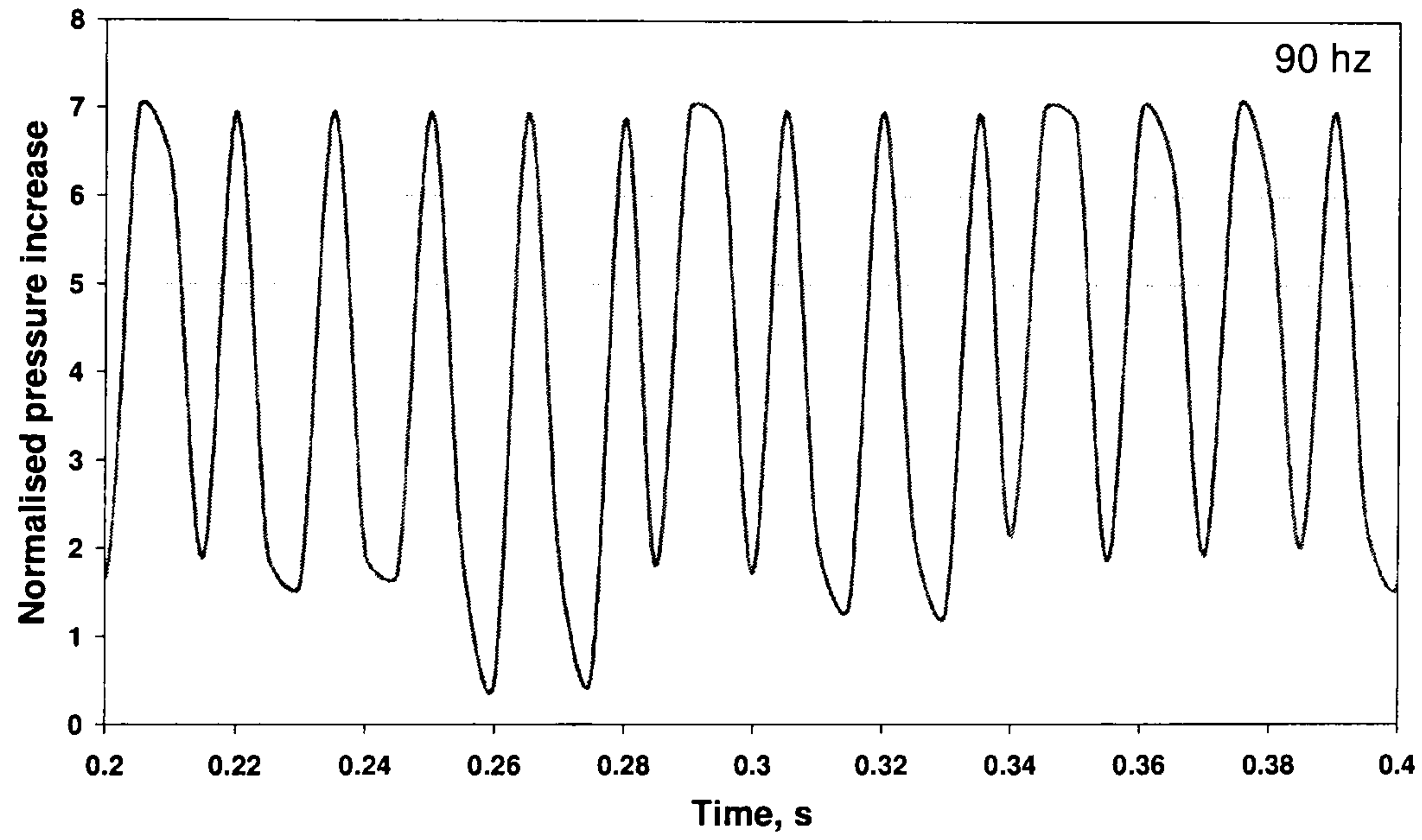

Figure 4.11(c) Pressure rise at nozzle outlet for injection pressure of 6 bar using OMVL Dream XXXI solenoid at 90 Hz

Since both the developed solenoid and OMVL Dream XXXI solenoid were not up to the requirements of methane direct injection, it was decided that the SPFI system could utilize off-the-shelf gasoline direct injector (GDI) instead of using the ones developed and tested. This was because the time needed for understanding, designing and fabricating a fully working solenoid valve injector was very consuming based on the operational requirements for methane direct injection. Even though the cost for developing another solenoid valve may be cheaper due to the availability of raw materials and laboratory facilities, the initial design was proven to be unsuccessful even though theoretical calculation indicated otherwise. The GDI injector on the other hand is proven for high pressure liquid injection requirements with currently typical gasoline injection pressure of 100-130 bar [Zhao, 2002], and therefore should be able to do similarly with relatively lower methane injection pressure of 60-80 bar. Moreover the energy requirement for nozzle opening by needle lift is reduced due to the fact that gaseous methane is more compressible than liquid gasoline. It was relatively more expensive but with a guaranteed workability, the experimental work needed to proceed.

The GDI injector used was obtained from an Audi/VW dealer. It is the fuel injector used for Audi A3 2.0litre FSI gasoline direct injection car. The injector has a single 0.5 mm nozzle diameter and was capable of operating at 100bar methane pressure, the highest tested pressure in this experiment. This injector was selected because it operates for a 0.5litre combustion chamber (the swept volume of the Ricardo E6 engine) and capable of delivering at above 100 bar gasoline pressure. Since methane is more compressible and less dense than gasoline [Goodger, 1982], the injector should be able to fulfil SPFI methane direct injection task. Figure 4.12 shows the Audi FSI injector and Figure 3.13 shows the enclosure used to connect this injector with fuel pipe and SPFI.

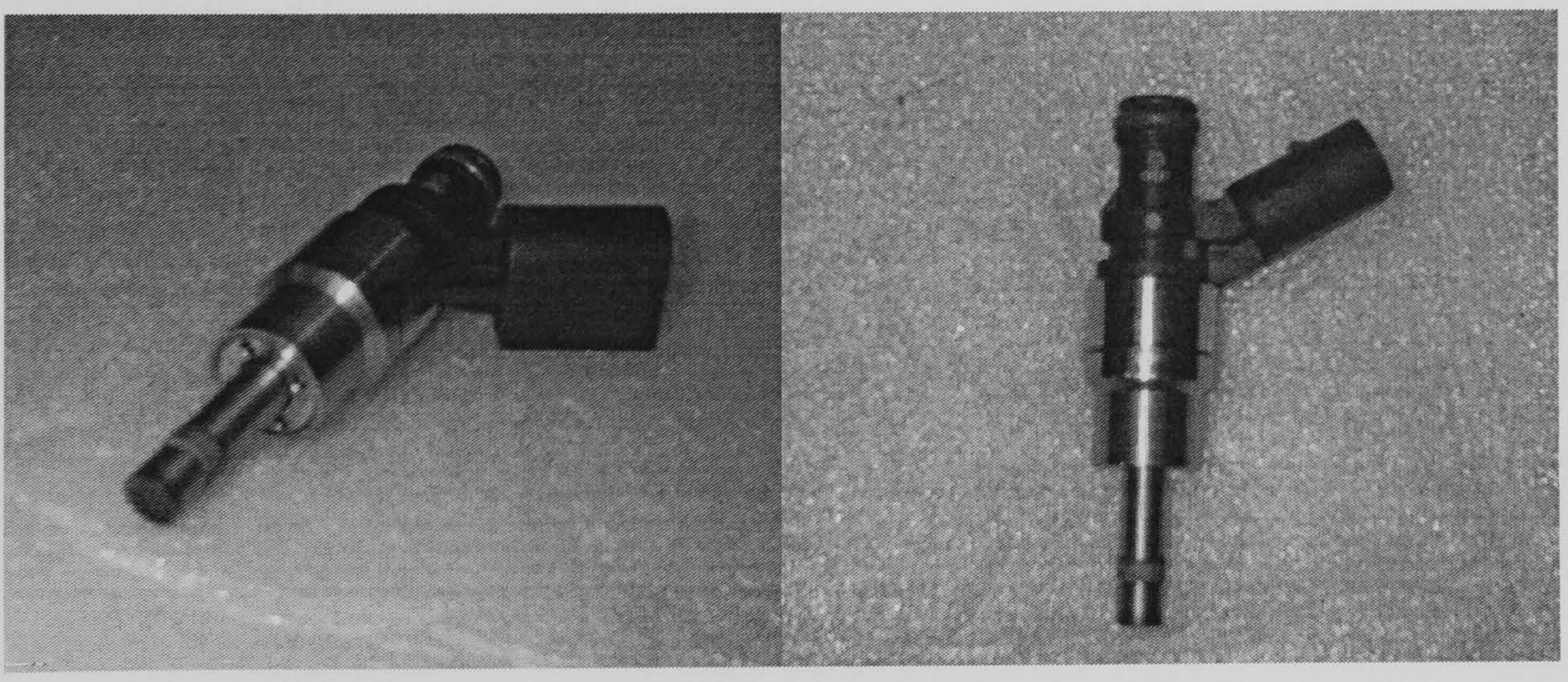

Figure 4.12 Audi A3 FSI injector

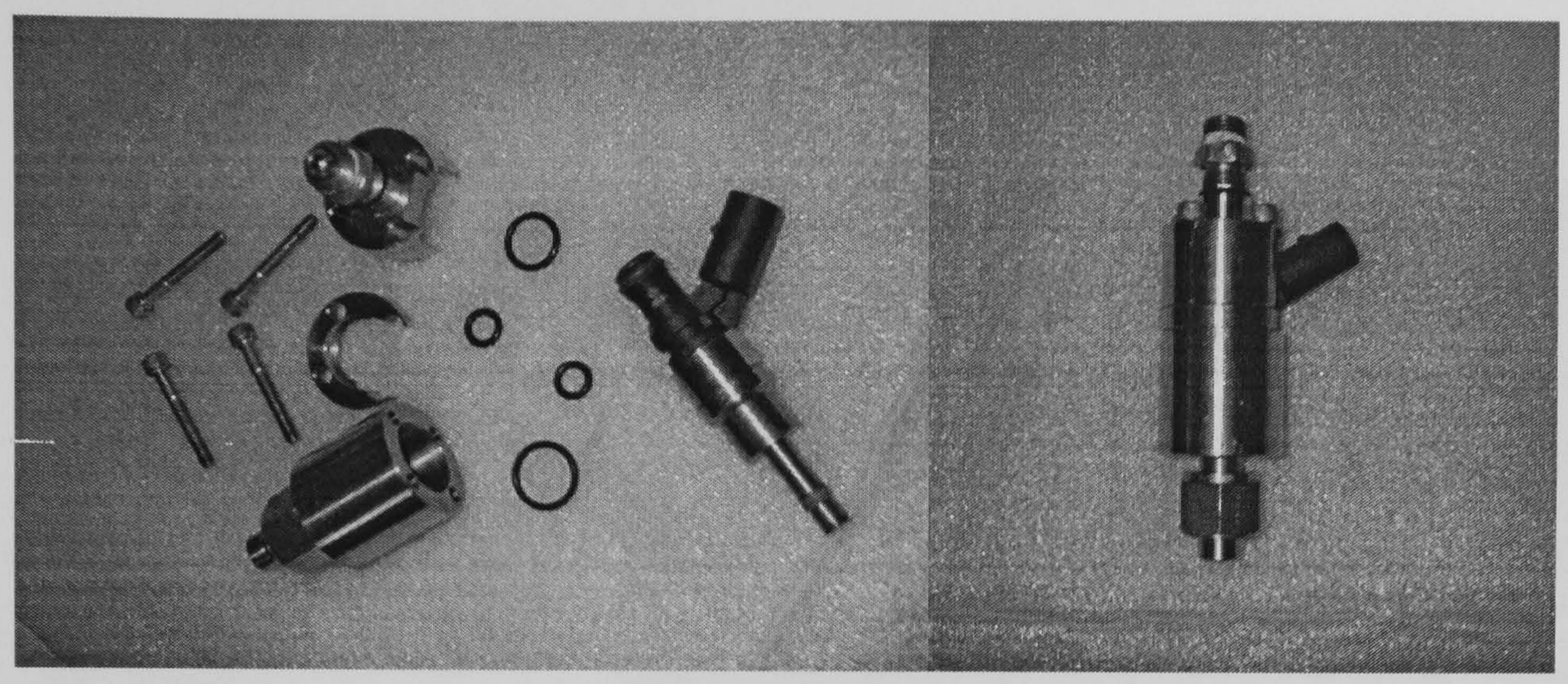

Figure 4.13 FSI injector and enclosure component (left) and FSI injector in the enclosure (right)

4.4.2 First prototype

The first prototype was designed and fabricated as shown in Figure 4.14. It consisted of a screw-tightening effect T-piece, a central electrode (anode), body shell (cathode) and an anode retainer, consisting of a steel cap and a set of O-rings, as shown in the schematic. A hollow ceramic glass cylinder was inserted around the central electrode to provide sufficient electrical insulation. The fuel path is shown as in the dark area. Four fuel injection nozzles of 0.5 diameters are located at the very end of fuel path. Spark plug operation is achieved indicating proper insulation between two electrodes. The spark gap was set at 0.75 mm.

4.4.2.1 Fuel path volume reduction

It was noticed that the volume making up fuel path was significant with respect to fuel injection amount. It could also reduce the compression ratio of the engine tested with the injector fitted. A set of volume reducers were fabricated and fitted to the fuel path as shown in Figure 4.15. Detail designs of first prototype and its volume reducers are presented in Appendix A

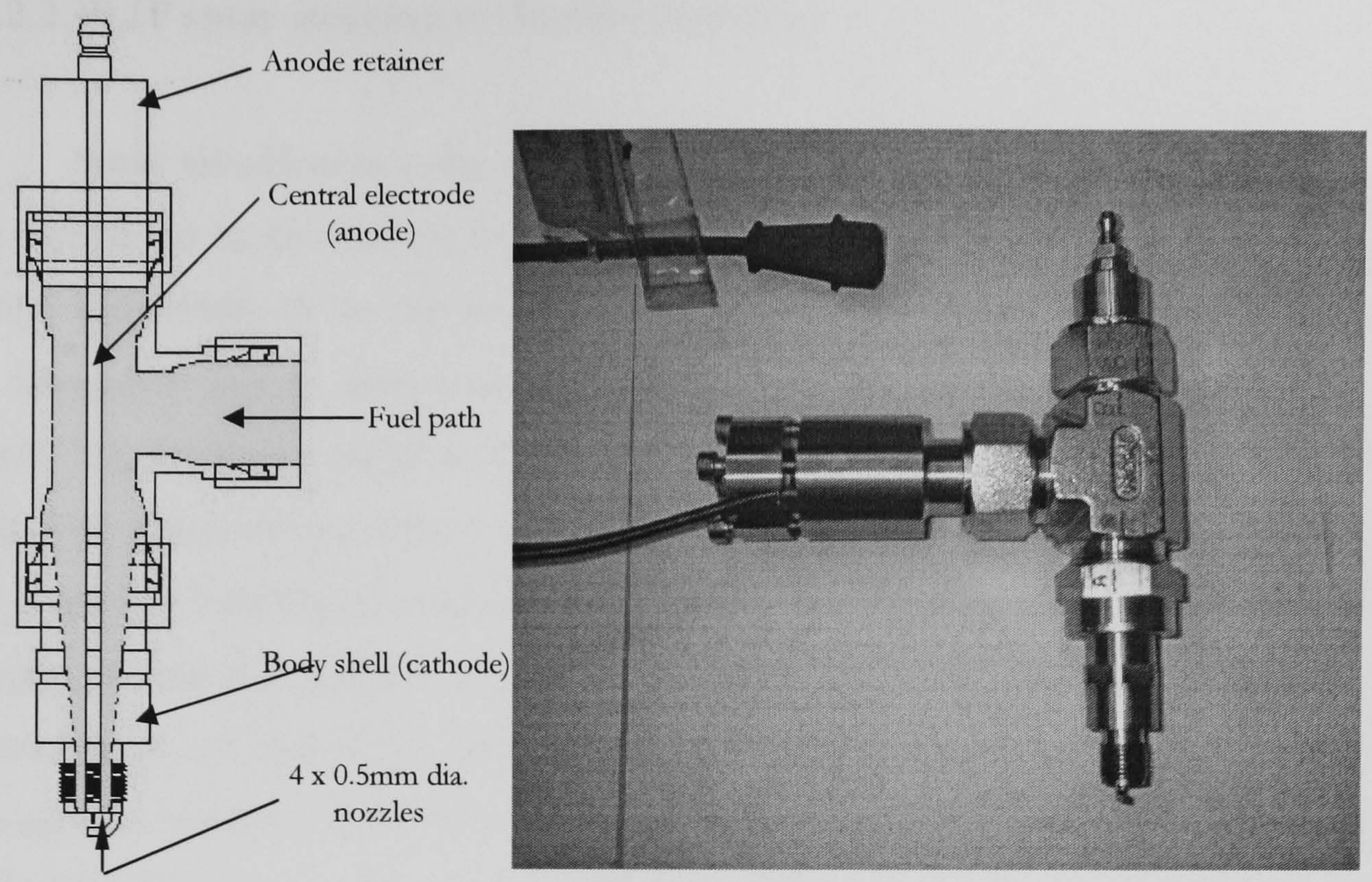

Figure 4.14 SPFI first prototype

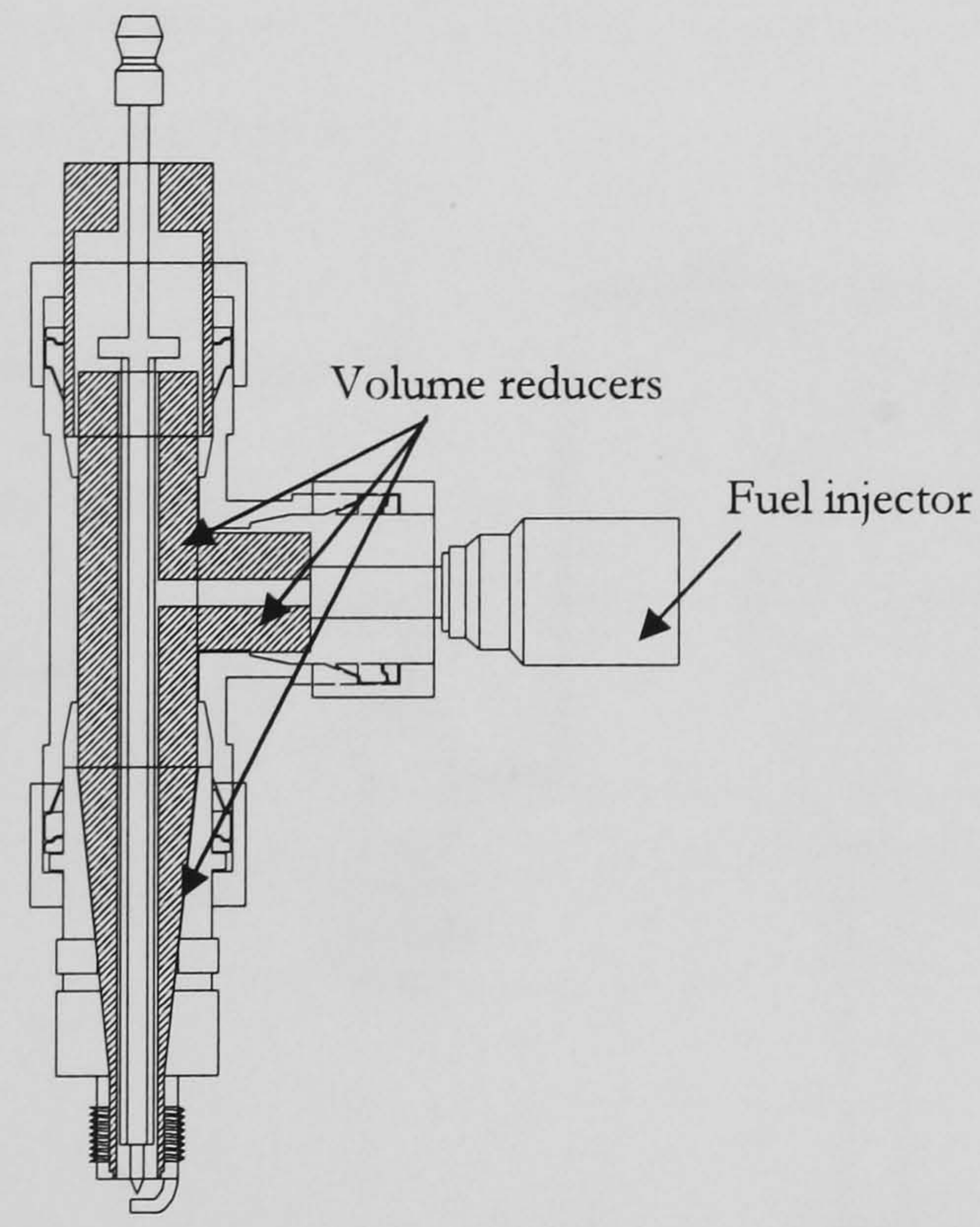

Figure 4.15 First prototype SPFI with inserted fuel path volume reducer

4.4.2.2 PLIF spray imaging of the first prototype

Spray visualization using Planar Laser Induced Fluorescent (PLIF) technique was carried out to measure the depth of jet penetration of the first prototype. Figure 4.16(a) and 4.16(b) shows the schematic of the experiment and Figure 3.16(c) shows the laboratory setting. The spray imaging chamber (known as the Cranfield spray bomb) has 4 viewing windows located around the periphery and perpendicular to each other. Acetone was used as the tracer. Pressurised nitrogen gas at 20 bar which was doped by bubbling through it through acetone. It was sprayed into the ambient pressure confined bomb for a 2.5 milliseconds duration. A laser sheet which was formed from an Nd-YAG laser source and optical lenses arrangement passed through two windows of the bomb. The fuel injector was placed in-line with the laser sheet. The injection process was synchronized with the laser pulse and a high speed CCD camera. The camera, which was arranged in the direction normal to the laser sheet, captured one image in every 0.5 milliseconds through the perpendicular window.

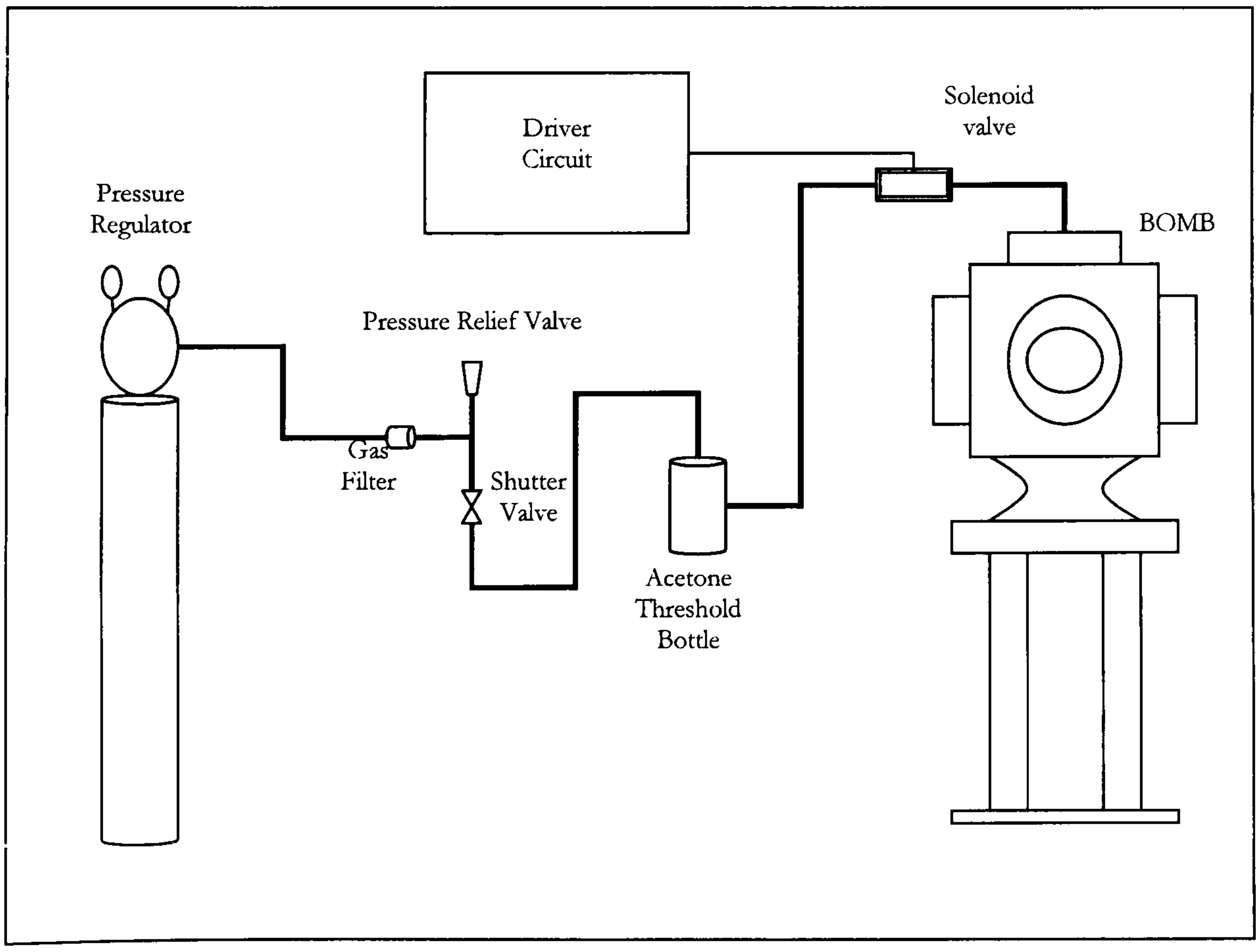

Figure 4.16(a) Bomb experiment for spray visualization schematic

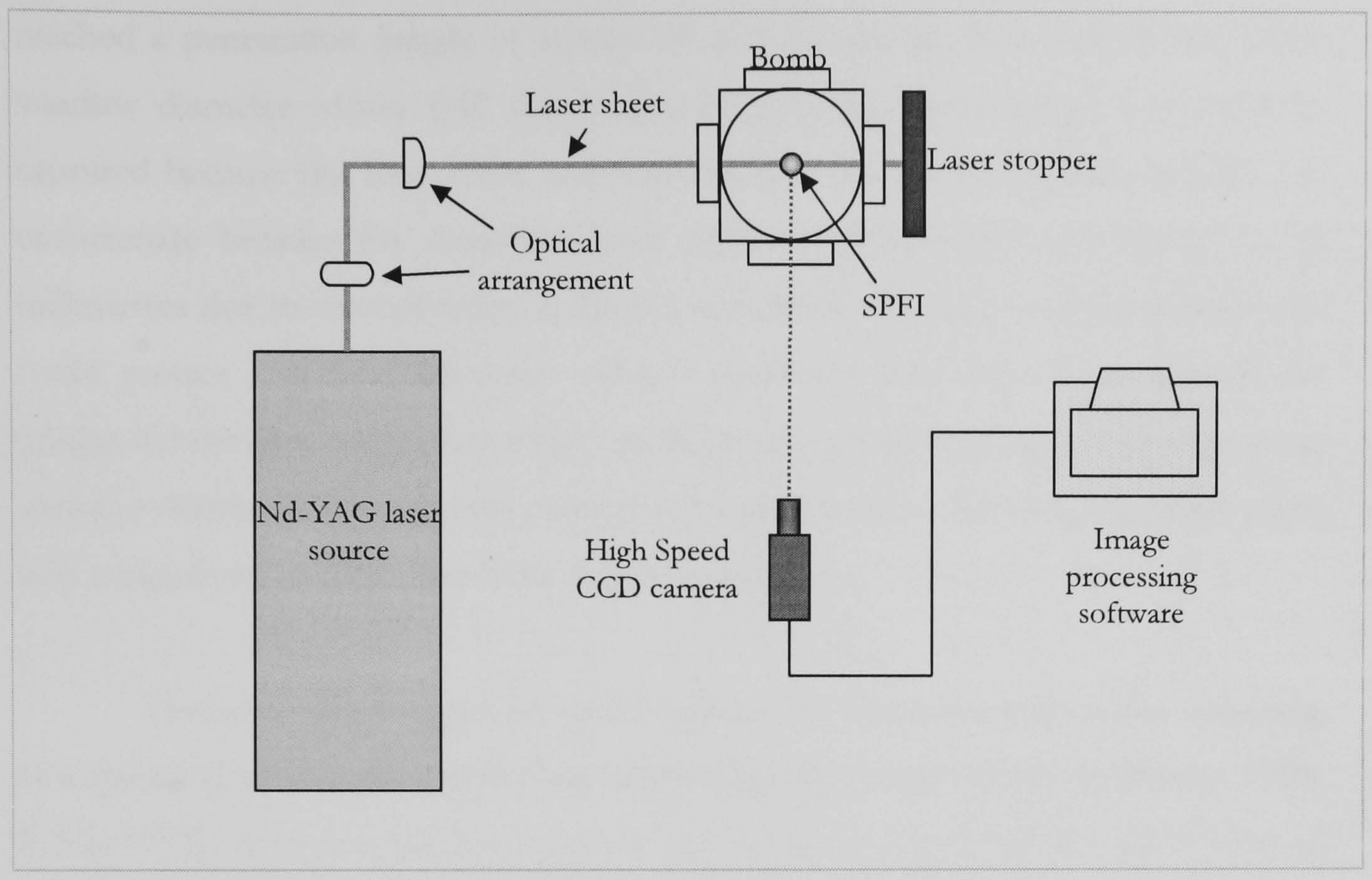

Figure 4.16(b) Laser and camera arrangement for spray visualization experiment

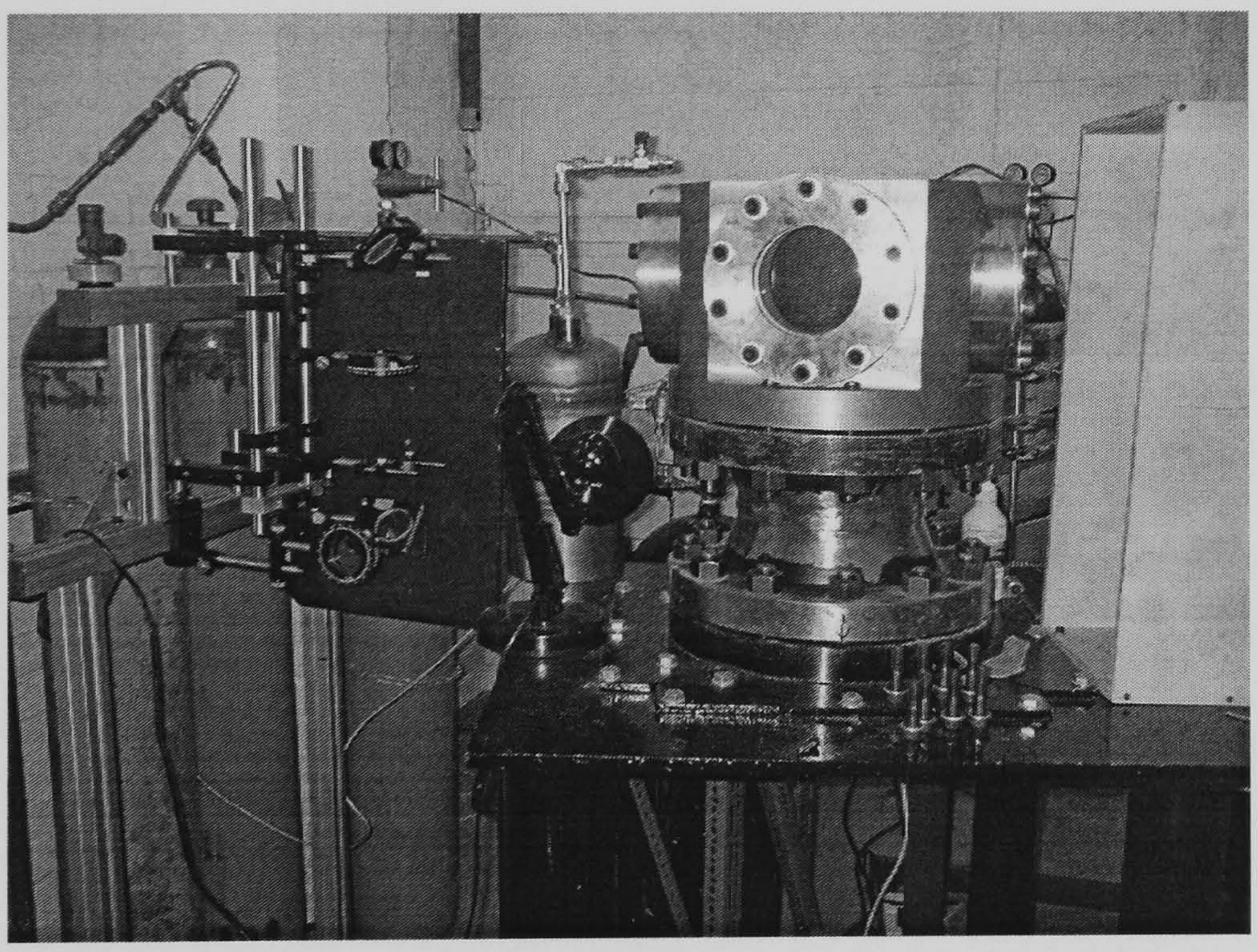

Figure 4.16(c) Bomb experiment for spray visualization schematic

Figure 4.17 shows the development of a gas jet from a 2.5 milliseconds period injection over a period of 5.46 milliseconds after start of injection. The bright greenish areas on the images are indications of the presence of acetone-doped nitrogen. The spray plume had fully developed at 1.45 milliseconds and started to reduce in size around 2.76 milliseconds. The spray from SPFI first prototype had reached a penetration length of at least 55 millimetres which is half of the Bomb window diameter within 1.45 ms. Images beyond that spray length could not be captured because the laser sheet only covered half the window diameter. This was unfortunate because the maximum laser sheet width achieved was limited to 55 millimetres due to unavailability of optical equipment at the time of experiment that could project a wider laser sheet without significant refraction. Even though the images did not give full picture of the whole injection process, they did provide some useful overview of the injection process into combustion cylinder using SPFI which is at a significant distance from the solenoid valve.

The initial shape of gas jet can be referred to the vortex ball model consisting of a spherical non-steady vortex flow interacting with a quasi-steady jet [Boyan, 1998, Rubas 1998]. However, the lower part of gas jet where vortex ball should be formed was not visible due to imaging restriction. The idea of gas jet vortex ball model was based on a model originated with Turner [1962] and verified experimentally by Tanabe [1985]. The shape of gas jet slightly differs from a gasoline spray. A data from Masahisa [2001] is taken as comparison between gas jet and liquid spray as shown in the leftmost column in Figure 4.17. Gasoline was sprayed at 10 bar pressure within 0.88 milliseconds. The images were captured through a 75 millimetres window. The spray shape is a hollow cone type at 1.0 millisecond and had penetrated a distance of 40 millimetres. As the spray detached from the injector after completion of injection, a part of spray periphery flows up and a large vortex is formed. The vortex formed expands, providing a wider area of air-fuel mixing. In the gas jet however, most of the methane is confined within the vortex ball and cone, where mixing appears to take place at the periphery.

In order to verify its effectiveness and reliability, the first prototype was installed on the Ricardo E6 engine and run with stoichiometric methane direct injection at compression ratio of 10.5:1. The engine was motorised to 700rpm where combustion took place. However, the combustion was very unsteady and occurrence of misfire was obvious. Misfiring was thought to be due to either poor mixing or unreliable spark plug. To check to reliability of spark plug, the engine was run on gasoline carburetion mode. It ran well until a point where steady combustion caused leakage on the top part of the SPFI. This was due to the breakage of the ceramic insulator of the central electrode resulted from series of combustion events causing combustion to penetrate the fuel path and subsequently melt the O-rings that provide electrical and fuel seal to the upper part of the SPFI fuel path. This called for a review of the strength of non-metallic materials making up the SPFI.

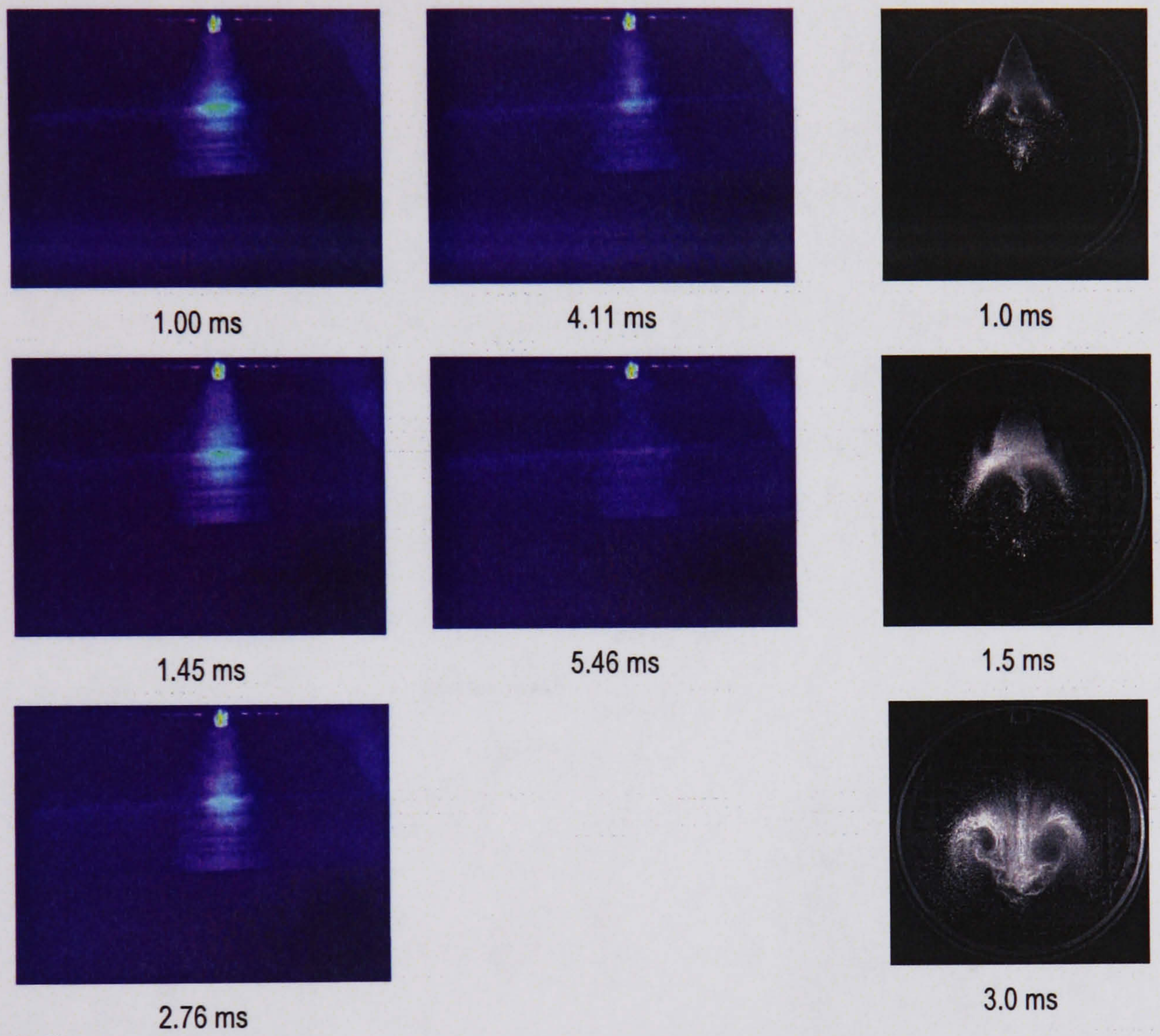

Figure 4.17 LIF images of gas spray development from SPFI first prototype (first and second columns), and LIF-PIV Tomogram images from direct injection gasoline spray [Masahisa, 2001] (leftmost column)

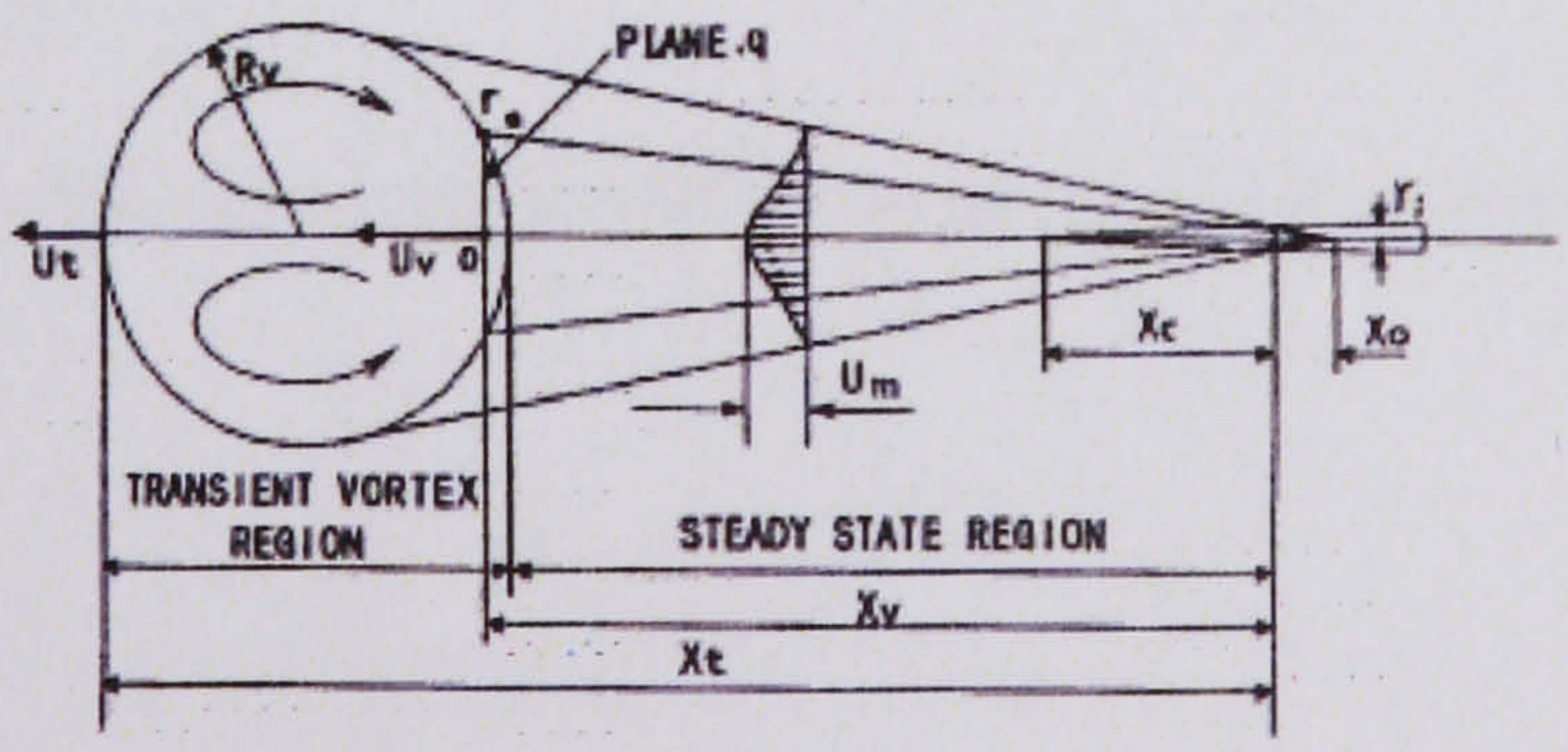

Figure 4.18 Vortex ball model [Boyan, 1998]

4.4.3 Second prototype

The second prototype was developed with the aim of reducing the overall size of the SPFI but at the same time, increasing its durability and temperature resistance. Figure 4.19 and 4.20 shows the components and assembly of the second prototype. The components are of the same as the first prototype but with major reduction in overall dimensions and particularly the total volume of fuel path. The same ceramic insulator was used but it was made thicker around the central electrode. A new set of O-rings with 50% more temperature resistance were used. Methane at 30 bar was injected through it in an open air to assure adequate sealing. Then, it was again put under engine test but for the same reason, failure occurred on the ceramic insulator. However, the time taken before failure happens was longer than in the case of first prototype. This suggests that fuel path size and the tightness between components plays an important role for design durability.

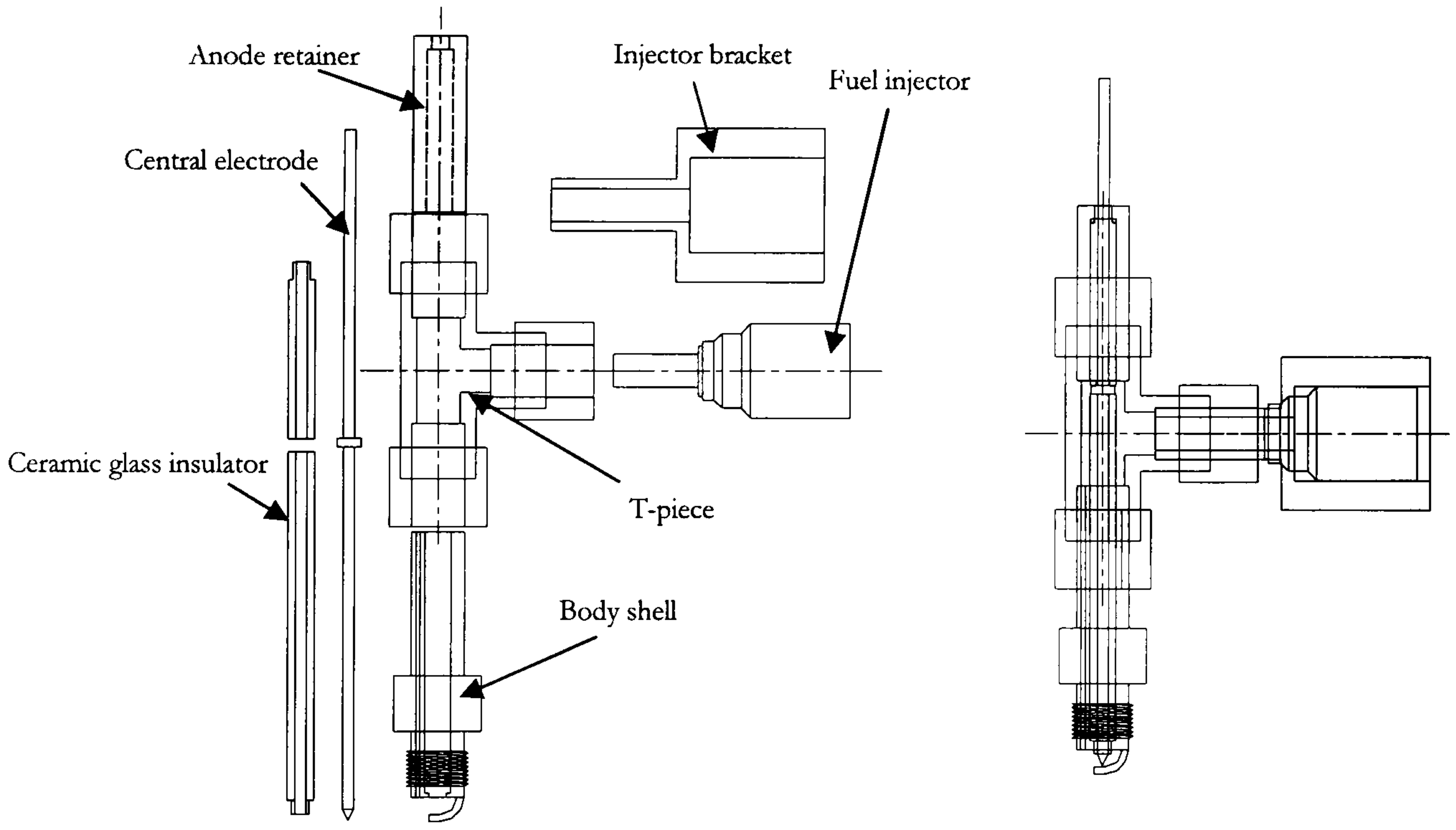

Figure 4.19 Second prototype SPFI components and assembly drawing

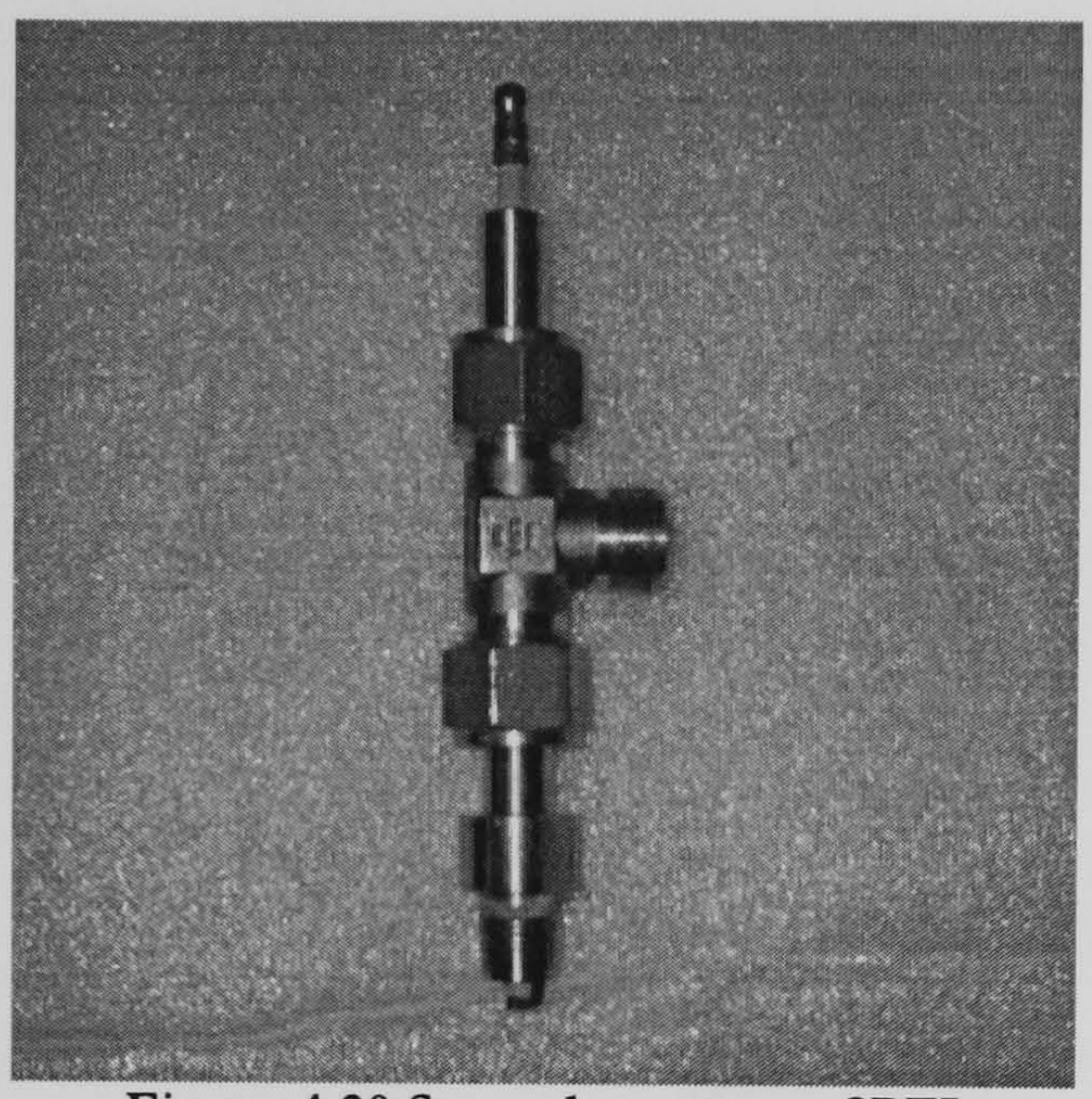

Figure 4.20 Second prototype SPFI

4.4.4 Final design

Since the two prototypes failed due to poor durability and temperature resistance, it was decided that the SPFI should be designed around a market-available spark plug which has proven strength for IC engine operation. The fuel path would be incorporated with the available spark plug and proper soldering and enclosure would be undertaken to assemble GDI injector, fuel path and spark plug into one component.

The final design utilises a Champion N9YC spark plug with M14 thread. A fuel path is cut along the edge of the main body and a fuel line is soldered onto it. The fuel line is a 6 mm steel pipe with 4 mm inner diameter with a threaded section for attaching a fuel injector enclosure. As the fuel pipe attaches to the main body of spark plug, the cross-sectional area is reduced to a 2 mm by 1 mm square area path which extends to spark plug tip. A small step of 1mm diameter and 1mm length separates the wide and narrow sections in the fuel path. This is used as a combustion retarding measure to avoid backfiring into fuel path. The final SPFI unit is as shown in Figure 4.21(a) and (b). Detail design of the final SPFI is presented in Appendix A.

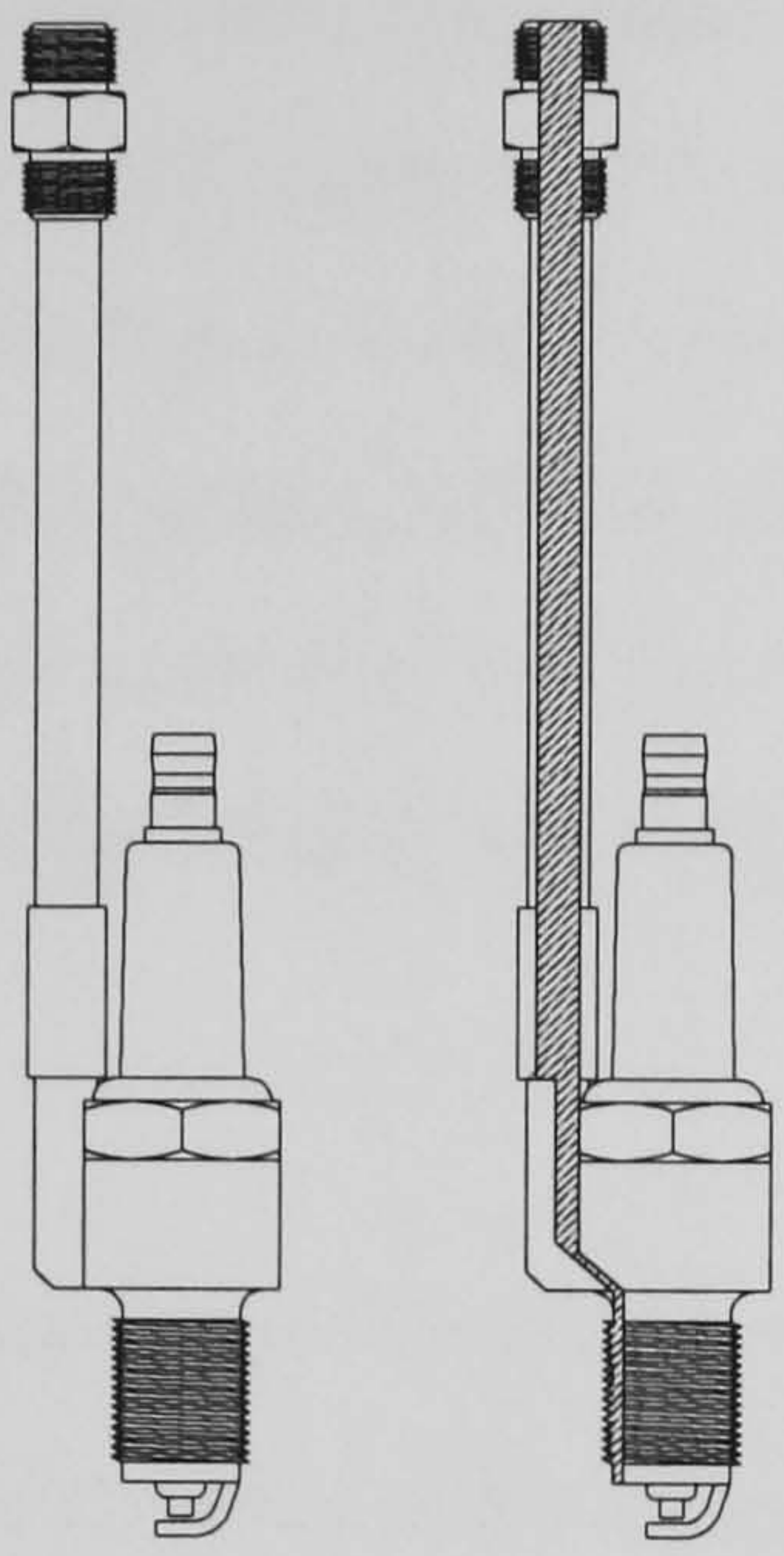

Figure 4.21(a) SPFI final design schematic drawing. Fuel path denoted by hatched area

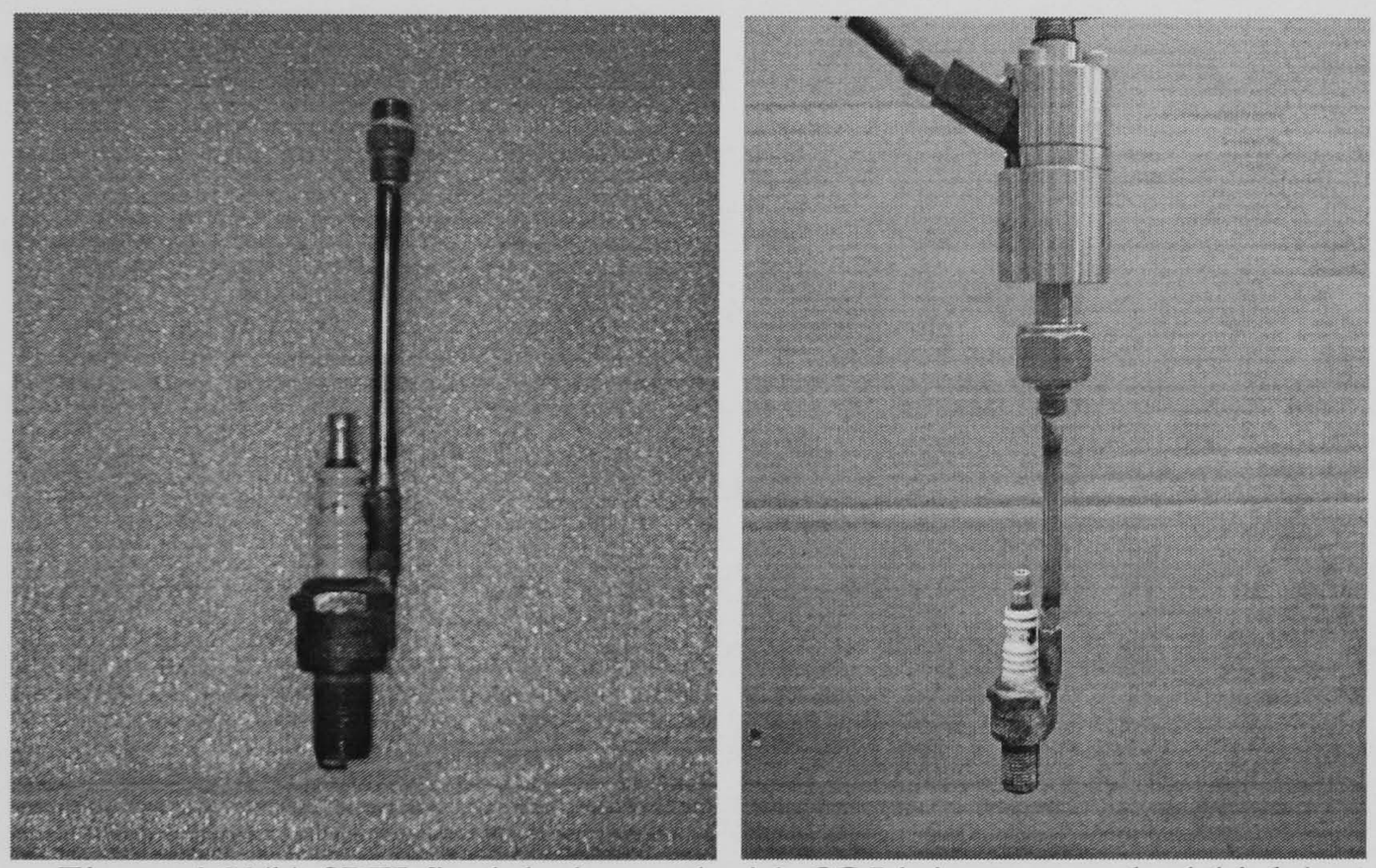

Figure 4.21(b) SPFI final design and with GDI injector attached (right)

4.4.4.1 Fuel arrival delay

The distance between the GDI injection nozzle and the SPFI nozzle causes delay in fuel arrival and the delivery process. A simple experiment was carried out to measure this delay. The tip of the SPFI was immersed in a beaker of water as shown in Figure 4.22. Nitrogen was injected at different pressures and as it exited the SPFI nozzle, bubbles were formed. A CCD camera with adjustable exposure time was used to capture the bubble image that first appeared from the SPFI nozzle. A flash light that was synchronized with fuel injection control by two pulse generators set to flash at some delayed time after injection was initiated. The CCD digital camera and the SPFI submerged in a water-filled beaker were placed in a lightless surrounding and arranged inline with the flash light. A small window allowed flash light to enter from the opposite direction of the camera. The exposure time on the camera was set to be 3 seconds and fuel injection occurs at the same time of flash light. If no bubble was captured by the camera, the flash light was delayed up to the point where initial bubble image was captured.

Gas bubble first appearance and partially developed gas jet are shown in Figure 4.23. Results in Table 4.1 indicate delay ranging from 5.5 to 3.3 milliseconds by increasing injection pressure from 10 bar to 30 bar. These figures have significant effect on fuel injection when operating with high engine speed and must be corrected accordingly. The total injection durations to form a stoichiometric mixture in the Ricardo E6 0.507 litre cylinder with volumetric efficiency of 75% from this SPFI prototype injection nozzle for 10 bar, 20 bar and 30 bar injection pressures were 40, 35 and 23 milliseconds respectively. The delay accounts for about 13% of injection duration. The delay can related to the engine cycle by the time allowed for injection process described by the closed valve injection. Referring to the Ricardo E6 cam profile, the close valve injection operation is confined between the time where intake valve fully close (34° ABDC) and the time of ignition TDC. This results in 146° CA. The duration for piston to travel with respect to this crank angle depends on the engine speed. At 1000 rpm, the duration is 24 milliseconds, and at 6000 rpm, the duration reduces to 4 milliseconds. The fuel arrival delay must be reduced and adjusted to compensate for the reduction in fuel injection time as engine speed goes up. From this experiment alone, it can be concluded that the minimum injection pressure should exceed 30 bar for the engine to run faster that 1000 rpm.

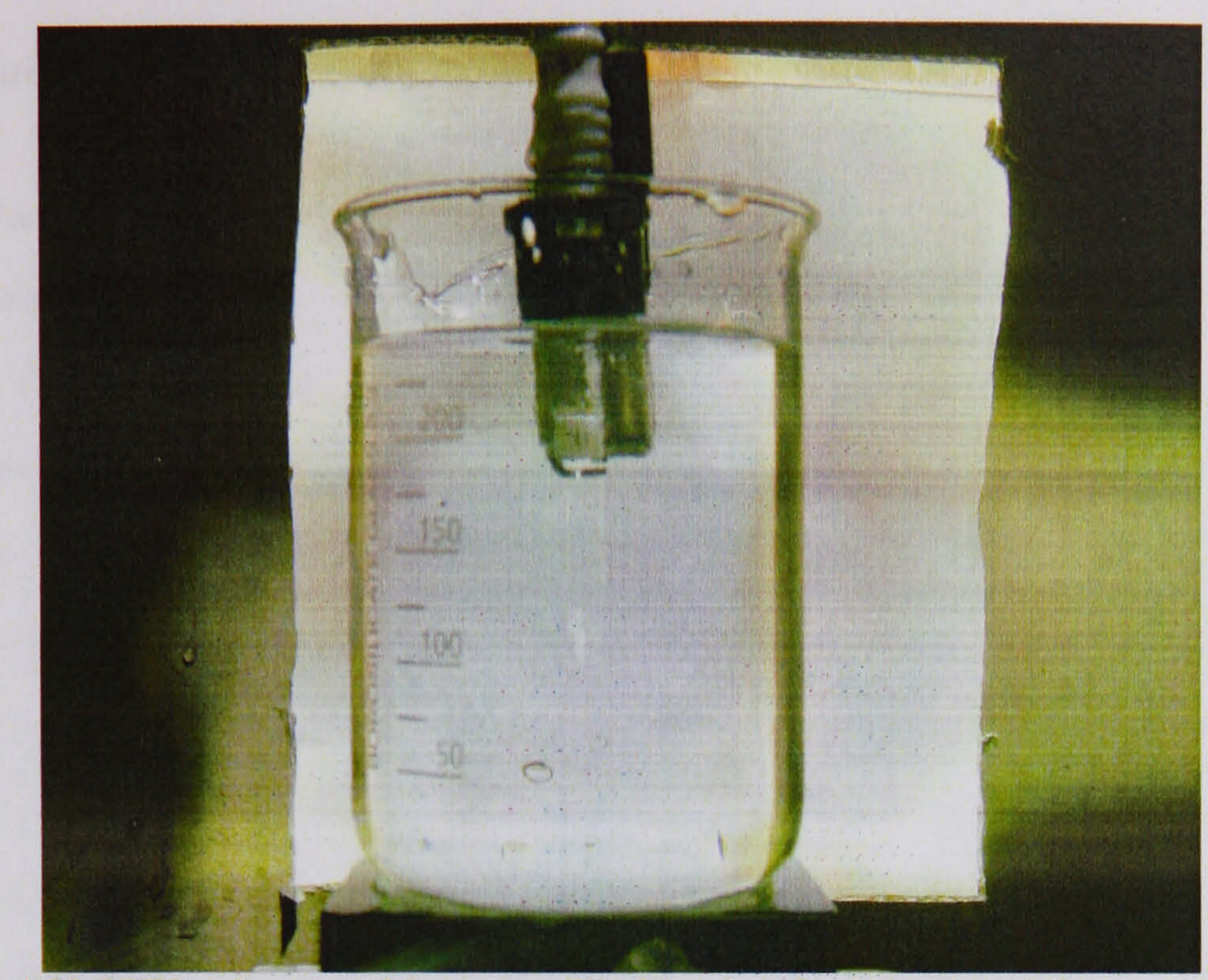

Figure 4.22 SPFI submerged in water-filled beaker for injecting delay measurement

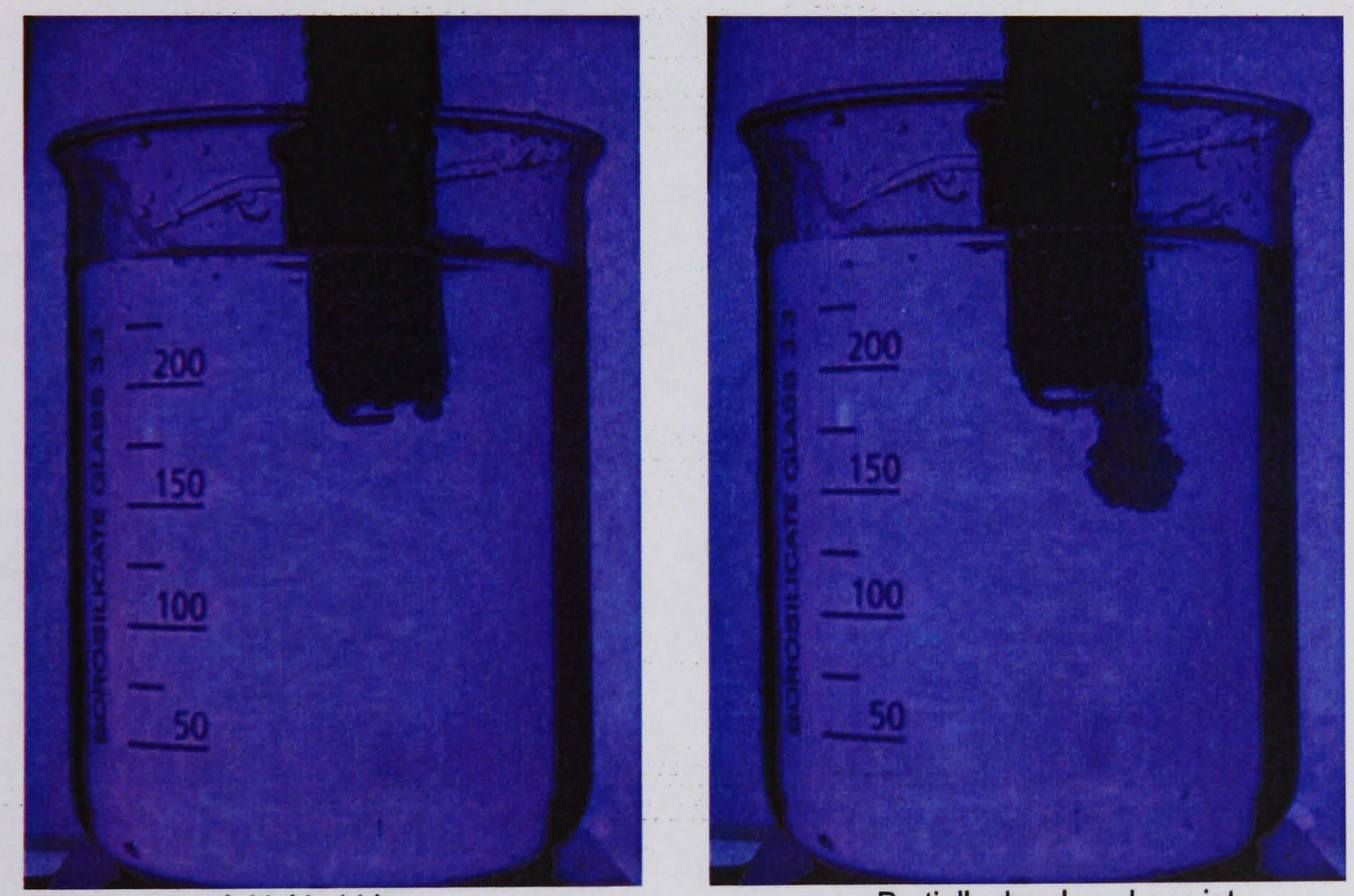

Initial bubble

Partially developed gas jet

Figure 4.23 SPFI fuel arrival delay as bubble appearance.

Injection pressure	10 bar	20 bar	30 bar
Fuel arrival delay, ms	5.5	4.1	3.3

Table 4.1 Results of fuel Arrival delay at injection nozzle of SPFI final design

4.4.4.2 Fuel path adjustment

Due to the delay in fuel arrival in the combustion chamber described in the previous section, an adjustment of fuel path was undertaken. This was done in order to reduce fuel arrival delay time which was caused mainly by the length of fuel path and the pressure drop within in. The modification works involved shortening the fuel pipe from overall length of 14.80 cm to 11.85 cm. To reduce pressure drop, the cross-sectional area of bored section before it reaches the SPFI nozzle was expanded and the inner diameter of the fuel pipe that connect to the spark plug was made wider. However, a small cylindrical fuel path with 1.5 millimetres diameter section connecting fuel pipe with bored section was left unchanged. This was a measure to avoid combustion penetration further in the SPFI fuel path. As a result, fuel arrival delay time was shortened and pressure loss was reduced. Figure 4.24 shows the adjusted final SPFI with shorter and wider overall fuel path, but a section in the fuel path narrowing to the quenching distance of methane-air combustion. The hatched area on the drawing is the sectional area of fuel paths. This final design underwent two basic analyses. First is the fuel arrival delay measurement and secondly, determination of effect on engine cylinder pressure as described in the following sections.

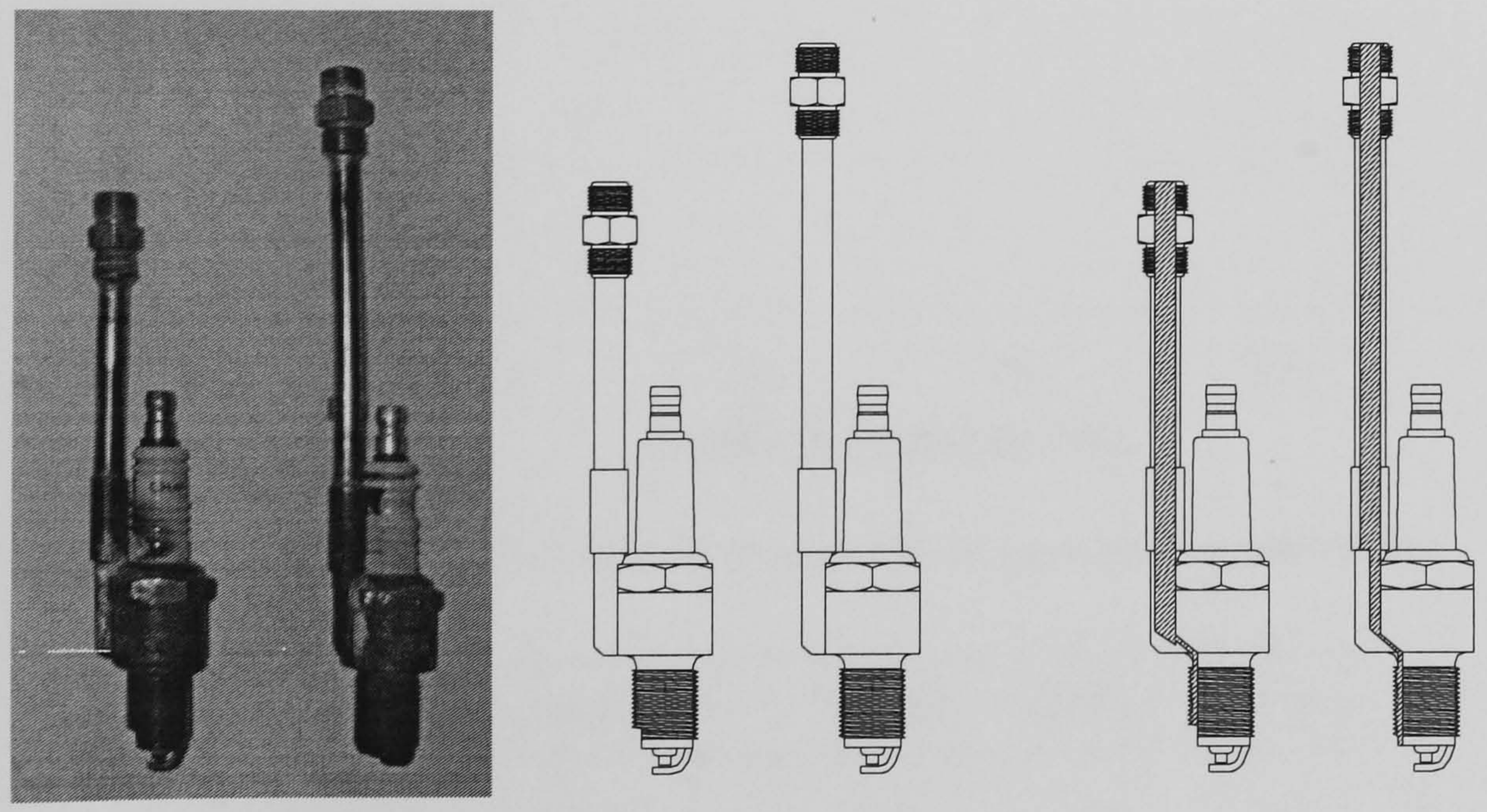

Figure 4.24 Final design SPFI with fuel path adjustment (unadjusted final SPFI on the right of each set)

4.4.4.3 Fuel injection delay improvement

The fuel arrival delay experiment described in the previous section was repeated for the newly adjusted SPFI. Table 4.2 presents the results. Results show a minimum of 1 ms or 30% of delay time reduction at 30 bar injection pressure was achieved. Comparison between delays of the two designs is shown in Figure 4.25 with projection curve for higher injection pressure included. Figure 4.26 shows the development of gas spray in the water up to 40 milliseconds from the time of injection initiation. Having water as the surrounding, with different viscosity and density than air, fuel delivery process takes more than 40 milliseconds to complete. The delivery process in air surrounding as in the combustion chamber is expected to be of significantly shorter time and must be verified through engine experiment.

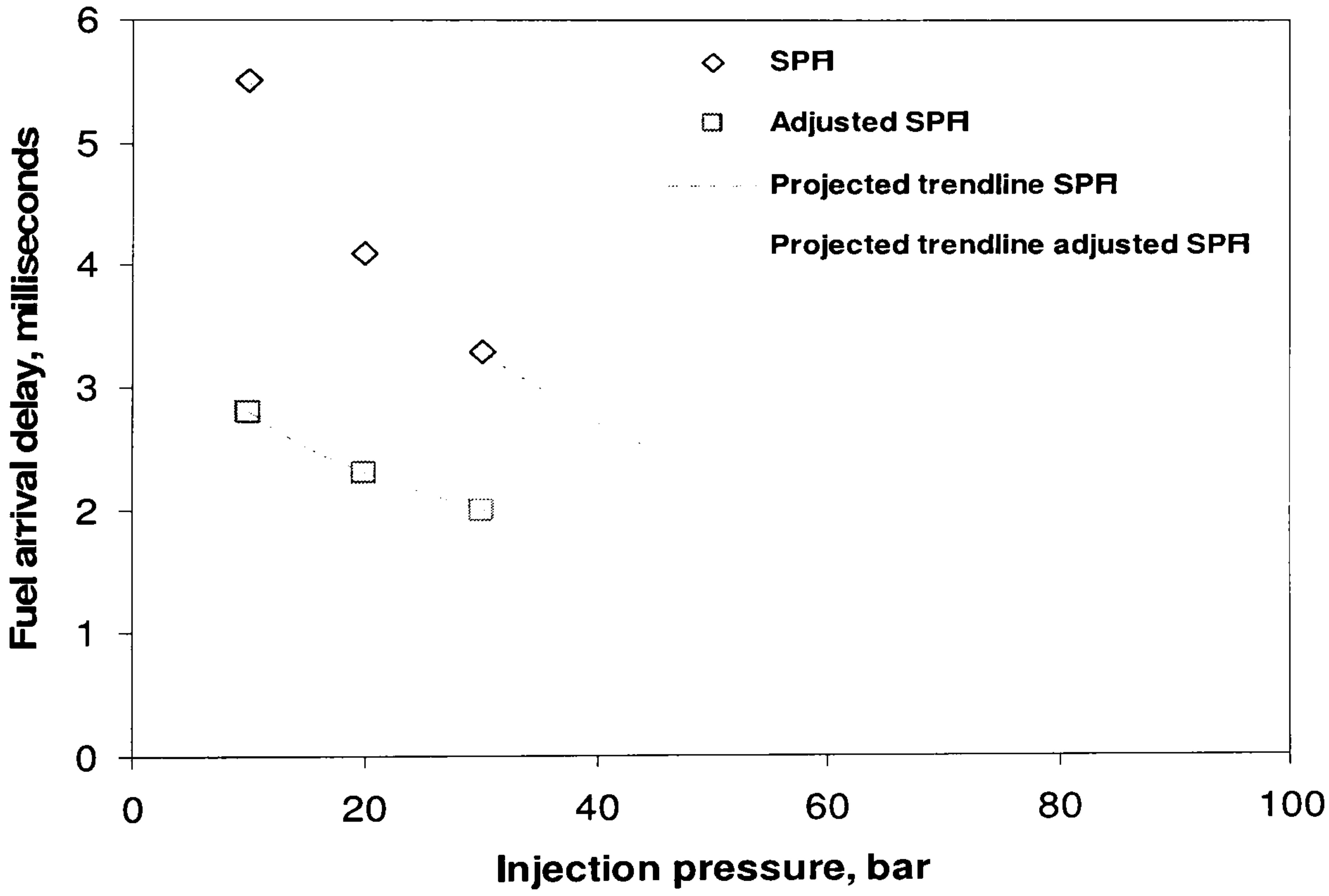

Figure 4.25 Fuel delay of adjusted and unadjusted fuel path SPFIs

Injection pressure	10 bar	20 bar	30 bar
Fuel arrival delay, ms	2.8	2.3	2.0

Table 4.2 Results of fuel Arrival delay at injection nozzle of modified SPFI final design

Figure 4.26 SPFI injections into water-filled beaker at various injection pressures

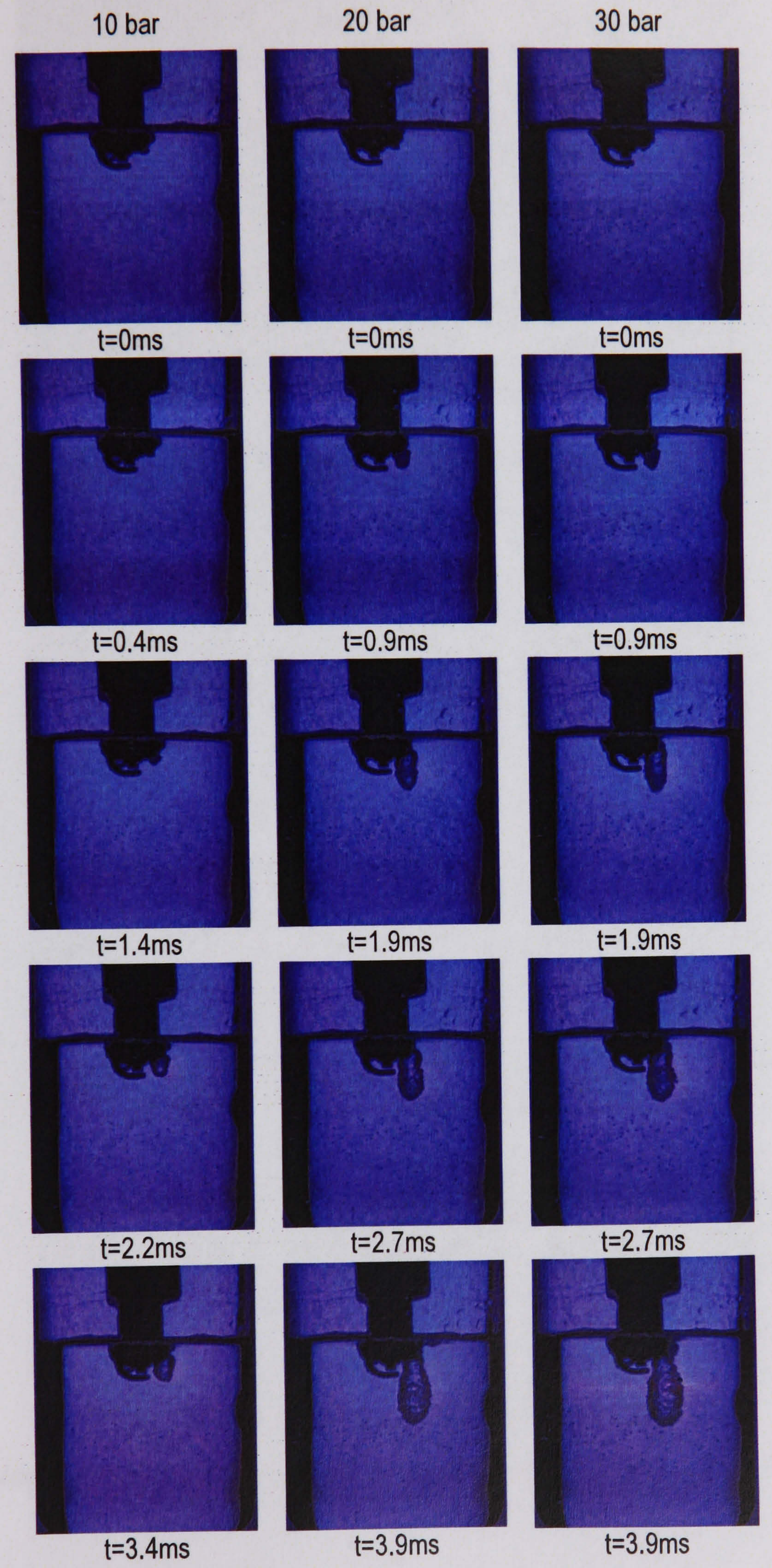

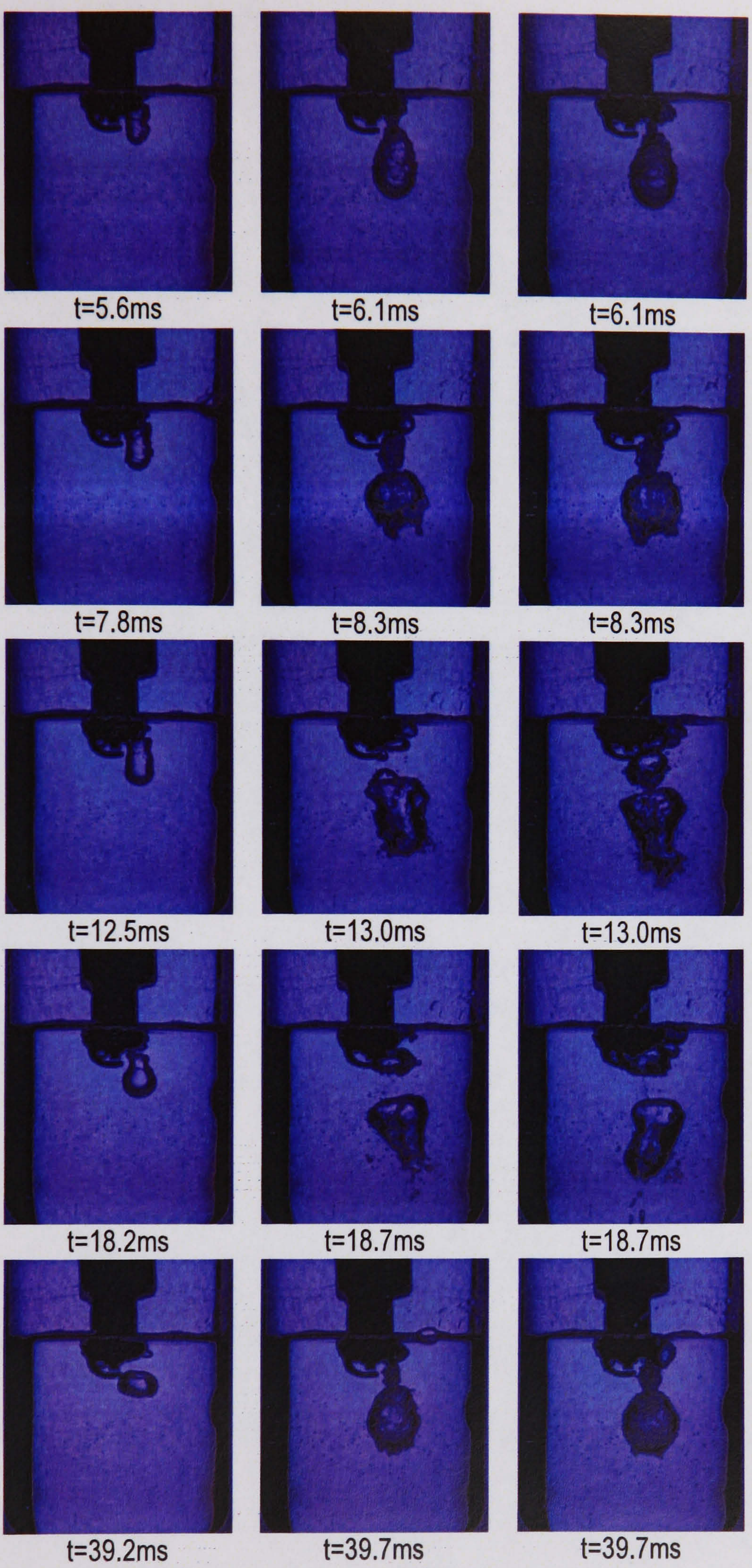

t=5.6ms t=6.1ms t=6.1ms

t=7.8ms t=8.3ms t=8.3ms

t=12.5ms t=13.0ms t=13.0ms

t=18.2ms t=18.7ms t=18.7ms

t=39.2ms t=39.7ms t=39.7ms

Figure4.26 (continued) SPFI injections into water-filled beaker at various injection pressures

4.4.4.4 Motorised peak cylinder pressure reduction

One of the most important effects when SPFI is installed on the engine is reduction of motorised engine peak cylinder pressure. Figure 4.27 shows cylinder pressure over one engine cycle of a motorised engine based on the original setting of 10.5 to 1 compression ratio. The peak pressure using normal spark plug is 15 bar. The pressure is reduced to 13.9 bar when SPFI is used in replacement as shown in Figure 3.27. This change, which is in the order of 7% peak pressure reduction, is due to the fuel path volume involved in the compression process. It was calculated that the volume inside the fuel path is 2.5533 x 10^{-6} m^3. The clearance volume in the Ricardo E6 with the above-mentioned compression ratio is 5.3322 x 10^{-5} m^3. The 4.8% of clearance volume increase caused by installing the SPFI reduced the compression ratio to 10.07:1. The reduction will have significant effects on the performance of SPFI methane direct injection. In Chapter 6, results from engine experiment are presented and engine data from methane port injection performance are presented. It will further prove this expected consequence of direct conversion.

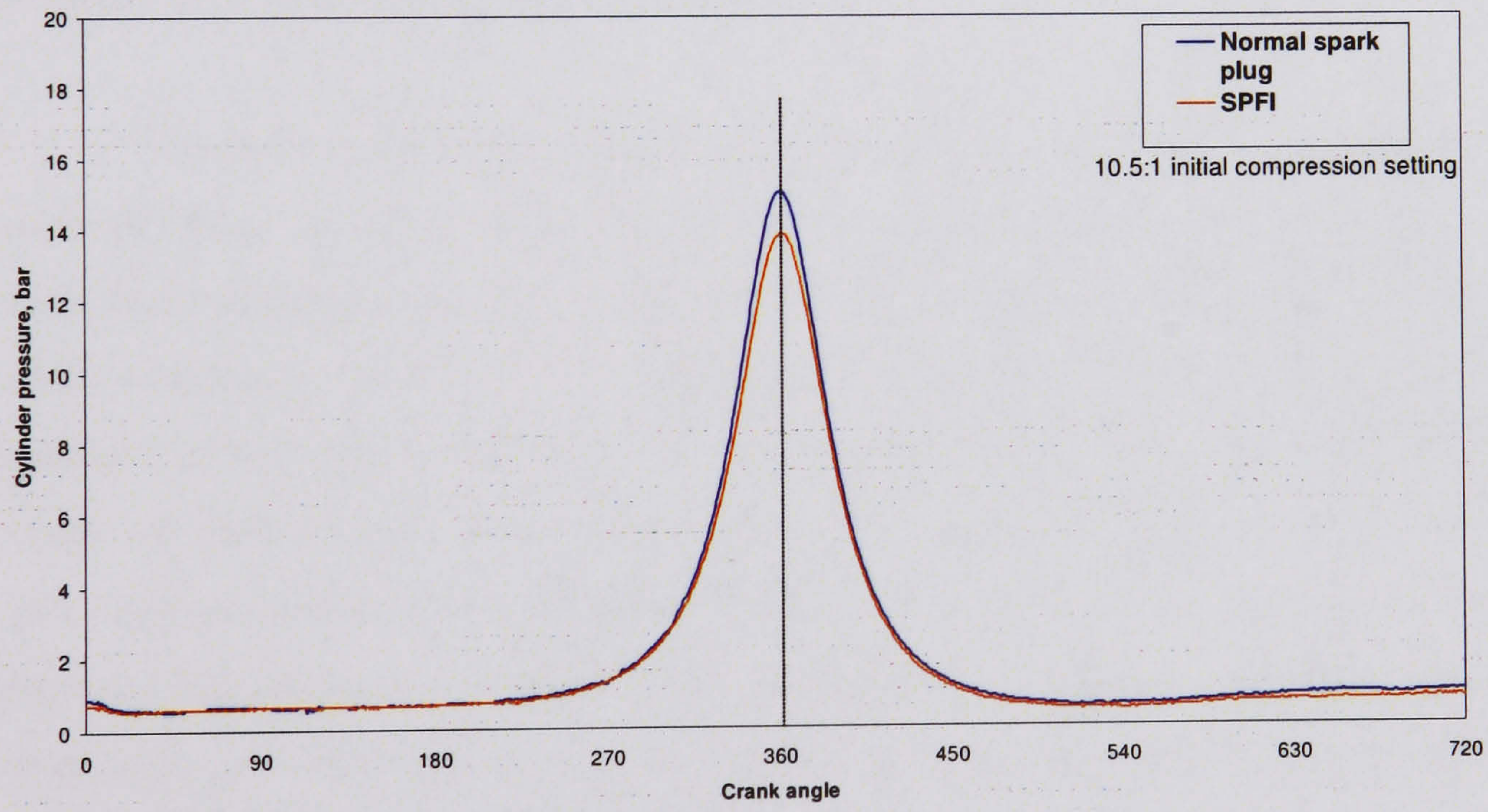

Figure 4.27 Motorised cylinder peak pressure reduction with SPFI installation

4.5 Discussion and conclusion

The design process for SPFI has been presented with four major steps undertaken to reach a fully working component. The aim of developing a full working SPFI on a Ricardo E6 engine was achieved after reviewing and refining each design. The solenoid and spark plug components of the SPFI which were initially planned to be developed from scratch failed to reach success. However, the design, fabrication and testing work have given valuable experience and realization of complexity of transforming theoretical determination to fully working component.

There were two main issues with the development process of the SPFI. First was the difficulty and compromise to arrive at a fully working design, and second was to measure SPFI effects on engine operation. Injection of fuel, which occurs at a distance from the main combustion area, causes delay in fuel arrival and need proper compensation during transient engine operations. The fuel path, adding a significant volume to the combustion chamber, reduces engine compression ratio, and thus the potential thermal efficiency [Heywood, 1988].

The first compromise made was to use a GDI injector as replacement for the solenoid valve as described in the earlier part of this chapter. Even though the theoretical calculation for the solenoid valve design provided convincing results, under achieving performance was realised as it was put into practice. The foremost weakness of the fabrication process was the uncertainty of coil and metal properties which are vital for calculating solenoid effects. Secondly, the weakness came from poor thermal resistance of coil element to high temperature induced by high electric current. The decision to utilise GDI injector was mostly due to the proven workability of GDI injector for the proposed operational parameters of SPFI methane direct injection in the Ricardo E6 engine.

The second rational compromise was to develop the SPFI around an off-the-shelf spark plug. This reduced the originality of the SPFI design but was undertaken due to time limitation and the expected higher cost for purchasing better raw materials making up the SPFI components, especially the ceramic insulator and the

O-rings. The properties of the materials making up these two components were the key parameters to successful SPFI design. These two compromises simplified the design process to developing fuel path specifications and SPFI components assembly techniques. The two requirements were met with the final SPFI and engine operation was successful with it.

As a result of the installation of the SPFI as replacement on Ricardo E6 port injection engine, two main effects were realised. One is the peak and overall cylinder pressure drop due to additional volume involve in compression stroke. This extra volume was gained from the fuel path of the SPFI which reduced the compression ratio of 10.5:1 to 10.07:1. Thus, for the same cylinder charge, engine output performances are expected to be reduced based on the correlation between compression ratio, CR and thermal efficiency, η_{th}, as described in Equation (3.8), where γ is specific heat ratio for cylinder gas mixture. Theoretically, the reduction of compression ratio from 10.5:1 to 10.07:1 results in 8% reduction in thermal efficiency.

$$\eta_{th} = 1 - \left[\frac{1}{CR^{\gamma-1}} \right] \qquad \text{Equation (4.8)}$$

The question was, when SPFI is installed and direct injection strategy improves volumetric efficiency, will the increase cylinder charge mass offset the compression ratio drop to achieved better performance? Though the answer can be sought theoretically, the data from engine experiment will provide real proof.

The second significant effect of SPFI installation is the fuel arrival delay due to lengthy fuel path and the extended fuel delivery time due to pressure loss inside the fuel path. The experiment of injecting bubbles in water showed that delay time can be reduced by increasing injection pressure as well as shortening and widening fuel path cross sectional area. These measures will significantly reduce pressure loss as well. However, expanding fuel path cross sectional area must not exceed the limit of quenching distance of methane-air combustion, which is the measure to avoid flame penetration into the fuel path.

Chapter 5

ENGINE EXPERIMENTS

5.1 Introduction

Experimental works on the Ricardo E6 engine were carried out to demonstrate the operation and performance characteristics of the SPFI methane direct injection system. The engine was initially run with methane port injection, then it was run with SPFI methane direct injection with the same variation of operational parameters as with port injection. The performance data from the methane port injection and SPFI methane direct injection delivery methods were compared. It should be noted that gasoline port injection results are not shown for comparison here. This is because the performance of the Ricardo E6 is poor when operated on gasoline (due to inadequacies in gasoline fuel preparation system) and to include them would create a false impression on the impact of converting a gasoline engine to methane operation.

The operation of methane direct injection is characterised by the induction of air when the intake valve is open and subsequent methane injection directly into the cylinder. The cylinder, thus, receives a maximal amount of air during intake stroke. Mixture air-fuel ratio is determined by the length of injection pulse of methane at a fixed injection pressure. Early injection, during the final part of intake stroke or early part of compression stroke, leads to a more homogeneous mixture that can produce more power for high load but with volumetric efficiency reduction. Late injection, near or after the intake valve closes, leads to a stratified mixture for better fuel economy especially at part and low loads, and greater volumetric efficiency. In general, direct injection allows more air intake per cycle than port injection thus increases the volumetric or charging efficiency.

In the experiment, methane was supplied at a pressure between 30 and 80 bar to the fuel injector through a pressure regulator from a 200 bar methane container. Port fuel injection was achieved by installing the fuel injector to the intake manifold.

Methane direct injection was achieved by installing SPFI in one of the two spark plug holes available on the engine. The objectives of this experimental works were;

1. To determine the best injection and ignition setting for SPFI direct injection of methane in order to achieve optimal performance on a Ricardo E6 single cylinder engine.
2. To determine the effect of different injection pressures, fuel path lengths, mixture stoichiometry, engine speeds and engine loads on the performance of SPFI methane direct injection.
3. To compare the performance of the Ricardo E6 engine fuelled by SPFI methane direct injection with the one using methane port injection.

5.2 Spark Plug Fuel Injector

The development of SPFI and its detail design has been described in Chapter 4. It consists of an original M14-threaded single tip spark plug with a fuel passage bored on one side of the thread. A gasoline direct injection (GDI) fuel injector is attached to the spark plug using a specially designed housing. The fuel path drawn on the threaded section of the spark plug ends 2 mm before reaching the tip. The width of the path increases near the tip to allow spray expansion. The fuel injector is connected to a 200 bar methane tank by a 1.5 meter, 4-mm inner-diameter (6-mm outer diameter) copper pipe. Injection pressure is controlled by a pressure regulator at the tank exit. The GDI nozzle and SPFI nozzle is connected by a 12-cm long variable surface area fuel path. Due to the location of fuel injector, fuel delivery is delayed and injection timing must be adjusted to compensate the delay accordingly. Figure 5.1 shows the SPFI.

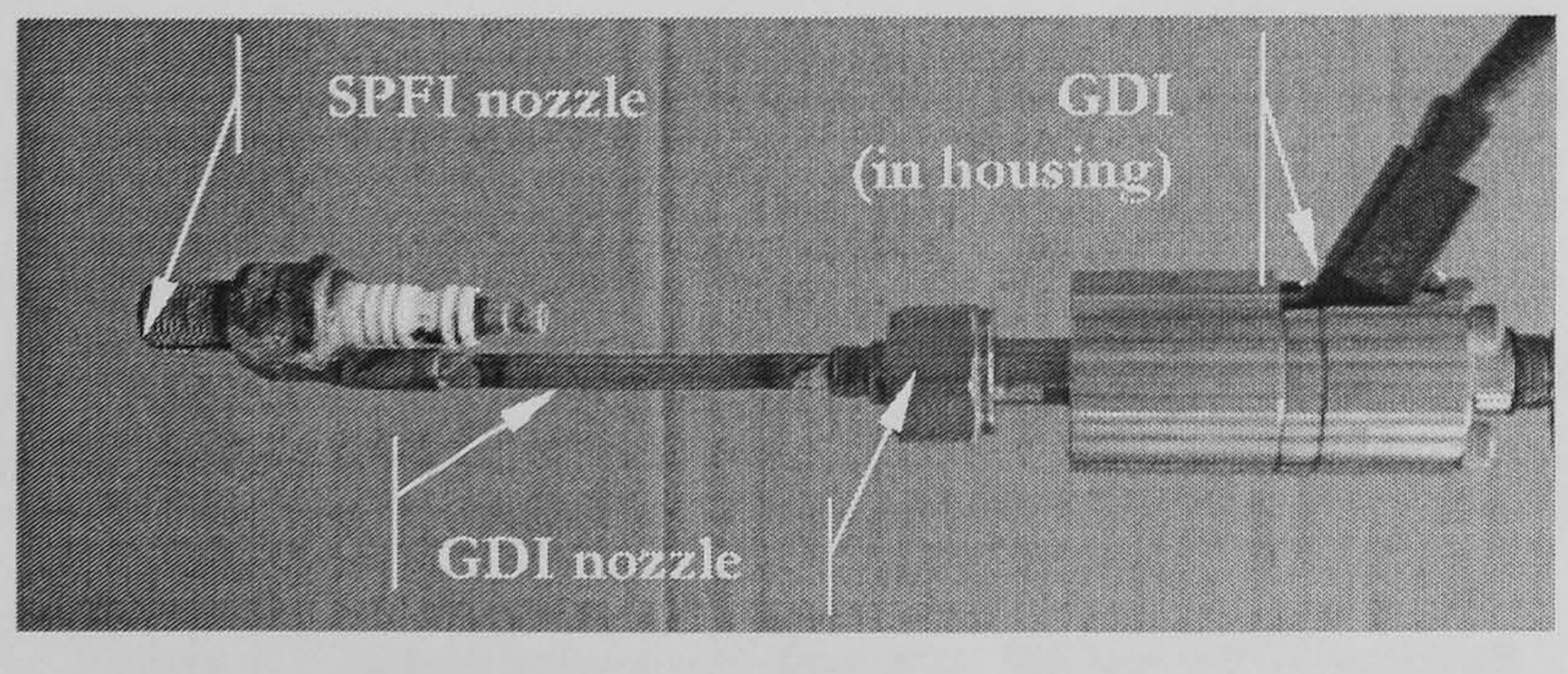

Figure 5.1 Spark Plug Fuel Injector

5.3 Ricardo E6 Single Cylinder Engine

The test engine used in the measurement was a Ricardo E6 single cylinder variable compression engine. The combustion chamber has two poppet-type valves, one for air intake and another for exhaust gas. The compression ratio can be varied between 4 and 22 by a sliding element in the cylinder case. The maximum rated speed was 4000rpm but due to the age of the engine that has been operating for 32 years and the insertion of a spacer plate between the main body and cylinder head of the engine for placing a viewing window and a pressure transducer, which may affect the dynamic balance of the structure, engine speed is limited to 2000 rpm. An electric dynamometer is connected to the engine crankshaft by a coupler which can motorise the engine. It is rated at constant torque of 95Nm at 0-3000rpm and a constant power of 30kW at 3000-4000rpm. This research engine was designed for reliable operation even at severe combustion knock. It can be operated as spark ignition or compression ignition and run with various fuel modes. The cylinder head and shape of piston crown can be interchanged to serve various purposes and objectives of research works. In this project, a gasoline cylinder head with a flat-top piston crown were used. Table 5.1 shows the physical parameters of the engine. Figure 5.2 shows the cam profile where inlet and exhaust valves lifts are described with respect to piston position.

Bore (mm)	76.2
Stroke (mm)	111.125
Displacement volume (litre)	0.507
Compression ratio	10.5 : 1
Intake valve open	8° BTDC
Intake valve close	33° ABDC
Exhaust valve open	42° BBDC
Exhaust valve close	8° ATDC
Ignition starts	0-60° BTDC$_{power}$
Injection starts	60°BTDC$_{intake}$-30°ABDC$_{compression}$
Cooling method	Water cooling
GDI Injector nozzle	1 x ϕ0.5 mm
SPFI nozzle	Variable surface areas
Valve clearance (intake/exhaust)	0.15 mm / 0.20 mm

Table 5.1 Specification of Ricardo E6 for SPFI system

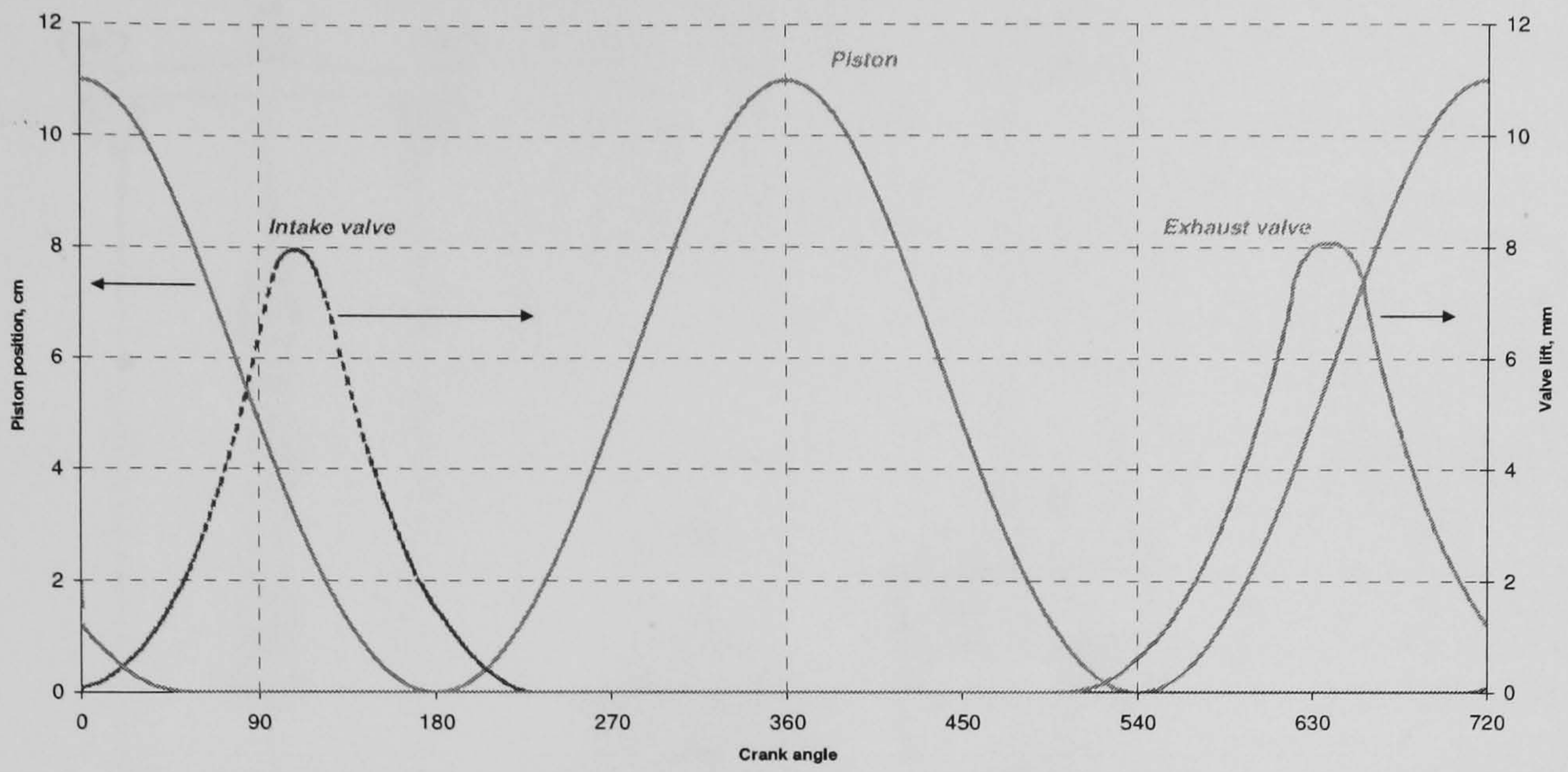

Figure 5.2 Piston position and cam profile of Ricardo E6 with gasoline head, compression ratio of 10.5:1.

The Ricardo E6 engine is capable of operating with liquid and gaseous fuels. The fuel intake system for the engine was made changeable for various fuel modes; mixing chamber, carburettor, manifold/port injection. Direct fuel injection can be realised by using one of the spark plug holes on the available gasoline cylinder head. Figure 5.3 and 5.4 show the Ricardo E6 engine used in this work.

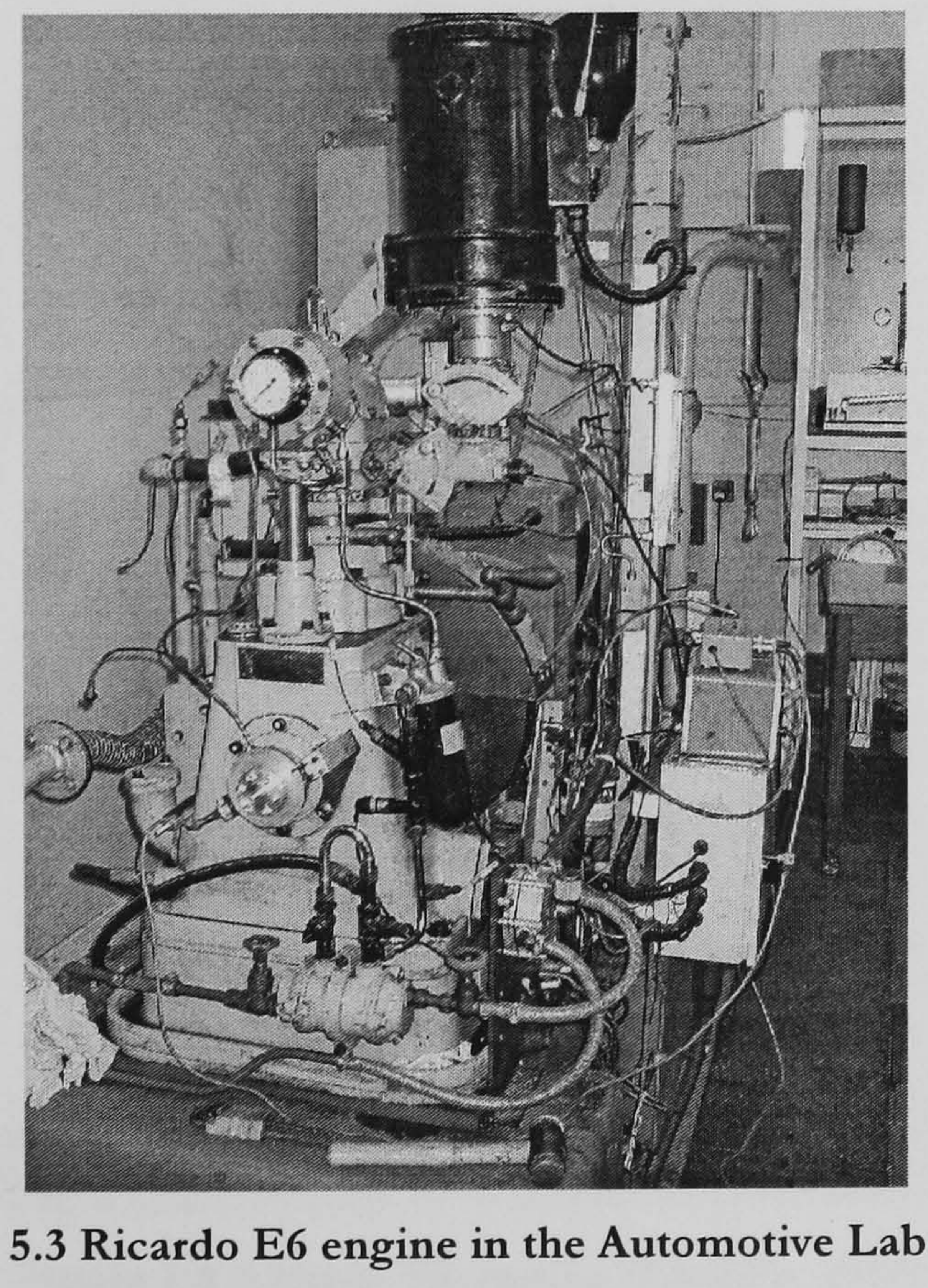

Figure 5.3 Ricardo E6 engine in the Automotive Laboratory

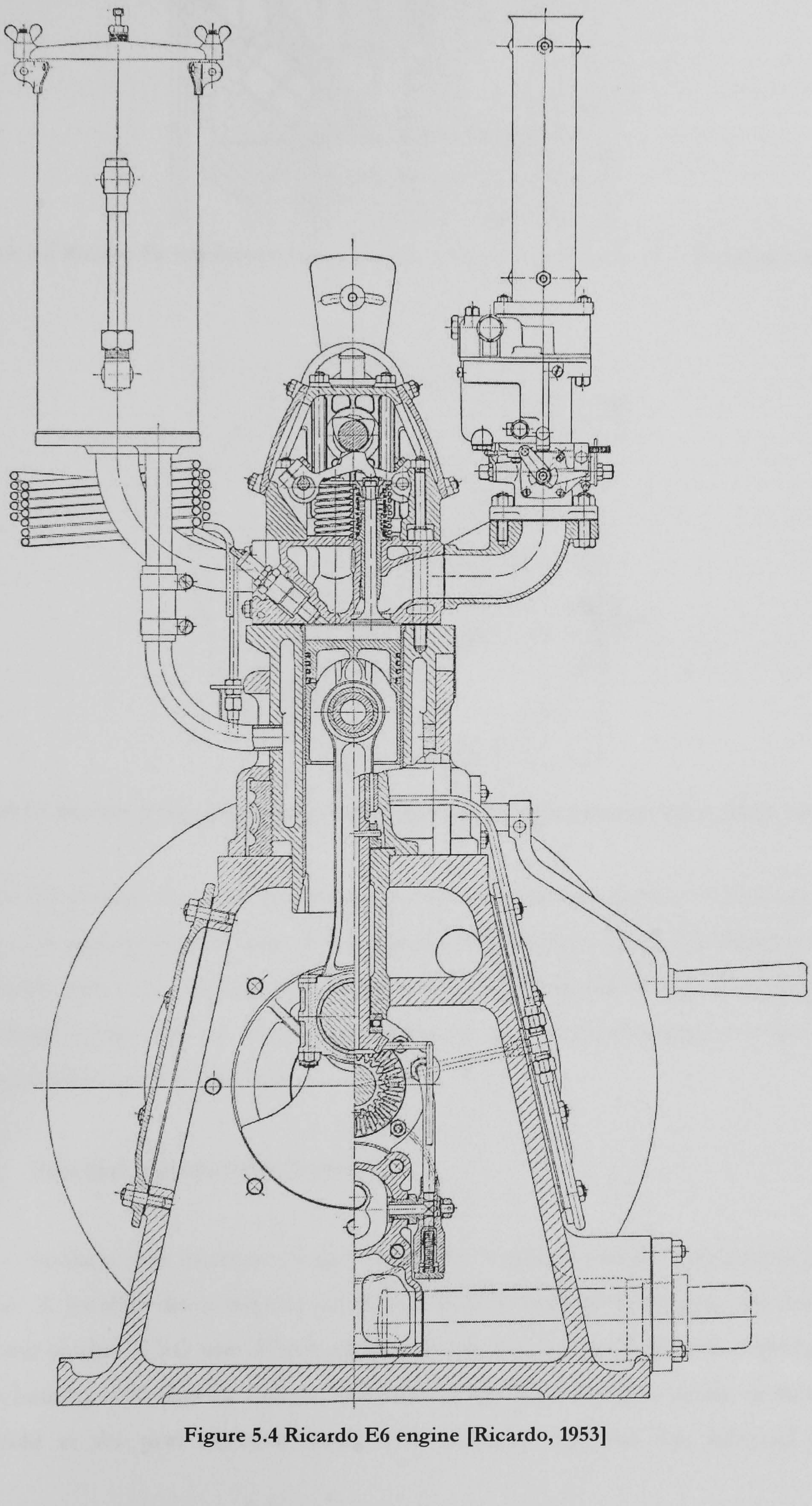

Figure 5.4 Ricardo E6 engine [Ricardo, 1953]

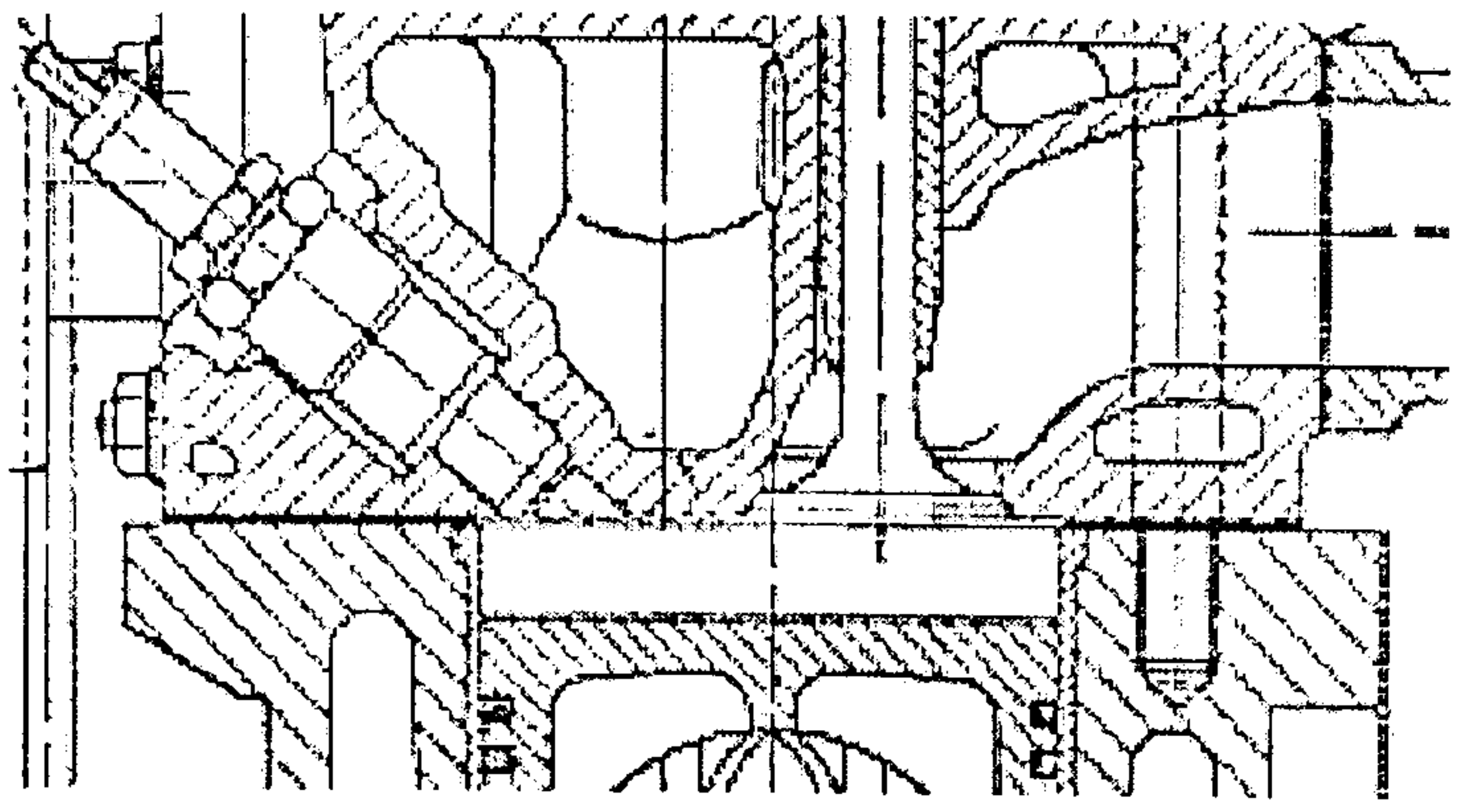

Figure 5.5 Ricardo E6 spark ignition/gasoline type cylinder head (side view) [Ricardo, 1953]

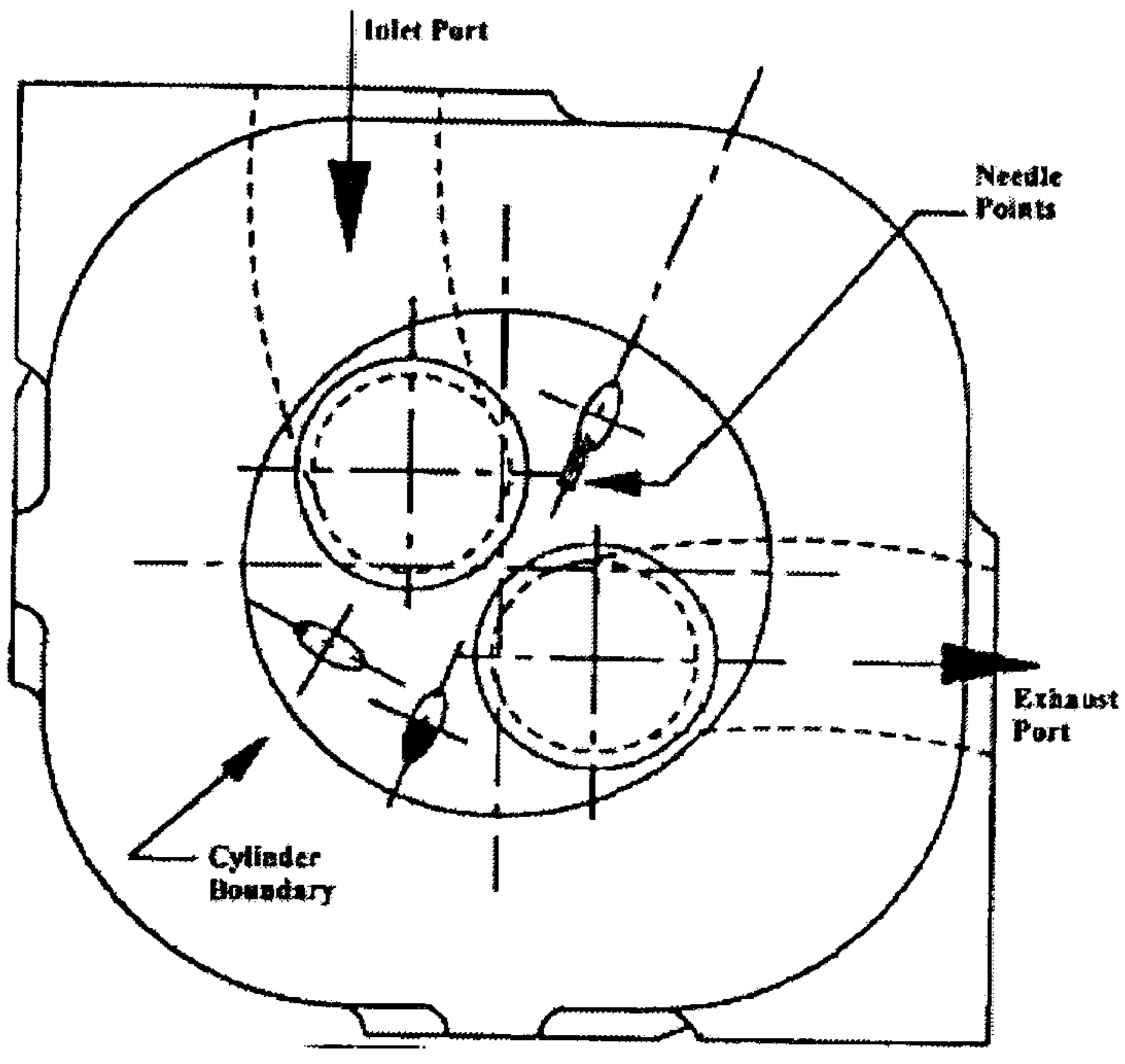

Figure 5.6 Ricardo E6 spark ignition/gasoline type cylinder head (bottom view) [Erdil, 2002]

Figure 5.5 shows the cross section of the Ricardo E6 combustion chamber and Figure 5.6 shows the plan view of the cylinder head. Lubrication is provided by an externally driven electric motor and water coolant is circulated by separately driven centrifugal pump. An oil heater is available to make sure the engine is run at sufficient lubrication temperature.

5.3.1 Port fuel injection (PFI) system

Methane port injection on the Ricardo E6 is taken to be the base case in the project. A gasoline direct injector (GDI) was used in both port injection and direct injection modes. It has one 0.7mm injector nozzle and is being placed in a specially made housing to bridge the fuel rail and SPFI in the direct injection mode, or intake manifold in the port injection mode. Port injection methane was achieved by attaching the GDI injector to a hole available on intake manifold using the adaptor shown in Figure 5.7. Methane was supplied from a 200bar bottle and a pressure regulator reduced it to the desired injection pressure. By varying pulse length from a pulse generator controlling the GDI injector, lambda values between 0.9 and 1.1 were achieved.

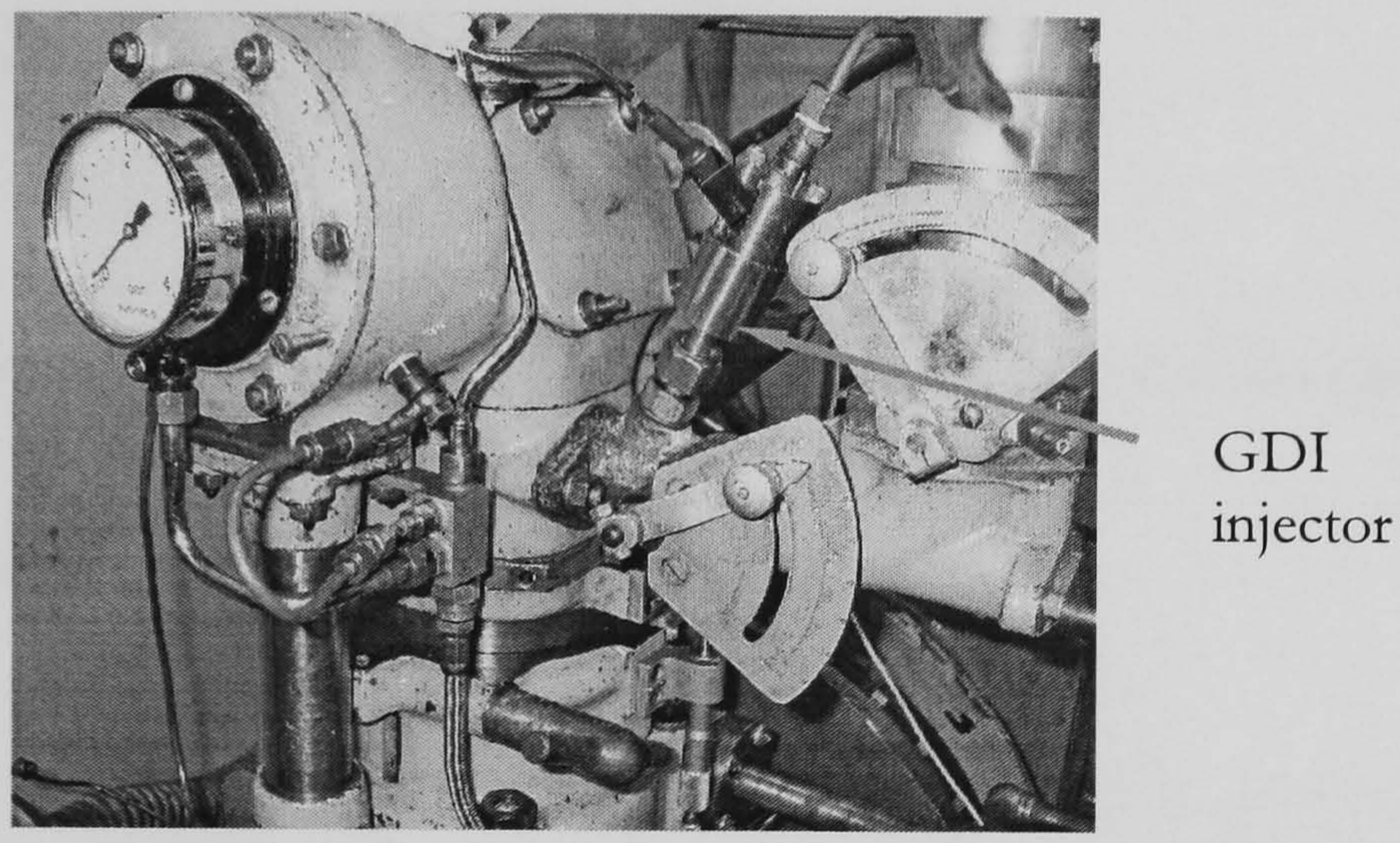

Figure 5.7 Port injection intake arrangements

5.3.2 Direct injection (DI) fuel system

The GDI injector was connected to the modified spark plug shown and attached to the spark plug hole next to the exhaust valve as shown in Figure 5.8 and in Figure 5.9. The same arrangement for fuel delivery is applied as in port injection mode. However, methane is injected at a higher pressure in order to compensate the cylinder pressure, fuel path length and the time limits.

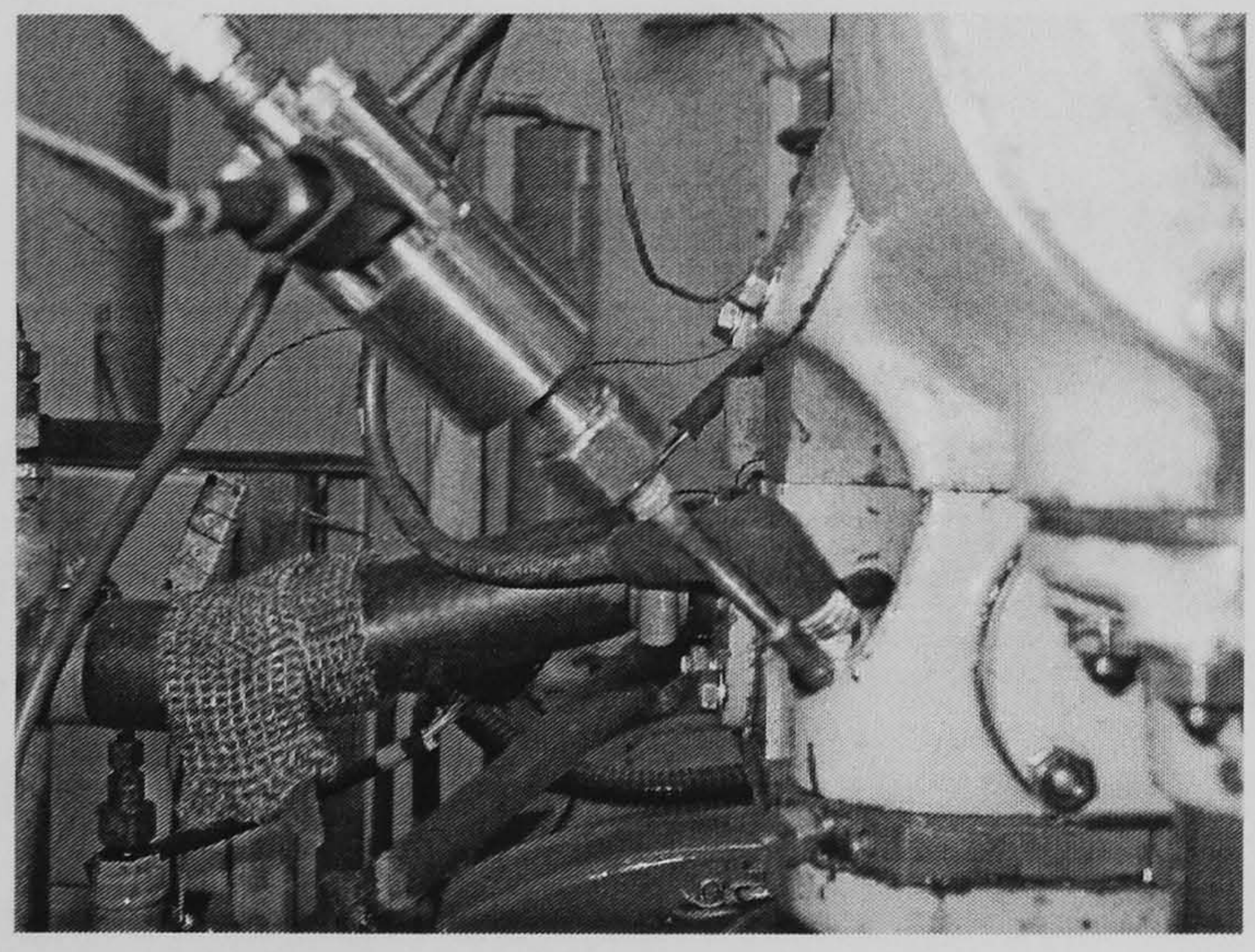

Figure 5.8 SPFI direct injection on the cylinder head

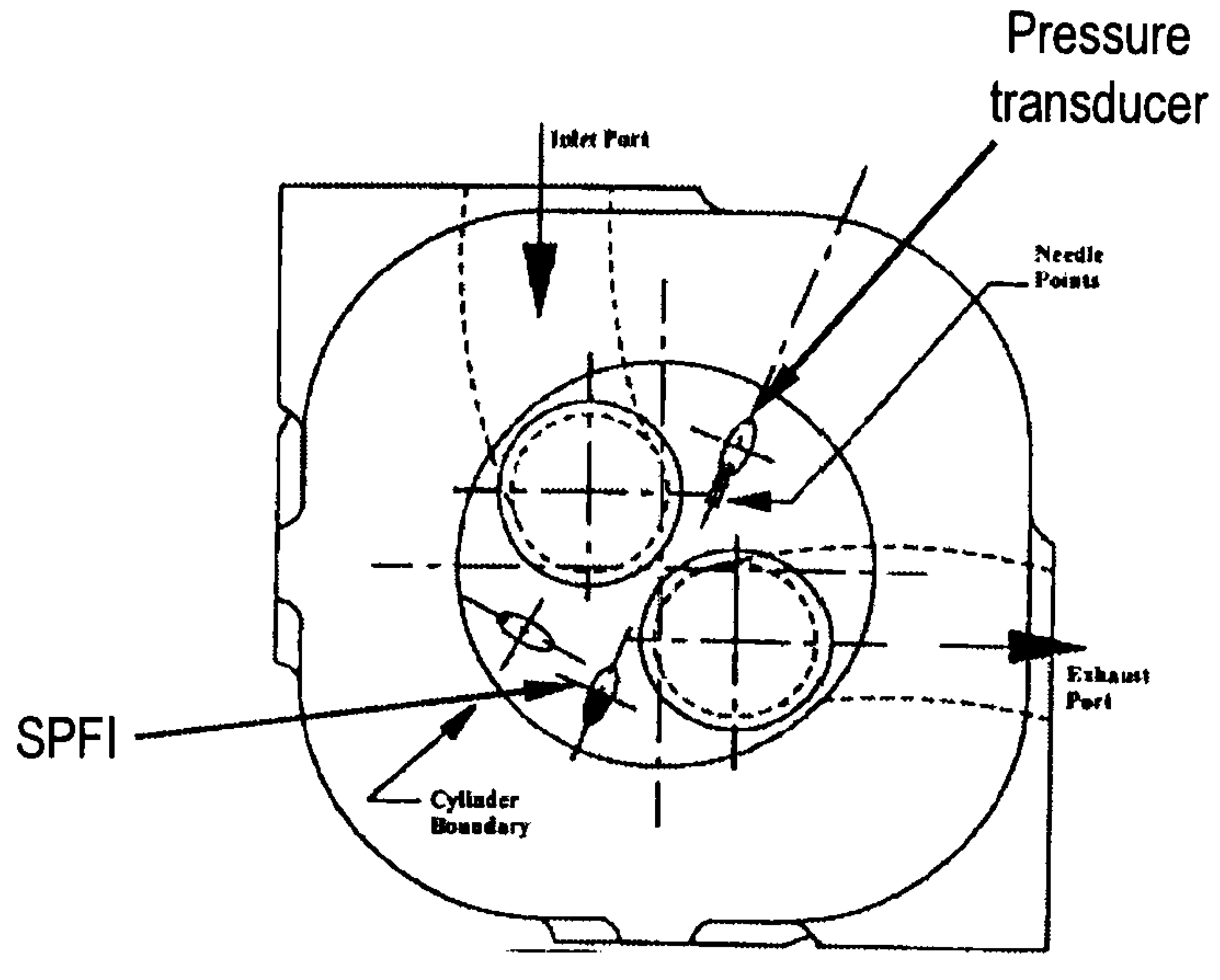

Figure 5.9 Location of SPFI and pressure transducer on the cylinder head [Erdil, 2002]

5.3.3 Ignition system

The ignition system consists of three components; pulse generator unit, ignition coil and trigger pick-up. The spark ignition system is of capacitor discharge type where a capacitor, charged from a DC source, is periodically discharged via a silicon controlled rectifier through the primary of an ignition coil. The discharge is initiated by a signal from a magnetic pick-up system fitted to the crankshaft which gives one signal per crank revolution. The ignition timing is variable over the range of 60° crank angle without change in peak voltage. The spark plug fires twice on each cycle; near the TDC of both compression and exhaust stroke.

5.3.4 Dynamometer control unit

The dynamometer is an electric swinging field direct current type and driven by the engine via a flexible coupling. The two units are mounted on a common cast iron bed plate. The dynamometer is capable of absorbing the maximum power produced by the engine at all normal speeds. It can also motor the engine over the indicated speed range which provides the initial drive to the engine before firing takes place. The dynamometer is controlled by an AC solid state controller, shown in Figure 5.10, which also rectifies the main current so that DC dynamometer can be used. Simple switchgear enables the dynamometer to be operated as a motor to start the engine, of in order to motor it for determination of friction and pumping losses. The controller also houses the controls and indicating lights for the oil heater, water pump, oil pump, fuel pump and air heater. Energy developed by the dynamometer is absorbed by a self contained water cooled load bank. A flow of water through the tank is required in order to control the temperature.

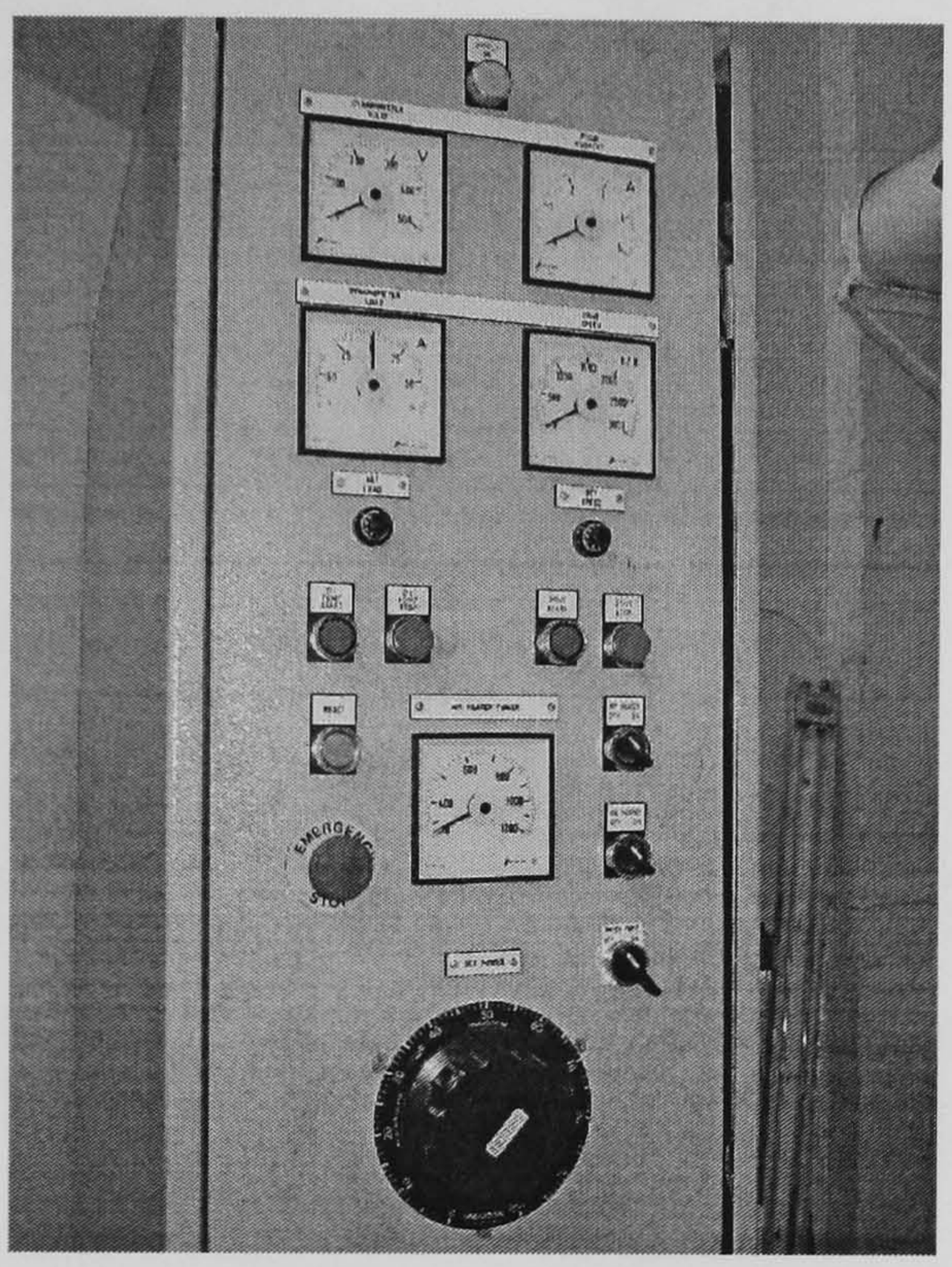

Figure 5.10 Main control unit

5.4 Instrumentation

The schematic of engine and instruments is shown in Figure 5.11. Figure 5.12 shows the setup for performance measurement in the engine laboratory as represented by Figure 5.11. Instrumentation for measuring the performance of the engine includes a pressure sensor and a charge amplifier for cylinder pressure measurement, six units of thermocouples for temperature measurements at various locations, an air flow meter, a Tri-flat Variable-Area gas flow meter, a lambda sensor for air-fuel ratio indication, a load cell and signal amplifier for torque measurement, a camshaft encoder, a crankshaft encoder for crank angle and engine speed measurement. The data acquisition system consists of a National Instrument DAQ box and LabView v.7.0 software installed in computer for data recording and real time data display.

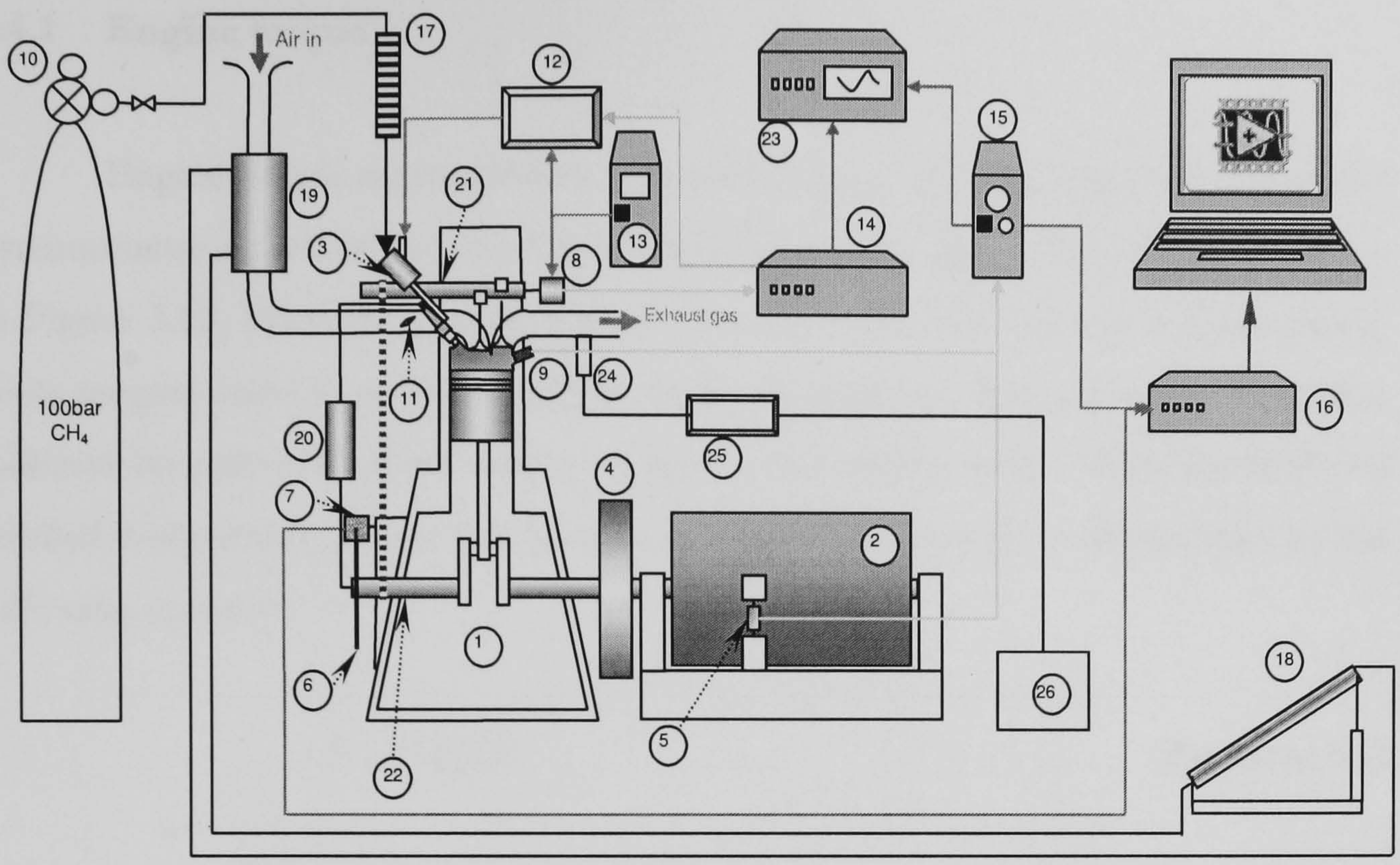

1.RICARDO E6 ENGINE
2.ELECTRIC DYNAMOMETER
3.SPARK PLUG FUEL INJECTOR
4.FLYWHEEL
5.LOAD CELL
6.SLOTTED DISK
7.PHOTODIODE
8.SHAFT ENCODER
9.PRESSURE SENSOR
10.PRESSURE REGULATOR
11.THROTTLE VALVE
12.MOSFET
13.POWER SUPPLY UNIT
14. PULSE GENERATOR
15.CHARGE AMPLIFIER
16.DATA ACQUISITION UNIT
17.FUEL FLOW METER
18.MULTISLOPE MANOMETER
19.VISCOUS AIRFLOW METER
20.SPARK IGNITION UNIT
21.CAMSHAFT
22.CRANKSHAFT
23.OSCILLOSCOPE
24.LAMBDA SENSOR
25.LAMBDA METER
26.CAR BATTERY

Figure 5.11 Schematic of instrumentation and data acquisition system

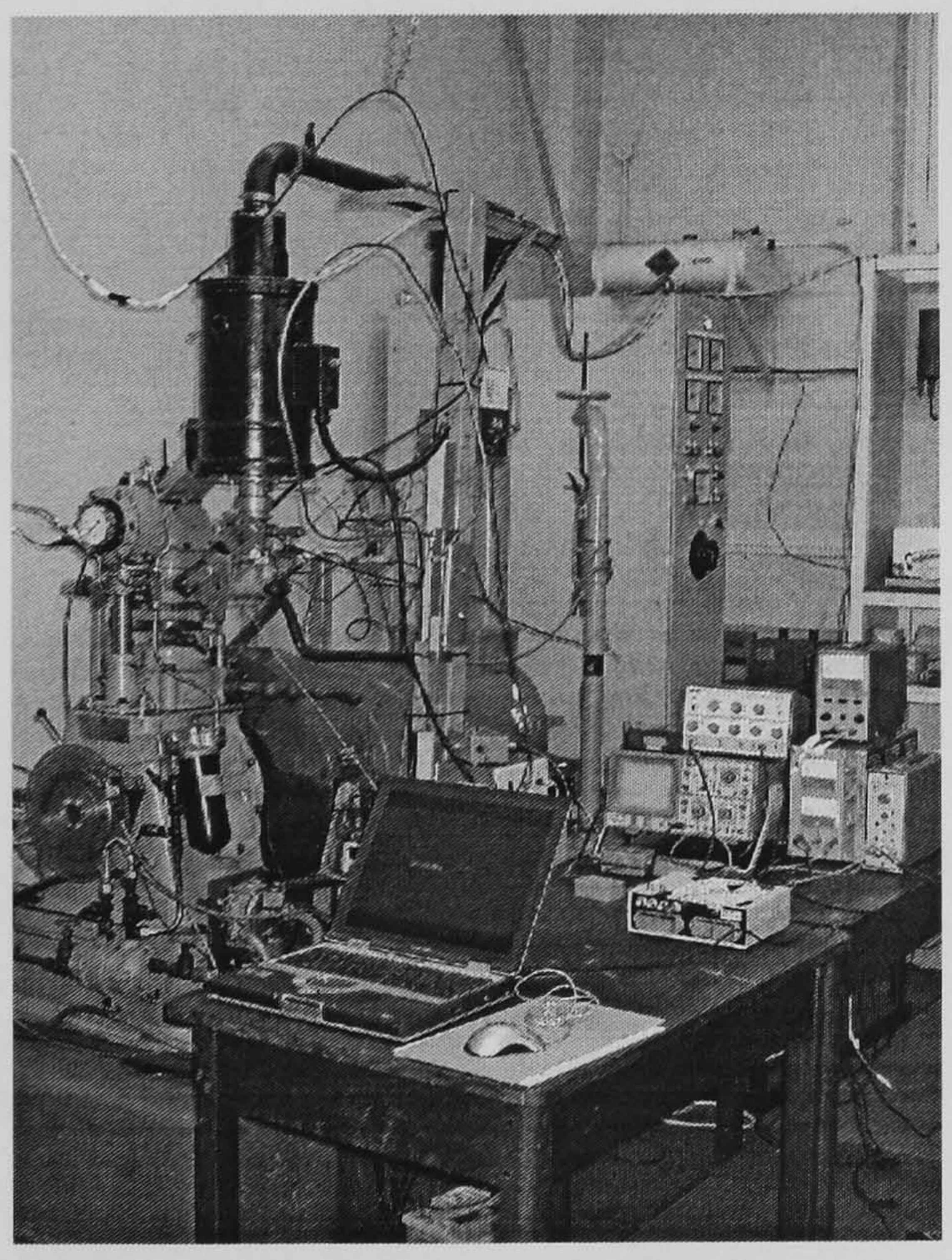

Figure 5.12 Instrumentation and data acquisition system

5.4.1 Engine torque

Engine torque measurements are made using a 0.457 m long load arm on the dynamometer on which a load cell is vertically connected to the test bed plate, shown in Figure 5.13. Prior to the experiments, the load cell was calibrated against static loads ranging from 0 to 200N weights. Figure 6.15 shows the calibration curve that indicates linearity of load cell output voltage to the applied weight. With the load arm levelled horizontally, at any steady engine speed, engine torque is determined by the following equation.

$$T = 0.457W \qquad \text{(Equation 5.1)}$$

Where T is engine torque and W is the weight in Newton determined from converting voltage reading, V from the load cell based on the equation on Figure 5.14.

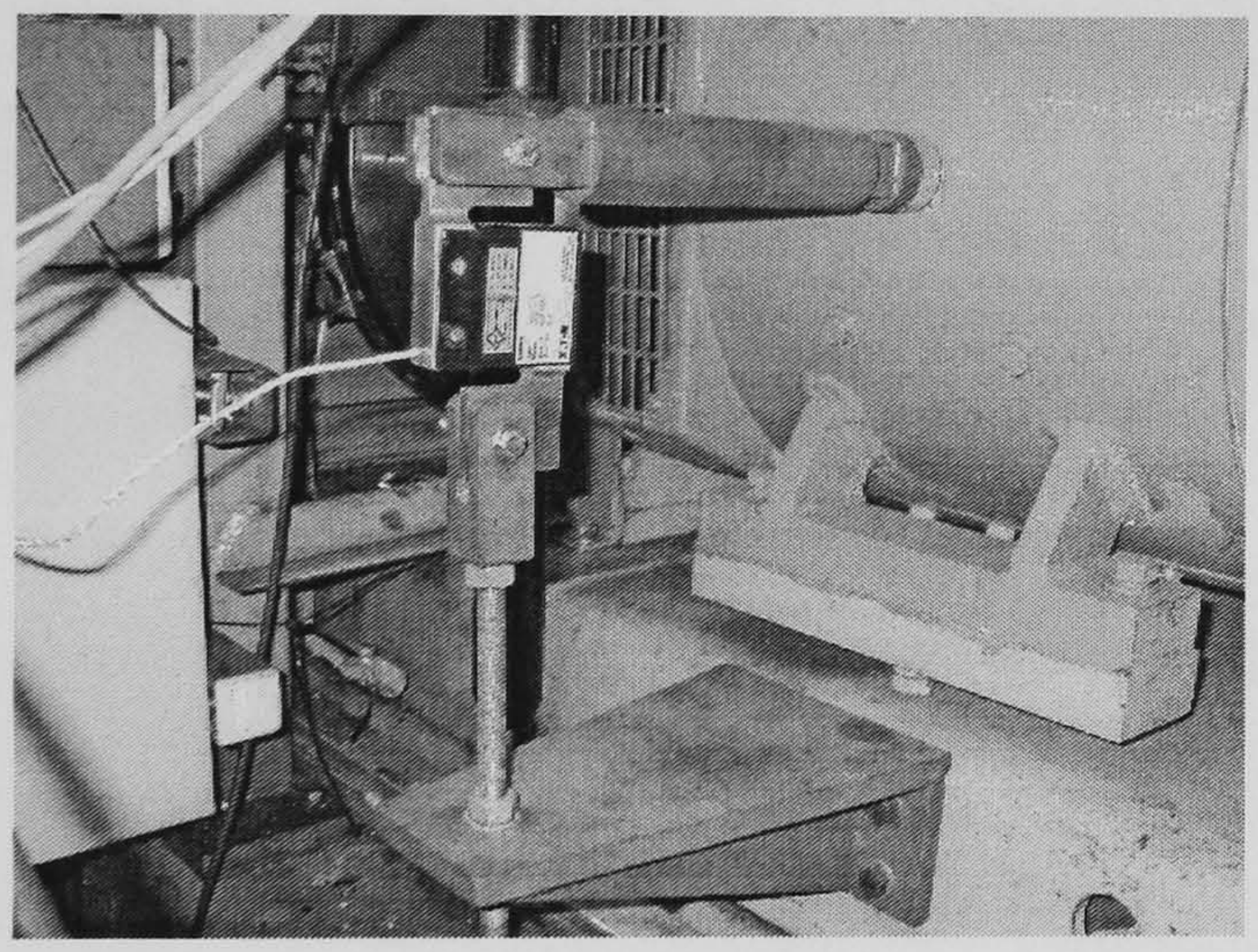

Figure 5.13 Load cell and load arm for torque measurement

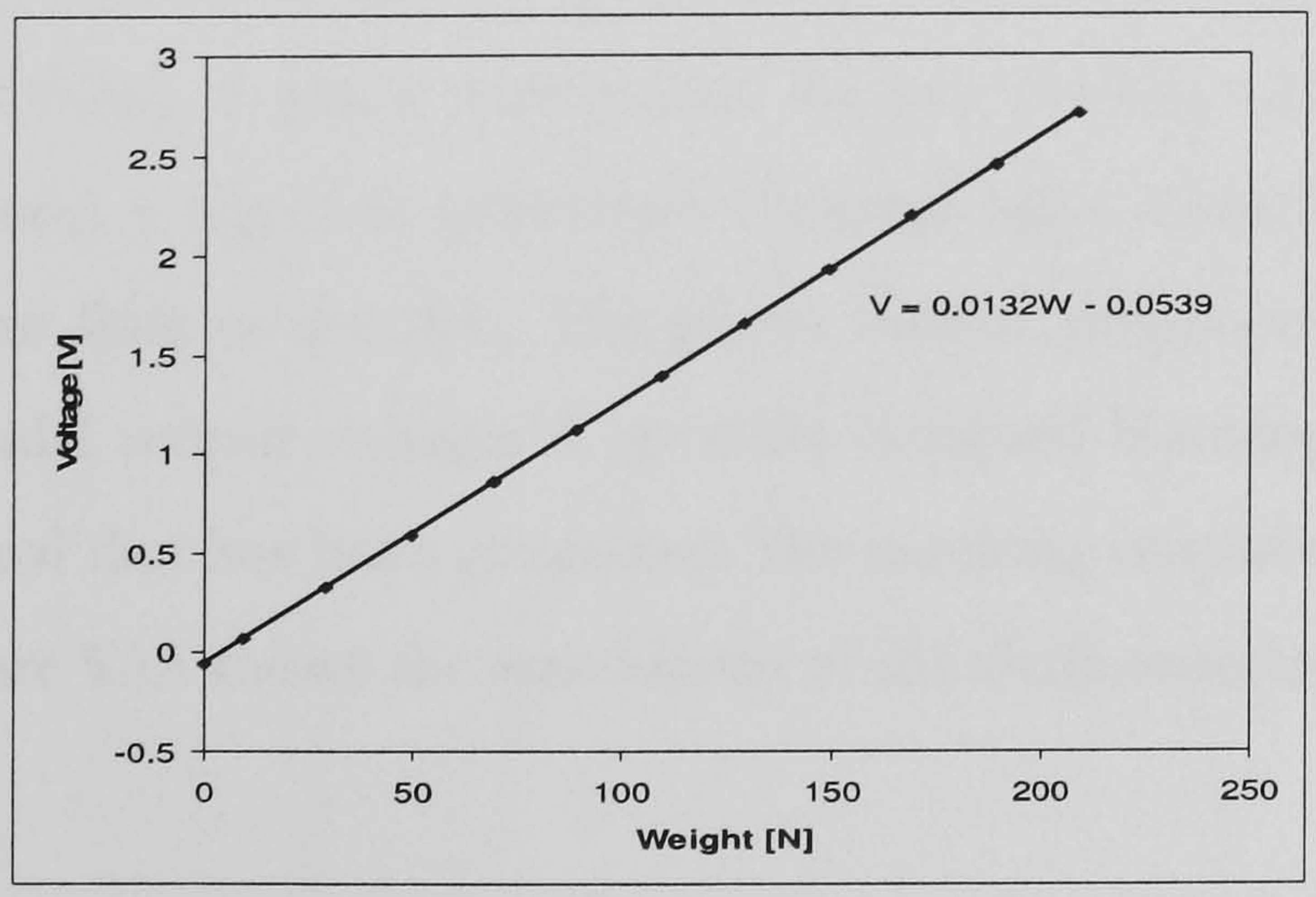

Figure 5.14 Load cell calibration curve

5.4.2 Crank angle and speed

The electric dynamometer with its control unit motorise the engine to a constant speed. Engine crank angle is determined by a photodiode that record two sets of signals from a slotted disk attached to the crank shaft as shown in Figure 5.15. The disk has two layers of slots, one is a single slot and another is a set of 180 slots. Because in every engine cycle there are two crank shaft rotations, the photodiode and slots system gives 2 TDC signals and 360 pulse per engine cycle (720°).

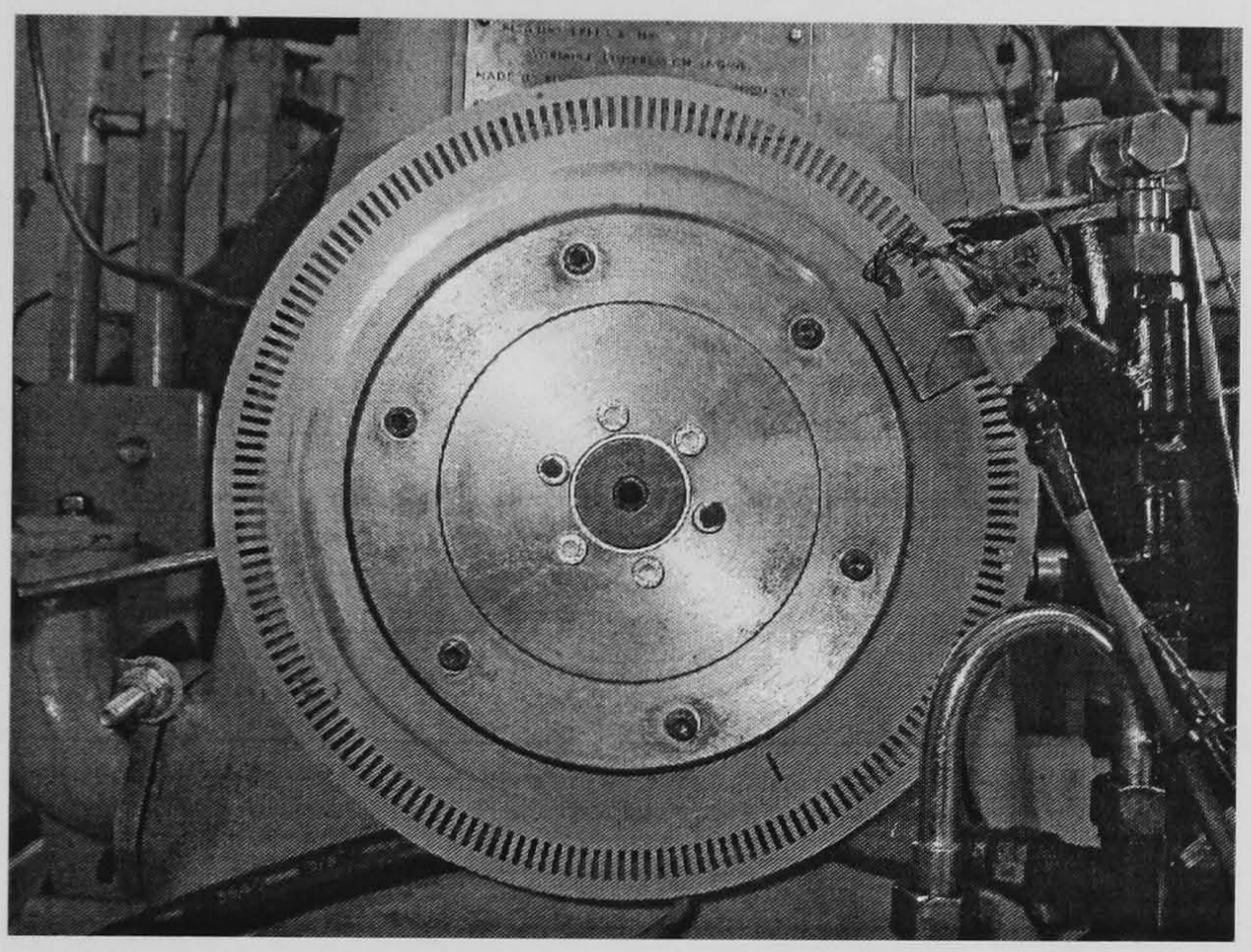

Figure 5.15 Photodiode and slotted disk attached to crankshaft

In addition, a shaft encoder is mounted on the camshaft to locate one signal per cycle because there is one camshaft rotation per two crankshaft rotation. This signal is set to be the input of the fuel injector control. A shaft encoder model BDK 06.05A360-5-4 made by Baumer electric was used. A set of bright/dark segments on a disc are photoelectrically scanned. A high quality infrared LED emits light in the invisible range (800nm). A plane convex lens focuses the light into a parallel beam. Once per revolution a signal is generated. Infrared light is transmitted through a diaphragm and the slots of the disc. The photo diodes, positioned behind the disc, generate a sinusoidal output voltage. A specially designed blanking circuit processes the sinusoidal signal that has been generated. The resulting output of the encoder is a square wave. Figure 5.16 shows the attachment of the shaft encoder to the camshaft.

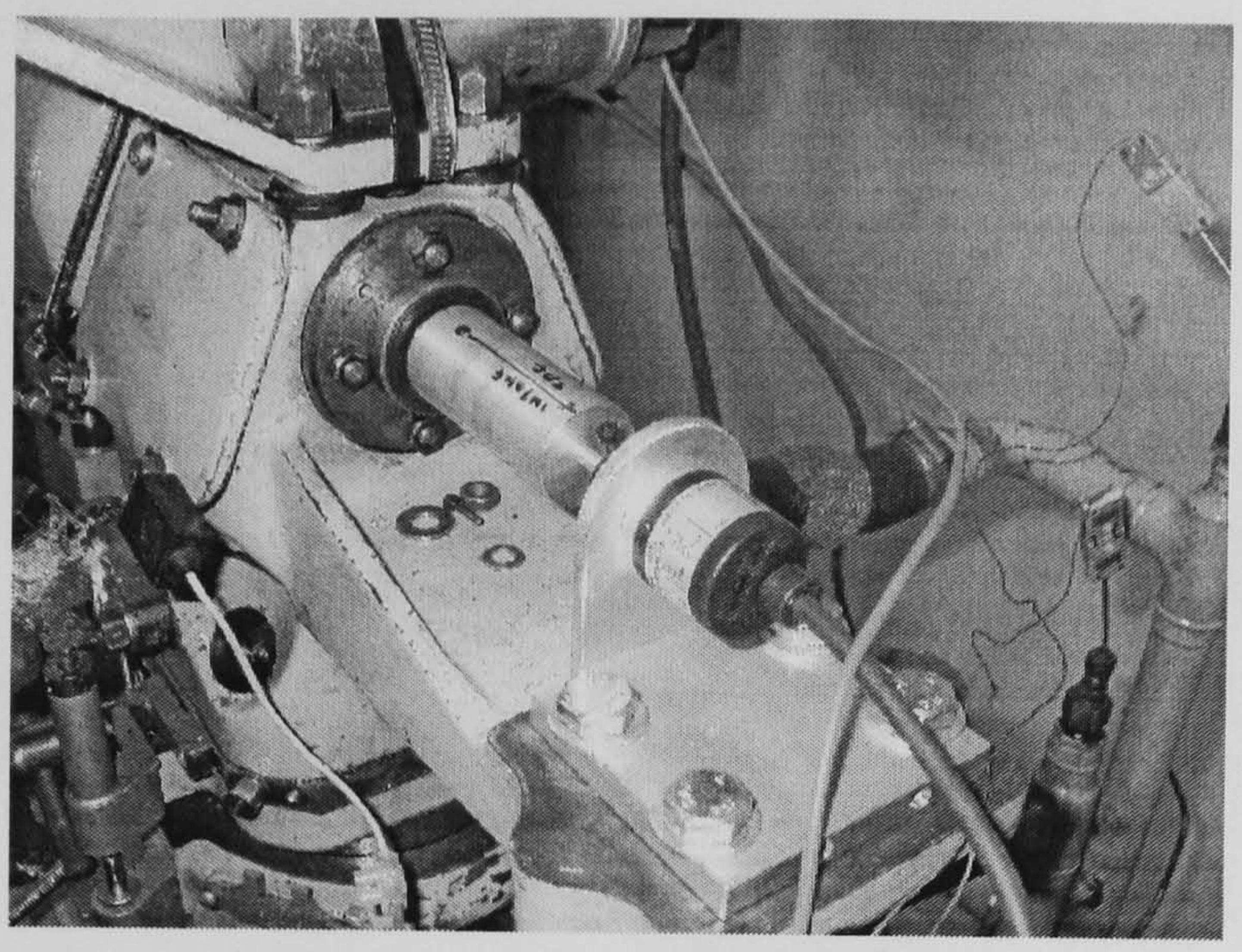

Figure 5.16 Camshaft encoder

5.4.3 Methane flow rate

Initially, methane flow rate was determined from the setup in Figure 5.17 and 5.18. A Tri-flat Variable-Area flow meter by Fischer Porter was used. Methane from 200 bars bottle passed through a pressure regulator and its pressure drop to near the injection pressure. Then the pressure gauge at the exit of the flow meter determined the injection pressure by adjustment on the pressure regulator. However, this flow meter operating pressure is limited at 35 bar. Initially the engine was run with 30 bar methane injection pressure, which was within the operating range of the fuel flow meter. An oxygen sensor (a lambda meter) was attached to the exhaust manifold as a direct indicator of charge mixture stoichiometry. The measured AFR data from fuel and air flow meters was in good agreement with the lambda meter reading with 1.0% accuracy. As the injection pressure was increased to more than 35 bars, the gas flow meter use was terminated, and AFR was determined using lambda meter only.

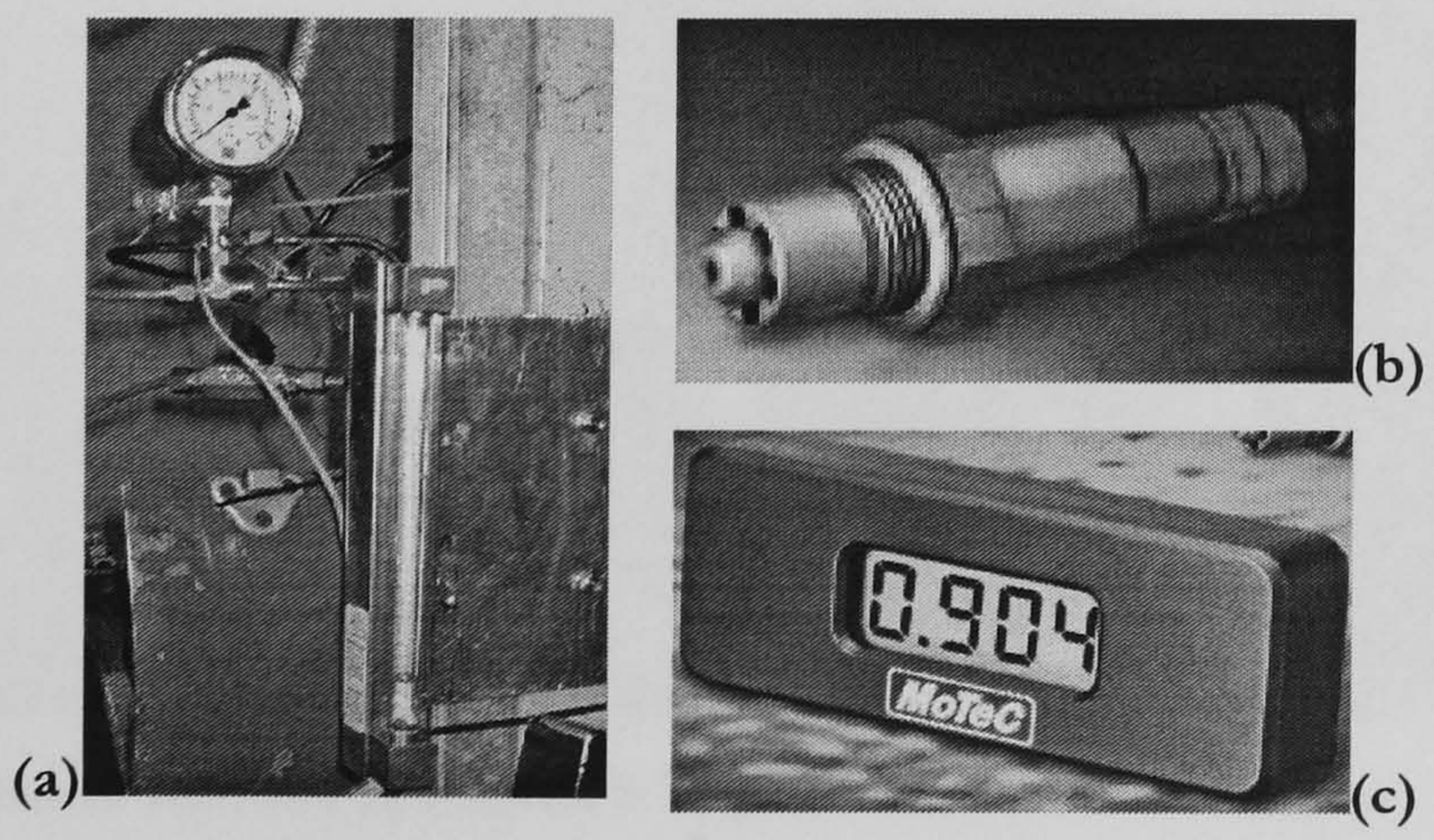

Figure 5.17 Tri-flat gas-flow meter (a), lambda sensor (a) MOTEC lambda meter (c)

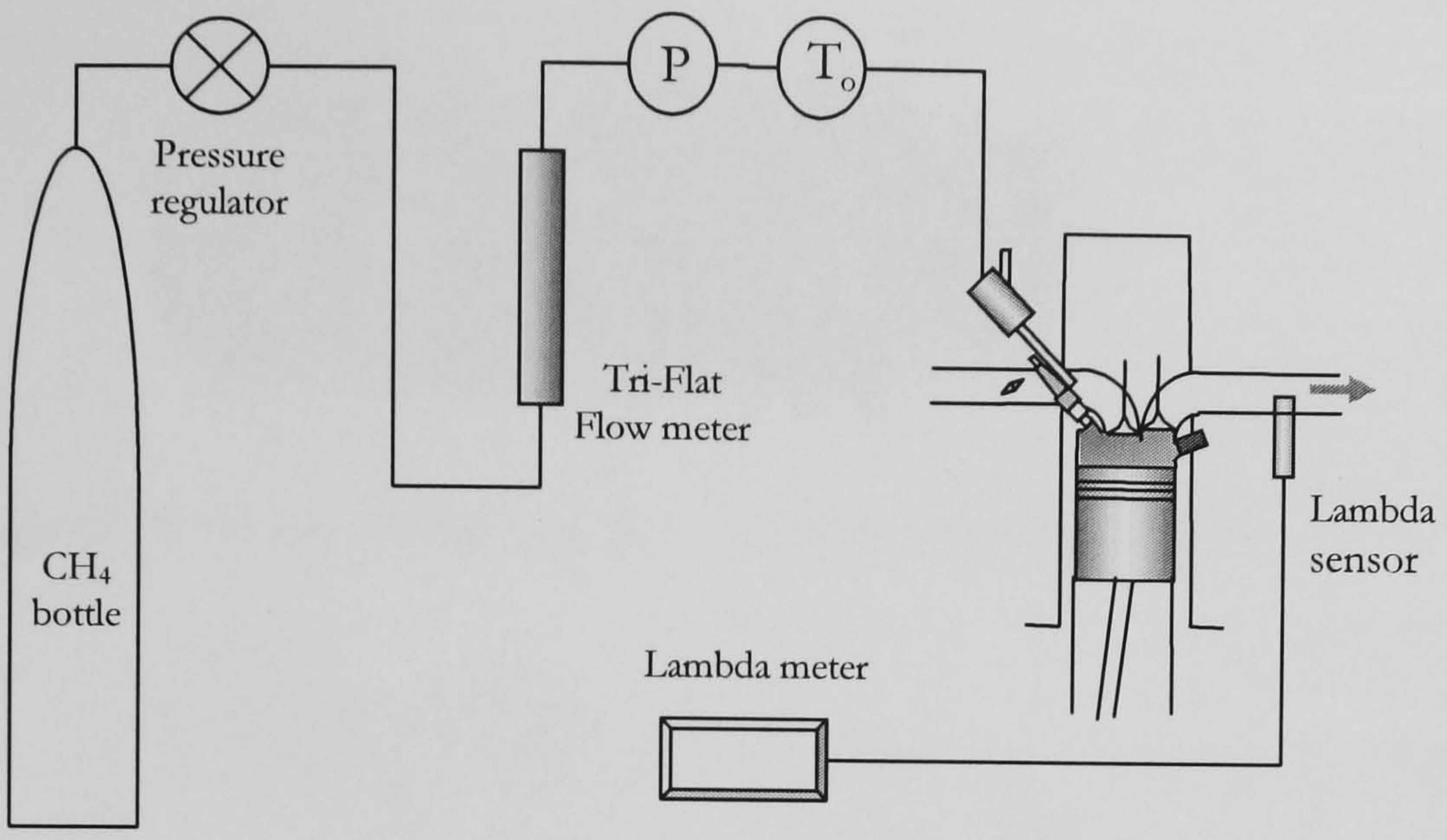

Figure 5.18 Methane flow measurement

5.4.4 Air flow rate

Measurement of air flow is a vital parameter to determine air consumption and mixture stoichiometry in the combustion process. Air movement in the intake system is a pulsating flow because air is induced only during 180° CA in every 720° CA. Therefore, the effect of flow fluctuation must be corrected to get proper mass air flow rate reading. This was done by using a viscous air flow meter as shown in Figure 5.19

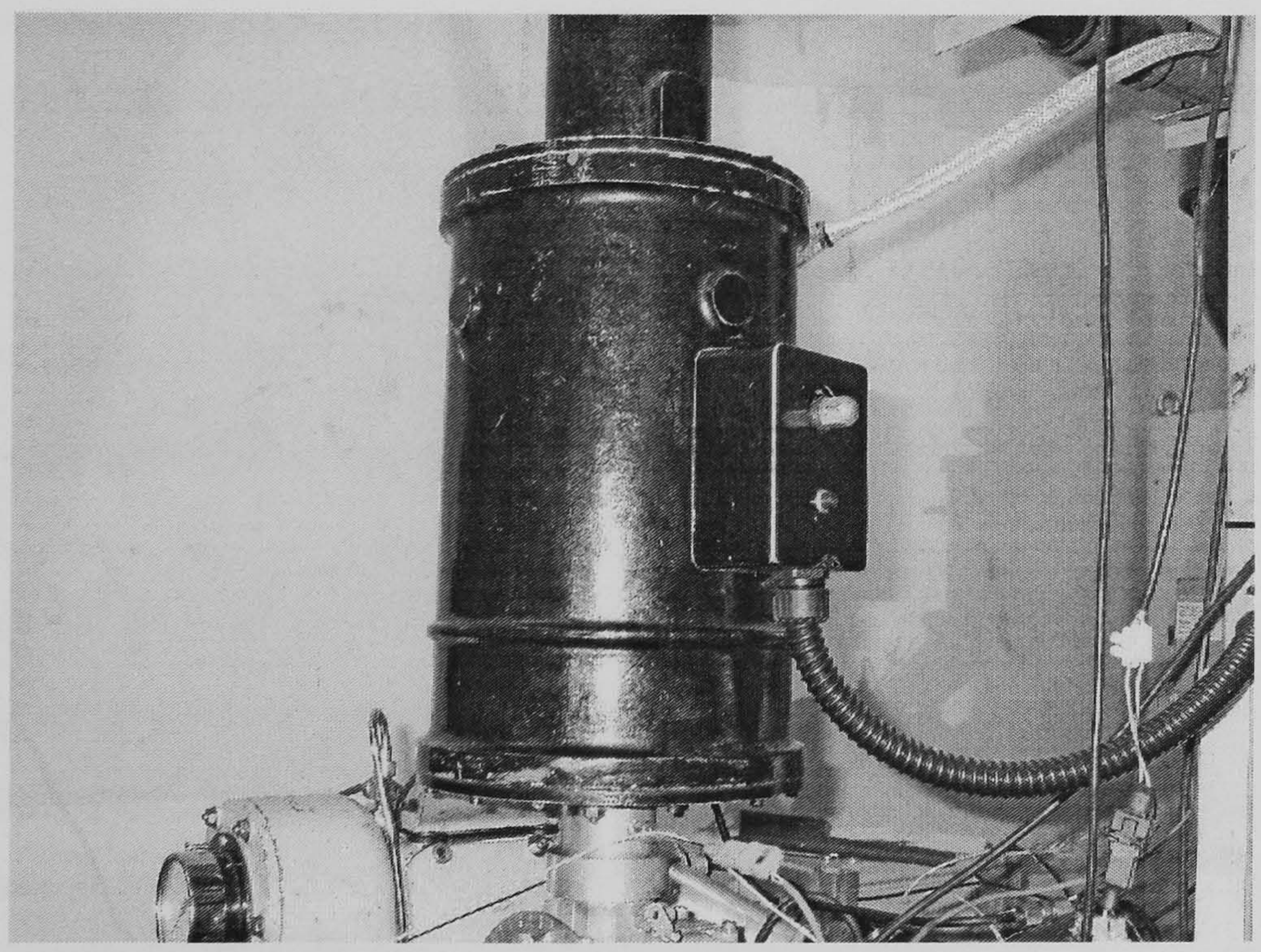

Figure 5.19 Ricardo & Alcock S Type N° 510V viscous air-flow rate meter

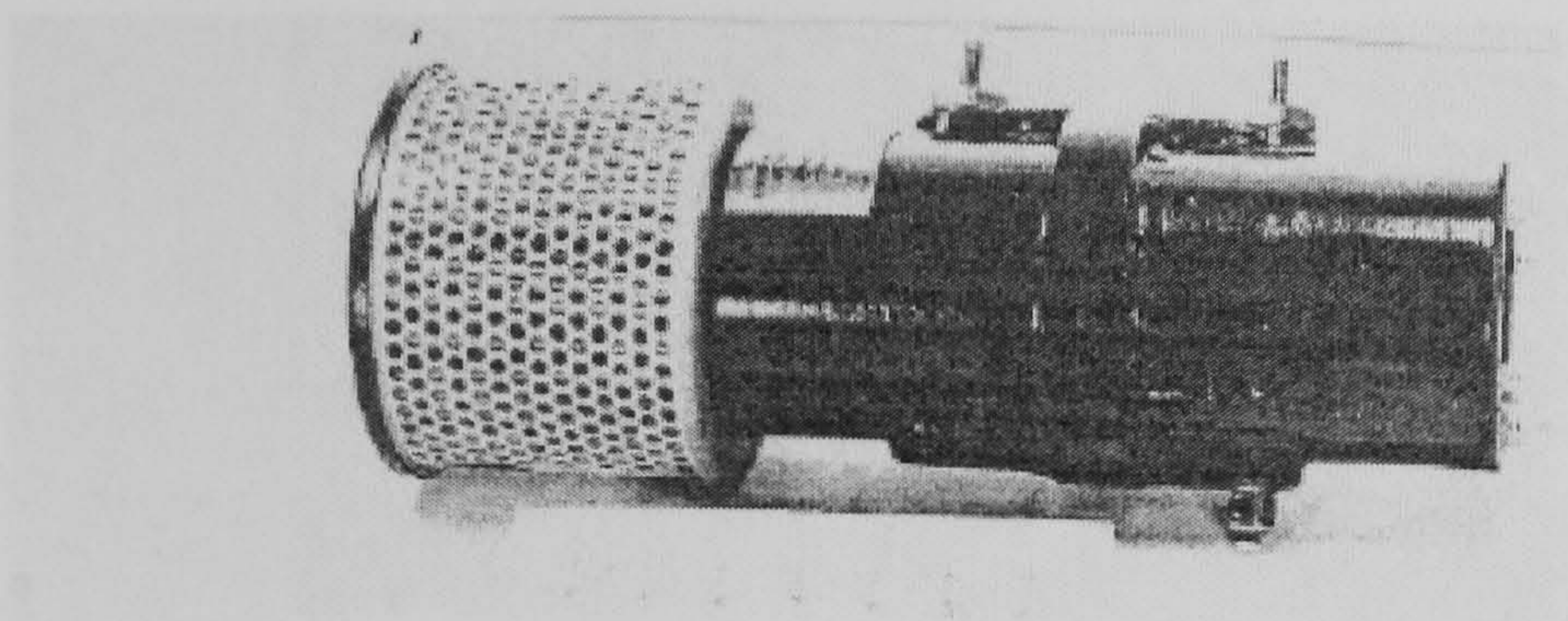

Figure 5.20 Viscous air flow rate meter element [Theodoridis, 2003]

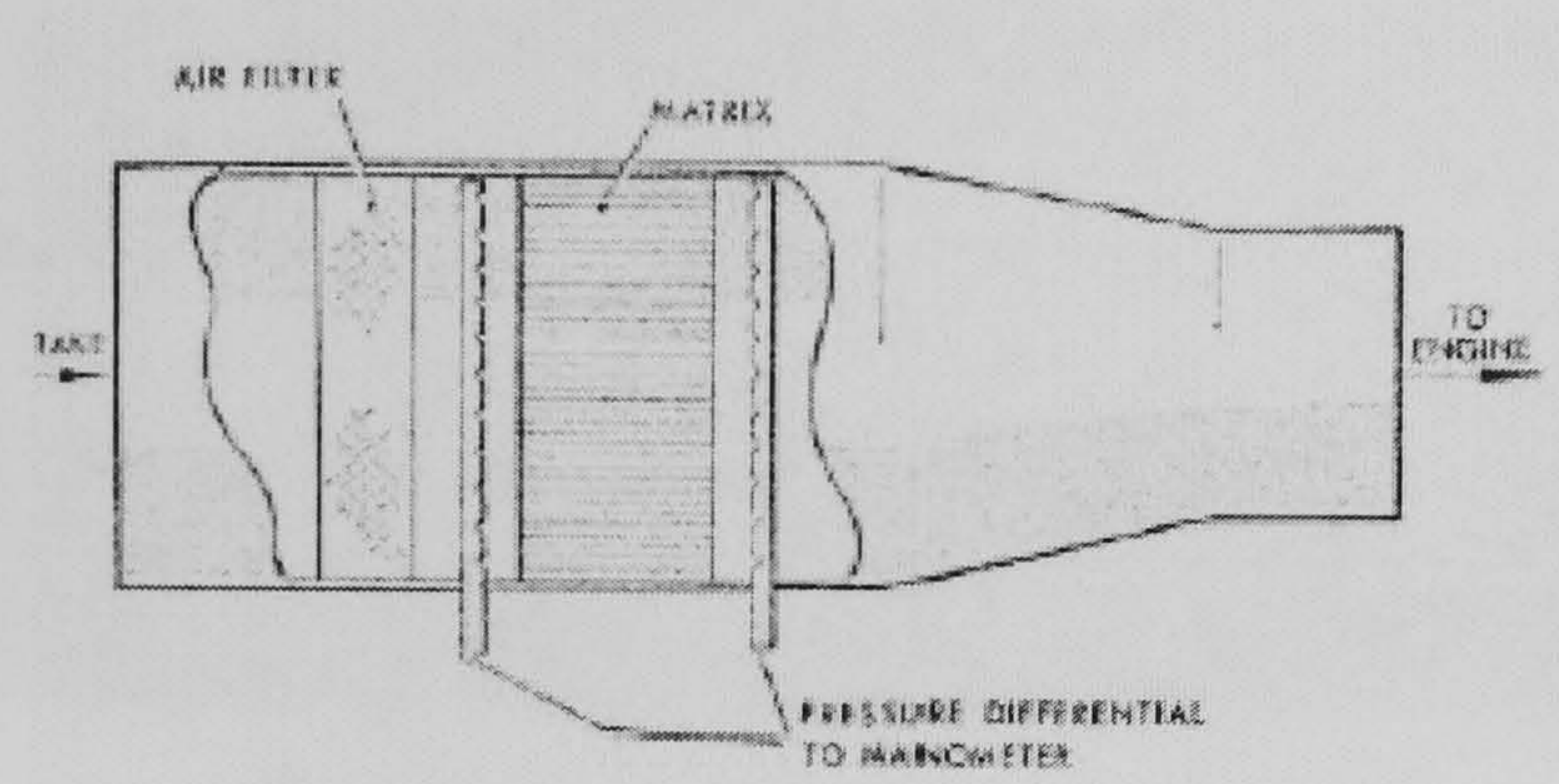

Figure 5.21 Cross section of viscous air flow meter [Theodoridis, 2003]

The viscous air flow meter was invented by Ricardo and Alcock In 1936. This type of air flow meter gives sufficient accuracy because it eliminates serious errors as a result of pulsating air flow when air flow rate is measured using kinetic air meters of orifice, Venturi or other types. In addition, it has the advantage of being relatively small in size compared to bulky air box like in the case of orifice air meter.

The operation of the viscous air flow meter is based on the fact that pressure drop across a laminar air flow passage is directly proportional to the flow velocity. Figure 5.20 shows the S-type N° 510V viscous flow meter and its cross-section is shown in Figure 5.21. Air flow from the intake pipe passes through the 76 millimetres long honeycomb section which consists of a set of small triangular passages of 0.44 millimetre diameter filling up the cylindrical section. Within the passage, air flow becomes laminar, thus its pressure drop is proportional to flow velocity. Pressure transducers are placed on the inlet and exit of the honeycomb section and the differential are measured by a Ricardo Multislope Manometer (Figure 5.22). This inclined multislope manometer was specially designed for the viscous flow meter requirements. It has five alternative positions, four inclined and one vertical, to suit a wide range of flow rates. The vertical arrangement is for measuring higher vacuums and has the least sensitivity.

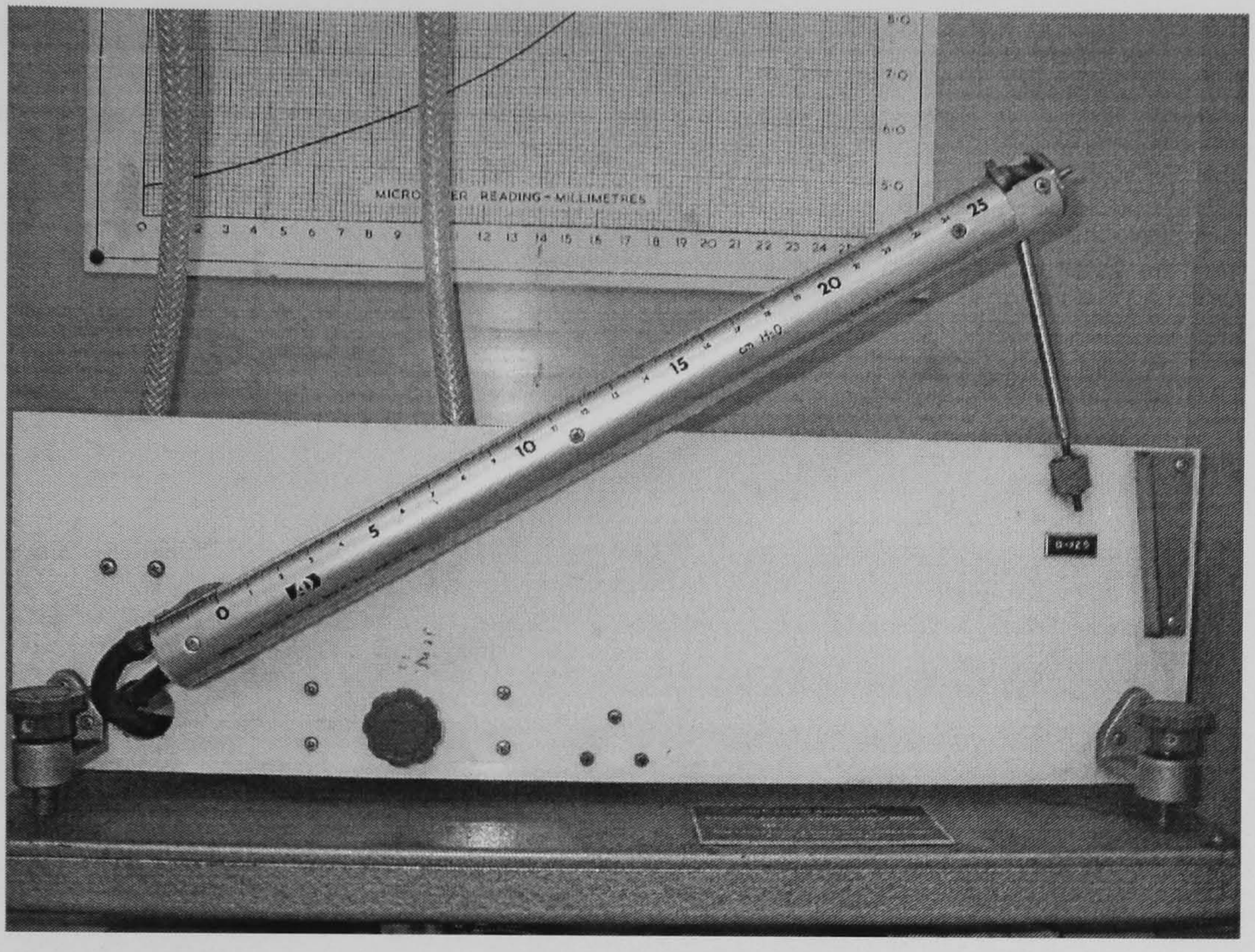

Figure 5.22 Ricardo Multislope manometer

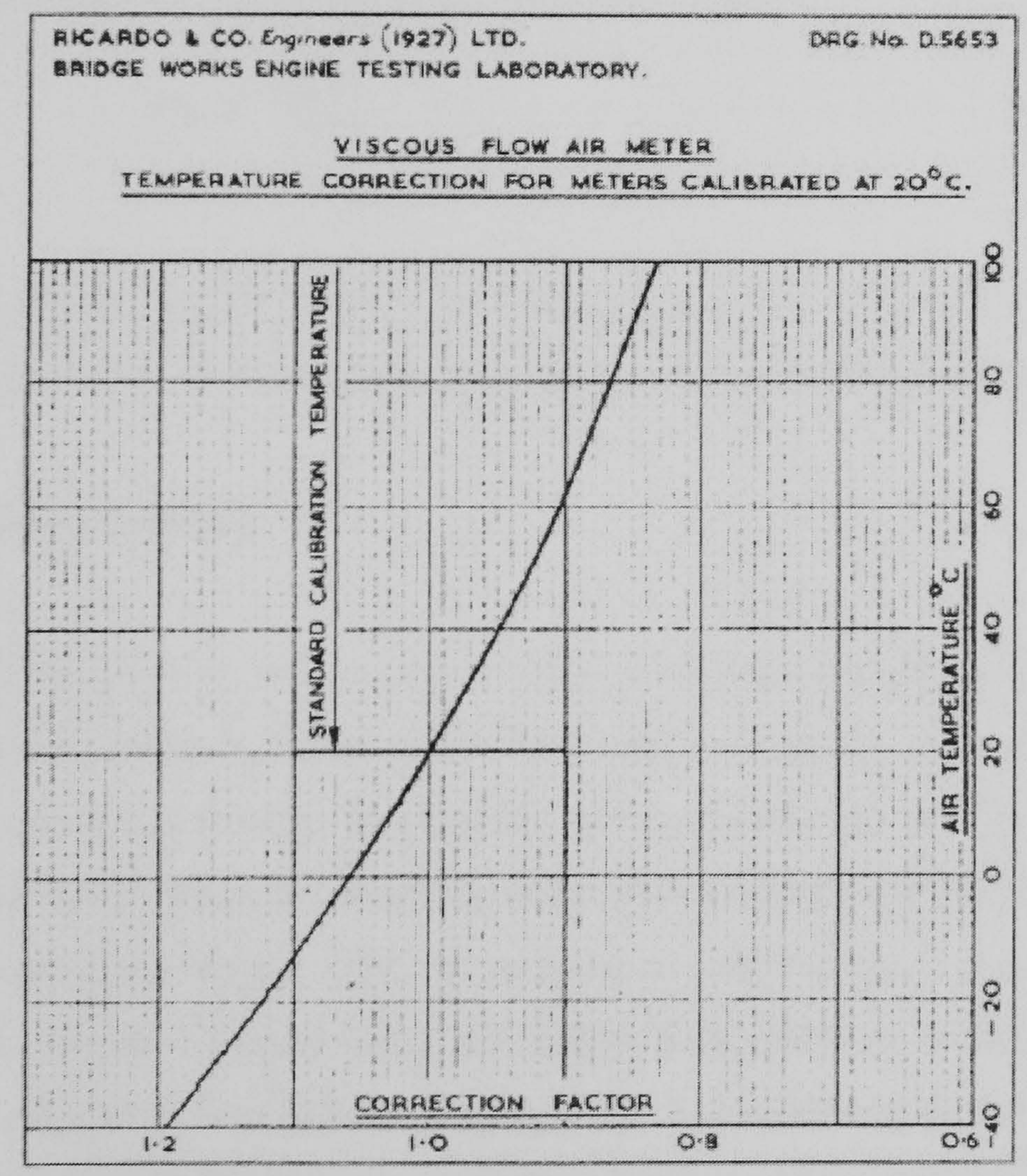

Figure 5.23 Temperature correction factor for air flow rate measurement

The upstream and downstream pressure lines were connected to each side of the manometer. For this experiment work, the manometer was position at top incline and the air mass flow rate is calculated by the following correlation.

$$\dot{m} = C_m h \rho_{air} C_f \qquad \text{(Equation 5.2)}$$

where:

$\dot{m}$ = air mass flow rate (kg/s)

h = manometer reading (cm)

C_m = multislope manometer calibration constant (7.37 x 10^{-4} for top incline)

C_f= temperature correction factor (Figure 5.23)

ρ_{air} = air density (kg/m^3)

The density of air can be obtained from the equation below.

$$\rho_{air} = \frac{\rho_n T_n P_i}{P_n T_i} \qquad \text{(Equation 5.3)}$$

Where ρ_n is specific gravity of air at STP (kg/m3), T_n is 273.15 K, P_n is 101.325 kPa and T_i and P_i are the air inlet temperature (K) and pressure (kPa) respectively.

5.4.5 Cylinder Pressure

Cylinder pressure was measured using a Kistler type 6121 A1 piezoelectric pressure sensor shown in Figure 5.24. The sensor is capable of operating at high frequency transient and high temperature and can sense up to 250 bar cylinder pressure. The signal from the transducer was sent to a charge amplifier Type TA-2/C by Vibro-meter Corp. (Figure 5.25) before being recorded in the by a data acquisition system. Prior to the measurement, the signal from pressure sensor and charge amplifier combination was calibrated against two pre-calibrated sensors. One is the Kistler type 4042 piezoelectric sensor which indicates pressure in the intake manifold and another is a GS type XPM10 sensor that measures cylinder pressure. The pressures at two positions on each engine cycle were made as reference for actual pressure measurement. One is the pressure during the compression stroke and second is the pressure when piston is at BDC of the start of compression stroke. The cylinder pressure at this BDC is set equal to manifold pressure at the same crank position.

Figure 5.24 Kistler 6121 A1 pressure transducer

Figure 5.25 Charge amplifiers for pressure transducer

5.4.6 Temperatures

Six type-*k* thermocouples were used to measure fluid temperatures at different locations. These are intake air, exhaust gas, oil sump, oil line, inlet cooling water and outlet cooling water temperatures. The temperature readings are shown on a display unit and a dial was used to select viewing of one temperature at a time. Temperature readings were used to determine to appropriate temperature for motoring the engine and recording of engine data as recommended by operation manual [Ricardo, 1953].

5.5 Experimental Methods

Figure 5.26 below shows the timing with respect to crank angle of fuel injection for both direct injection and port injection modes, starting from 0° at intake TDC. The injection periods for port injection are denoted as 0° BTDC for open valve injection and 60° BTDC for close valve injection, where TDC is the intake TDC. In the direct injection mode, injection timings are denoted as 115° to 220° ATDC where TDC is the compression TDC.

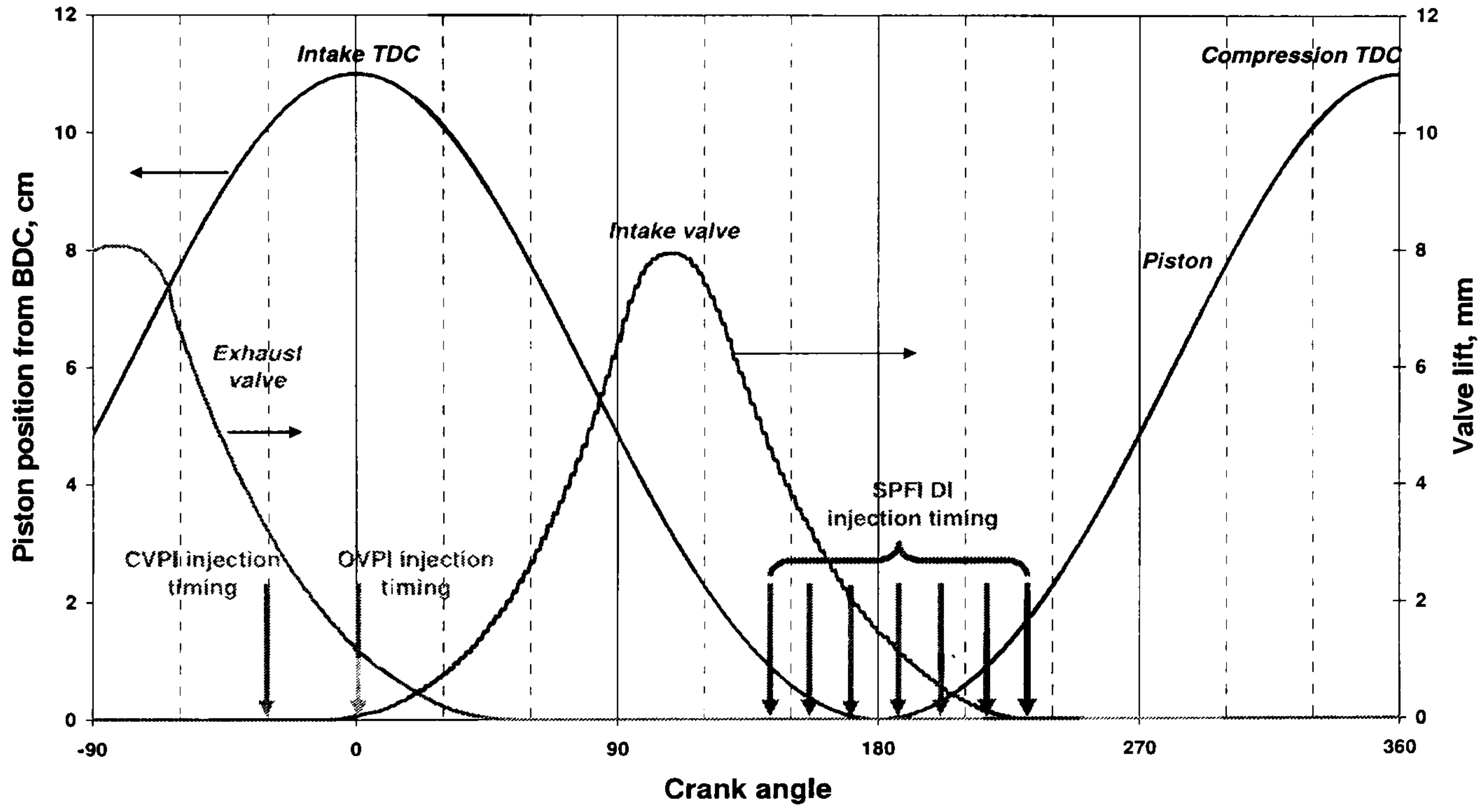

Figure 5.26 Location of fuel injection start on PFI and DI modes

5.5.1 Port injection

For the case of port injection, two injection periods were tried; open valve and closed valve. Methane at 30 bars was supplied to the injector and injection length was adjusted to achieve the desired air fuel ratio (AFR). Lambda value, which is the ratio of stoichiometric AFR to actual AFR, was used to indicate mixture stoichiometry. The minimum spark advance for best torque (MBT) was determined for 1100rpm speed by measuring the IMEP for combustion at spark advance between 14° and 35° BTDC. Then the effect of stoichiometry was measured for lambda values of 0.9, 1.0 and 1.1. This was followed by the effect of varying injection pressures between 30, 40 and 50 bars. Finally the engine was run at speeds from 900 to 1700rpm to measure the speed effects. All individual measurements were taken with MBT ignition timings.

5.5.2 Direct injection

In the direct injection mode, the injection timing is one of the most critical operational characteristics. Injection timing determines the effectiveness of the air-fuel mixing process and also the volumetric efficiency. The later the injection starts during intake stroke, the better the volumetric efficiency. Ideally, injection should start after the intake valve closes but due to the fact that SPFI causes delay in the fuel arrival and delivery time into the combustion chamber, a proper adjustment must be made. A set of injection timings were applied to the engine which was run at various ignition advances to determine MBT for each injection timing. IMEP, volumetric efficiency and thermal efficiency data were calculated and the injection location that yields the optimal balance between these parameters was selected as the setting for further investigation.

5.6 Data Reduction

The scope of this project was to measure and process a selected set of indicated engine performance parameters. These parameters are,

1. Cylinder pressure
2. Indicated mean effective pressure (IMEP)
3. Indicated power.
4. Volumetric efficiency
5. Indicated thermal efficiency
6. Mass fraction burnt (MBF)

The brake data was taken during the experiment which was mainly the output voltage from the load cell for engine torque measurement. However, due to the unsteadiness and unreliability of the load cell output voltage readings, torque data was significantly distorted. Therefore, a decision was made not to present those data in this thesis.

5.6.1 Cylinder pressure

Cylinder pressure was measured by a piezoelectric pressure transducer (Kistler A2) that was mounted to the cylinder through one of the spark plug holes. Pressure history was recorded through the National Instrument NiDAQ data acquisition board and recorded by Labview v.7.0 software at 10,000 samples per second rate. This gives 0.5 degree crank angle resolution at maximum experimental speed of 1700rpm. The conversion factor gained from transducer calibration (as described in **5.4.5**) is used in each set of data given by this correlation where $V_{transducer}$ is the voltage reading from the Kistler A2 pressure transducer/amplifier combination and subscript 180° denotes the voltage reading corresponds to the BDC of intake stroke.

$$P_{cyl} = (10.16V_{transducer}) + 0.70 - (10.16V_{transducer})_{180^o} \text{ (bar)} \qquad \text{(Equation 5.4)}$$

5.6.2 Indicated Mean Effective Pressure (IMEP)

Indicated mean effective pressure was calculated from the pressure data over 720° of engine rotation. Indicated work is defined as the cyclic integral of cylinder pressure with respect to cylinder volume. First, indicated work was calculated based on numerical integration of cylinder pressure data (Equation 5.5), where pressure is converted to N/m^2 and cylinder volume in m^3. The indicated work is then divided with the swept volume, V_s to attain IMEP.

$$W_{indicated} = \oint PdV_{cyl} \text{ (Joule)} \qquad \text{(Equation 5.5)}$$

Instantaneous cylinder volume, V_{cyl} was calculated using the following equations, where s_p is piston vertical position with respect to crank shaft, s is piston stroke, b is cylinder bore, θ is instantaneous crank angle, r is ratio of connecting rod length to crank radius (l/a) ,a is the crank radius, and V_c is clearance volume as shown in Figure 5.27. CR is the compression ratio.

$$s_p = a\cos\theta + \sqrt{r^2 - a^2 \sin^2\theta} \quad \text{(Equation 5.6)}$$

$$V_{cyl} = V_c + (s - s_p)\pi \frac{b^2}{4} \quad \text{(Equation 5.7)}$$

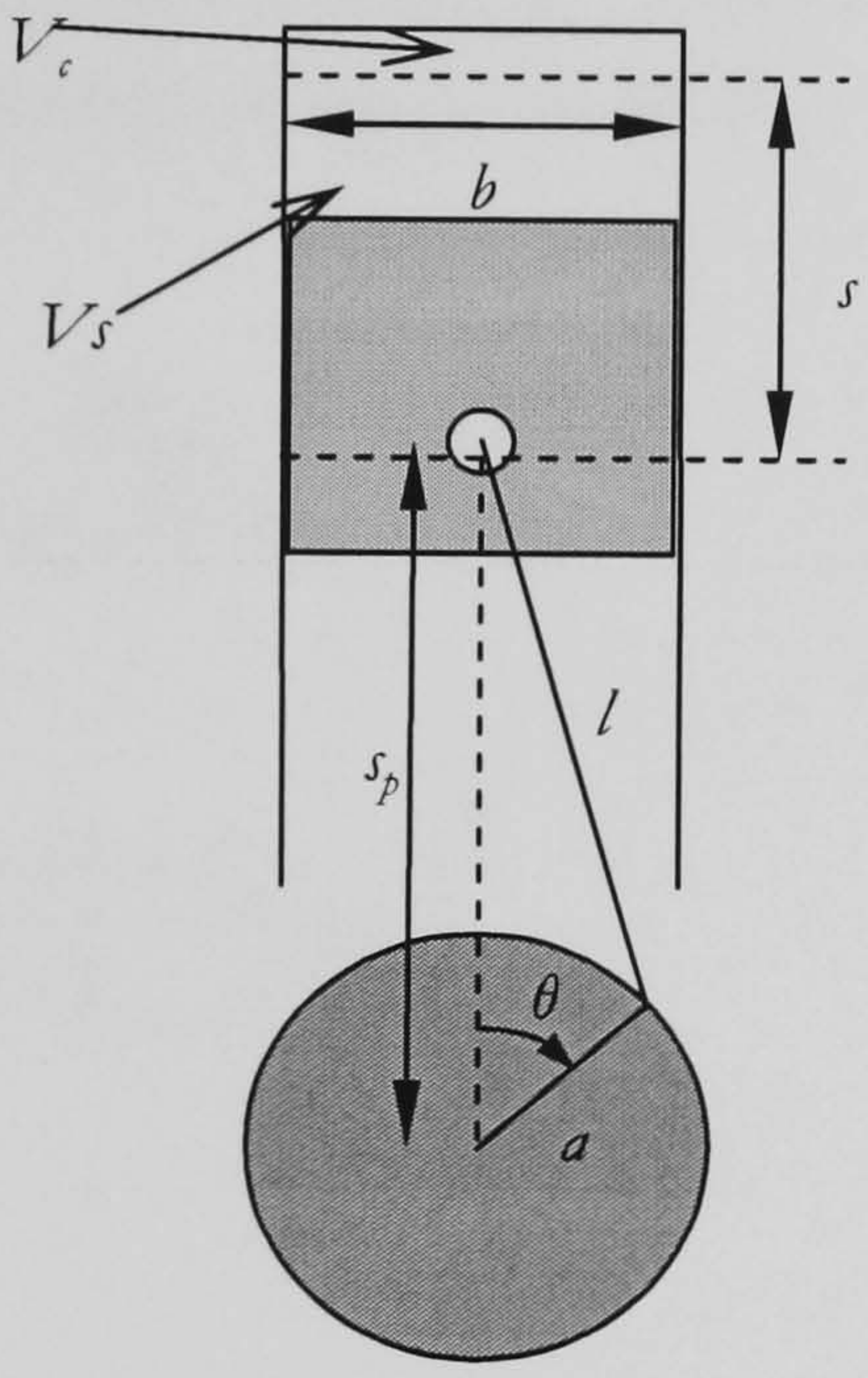

Figure 5.27 Cylinder and piston schematic

$$V_c = \frac{V_s}{CR - 1} \quad \text{(Equation 5.8)}$$

$$IMEP = \frac{W_{indicated}}{V_s} \quad \text{(Equation 5.9)}$$

5.6.3 Indicated power

Indicated power, $P_{indicated}$ can be calculated by the product of indicated work, $W_{indicated}$ multiplied by the engine speed, N (rev/sec) and divided with the number of rotation per cycle, n_R ($n_R = 2$ for 4-stroke engine) as shown in Equation 5.10.

$$P_{indicated} = \frac{W_{indicated} N}{1000 n_R} \text{ (kW)} \qquad \text{(Equation 5.10)}$$

5.6.4 Volumetric efficiency

Volumetric efficiency is calculated from the traditional correlation and corrected to the standard condition using the volumetric efficiency correction factor, c'_F suggested by Heywood [1988] where T_{std} is 29.4°C.

$$\eta_v = c'_F \frac{2\dot{m}_{air}}{\rho_{air} V_s N} \qquad \text{(Equation 5.11)}$$

$$c'_F = \left(\frac{(273.15 + T_{std}}{273.15 + T_{air,in}(^oC)} \right)^{0.5} \qquad \text{(Equation 5.12)}$$

5.6.5 Indicated fuel conversion efficiency

Indicated fuel conversion efficiency, $\eta_{f,\ indicated}$ is calculated by dividing the indicated power, $P_{indicated}$ with the input energy. The input energy is defined as the multiplication product of lower heating value of methane, $Q_{LHV,CH4}$ with methane mass flow rate, $\dot{m}_{CH_4}$.

$$\eta_{f,indicated} = \frac{P_{indicated}}{Q_{LHV,CH_4} \dot{m}_{CH_4}} \qquad \text{(Equation 5.13)}$$

5.6.6 Indicated specific fuel consumption

Indicated specific fuel consumption is the rate of fuel mass use per unit Watt of power produced it is calculated based on the following equation

$$ISFC = \frac{\dot{m}_{CH_4}}{P_{indicated}} \qquad \text{(Equation 5.14)}$$

5.6.7 Mass burnt fraction (MBF)

The most widely used method to characterize the process of combustion is to determine the fraction of mass burnt (MBF). Mass burnt fraction, x_b is defined as the ratio of total mass of mixture burnt to the total of combustible mixture mass at any time during combustion process. MBF profile is usually an s-shape curve on the x_b vs. crank angle chart and is actually the representation of combustion process in terms of energy release. Rate of heat release (ROHR), $dx_b/d\theta$, describes the rate of combustion relative to crank angle. The most commonly used definitions for MBF profile is described as the followings [Heywood, 1988].

1. Flame development angle, $\Delta\theta_d$. This is the interval between spark event and the time when small but significant amount of fuel is burnt (about 10%), and referred as ignition delay.
2. Rapid burning angle, $\Delta\theta_b$. The interval when bulk of fuel is burnt and bulk chemical energy released, typically the middle 10-90% of MBF curve.
3. Overall burning angle, $\Delta\theta_o$. The duration of overall burning process, which is the sum of $\Delta\theta_d$ and $\Delta\theta_b$. All angles are shown in Figure 5.28.

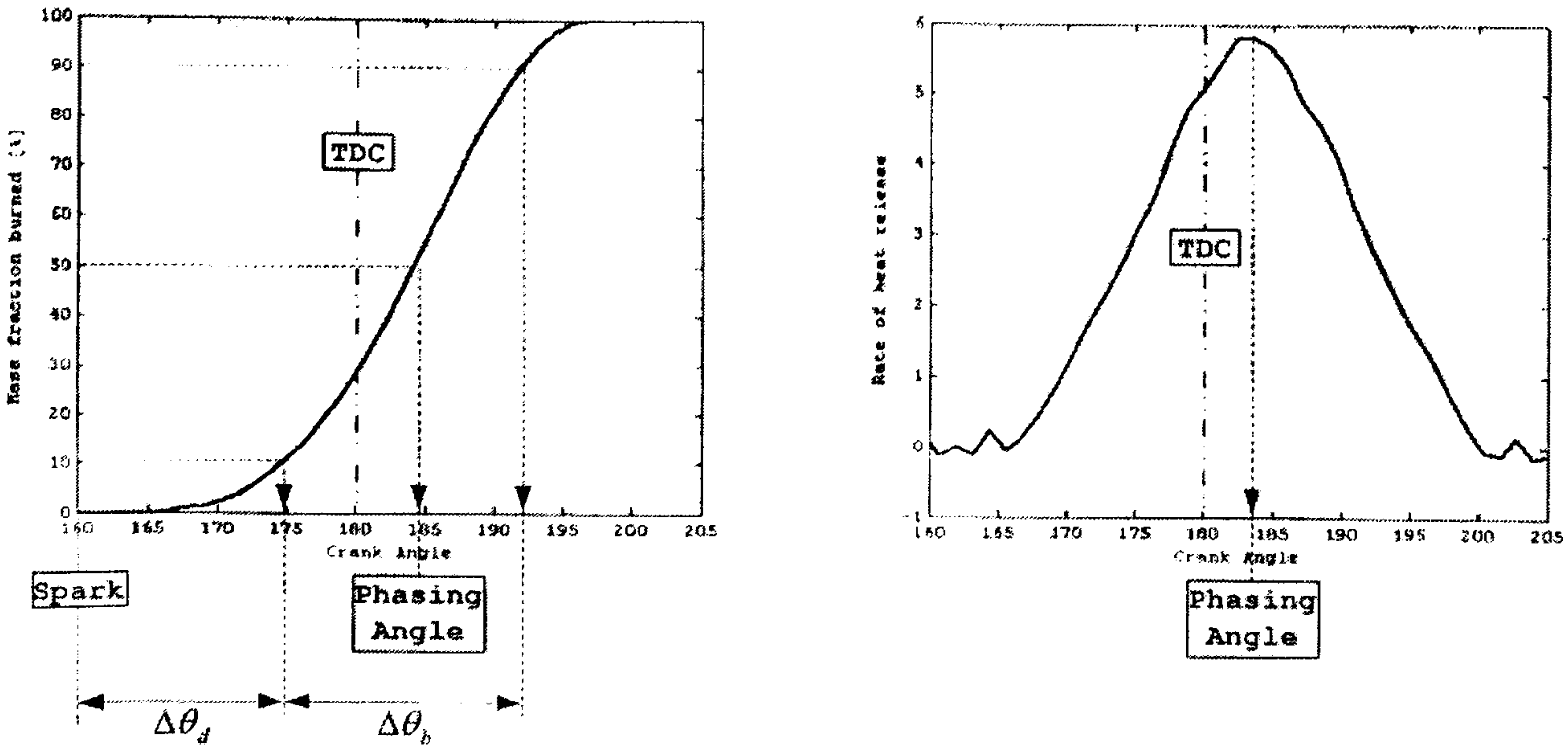

Figure 5.28 Mass burnt (left) and rate of heat release (right) [Vuorenskoski, 2004]

Another useful parameter obtained from MBF determination is the timing of the angle of maximum heat release, often referred to as combustion phasing angle and usually coincides with the 50% mass burnt fraction angle as shown in Figure 5.28. For most SI engines, this occurs between 5 and 10 °CA ATDC.

Several methods have been used to calculate the MBF which are mainly from the cylinder pressure-time history data. Among them are the methods to calculate the heat release based on first law of thermodynamics [Gatowski et al., 1984, Chun & Heywood, 1987, Eriksson, 1998]. Some of these computationally complex models treat the combustion chamber as a single zone and often referred as single zone model. In these models, the effect of wall heat transfer and mass flux across the system boundary are taken into account. Other models take into account two zones contributing to combustion process; unburned and burnt zones [Egnell, 1998, Guezennec & Hamama, 1999]. The above-mentioned methods that use pressure history are subjected to some errors typically due to incorrect absolute pressure referencing, thermal shock, measurement error from the pressure transducer, amplifier system calibration error, inaccurate crank angle phasing. However, these errors only result in 0.5 to 3% error on the MBF calculation [Brunt et al. 1998]

For this study, the calculation of mass burnt fraction (MBF) was based on a simplified method by Ressweiler and Withrow [1938]. This method was chosen for its simplicity and demonstrated accuracy [Stone & Green-Armytage, 1987]. It demonstrates the net heat release of the combustion process. In this method, a simple assumption is made that normalised pressure rise due to combustion is equivalent to the mass fraction burnt; i.e. the rise of pressure due to combustion is proportional to the mass of fuel burned at that specific crank angle. The total measured cylinder pressure is assumed to be a sum of pressure change due to combustion ΔPc, and pressure change due to cylinder volume, ΔP_v change is due to piston motion. In the absence of combustion, ΔP_v is assumed to follow the polytropic relation.

$$\Delta P = \Delta P_c + \Delta P_v \qquad \text{(Equation 5.15)}$$

$$P_i V_i^{\,n} = P_j V_j^{\,n} \qquad \text{(Equation 5.16)}$$

$$\Delta P_v = P_j - P_i = P_i \left[\left(\frac{V_i}{V_j} \right)^n - 1 \right] \qquad \text{(Equation 5.17)}$$

$$\frac{m_{b,i}}{m_{b,total}} = \frac{\sum_0^i \Delta P_c}{\sum_0^N \Delta P_c} \qquad \text{(Equation 5.18)}$$

where *V* is volume, *n* is polytropic index, *m* is mass and subscripts *b* and *c* refer to burnt and combustion respectively. This method includes some simplification as follows.

1. Time varying heat transfer to wall is neglected.
2. Pressure change due to cylinder volume change and heat transfer to cylinder walls can be represented as polytropic process.
3. Ratio of specific heat, γ is constant during combustion process.
4. Normalised pressure rise due to combustion is directly proportional to mass fraction burnt.
5. Flow in and out piston crevice and piston blow-by effects are neglected.
6. Combustion is complete.

5.7 Results

5.7.1 Methane port injection

The port fuel injection of methane in two modes; open valve (OVPI) and close valve (CVPI) were carried out. The method that yields the better performance between the two was selected as the basis of comparison with the performance of direct injection. The effects of varying these parameters on the overall performance are presented in the following tables and figures:

1. Fuel injection timing
2. Ignition advances
3. Injection pressures
4. Mixture stoichiometry
5. Engine speeds

The performances of comparison are IMEP, indicated power, volumetric efficiencies, thermal efficiencies, and indicated specific fuel consumptions. First, the effects of two fuel injections periods on performance were compared.

5.7.1.1 Effect of injection (OVPI vs. CVPI) and ignition timings

Figures 5.29 through 5.31 show the result from OVPI operation at 1100 rpm, stoichiometric AFR and 30 bar injection pressure at various ignition times. In Figure 5.29, cylinder pressures are plotted against degree crank angle for one cycle. The effect of spark advance can be seen from the values and timings of peak pressures. In Figure 5.30, cylinder pressures are plotted against cylinder volume. The area enclosed by the curve is the cyclic integral of pressures against volume which were used to determine indicated work and subsequently the IMEP. Figure 5.31 shows the cylinder work over one cycle which represent positive work due to combustion during expansion process and negative work values due to compression process and combustion. Figure 5.32 through 5.34 show the same set of results for the CVPI. From Table 5.2 and Figure 5.35 and Figure 5.36, it is clearly demonstrated that the performance of OVPI is superior to the one of CVPI with overall higher IMEP and thermal efficiency. In these figures, polynomial fit lines are drawn to show the trend of parameters change with different spark advances. Another observation is that OVPI shows steadiness of peak pressures shifts toward TDC as spark ignitions were advanced compared to CVPI. Volumetric efficiencies of OVPI also showed advantages over CVPI. These advantages were due to the fact that in OVPI operation, better air-fuel pre-mixture in the intake manifold was achieved because methane was injected into the flow of air. In the case of CVPI, methane occupies the inlet area and when the intake valve opens, the incoming flow of air pushes the bulk methane into the cylinder before further mixing inside the combustion chamber can happen.

In Table 5.2, the selected engine performance parameters are shown. The values on the table and the corresponding plots on Figure 5.35 and Figure 5.36 show that there are similar trends of performance change with varying spark timings where optimal calibration can be achieved. On average, the IMEP of OVPI operation are 7.7% higher than the one of CVPI. These result in better indicated power of 6.06% on average. The volumetric efficiencies of the two methods do not show significant difference; with the average efficiency of OVPI is only 0.17% better. The average fuel conversion efficiency of CVPI and OVPI are 23.51% and 25.25% respectively. The difference gives OVPI an advantage of 7.42% more efficient.

The optimal calibrations were found to be at 24° BTDC for CVPI and 25° BTDC for OVPI. At these optimal setting, IMEP and indicated power differ by only 1.54% and 1.71% respectively. The fuel conversion efficiency of OVPI is 1.55% better than CVPI. Volumetric efficiency is the only advantage of CVPI with 75.01% compared to 74.87% in the OVPI. However looking at the overall picture, the OVPI operation results in a more stable performance over the whole range of tested spark timings especially at spark advances more than 25° BTDC as shown in Figure 5.35 and Figure 5.36. At these spark advances, the performance drops in CVPI operation become more obvious.

The overall performance of OVPI operation are no more than 10% better but more importantly, they are less effected by the variation of spark timing compared to CVPI operation. Because of these advantages, the OVPI was further investigated with the effects of parameters and was chosen as the basis of comparison with direct injection mode.

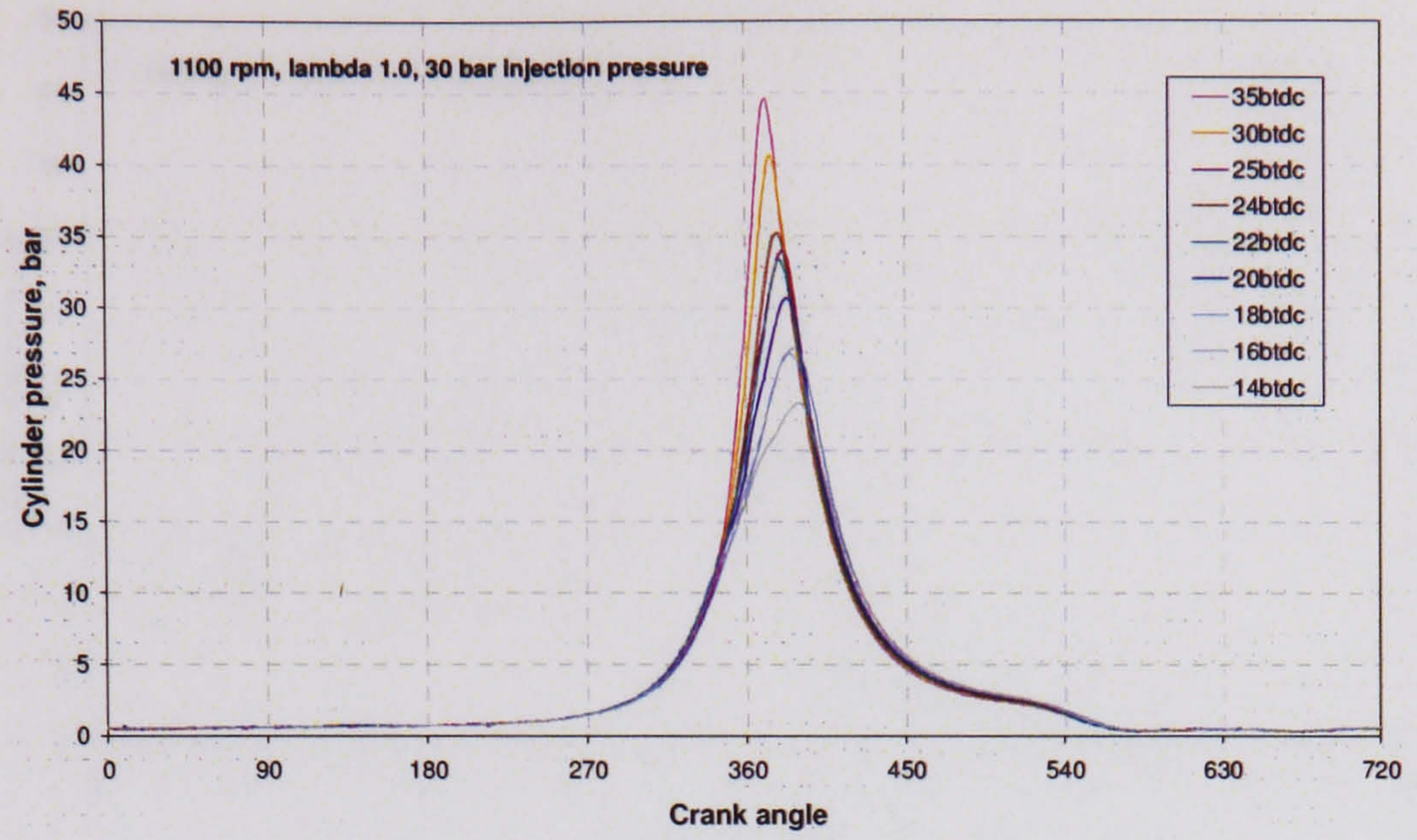

Figure 5.29 Cylinder pressures of OVPI at various spark advances

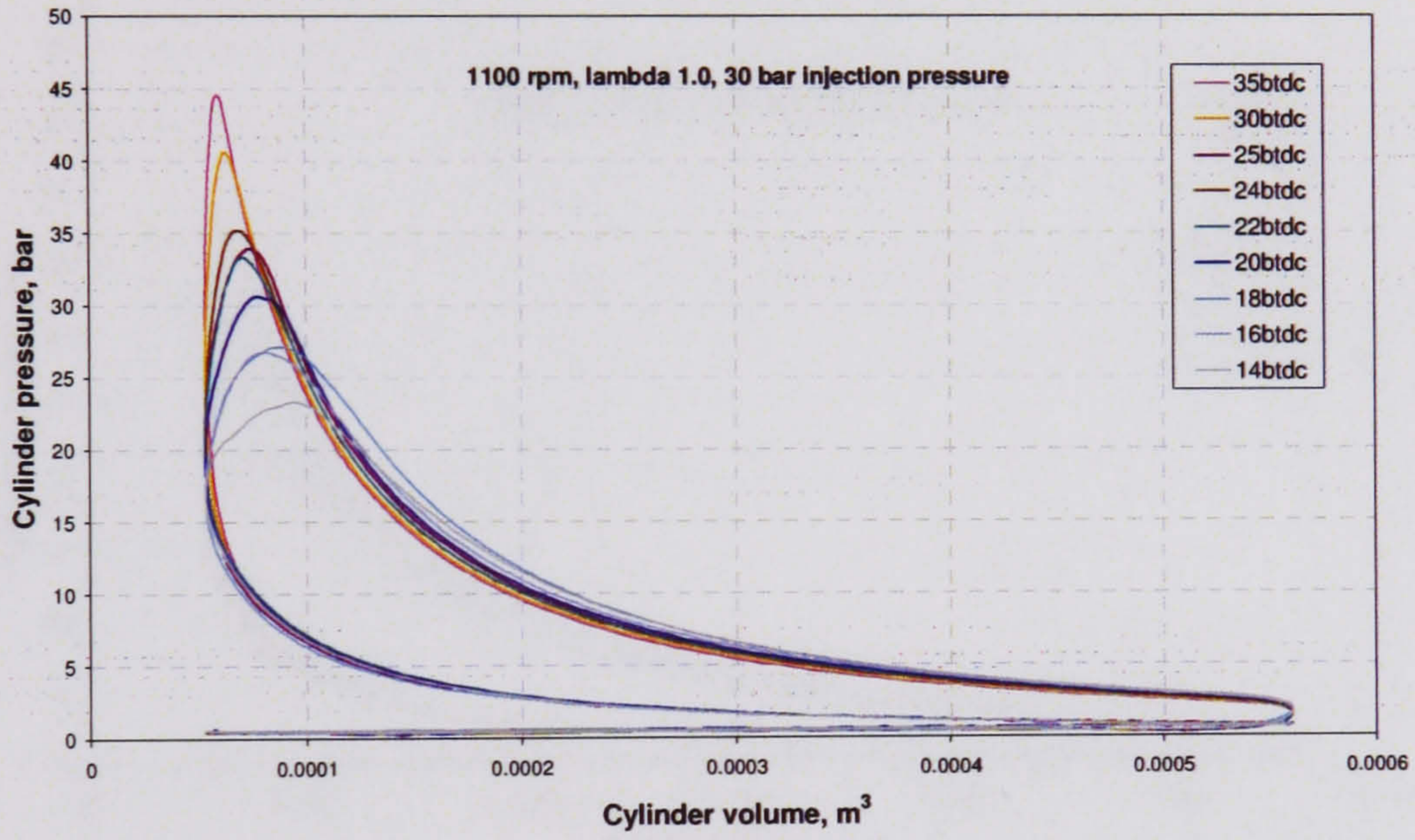

Figure 5.30 PV diagram of OVPI at various spark advances

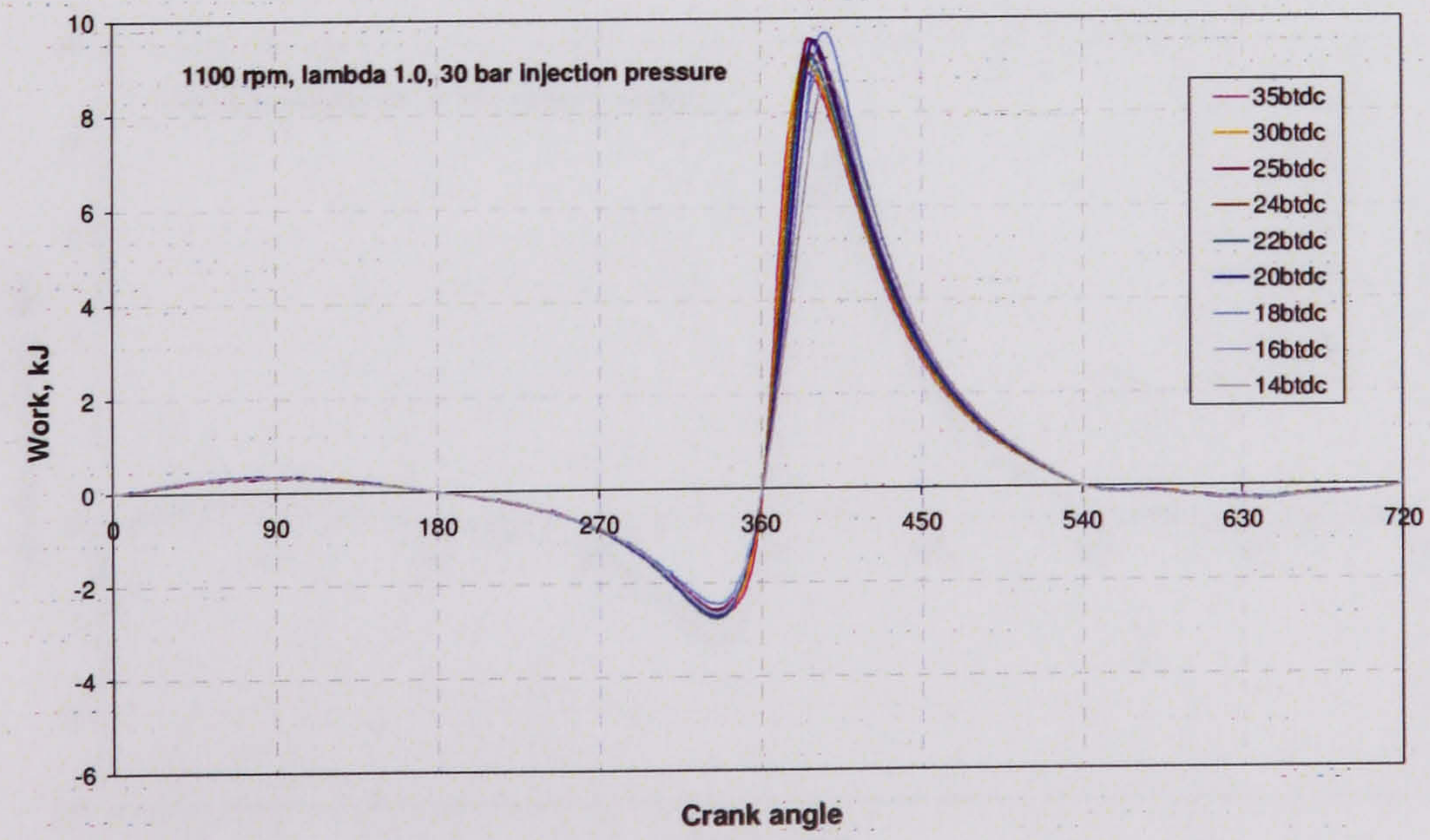

Figure 5.31 Cylinder work of OVPI at various spark advances

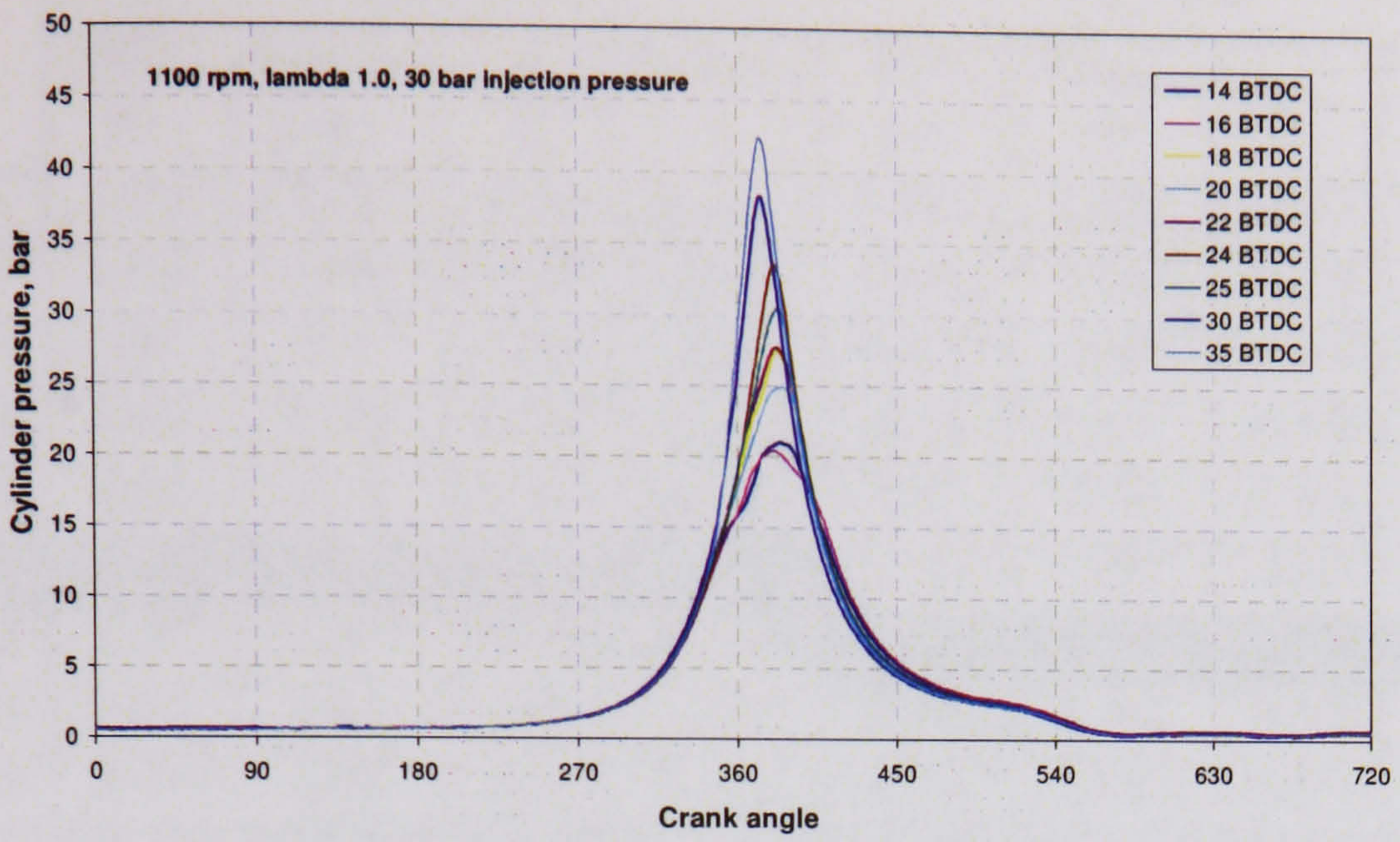

Figure 5.32 Cylinder pressures of CVPI at various spark advances

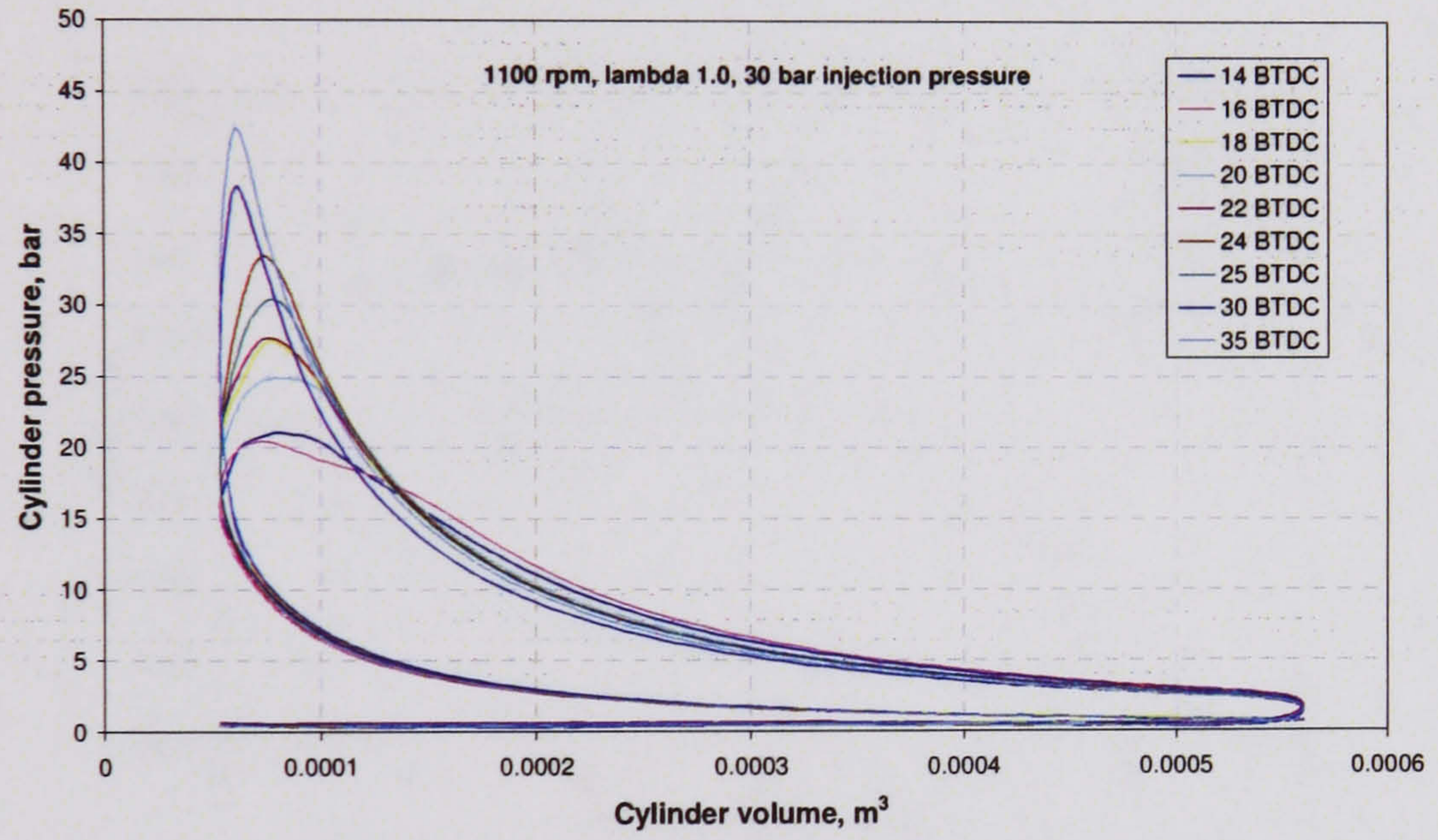

Figure 5.33 PV diagram of CVPI at various spark advances

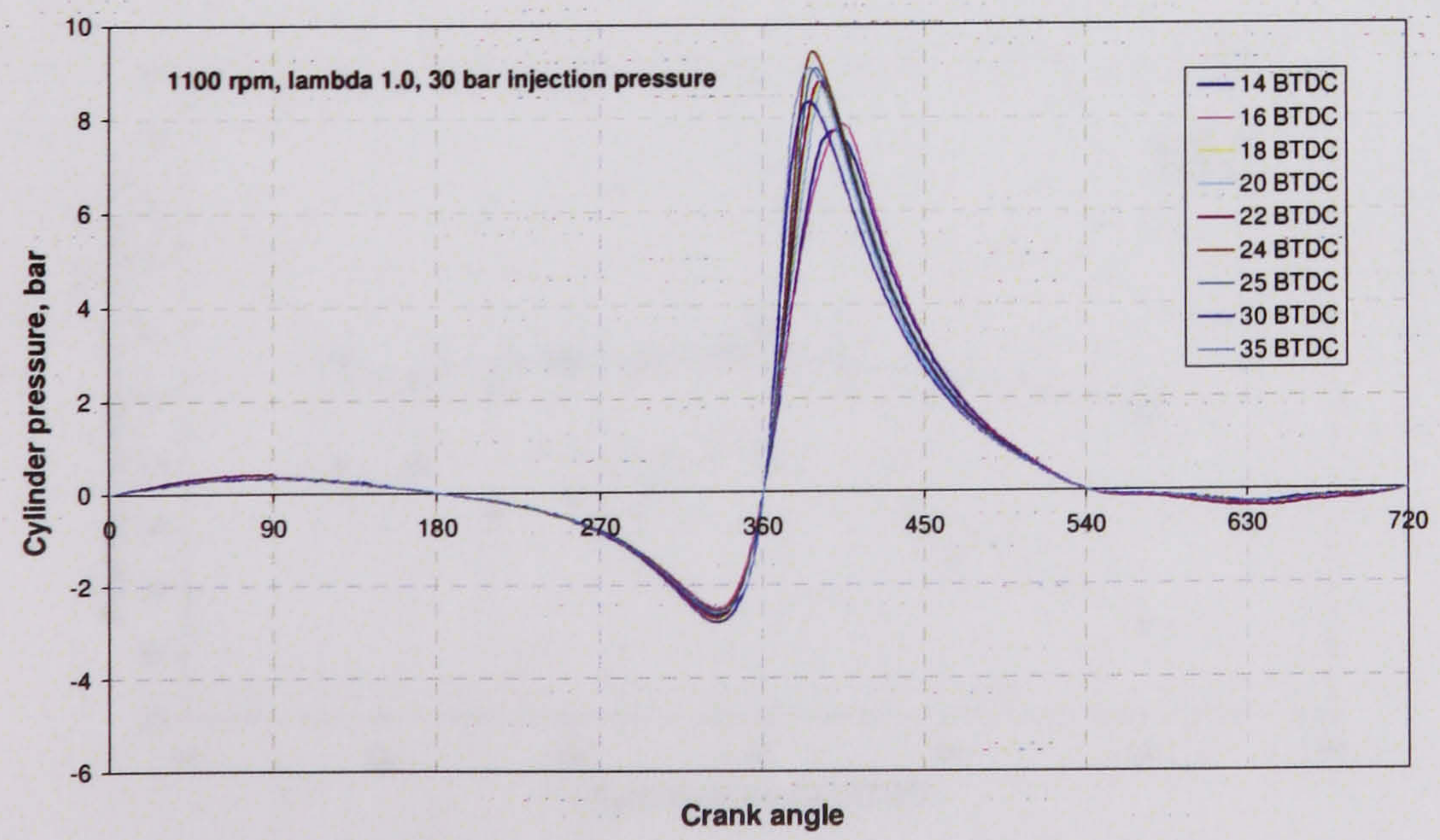

Figure 5.34 Cylinder work of CVPI at various spark advances

	CVPI				OVPI			
	IMEP, bar	$P_{indicated}$, kW	η_v, %	$\eta_{f, indicated}$ %	IMEP, bar	$P_{indicated}$, kW	η_v, %	$\eta_{f, indicated}$ %
Spark advances, BTDC 14	5.878	2.704	72.091	23.957	6.392	2.888	72.877	25.593
16	6.116	2.793	75.145	23.914	6.466	2.942	75.416	25.150
18	5.921	2.709	75.009	23.193	6.456	2.938	75.009	25.110
20	5.986	2.739	75.009	23.448	6.533	2.984	75.145	25.502
22	5.986	2.744	74.874	23.493	6.327	2.979	75.416	25.461
24	6.532	2.989	75.009	25.590	6.434	3.003	75.281	25.667
25	6.195	2.824	75.281	24.180	6.633	3.040	74.874	25.986
30	5.711	2.613	75.009	22.370	6.398	2.938	74.738	25.111
35	5.460	2.961	74.874	21.405	6.295	2.885	74.874	24.663

Table 5.2 Selected performances of CVPI and OVPI at 1100rpm, lambda 1.0 and 30 bar injection pressure (coloured row for optimum calibration)

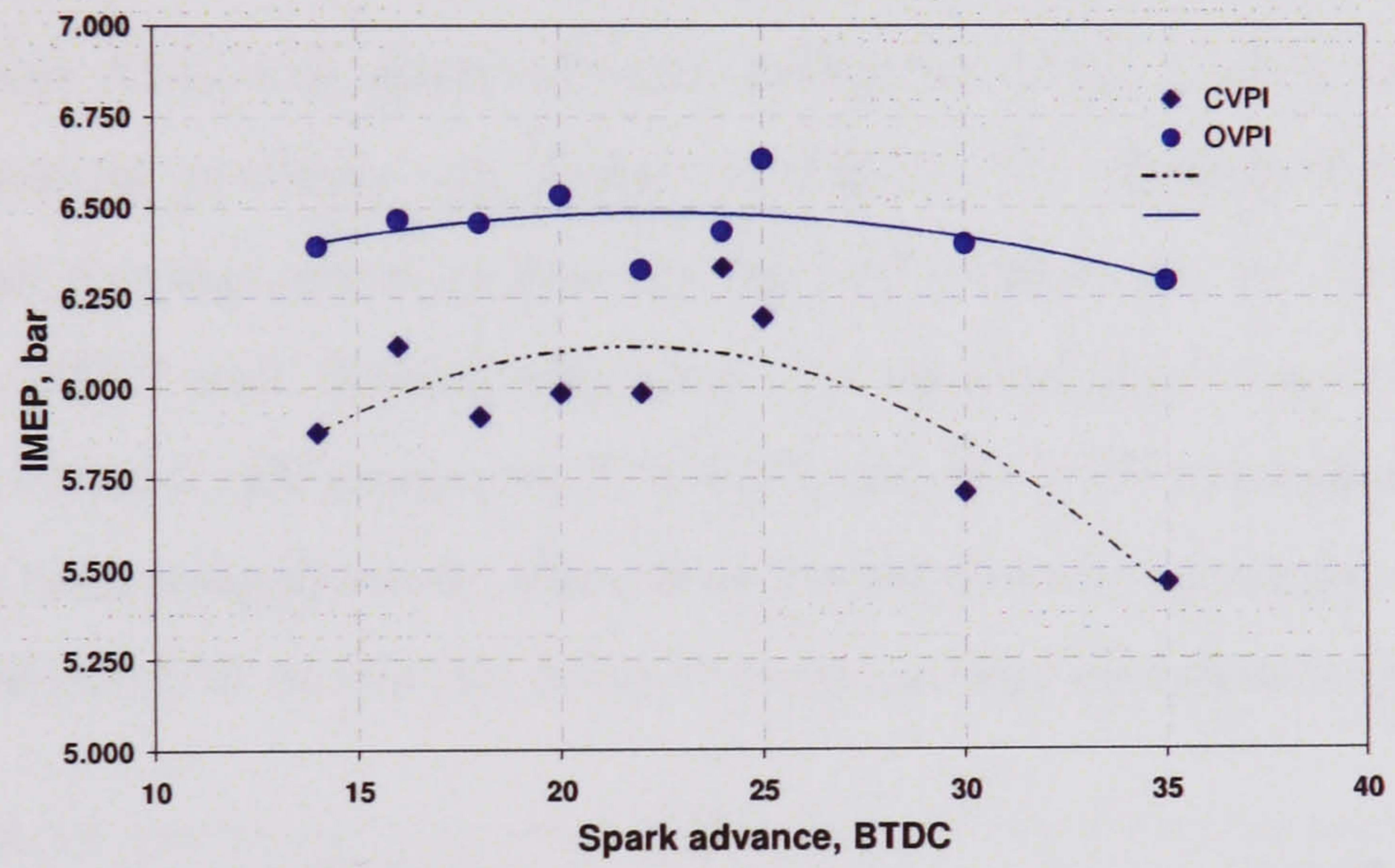

Figure 5.35 IMEPs of OVPI and CVPI at various spark advances

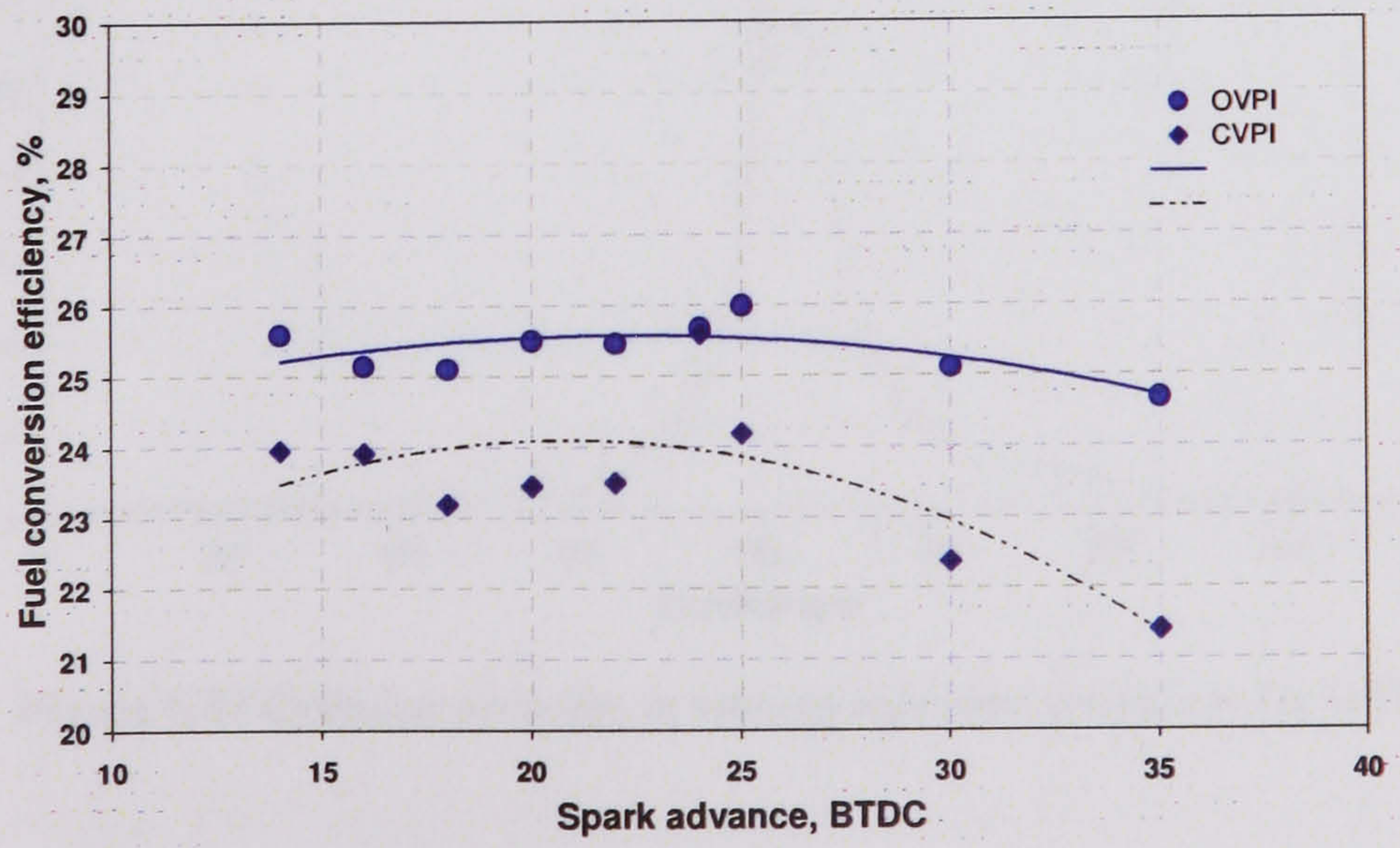

Figure 5.36 Thermal efficiencies of OVPI and CVPI at various spark advances

The performance of OVPI can be compared with the AVL Boost simulation results as described in 3.5. The IMEP from OVPI is 6.66 bar compared to 8.32 bar from the simulation. Volumetric efficiency is 74.87% compared to 76.03% in the simulation. The indicated fuel conversion efficiency of OVPI is 25.99% compared to 31.72% in the simulation. The indicated power is 3.04 kW compared to 3.86 kW in the simulation. The difference are due to the fact that results from the simulation was obtained from the setting of 'perfect mixing' and there is no lost due to blow by or any other deficiencies in engine operation.

5.7.1.2 Effect of injection pressure

Three methane injection pressures were applied for the OVPI operation; 30 bar, 40 bar and 50 bar. Data were taken while engine ran at 1100 rpm and stoichiometric AFR with spark advance setting for MBT. Results of the effect of varying injection pressures are shown in Figure 5.37 through 5.40. The results showed that varying injection pressure has little effect on the cylinder pressure behaviour, IMEP and thermal efficiency data of port injection with variation of IMEP and thermal efficiencies are 0.45-1.2% and 0.5-1.3% respectively. Volumetric efficiencies were insignificantly affected by varying injection pressures with values of 74.5%, 74.5% and 74.4% for 30, 40 and 50 bar injection pressures respectively.

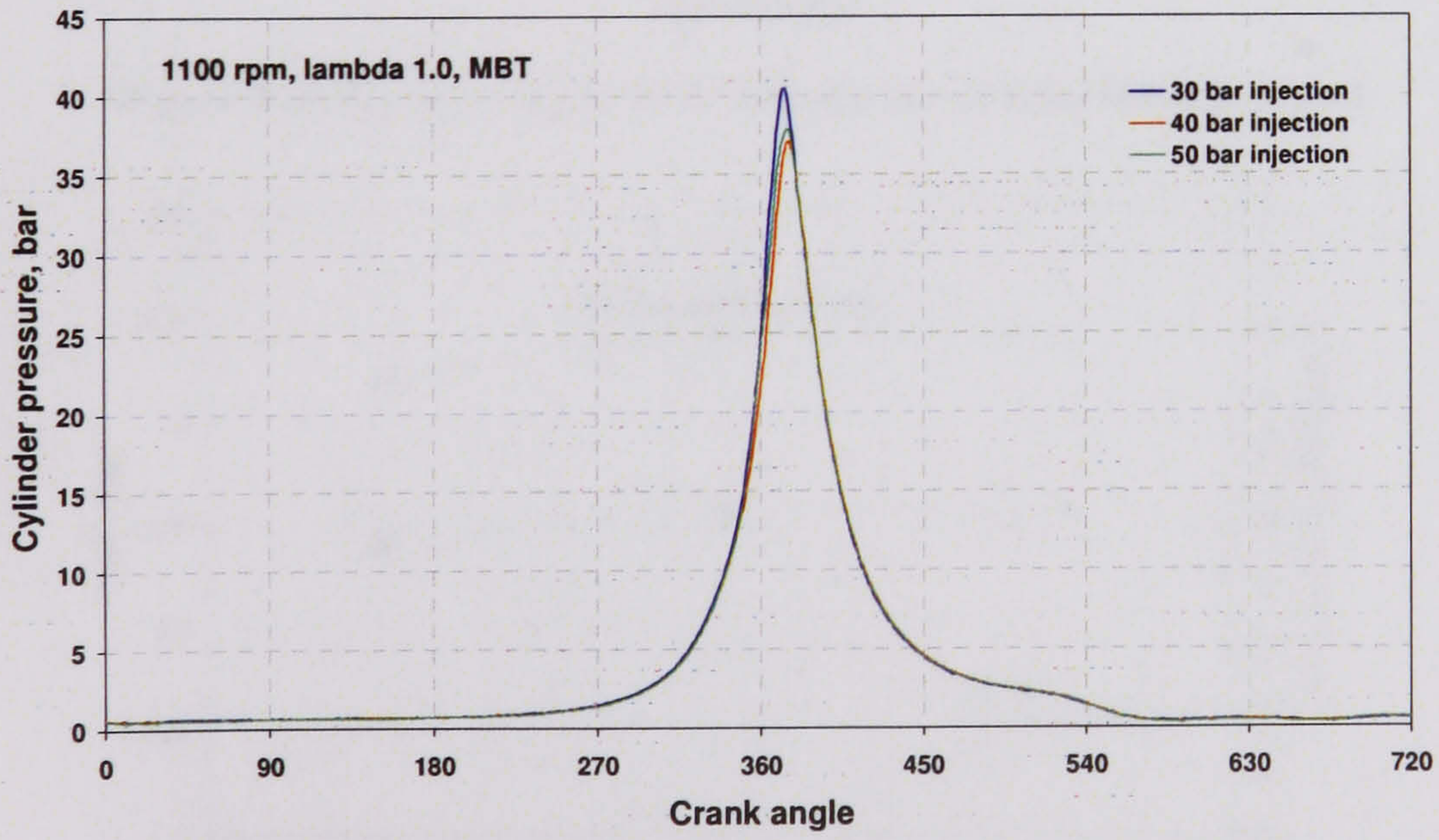

Figure 5.37 Cylinder pressure at various injection pressures for OVPI

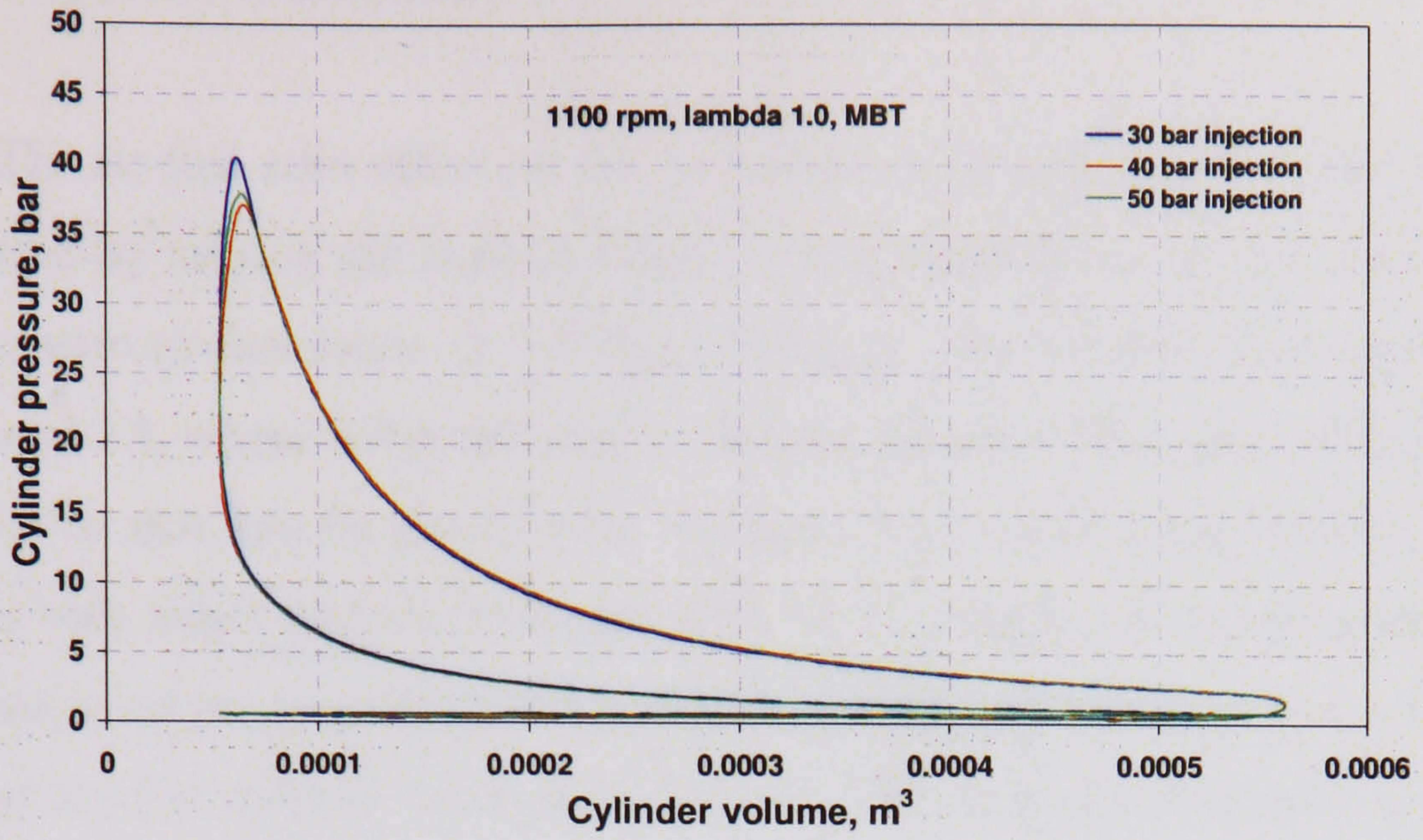

Figure 5.38 PV diagram for OVPI at various injection pressures

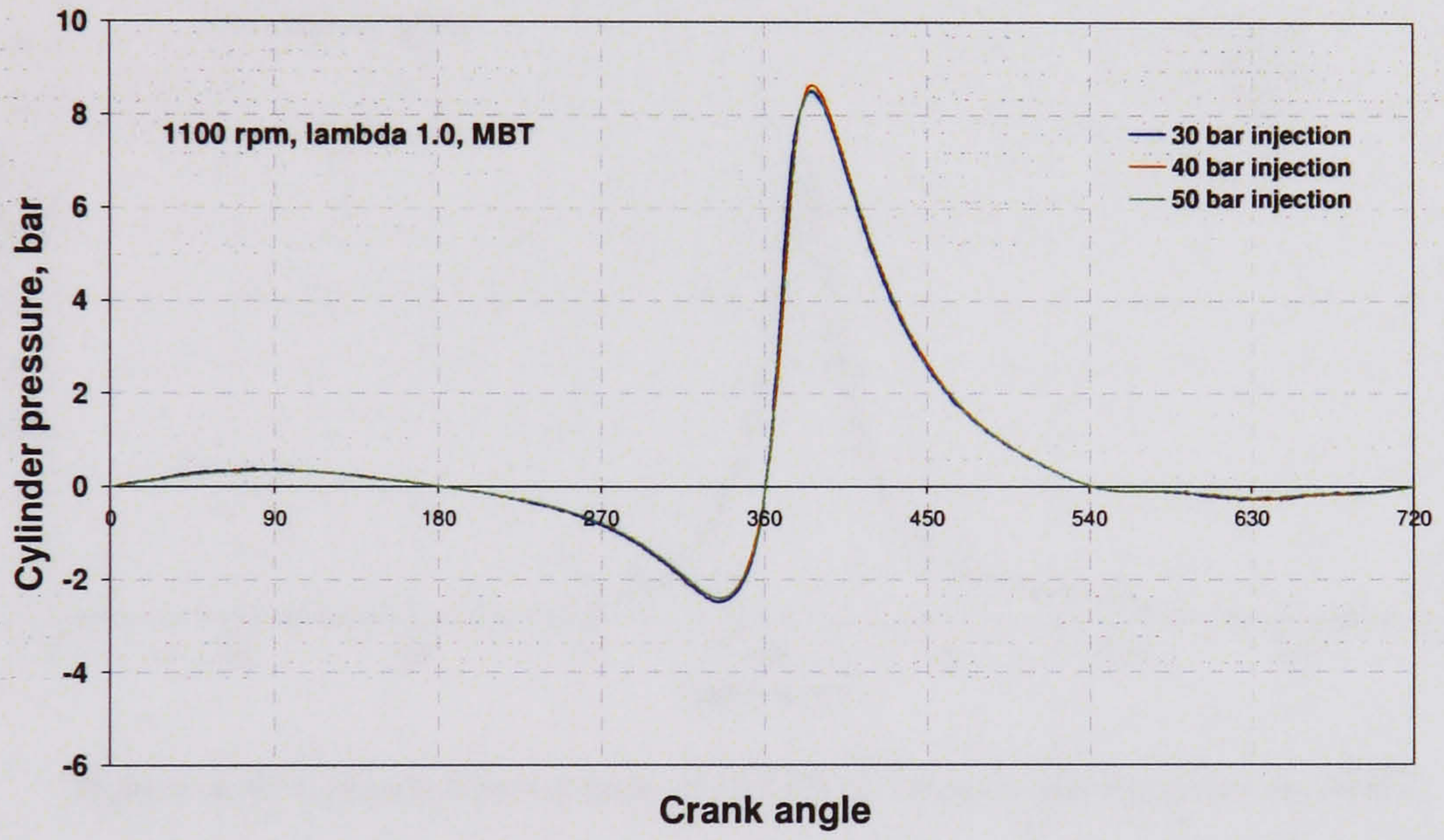

Figure 5.39 Cylinder work for OVPI at various injection pressures

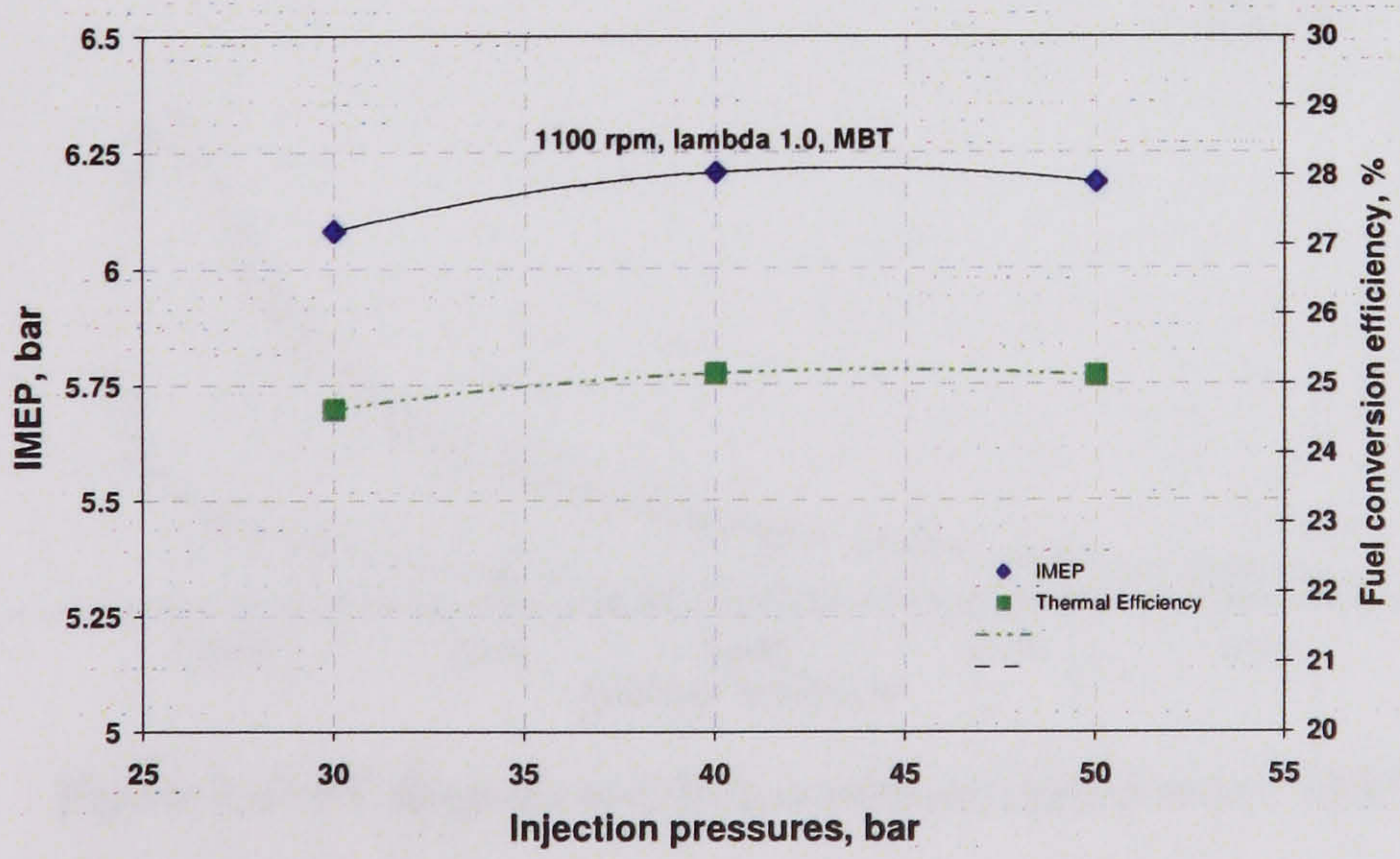

Figure 5.40 Effect of injection pressures on IMEP of OVPI at MBT

5.7.1.3 Effect of stoichiometry

The air fuel ratio effect on the performance of port injection operation was investigated by varying the lambda value, λ, where lambda is the ratio of actual-to-stoichiometric air-fuel ratios. ($\lambda = AFR_{real}/AFR_{stoich}$). The lambda values applied were 0.9, 1.0 and 1.1, where 0.9 is rich and 1.1 is lean mixtures. The effect different AFR from lean to rich can be clearly seen in Figure 5.41 where peak cylinder pressure increases with richer mixture. In Figure 5.42 the PV diagram shows increase of total area enclosed by the pressure curves with decreasing lambda values. This was further enhanced by the cylinder work curves which indicate more difference in positive work with varying lambda value shown in Figure 5.43.

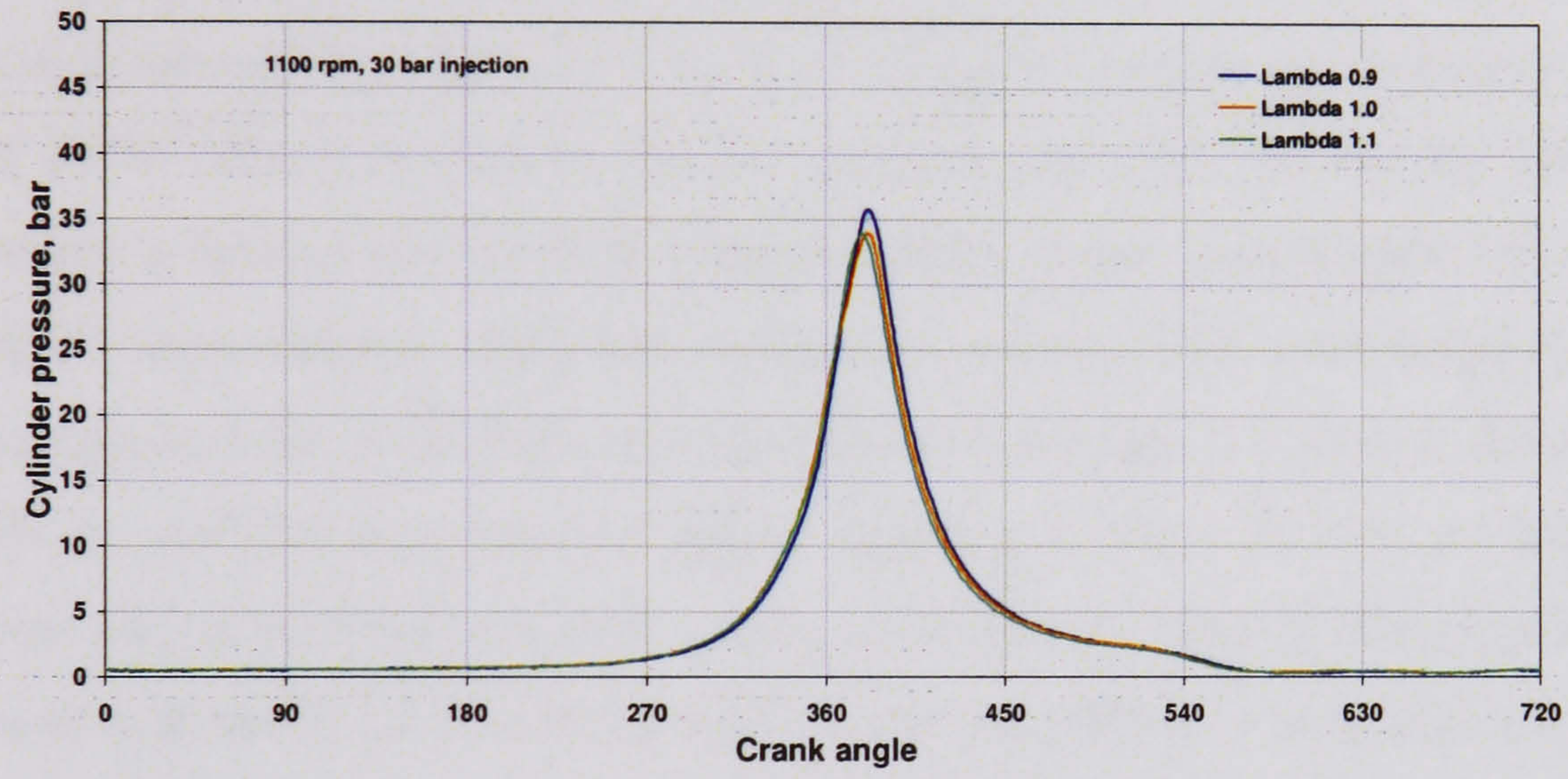

Figure 5.41 Cylinder pressures of OVPI at various air-fuel ratios, MBT

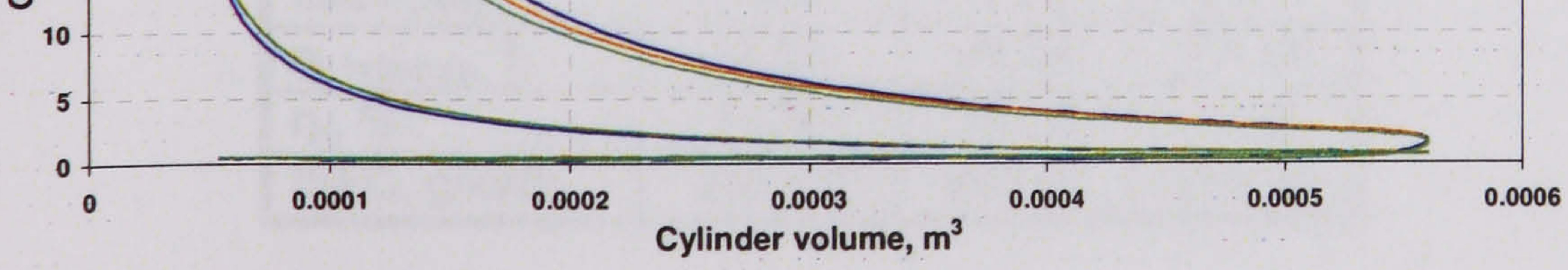

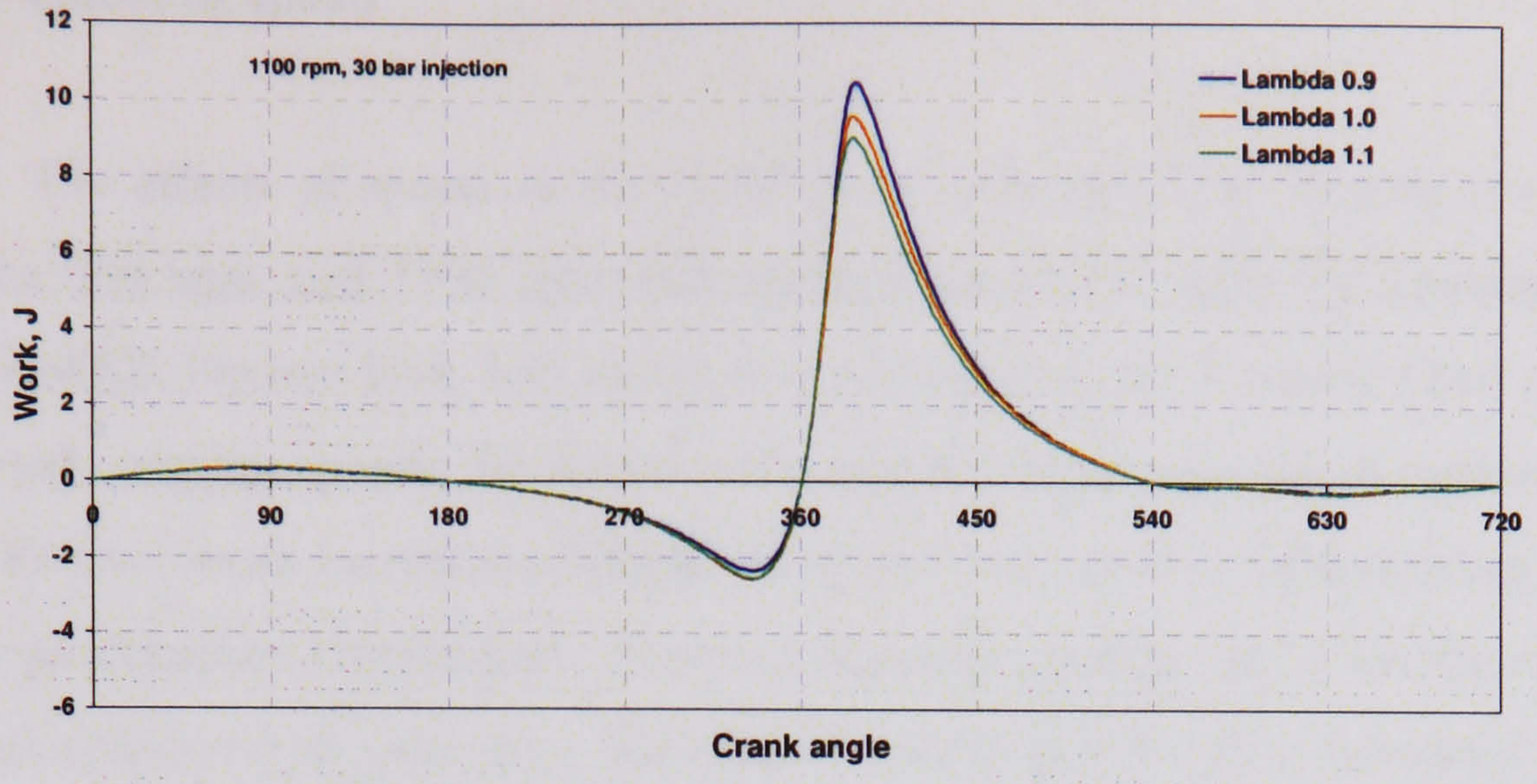

Figure 5.43 Cylinder work of OVPI at various air-fuel ratios and MBT

Table 5.3 shows the engine performance at these lambda values. Results show increase of IMEP from 6.21 bar to 7.42 bar as mixture stoichiometry become richer which directly related to the increasing mixture specific heating value. The volumetric efficiency increased as mixture became leaner than lambda 0.9 but with only 0.5% improvement. However, in terms of indicated fuel conversion efficiency, the maximum value of 27.76% was achieved with lambda 1.1, then it decreased to 26.94% at stoichiometric mixture before regaining a better 27.29% at lambda 0.9. This was also shown with the ISFC where the minimum value of 259.34 g/kWh was achieved with lambda 1.1, then increased to 267.28 g/kWh at stoichiometric air-fuel ratio before going down to 263.83 g/kWh at lambda 0.9. The variation in thermal efficiency and ISFC from the average values are less than 1.6%. These results indicates that IMEP and subsequently indicated power can be controlled by varying mixture stoichiometry without significantly change fuel conversion efficiency, fuel economy and volumetric efficiency.

λ	**0.9**	**1**	**1.1**
IMEP, bar	7.42	6.63	6.21
$\eta_{f,\ indicated}$, %	27.29	26.94	27.76
η_v, %	71.96	72.35	72.35
ISFC, g/kWh	263.83	267.28	259.34

Table 5.3 Effects of varying AFR on engine performance

5.7.1.4 Effect of speed

The effects of speed on the IMEP were determined by running the engine between 900 rpm and 1700 rpm and spark advance was adjusted accordingly to achieve MBT. Figures 5.44, 5.45 and 5.46 show the pressure behaviour and cylinder work with varying speeds. In figure 5.46, cylinder work are plotted against crank angle. Positive work increases as engine speed increases due to the increasing rate of energy produced by combustion. However, increasing engine speed has the effect of reduced cylinder peak pressures, but overall output powers were increased due to positive offset by the increasing speed (i.e. increase rate of work done). Thermal efficiency decreases with increasing speed and hence ISFC increases. Figures 5.47 and 5.48 show the performance and polynomial fit lines at various speeds. The results are summarized in Table 5.4.

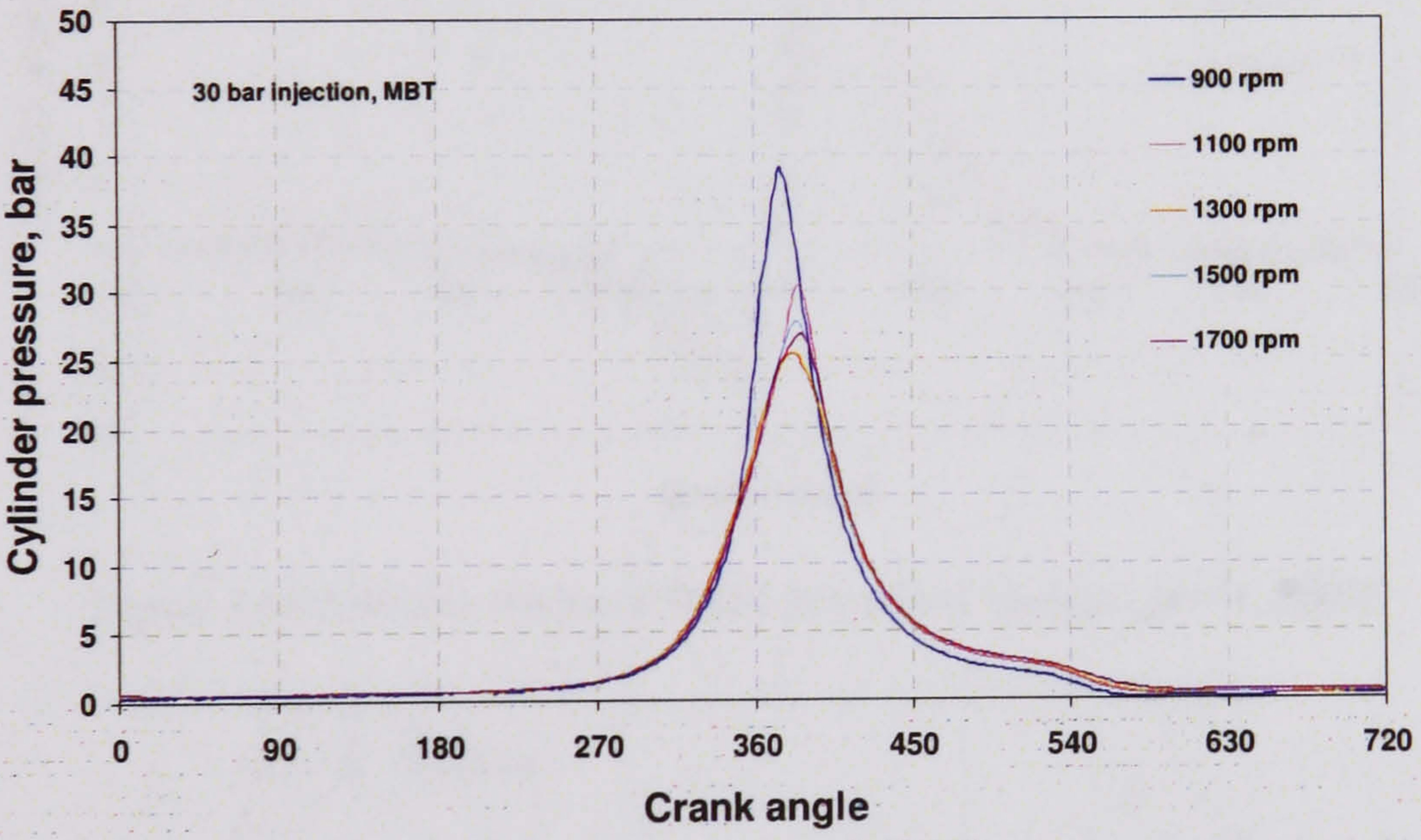

Figure 5.44 Cylinder pressures of OVPI at various engine speeds, MBT

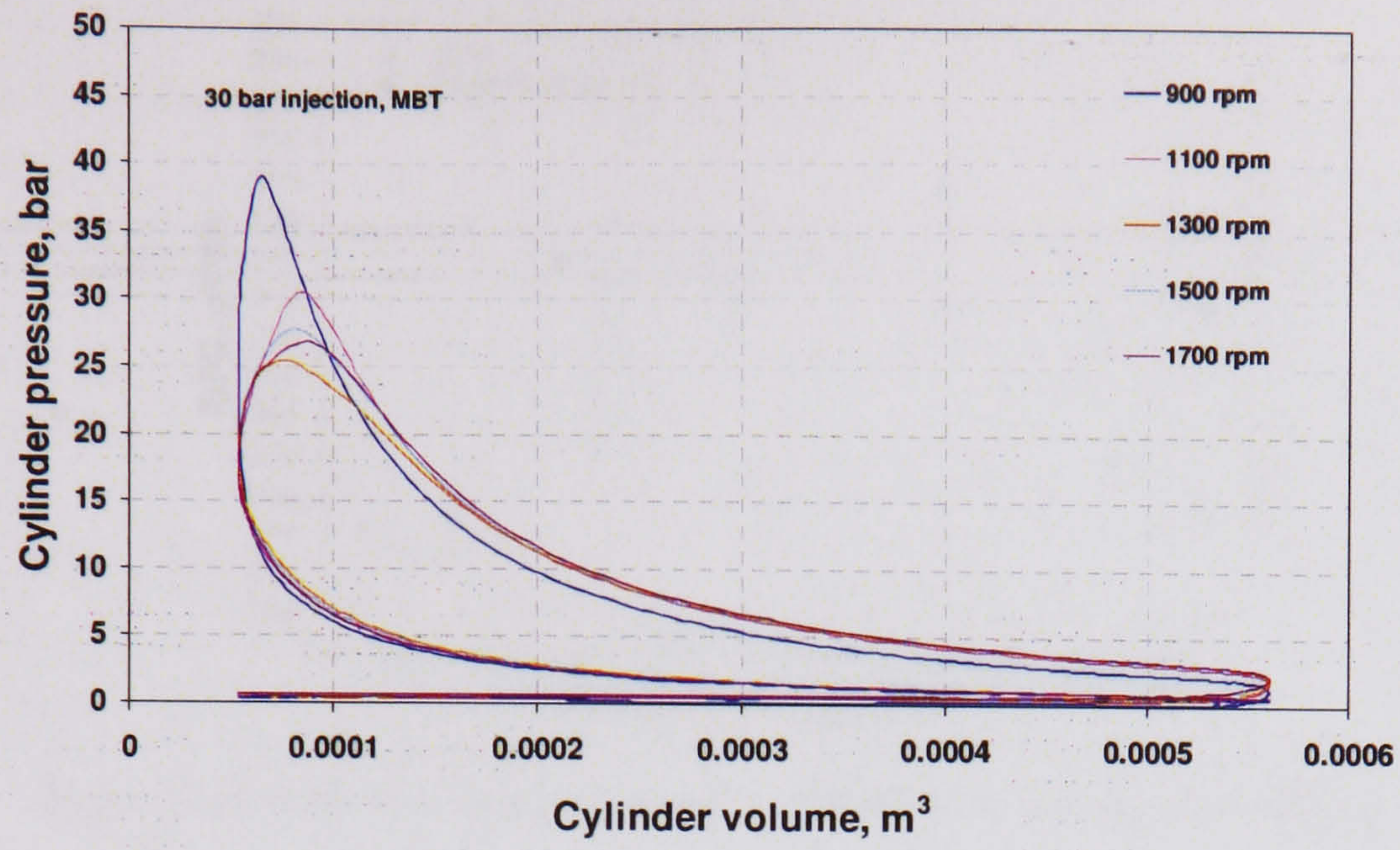

Figure 5.45 PV diagram of OVPI at various engine speeds, MBT

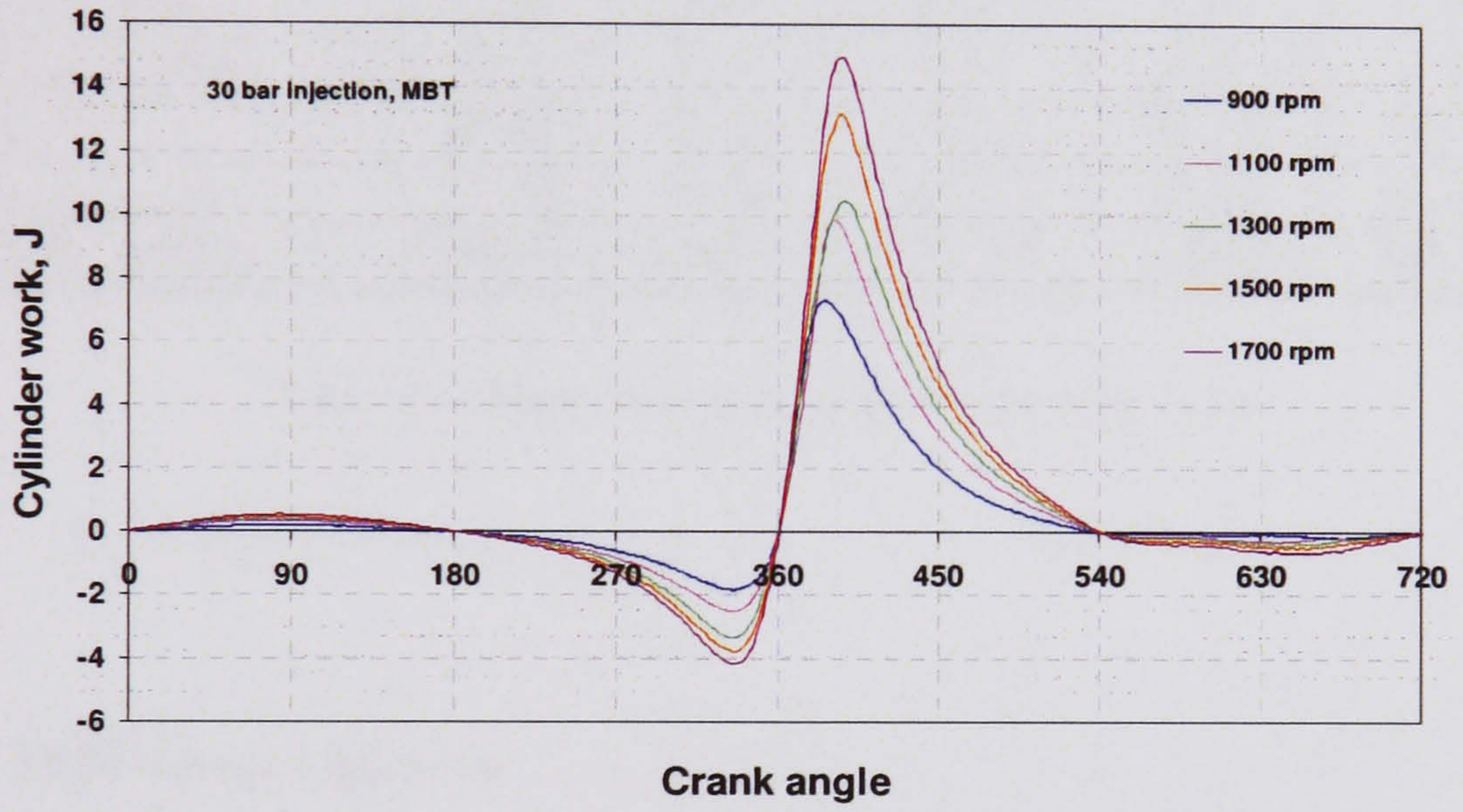

Figure 5.46 Cylinder works of OVPI at various engine speeds, MBT

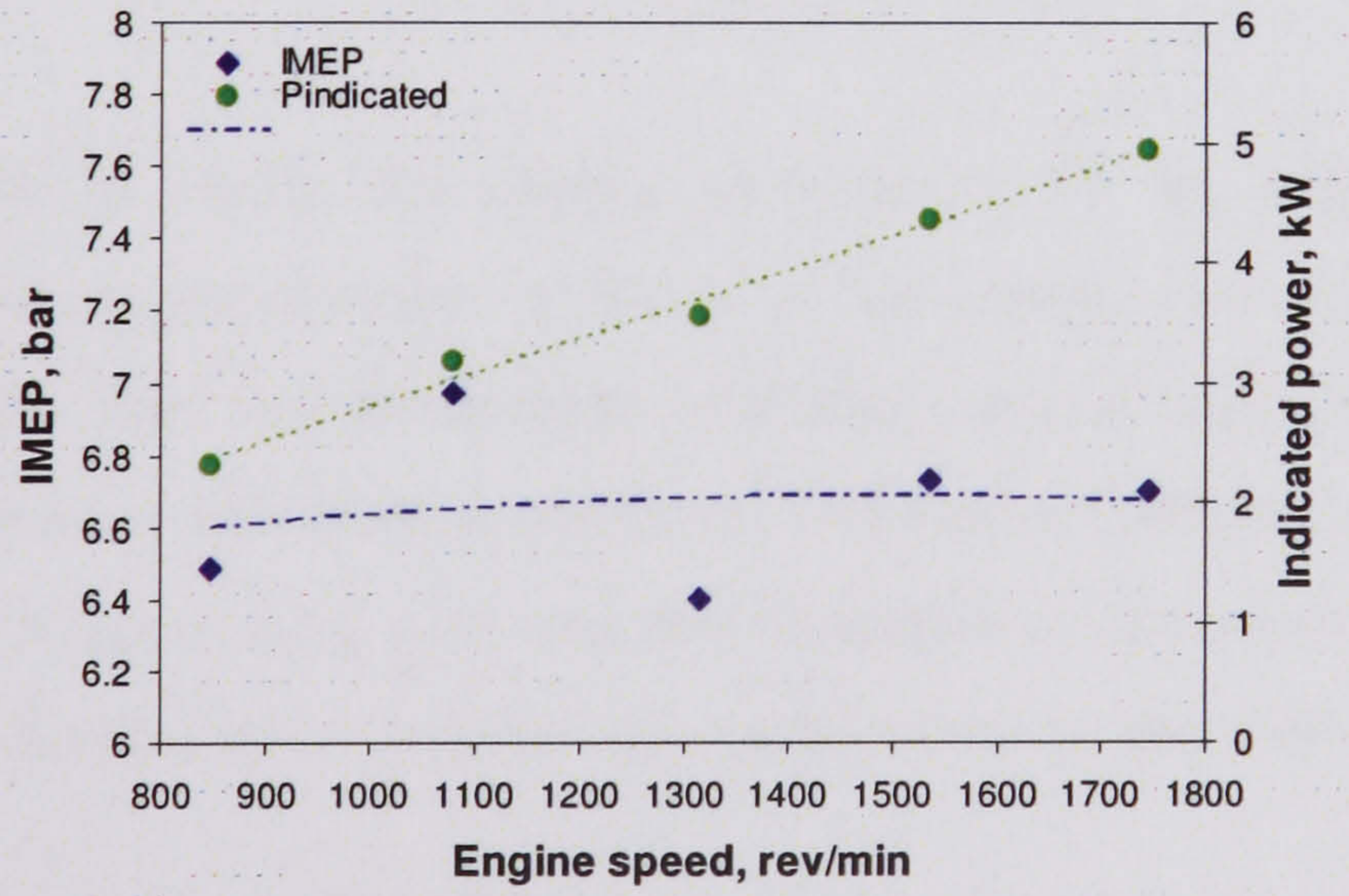

Figure 5.47 Effects of engine speeds on OVPI IMEP and indicated power

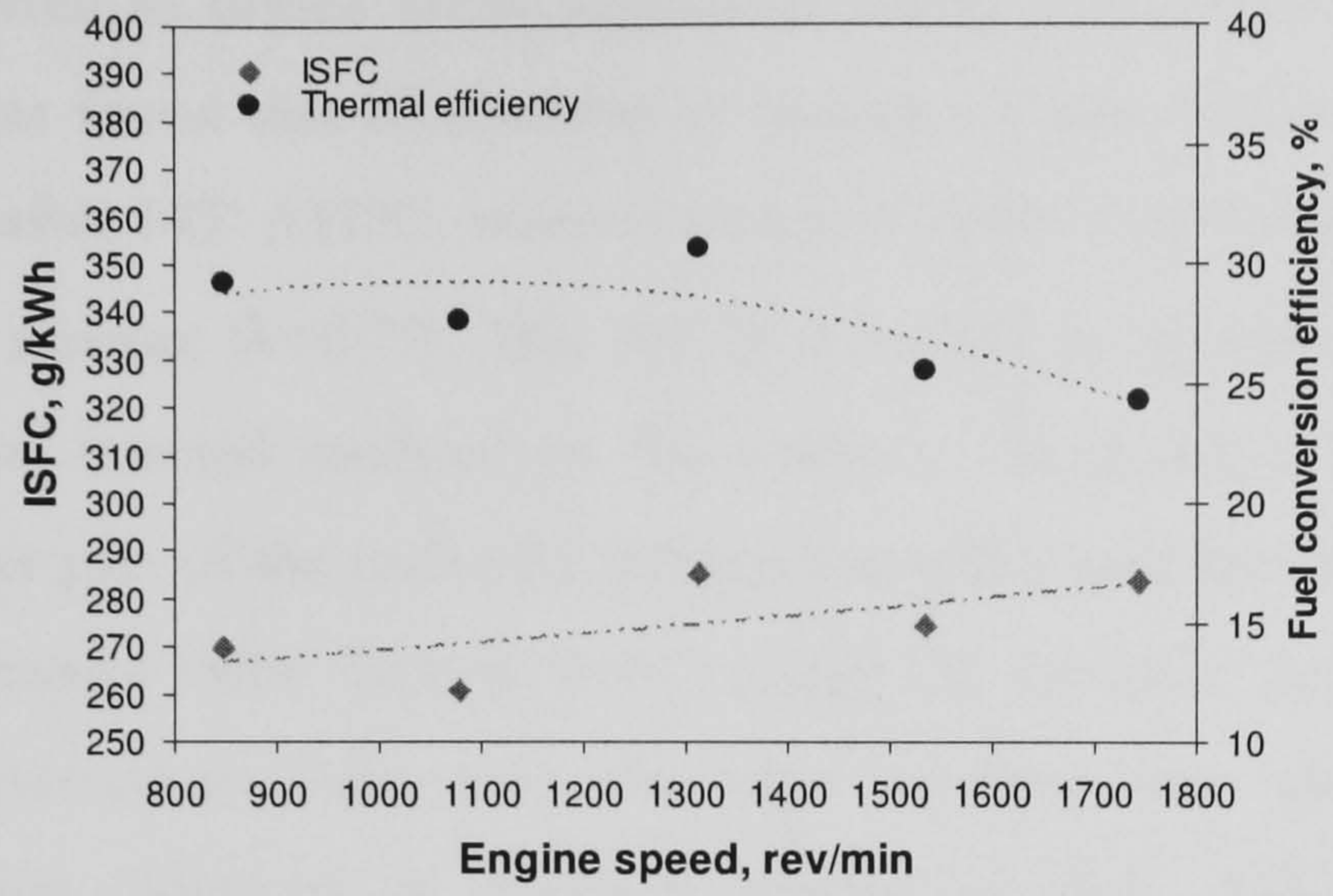

Figure 5.48 Effects of engine speeds on OVPI ISFC and thermal efficiency

Speed, rev/min	847	1079	1312	1534	1744
IMEP, bar	6.48	6.97	6.40	6.73	6.70
$P_{indicated}$, kW	2.32	3.17	3.54	4.35	4.93
η_v, %	70.64	73.42	73.76	74.58	76.72
$\eta_{f,\ indicated}$, %	27.75	26.30	29.11	24.24	23.10
ISFC, g/kWh	269.68	260.61	285.24	274.43	283.53

Table 5.4 Effects of engine speeds on performance

5.7.2 SPFI direct injection

5.7.2.1 Effect of Injection timings and ignition advances

In order to obtain the optimal performance of this engine under direct injection operation, the appropriate timing of fuel injection at a fixed fuel pressure must be known. This was achieved by obtaining optimal balance between IMEP, volumetric efficiency and thermal efficiency. Volumetric efficiency should be greater than the one of open valve port injection described in the previous section. This means more charge can be induced per cycle which is the basis of performance improvement.

Methane was injected at 60 bars at various crank angles during the intake or compression stroke at 1100 rpm and mixture lambda value of 1.0. The injection timing are referred to degree crank angle after intake TDC, describe as ATDC in Table 5.5. It was found that combustion at lambda 1.0 can only be achieved when fuel is injected after 145° ATDC, whereas injection earlier than this point would only result in richer mixture ($\lambda<0.75$). This can be described as cylinder air rejection due to expansion of injected methane in the cylinder. As injection time is retarded towards the later part of the cycle, the air rejection effect was reduced by the closing movement of intake valve. Results from varying the injection period and ignition timing are presented in Table 5.5. The table indicates that optimal balance of performance was achieved at injection timing of 190° ATDC. The engine performance with this injection timing was further investigated by varying other operational parameters which include;

1. Ignition advance
2. Injection pressure
3. Mixture stoichiometry
4. Load conditions
5. SPFI fuel path lengths
6. Engine speeds

Injection (ATDC)	Spark advance for MBT (BTDC)	IMEP (bar)	$P_{indicated}$ (kW)	η_v, %	$\eta_{f, indicated}$, %
160	20	5.66	2.64	80.15	20.35
170	25	4.87	2.26	81.57	17.58
180	20	6.03	2.80	82.67	21.43
190	25	6.20	2.85	83.43	21.84
200	25	6.04	2.81	82.58	21.48
210	25	5.81	2.76	82.75	20.33
220	15 **	3.76	1.79	83.40	13.06

Table 5.5 Performance of SPFI CH_4 DI at 1100 rpm, 60 bar injection pressure, stoichiometric AFR (no combustion after 20 BTDC) (coloured row for optimum calibration)**

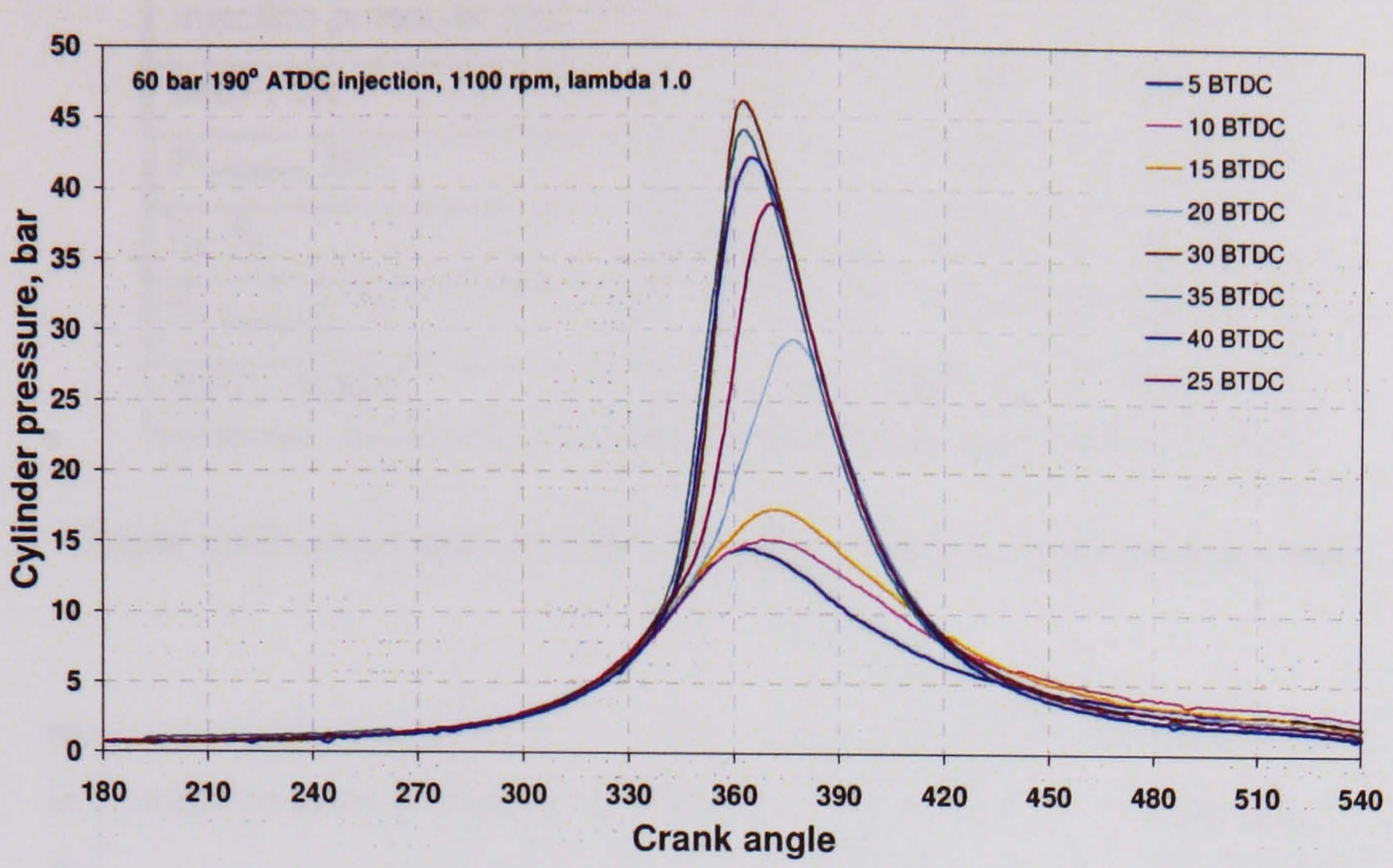

Figure 5.49 Effect of ignition advance to SPFI CH_4 DI cylinder pressure at 1100 rpm

In Figure 5.49, the effects of ignition advance on the cylinder pressure behaviour are shown in the case of 190° ATDC injection time. Peak pressures shift towards TDC as the ignition is advanced. The best torque was achieved with spark advance of 25° BTDC with peak pressure of 38 bar at 15° ATDC.

5.7.2.2 Effect of injection pressure

Three direct injection pressures were applied; 50, 60, & 80 bar. Injection was fixed at 190° ATDC and AFR is set at stoichiometric. Table 5.6 shows the results. In Figure 5.50 through 5.52, pressure behaviour changes with different injection pressures, with 60 bar yields the optimal overall performance at this specific operational set up, followed by 80 bar and 50 bar. Thermal efficiency was highest in the case of 80 bar injection. Volumetric efficiency decreases with increasing injection pressures but indicated fuel economy improves, shown in Table 5.6 as the reduction of ISFC. These results suggest that injection pressure has a significant effect on the engine performance and this can be described as the interaction between fuel injection jet penetration and in-cylinder air motion which are the governing factors for air-fuel mixing.

Injection pressure, bar	50	60	80
IMEP, bar	5.64	6.20	6.03
$P_{indicated}$, kW	2.63	2.85	2.83
η_v, %	82.25	83.43	79.45
$\eta_{f,\ indicated}$, %	19.75	21.84	22.30
ISFC, g/kWh	364.54	337.73	322.91

Table 5.6 Performance of SPFI CH_4 DI at various injection pressures

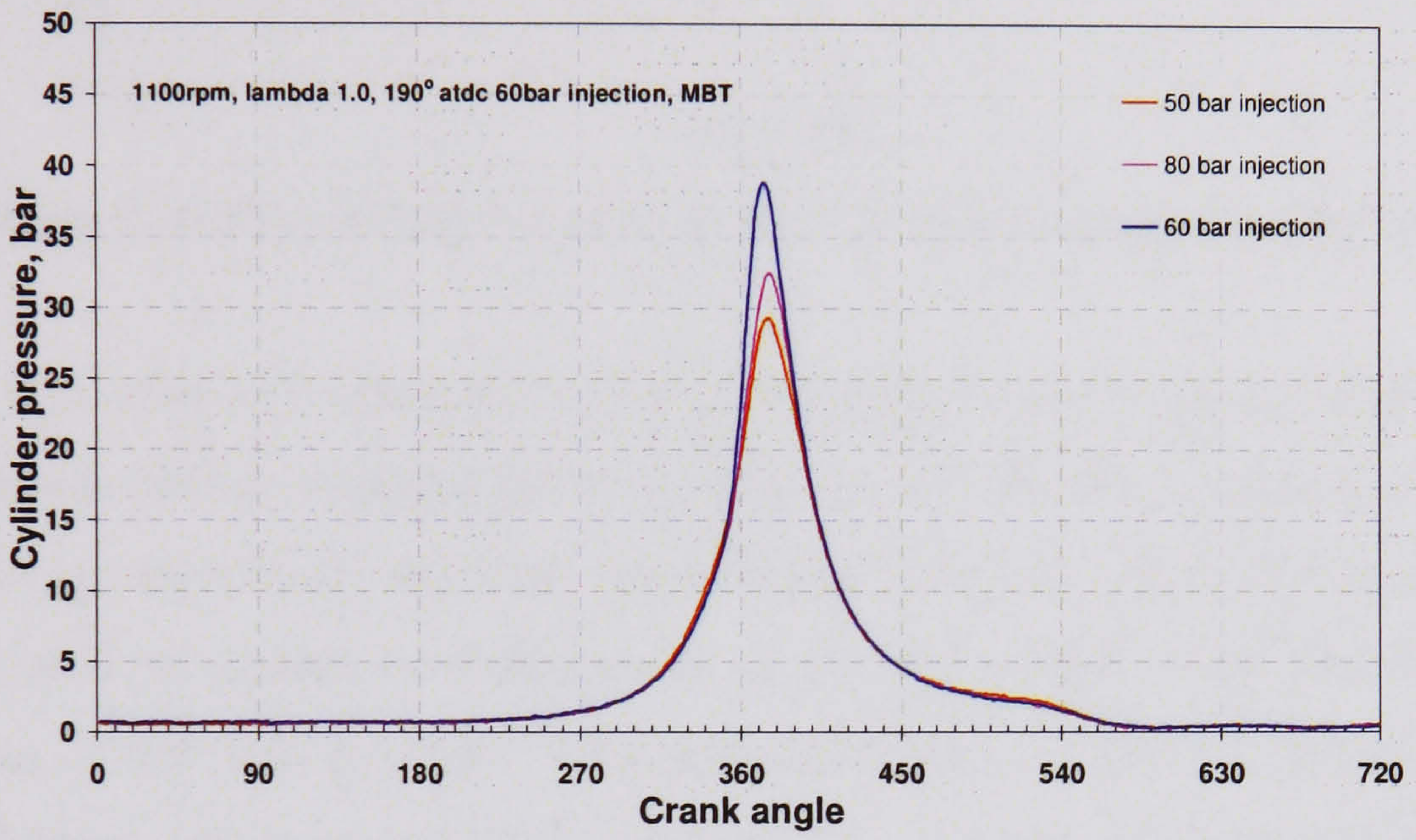

Figure 5.50 Cylinder pressure of SPFI CH_4 DI at various injection pressures, MBT

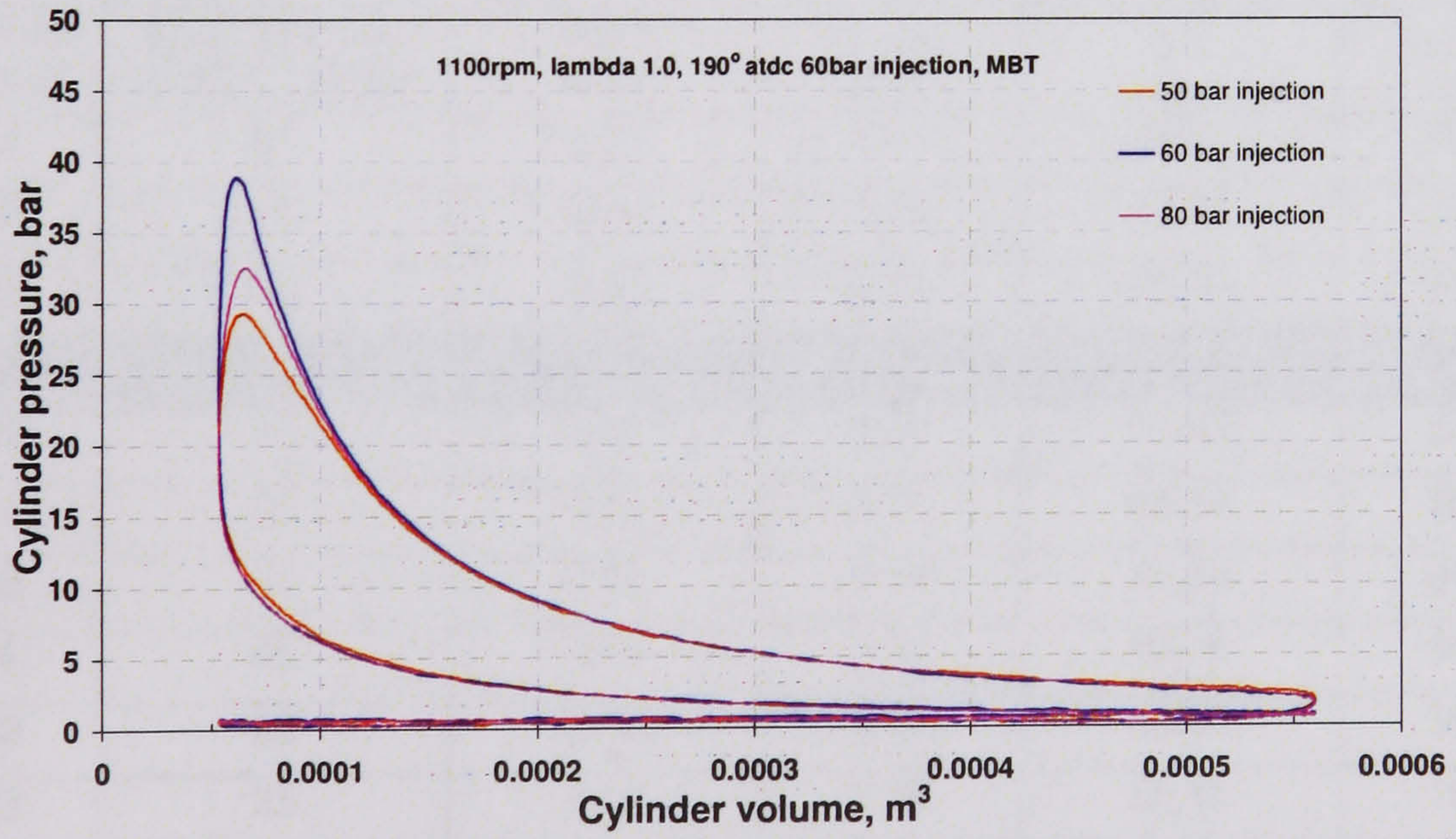

Figure 5.51 PV diagram of SPFI CH_4 DI at various injection pressures, MBT

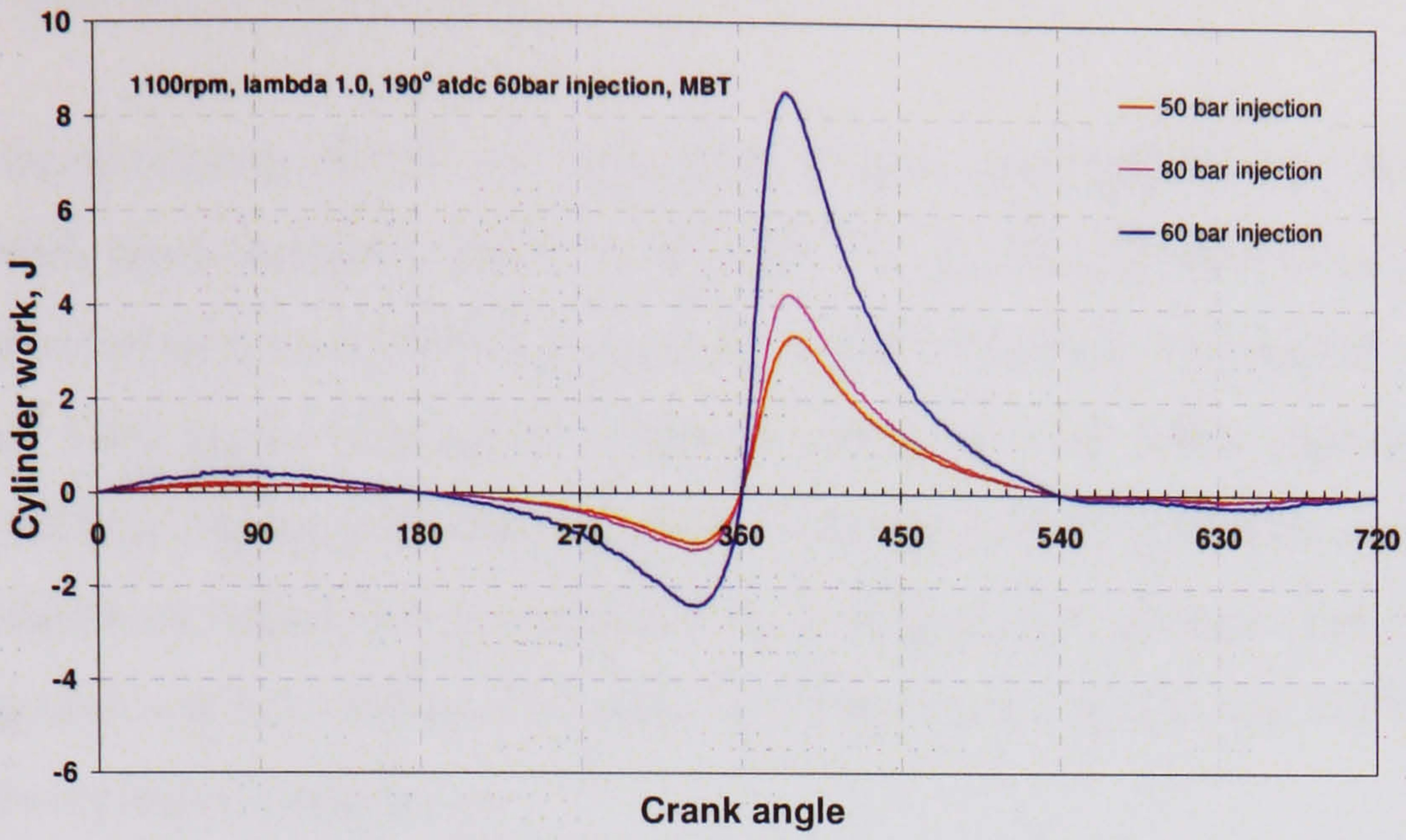

Figure 5.52 Effect of injection pressures on SPFI CH_4 DI cylinder works, MBT

The effects of changing injection pressure on the optimum injection time were determined by repeating the same procedures to find best injection timing with injection pressure of 80 bar rather than 60 bar. Table 5.7 shows the results which indicate shift in optimal injection timing to the earlier crank angle of 145° ATDC. However, at this injection time, volumetric efficiency was reduced which results in lower thermal efficiency and IMEP compared to the optimal injection timing for 60 bar injection.

Injection (ATDC)	Spark advance for MBT (BTDC)	IMEP (bar)	$P_{indicated}$ (kW)	η_v, %	$\eta_{f,\ indicated}$, %
115	25	5.60	2.60	78.63	20.80
125	25	5.64	2.62	78.66	21.08
135	25	5.85	2.74	78.40	21.94
145	25	6.03	2.83	79.45	22.30
160	25	5.97	2.82	83.68	21.01
170	30	5.64	2.65	80.59	20.62
180	25	5.72	2.69	80.59	20.91
190	25	5.76	2.72	80.46	21.06
200	25	5.12	2.42	80.69	18.69
210	25	5.05	2.39	80.47	18.48
220	Non-firing				

Table 5.7 Performance of SPFI CH_4 DI on Ricardo E6 engine at 1100 rpm, 80 bar injection pressure, stoichiometric AFR (coloured row for optimum calibration)

5.7.2.3 Effect of stoichiometry

Stoichiometry effects on engine performance were obtained by running the engine with three lambda values; 0.9, 1.0 and 1.1. Results are shown in Table 5.8. Both indicated power and IMEP increase with richer mixture. Volumetric efficiency increased with leaner mixture but thermal efficiency and ISFC experienced the reverse effects. Figure 5.53 through 5.55 show the cylinder pressure and cylinder work behaviours which clearly indicate that peak pressures increase with increasing fuel proportion in the mixture. The same trend was shown in the case of PV diagram and in the cylinder work curves.

λ	**0.9**	**1**	**1.1**
IMEP, bar	6.41	5.69	5.13
$P_{indicated}$, kW	2.94	2.61	2.37
η_v, %	79.45	79.57	79.85
$\eta_{f, indicated}$, %	21.14	20.84	20.83
ISFC, g/kWh	340.62	345.47	345.53

Table 5.8 Selected performance of SPFI CH_4 DI at various AFR

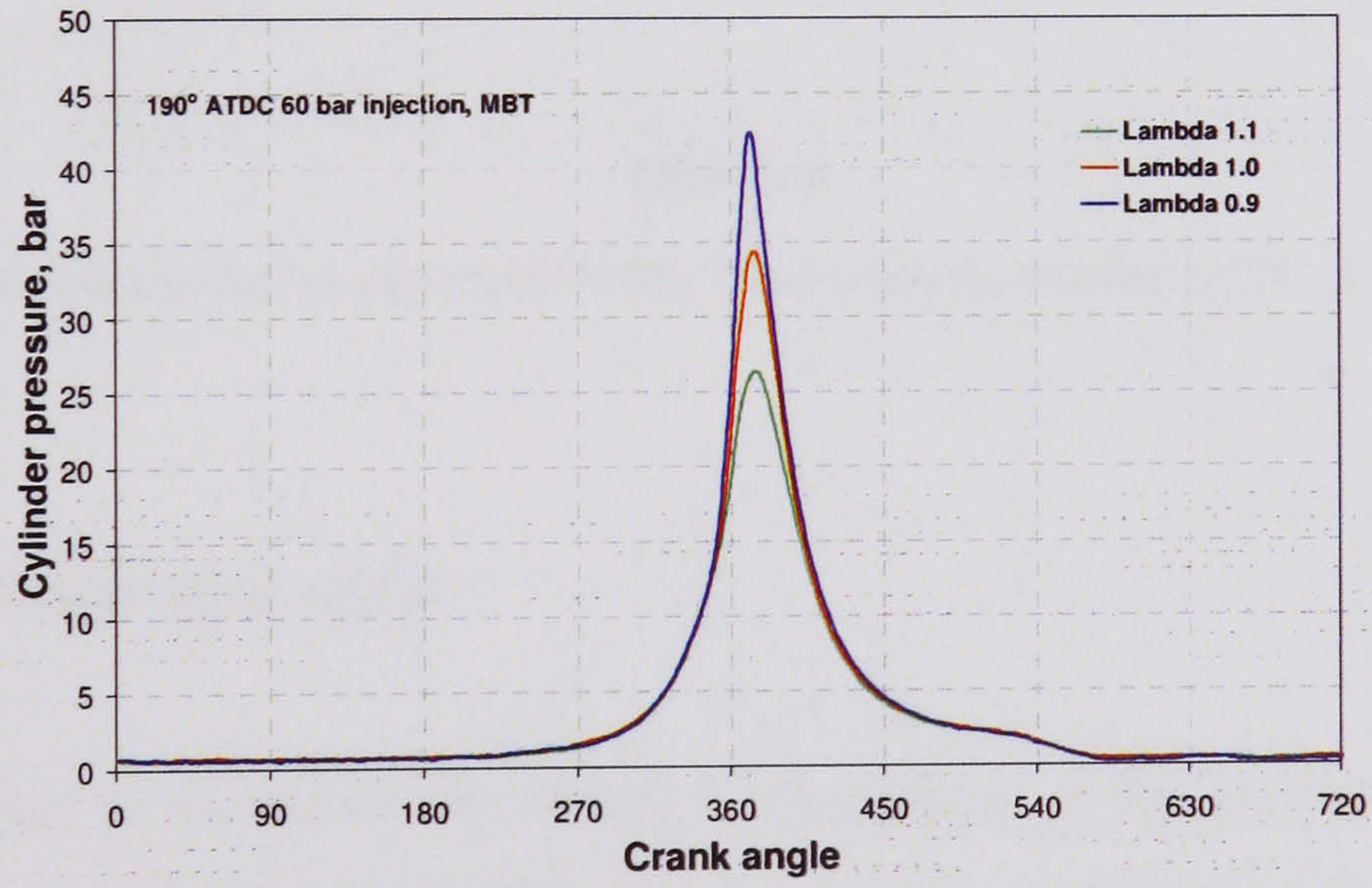

Figure 5.53 Cylinder pressures of SPFI CH_4 DI at various lambda values at 1100 rpm

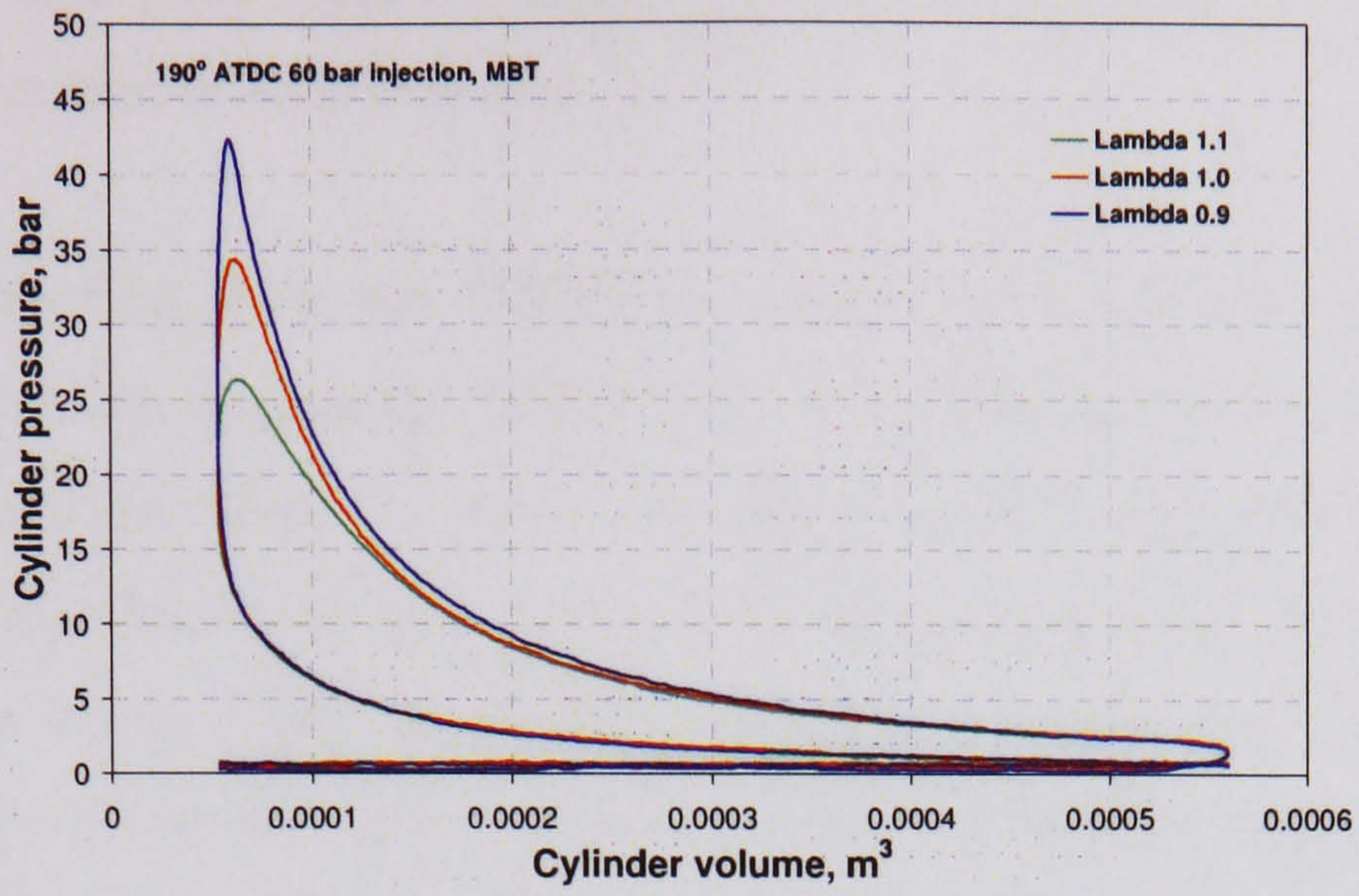

Figure 5.54 PV diagram of SPFI CH_4 DI at various lambda values at 1100 rpm

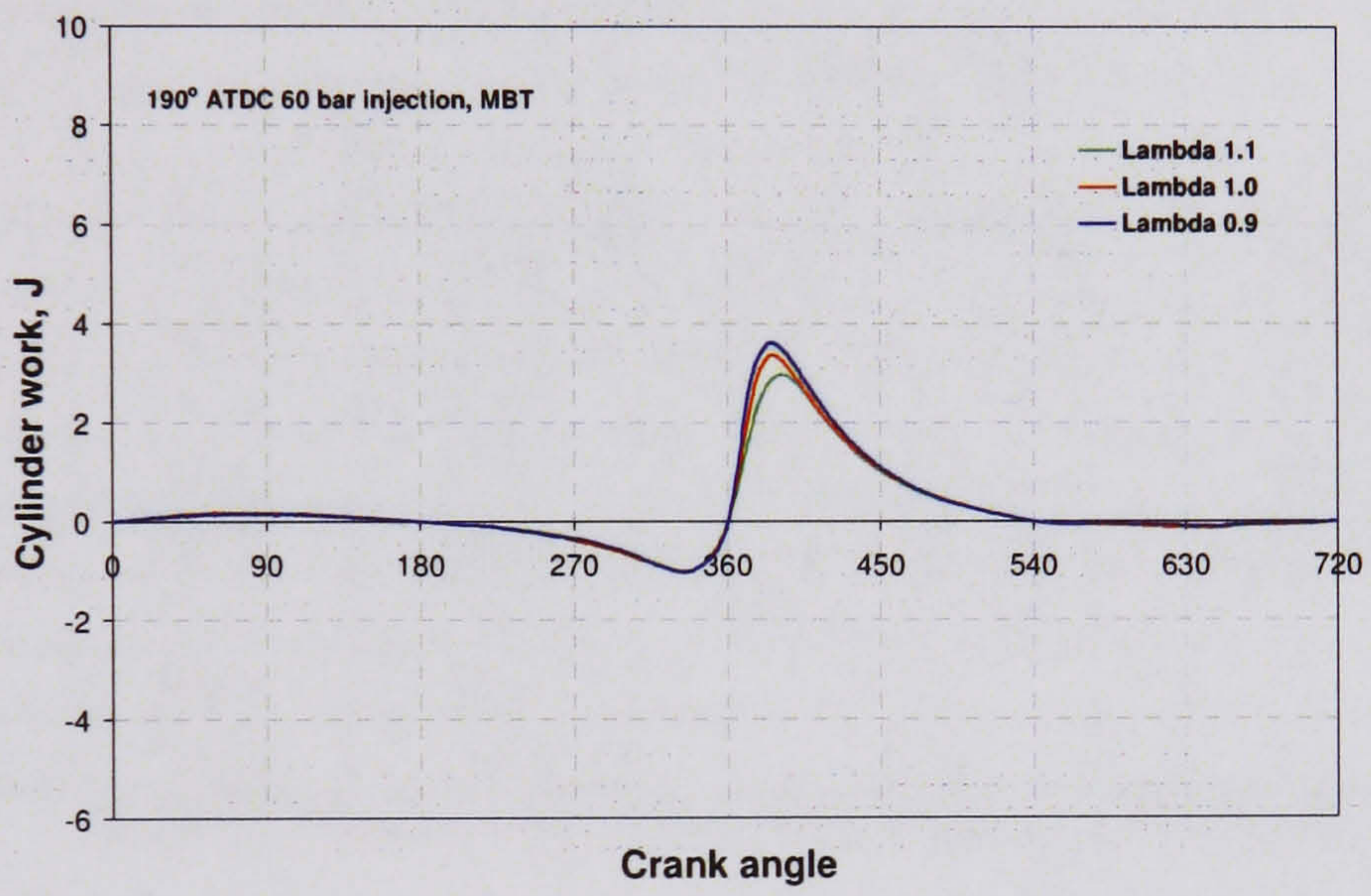

Figure 5.55 Cylinder work of SPFI CH_4 DI at various lambda values at 1100 rpm

5.7.2.4 Effect of engine speed

In order to determine the ability of the engine at the given injection timing and pressure to maintain the IMEP at higher engine speed, the engine was run at speed between 1000 rev/min to 1700 rev/min. Table 5.9 shows the results in thermal and volumetric efficiencies at these engine speeds with three air-fuel ratios. The blank cells on the table indicate unachievable combustion. In all lambda values, volumetric efficiencies initially increase with speed, reaching maximum value at 1300 rev/min before decreasing. The same pattern was shown with the thermal efficiencies with peak value at 1400 rev/min except for lambda 1.1 where peak efficiency occurred at 1300 rev/min.

Figure 5.56 show the IMEPs at various engine speeds with three lambda values. The ability to maintain IMEP with increasing engine speed decreases with increasing lambda value (i.e. leaner mixtures tend to lose performance at higher engine speeds). In Figure 5.57, indicated power was plotted against speed. As a consequence of the IMEP behaviour, leaner mixture produced slower increase in power compared to the richer ones. The offset of IMEP change with increasing speed is poorer than in the case of OVPI as discussed in Section 5.7.1.4.

Engine speed, rev/min	Lambda Value, λ					
	0.9		1.0		1.1	
	η_v, %	$\eta_{f,\,indicated}$, %	η_v, %	$\eta_{f,\,indicated}$, %	η_v, %	$\eta_{f,\,indicated}$, %
1000	79.14	19.08	79.47	21.07	79.90	20.91
1100	79.45	21.14	79.57	21.94	78.85	20.83
1200	79.58	21.68	79.91	20.93	79.78	19.04
1300	79.84	20.55	80.79	22.39	80.21	22.07
1400	79.59	23.58	79.90	23.10	79.59	18.09
1500	79.18	21.57	78.93	20.40		
1600	79.79	18.23				
1700	78.89	19.89				

Table 5.9 Effect of increasing engine speed on efficiencies

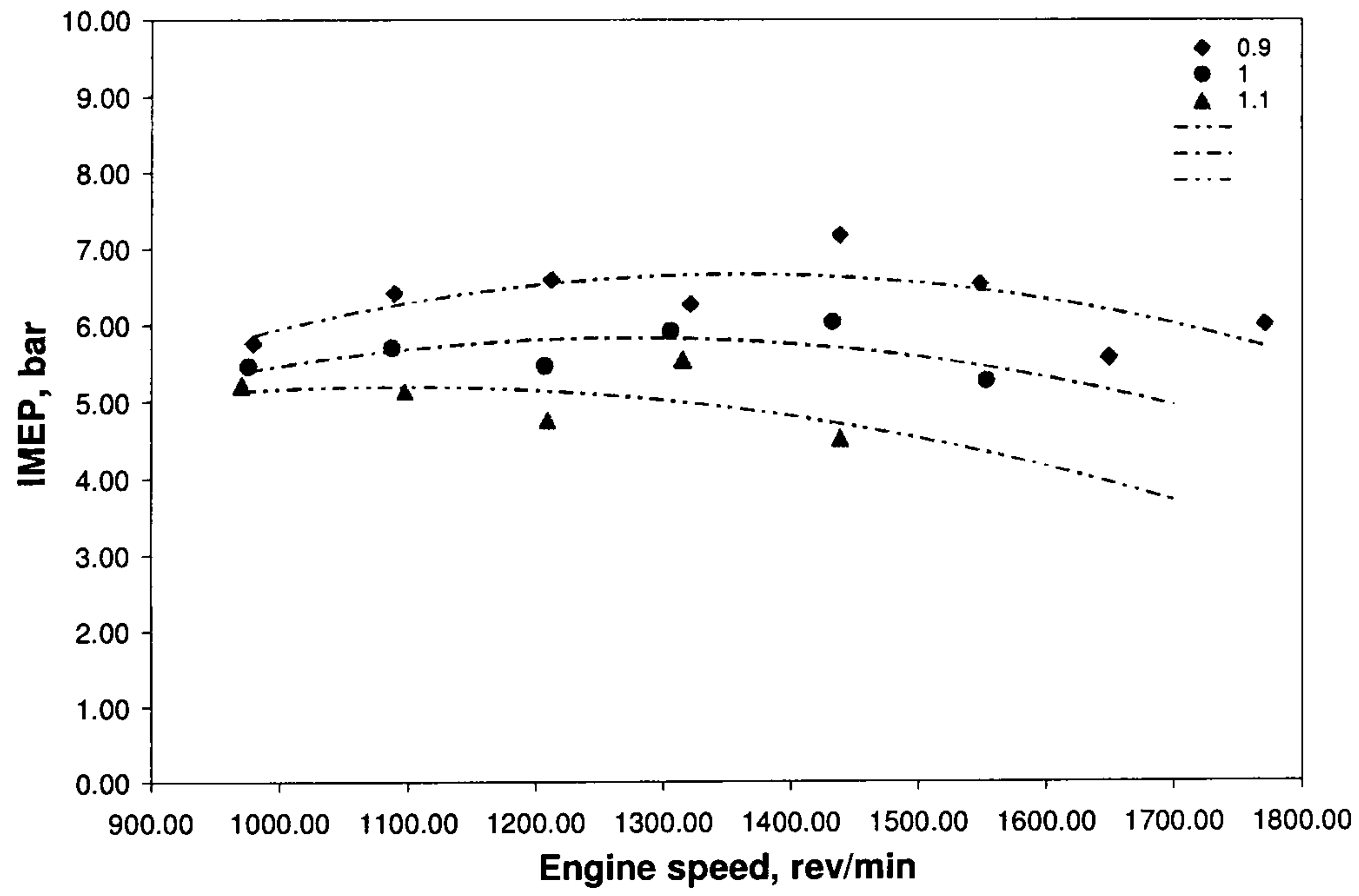

Figure 5.56 IMEP of SPFI CH_4 DI at various engine speeds, MBT

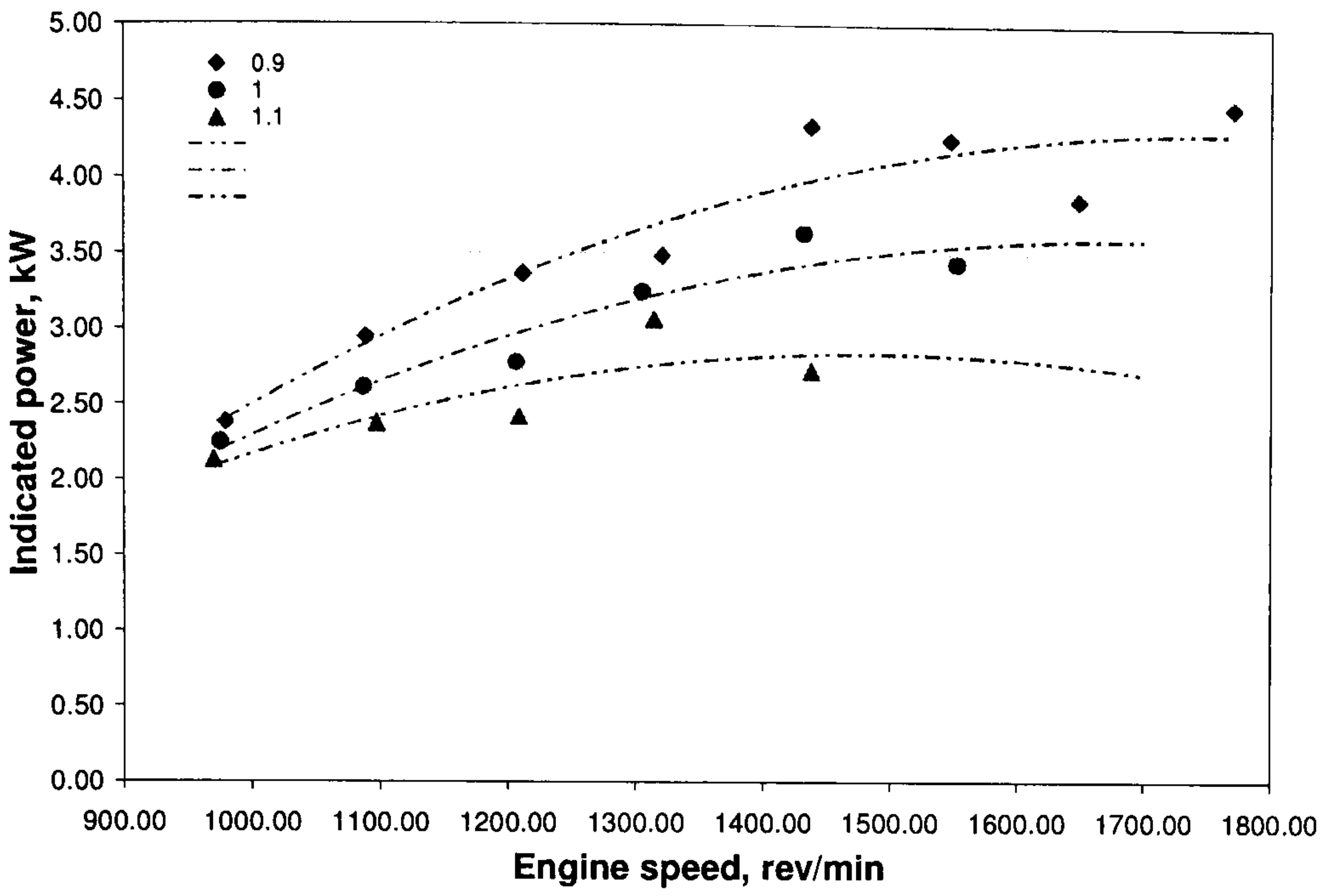

Figure 5.57 Indicated power of SPFI CH_4 DI at various engine speeds, MBT

5.7.2.5 Effect of fuel path length

In order to determine the effect of fuel path length on the performance of CH_4 SPFI DI, an additional fuel path of 4 millimetres inner diameter and 57 millimetres length was attached between the GDI and the original fuel path. The engine was run at 1100 rpm and stoichiometric AFR with injection retained at 190° ATDC and 60 bar injection pressure. Table 5.10 shows the results from the change. It is clear that extending the fuel path has adverse effects on engine performance which is due to extended fuel arrival delay and possibly the delivery time. The most probable effect of extended fuel path is increase in the amount of unburned hydrocarbon because not all methane arrives in the cylinder during combustion duration, which also explains the significant reduction of IMEP, indicated power, thermal efficiency and increase in ISFC. Figure 5.58 through 5.60 show the cylinder pressure and cylinder work behaviour between the two fuel path lengths. However, the negative effect of longer fuel path can be compensated for to some extent by advancing the injection time. Therefore, more fuel will arrive in the combustion chamber before and during combustion, but there can be some lost in volumetric efficiency if injection time is advanced too much.

Fuel path length	Normal	Extended
IMEP, bar	6.20	4.54
$P_{indicated}$, kW	2.85	2.12
η_v, %	83.43	82.25
$\eta_{f, indicated}$, %	21.84	15.59
ISFC, g/kWh	329.67	461.71

Table 5.10 Performance of SPFI CH_4 DI with fuel path extended length

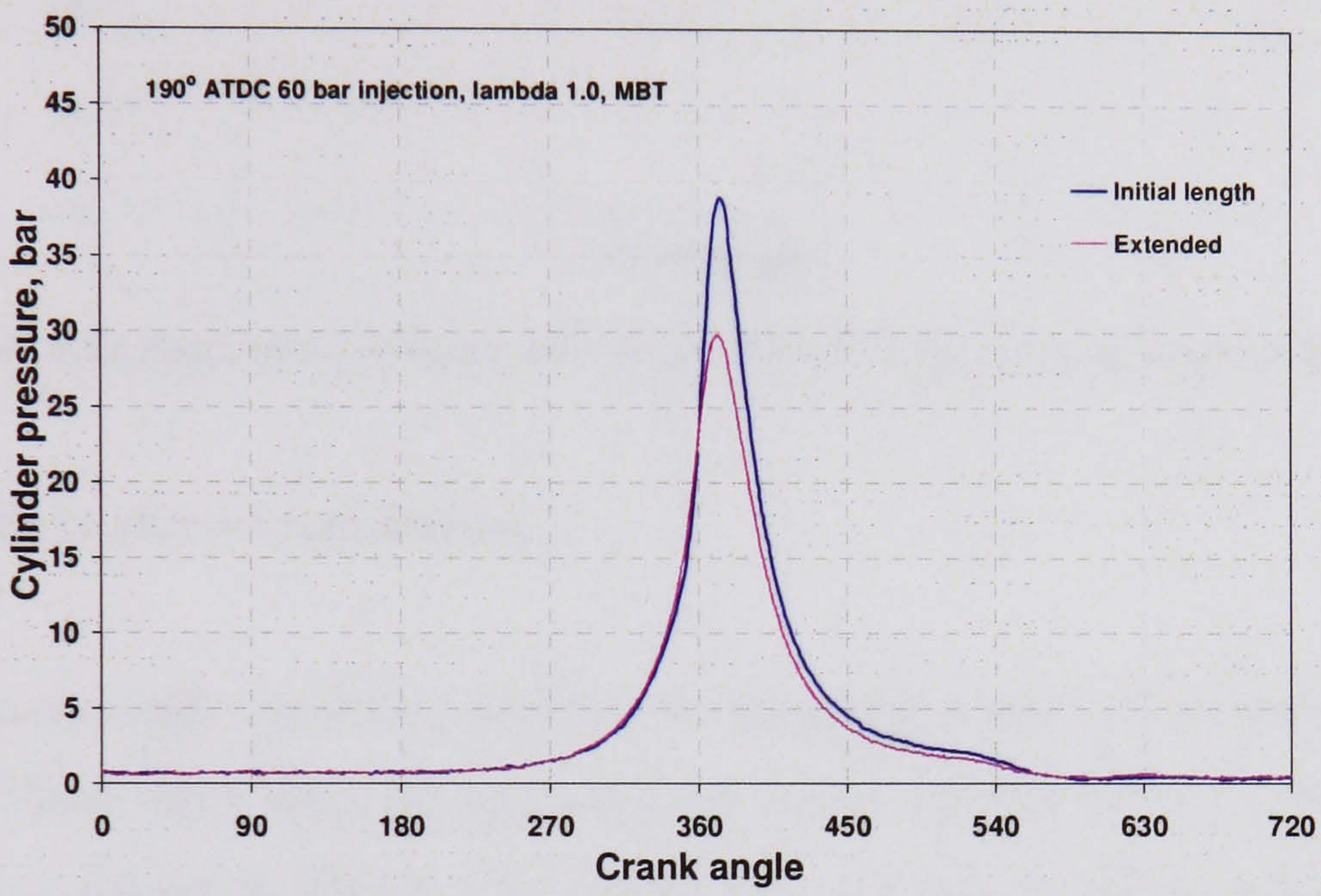

Figure 5.58 Extended fuel-path effects on SPFI CH_4 DI cylinder pressures at 1100 rpm

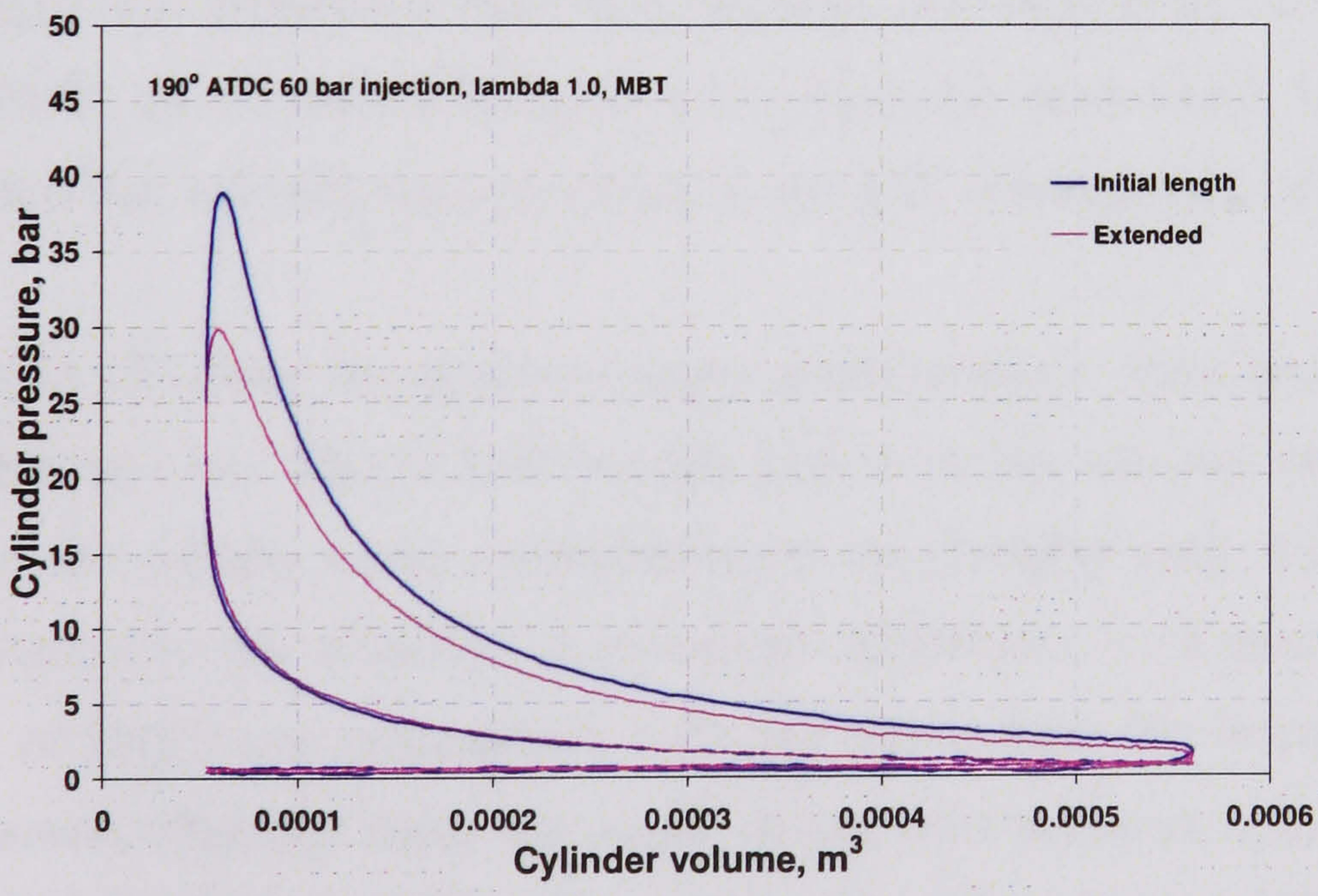

Figure 5.59 Extended fuel-path effects on SPFI CH_4 DI PV diagram at 1100 rpm

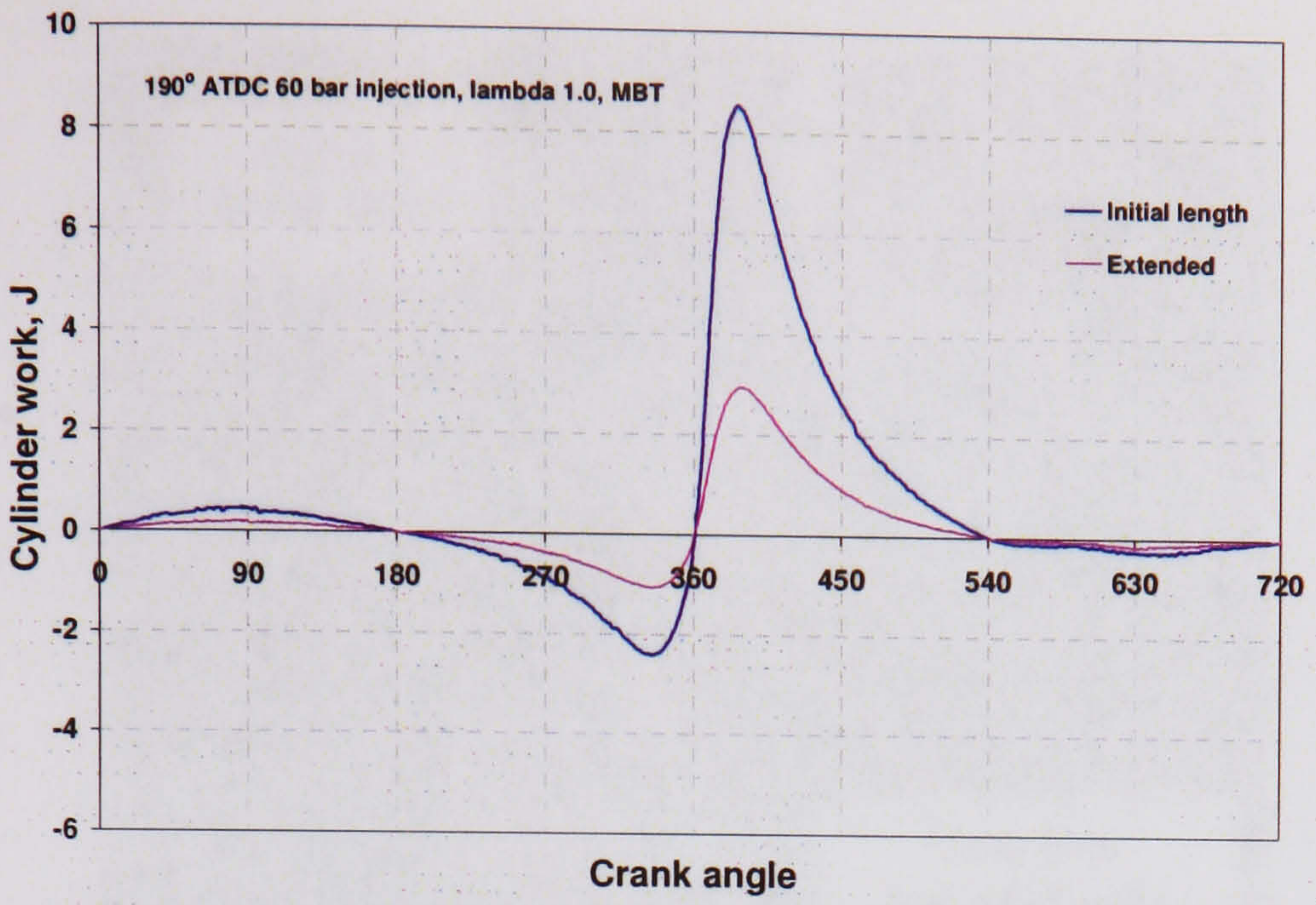

Figure 5.60 Extended fuel-path effects on SPFI CH_4 DI cylinder work at 1100 rpm

5.7.2.6 Effect of load conditions

Load conditions were varied by changing the amount of air induced into the cylinder. These were done by adjusting the intake throttle valve to three different positions as shown in Figure 5.61. There are two throttle valves available on the intake system with one fixed and another adjusted for varying air flow rate. The throttle valve was adjusted so that low, medium and wide open throttle settings produce 10.84, 14.73, and 15.54 kg/hr of air flow rate respectively. The methane injection duration was adjusted accordingly to produce stoichiometric mixtures.

Table 5.11 show the results of engine performance at three load conditions; full, medium and low. Figure 5.62 through 5.64 show the pressure behaviour, PV curves and also cylinder works corresponding to the changing loads. Reducing loads can be detected by the reduction in volumetric efficiencies. As a result, significant reduction of IMEP and consequently indicated power were discovered. However, fuel conversion efficiency show only slight change with minimum value at medium load. The behaviour of fuel conversion efficiency is reflected by the ISFC where at medium load, highest specific fuel consumption was found. Volumetric efficiency decreases with reducing load conditions and is due to air flow restriction as the throttle valve moves towards closing.

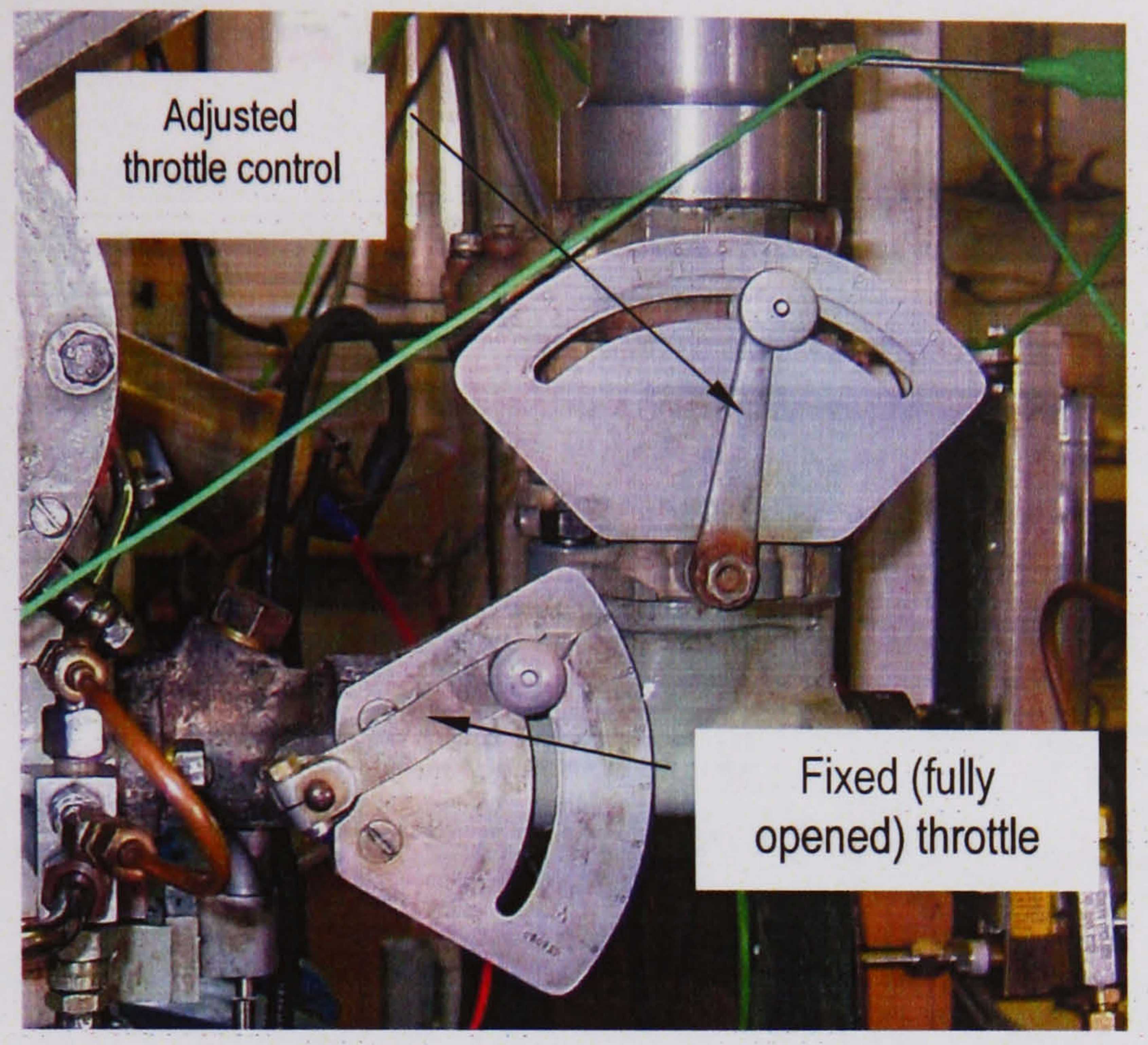

Figure 5.61 Throttle valve control

Load	Full	Medium	Low
IMEP, bar	5.69	4.97	3.96
$P_{indicated}$, kW	2.61	2.23	1.78
η_v, %	79.57	77.19	56.58
$\eta_{f, indicated}$, %	20.84	18.77	20.38
ISFC, g/kWh	345.47	383.60	353.29

Table 5.11 Selected performance of SPFI CH_4 DI at various load conditions

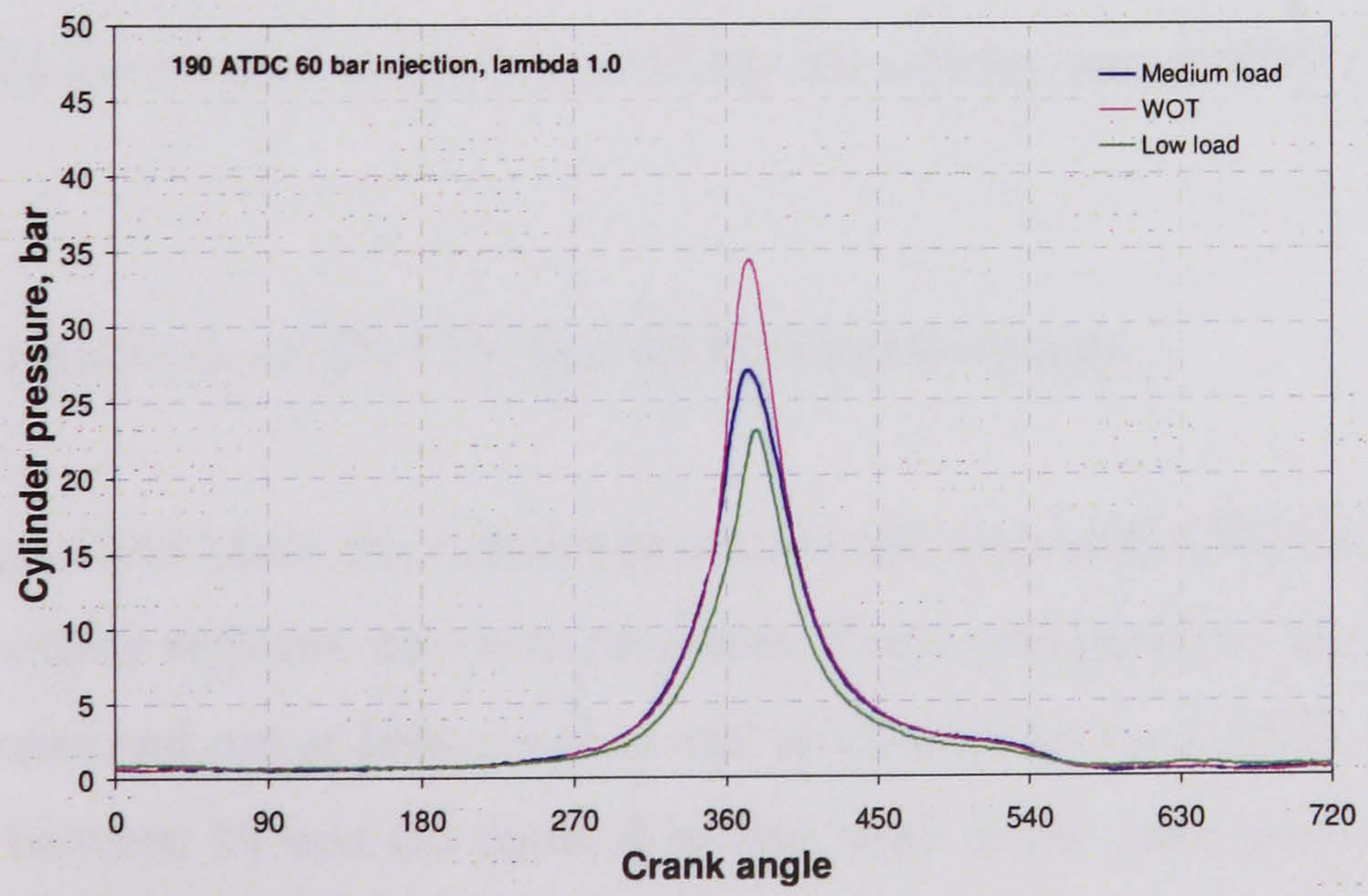

Figure 5.62 Load conditions effect on SPFI CH_4 DI cylinder pressures at MBT and 1100 rpm

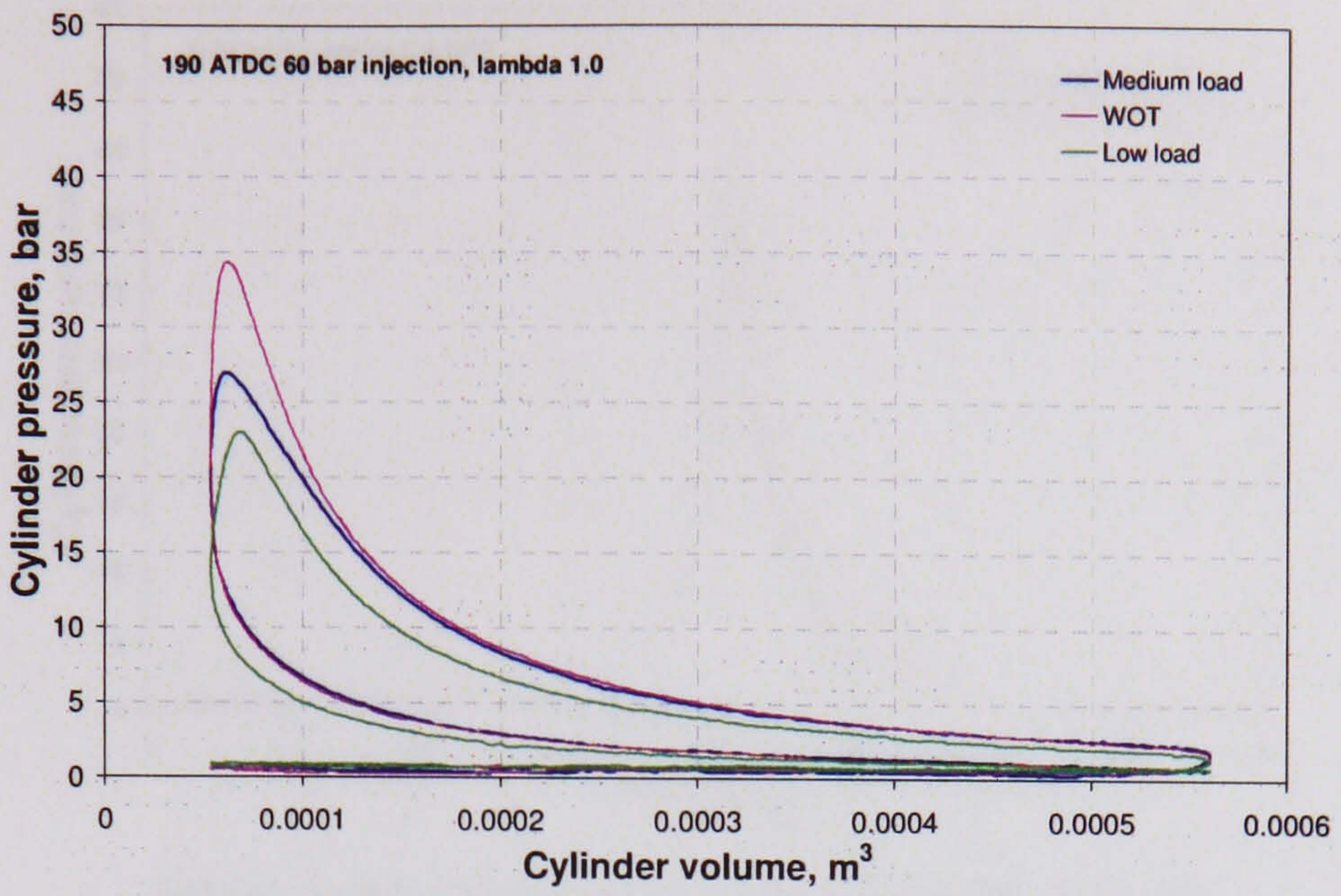

Figure 5.63 Load conditions effect on SPFI CH_4 DI PV diagram at MBT and 1100 rpm

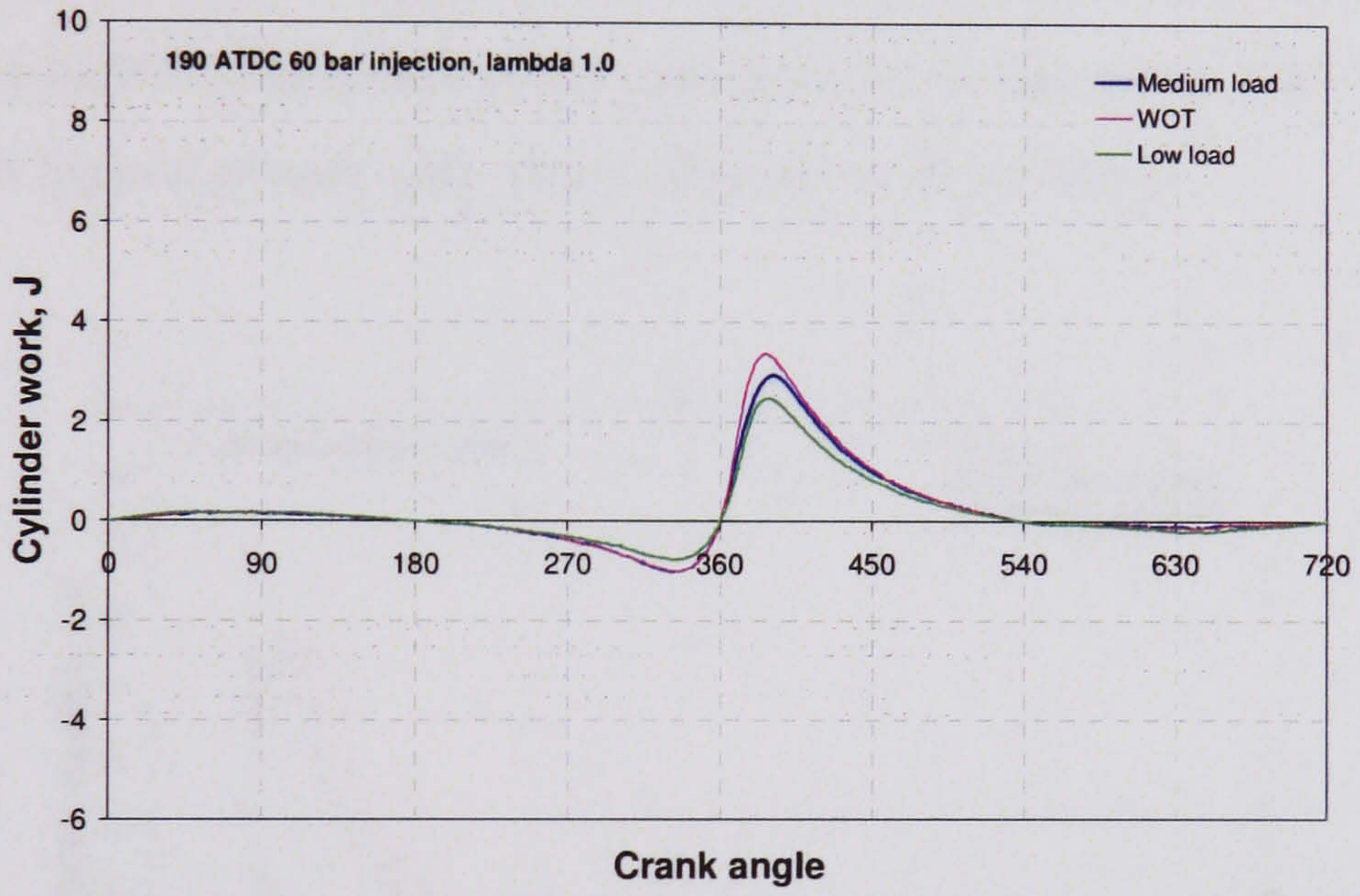

Figure 5.64 Load conditions effect on SPFI CH_4 DI cylinder work at MBT and 1100 rpm

5.7.3 Comparison of SPFI DI and PI best performance

Figure 5.65 show the cylinder pressure behaviour with OVPI method versus SPFI DI method with two injection pressures. These performances are the optimum calibrated ones and run at 1100 rev/min and spark advance set at MBT. One obvious difference between PI and DI method in this work is the peak pressure where DI methods yield higher magnitudes and earlier occurrences. In addition, with the DI operation, 60 bar injection yields higher peak cylinder pressure than 80 bar injection.

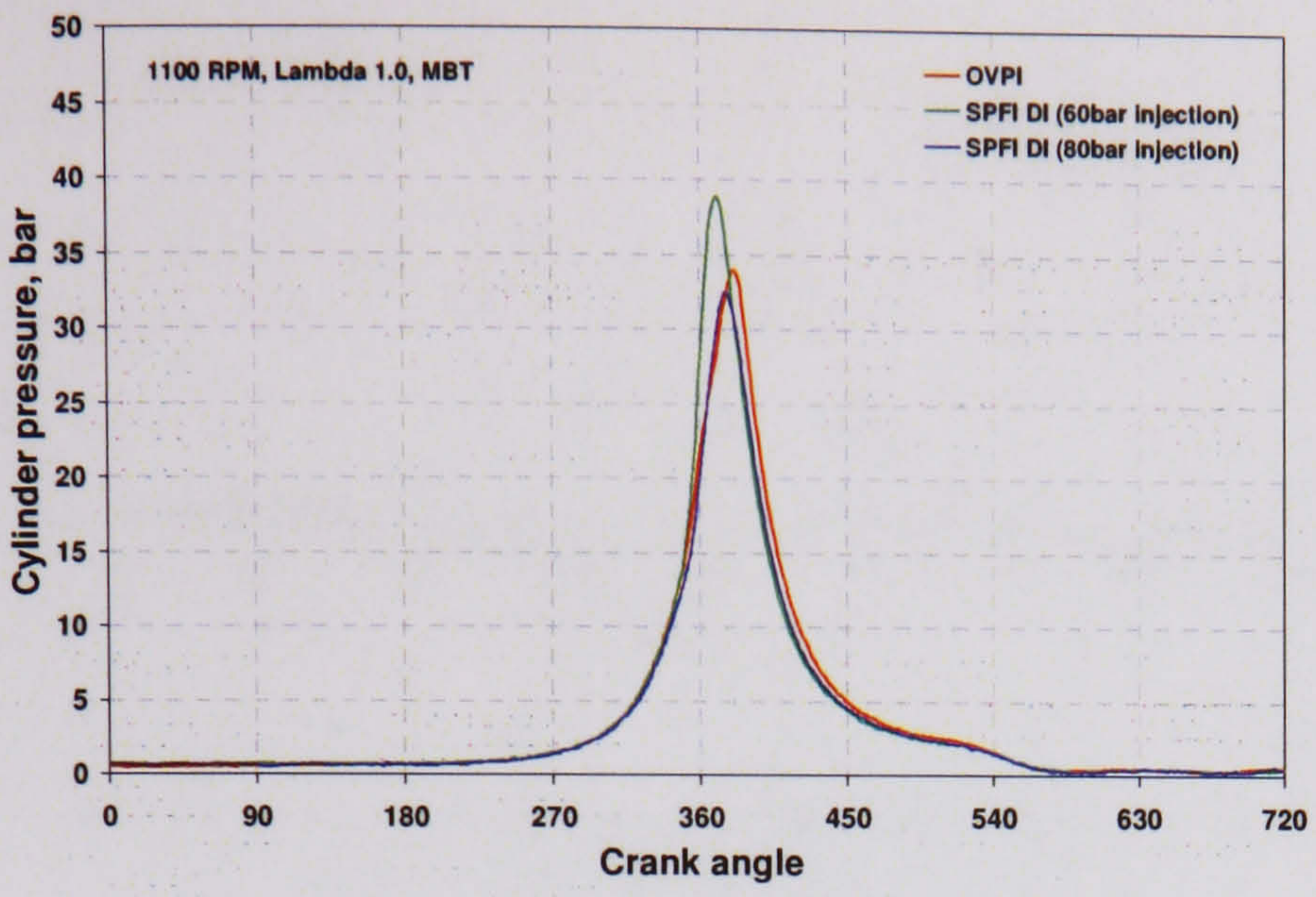

Figure 5.65 Cylinder pressures of OVPI and SPFI DI

Figure 5.66 shows the PV curves of these two methods. The areas enclosed by the upper curves correspond to the amount of work produced and OVPI method results in the highest of area with most indicated work produced.

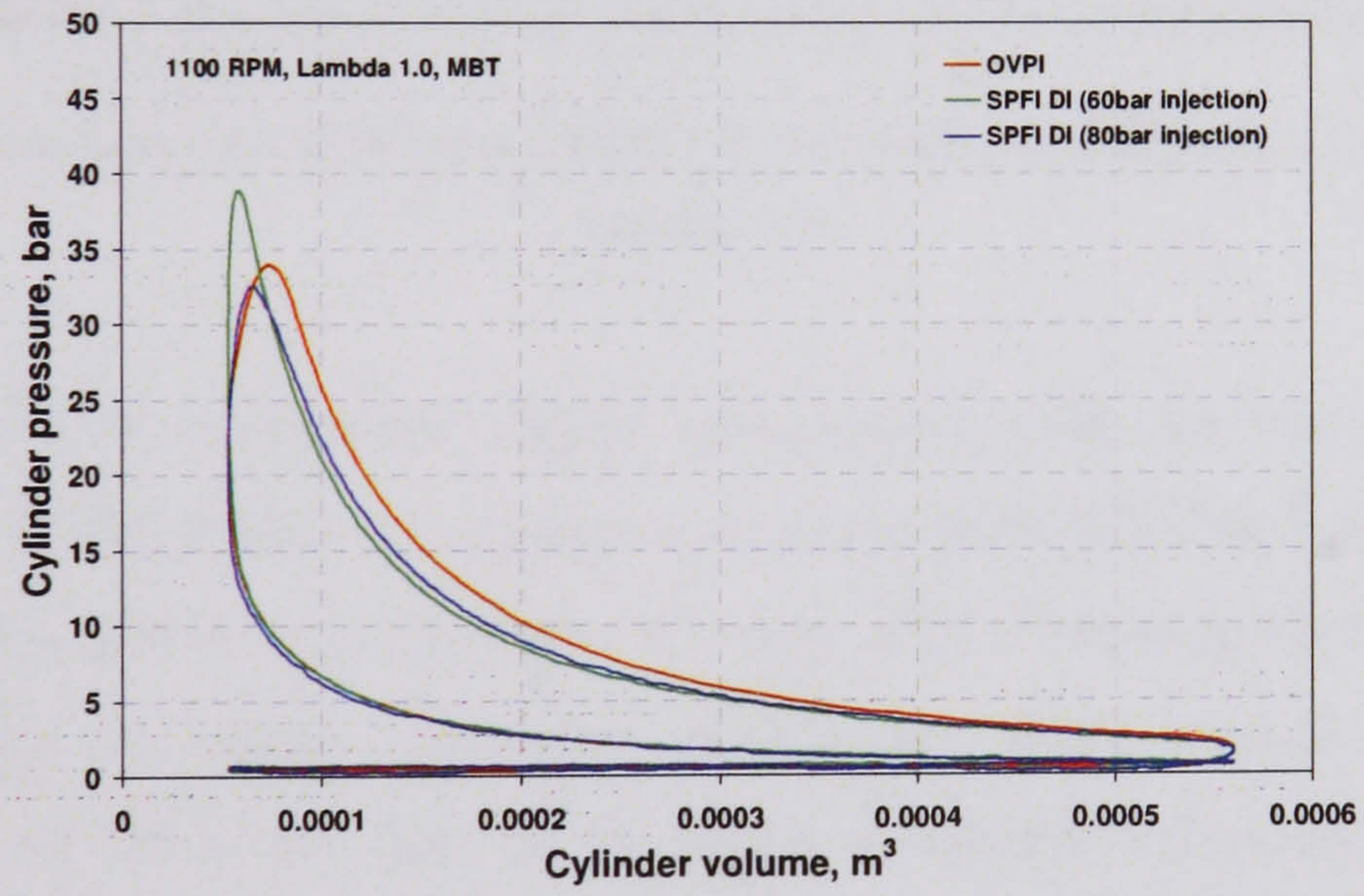

Figure 5.66 PV diagrams of OVPI and SPFI DI

In Figure 5.67, cylinder work are shown. The figure clearly shows that the OVPI produces more effective work than SPFI DI of both injection pressures.

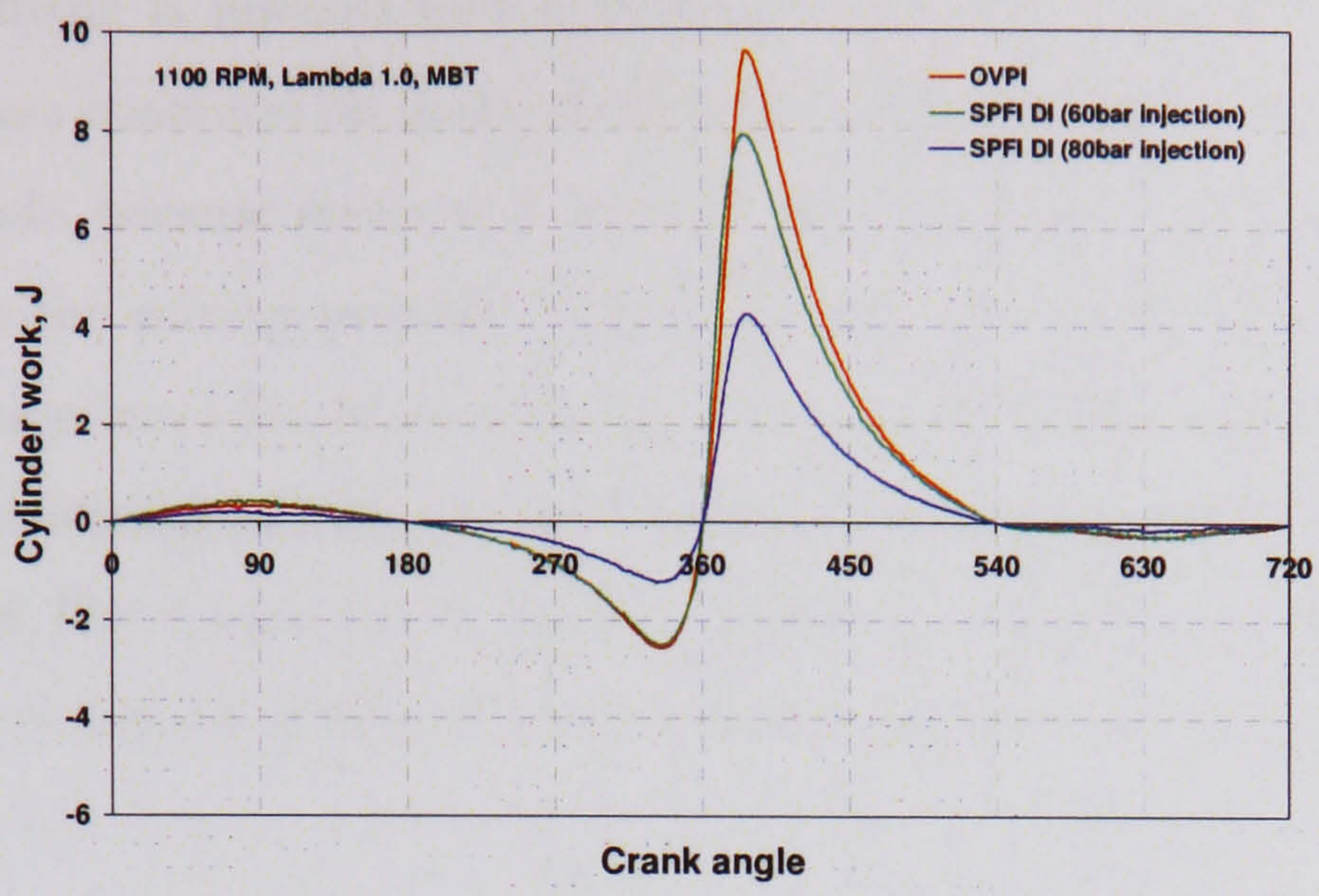

Figure 5.67 Cylinder works of OVPI and SPFI DI

Operation	OPVI	SPFI DI	SPFI DI
Injection pressure, bar	30	60	80
IMEP, bar	6.63	6.20	6.03
$P_{indicated}$, kW	3.04	2.85	2.83
η_v, %	72.35	83.43	79.45
$\eta_{f,\ indicated}$, %	26.94	21.84	22.30
ISFC, g/kWh	267.28	329.67	322.91

Table 5.12 Performance of PI versus SPFI DI with optimum calibration at 1100rpm and lambda 1.0

Table 5.12 summarizes engine performance with the two methods. The IMEP of the OVPI method is superior to the ones SPFI DI. The fuel economy and fuel conversion efficiency are better in the case of PI. However, the DI method has the advantage of higher volumetric efficiencies. Even though the indicated performance of DI is less than of PI, higher volumetric efficiency means greater mass of air and fuel can be induced per cycle which provides a strong basis for engine improvement due to increased inhaled energy.

The most probable explanation for the inferior performance of direct injection at this particular speed is that fuel-air mixing was less complete than in port injection method. Fuel-air mixing depends on many factors including the time and space availability as well as the relative movement of fluids inside the cylinder. In port injection mode, more time and space are available for mixture formation because methane is injected into a flowing air while the intake valve opens and mixing process continues on inside the cylinder before ignition starts. While in direct injection mode, because methane is injected after the intake valve closes, less time is available for the mixing process. Therefore, the main factor affecting the mixing process is the relative fluidic movement, or the turbulent intensity. As shown by the turbulent calculation in Chapter 3, turbulent intensity is directly proportional to engine speed. This means, by the fact that turbulent intensity positively affect mixing process, better fuel-air mixing in direct injection method can be achieved at higher speeds.

5.7.4 Combustion analysis - mass burnt fraction (MBF)

Combustion analyses were undertaken by the determination of the fraction of mass burnt. As described in the previous section, MBF was calculated by normalising the pressure rise due to combustion. It was assumed that the normalised pressure rise is directly proportional to the fraction of mass burnt. Figure 5.68 though Figure 5.78 show the mass burnt fraction of methane port injection and direct injection at various conditions. The graphs were plotted at a range between 330° and 390° where 360° corresponds to the compression TDC.

On each plot, the mass burnt fraction curve increases from 0 to 1 and then reduce to a certain value at the end of the graphs. These were done to indicate that mass burnt fraction was estimated based on the pressure rise due to combustion, which were obtained by subtracting instantaneous motorised cylinder pressure from instantaneous firing cylinder pressure. When there is no more combustion occurs, the pressure rise due to combustion becomes negative, and the MBF curve reduces to less than 1. Even though it is strongly believed that combustion completeness is not achieved, the value 1 for mass burnt fraction is used to simplify the results.

This section starts by separately discussing the effect of injection, ignition, injection pressure, stoichiometry, load condition (DI only), fuel path length (DI only) and speed on the MBF behaviour on the port injection method and the direct injection method. Then the two methods will be compared in terms of MBF and variation in pressure behaviour of consecutive cycles.

Before presenting the results, it is worth looking at the normal behavior of mass burnt fraction. Two main characteristics in the MBF are ignition delay and combustion duration. In this analysis, ignition delay is defined as the lag between ignition and start of combustion, indicated by the initial pressure rise due to combustion in the MBF curves (MBF > 0). Combustion duration, on the other hand, is the duration from ignition start to the point where MBF reach the value 1. The behaviors can be summarized as the followings [Harrison, 2002]:

- Combustion duration is shortest with a spark advance of around 45° BTDC
- Combustion duration increases as spark is retarded
- Combustion duration increases with engine speed
- Maximum burnt rate occurs with 50% point near TDC
- Combustion duration is greatest for part load
- Ignition delay increases with engine speed
- Ignition delay is greatest at part load
- Ignition delay is least if ignition timing is at TDC
- Ignition delay increases as the spark is advanced

The combustion durations for direct injection of natural gas is shorter than those of port injection as reported by Huang [2003] and Hassaneen [1998]. The time between injection and ignition also has strong effect on the combustion behaviour, and subsequently, the engine performance [Zeng, 2006]. However, all these reports were based on combustion chamber with close-to-optimal arrangements of fuel injection and spark plug, which are almost pointing towards each other. The direct injection of natural gas using SPFI has a different orientation of fuel injection and spark ignition where fuel is injected away from the point of ignition. The spray is weakly guided to the spark plug as compression stroke moves towards ignition. As a result, mixture formation and strength of mixture at the vicinity of spark plug electrodes may not be optimized. The following sections will give reflections to these facts.

5.7.4.1 Port injection

In this section, the MBF behaviour with the port injection method is discussed. However, each curve was obtained from pressure data taken on different days with different ambient condition which result in some degree of variation in the same engine setting. Figure 5.68 shows the MBF curve of the OVPI and CVPI at MBT (25° BTDC). Injection timing has significant effect on MBF which can be seen by the shift of combustion starts from 20° BTDC in OVPI to 18° BTDC in CVPI (ignition delay of 5° and 7° respectively). While the combustion durations almost remain the same, the difference of phase angle between the two methods results in the difference in indicated performance.

Figure 5.69 shows MBF at three ignition times near MBT for the OVPI method. The shifts of combustion processes with respect to crank angle are in order with ignition advance. Combustion duration increases and ignition delay decreases as the ignition is retarded. MBT was achieved at 25° BTDC where 50% mass burnt point or the phasing angle is about 7° ATDC.

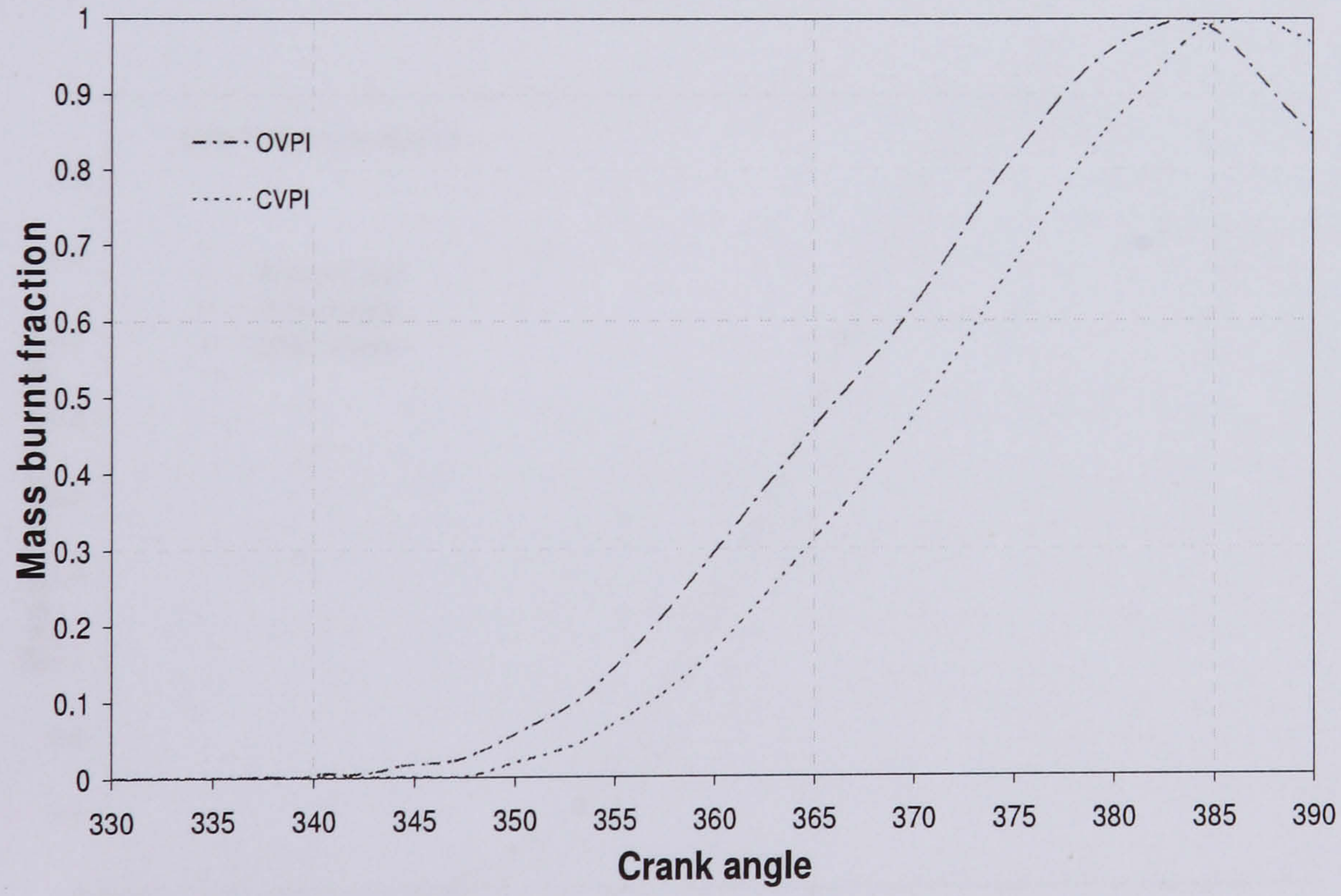

Figure 5.68 Mass burnt fraction for OVPI and CVPI

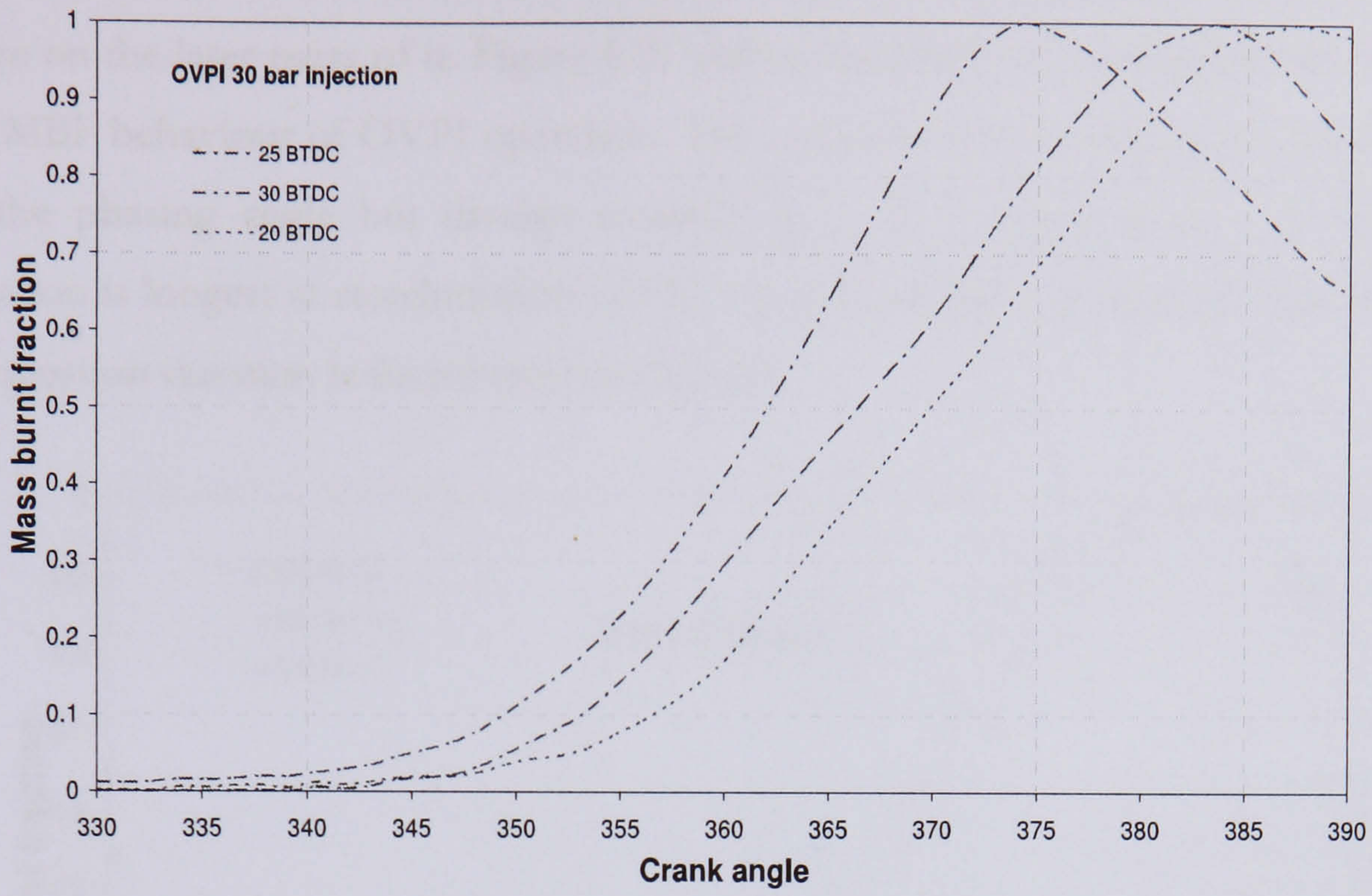

Figure 5.69 Mass burnt fraction for OVPI at various ignition times

In Figure 5.70, the MBF curves of OVPI operation at three different injection pressures are shown. The overall durations of combustion remain mostly unchanged but in the case of 40 bar injection, ignition delay shifts about 3° CA forward.

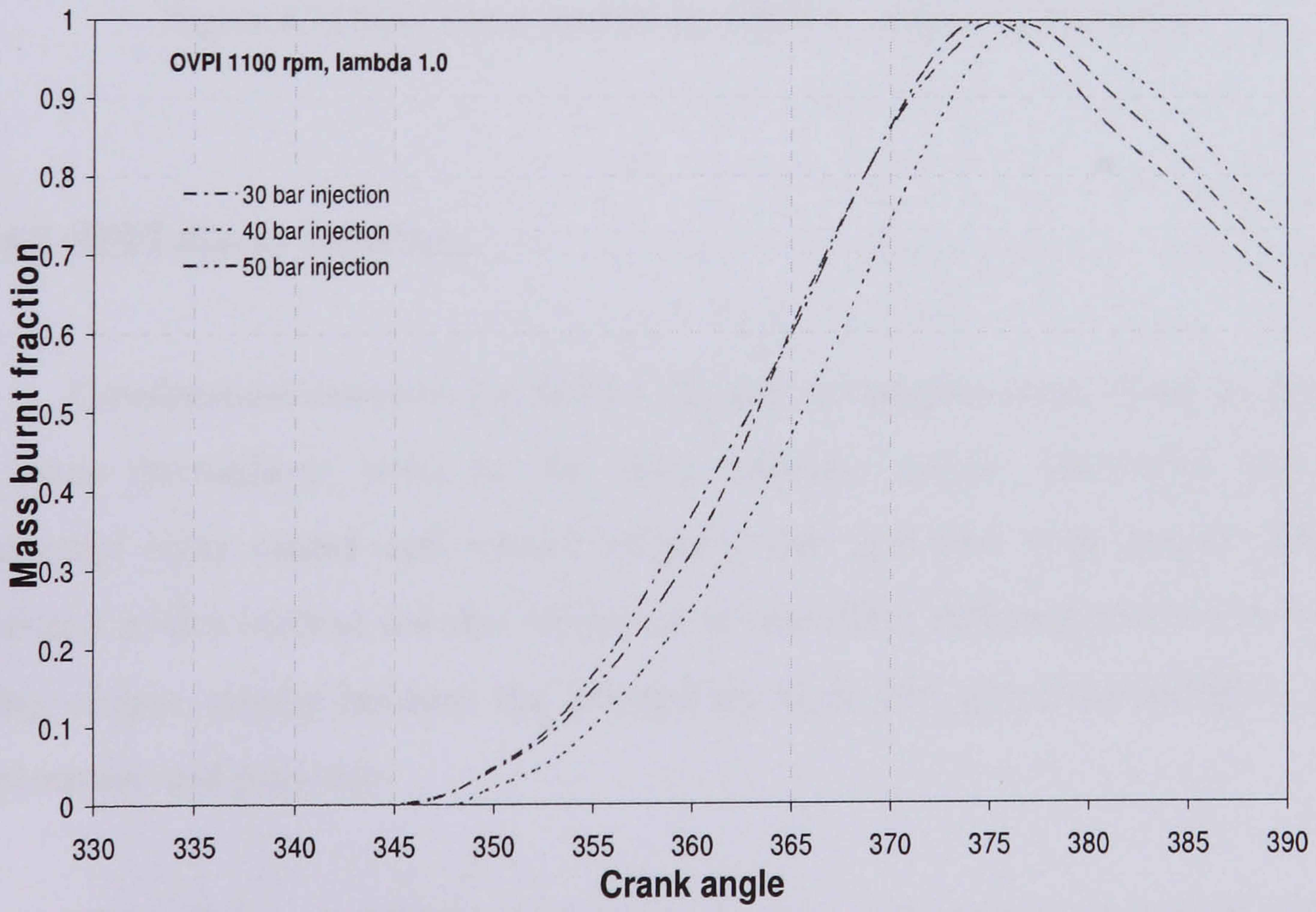

Figure 5.70 Mass burnt fraction for OVPI at various injection pressures

Mixture stoichiometry has little effect on the initial combustion process but more on the later parts of it. Figure 5.71 shows the effect of varying lambda value to the MBF behaviour of OVPI operation. The curves follow almost identical routes up to the phasing angle but diverge towards the end of combustions. Combustion duration is longest at stoichiometric AFR, but ignition delay is shortest. The shortest combustion duration is found with lambda 0.9.

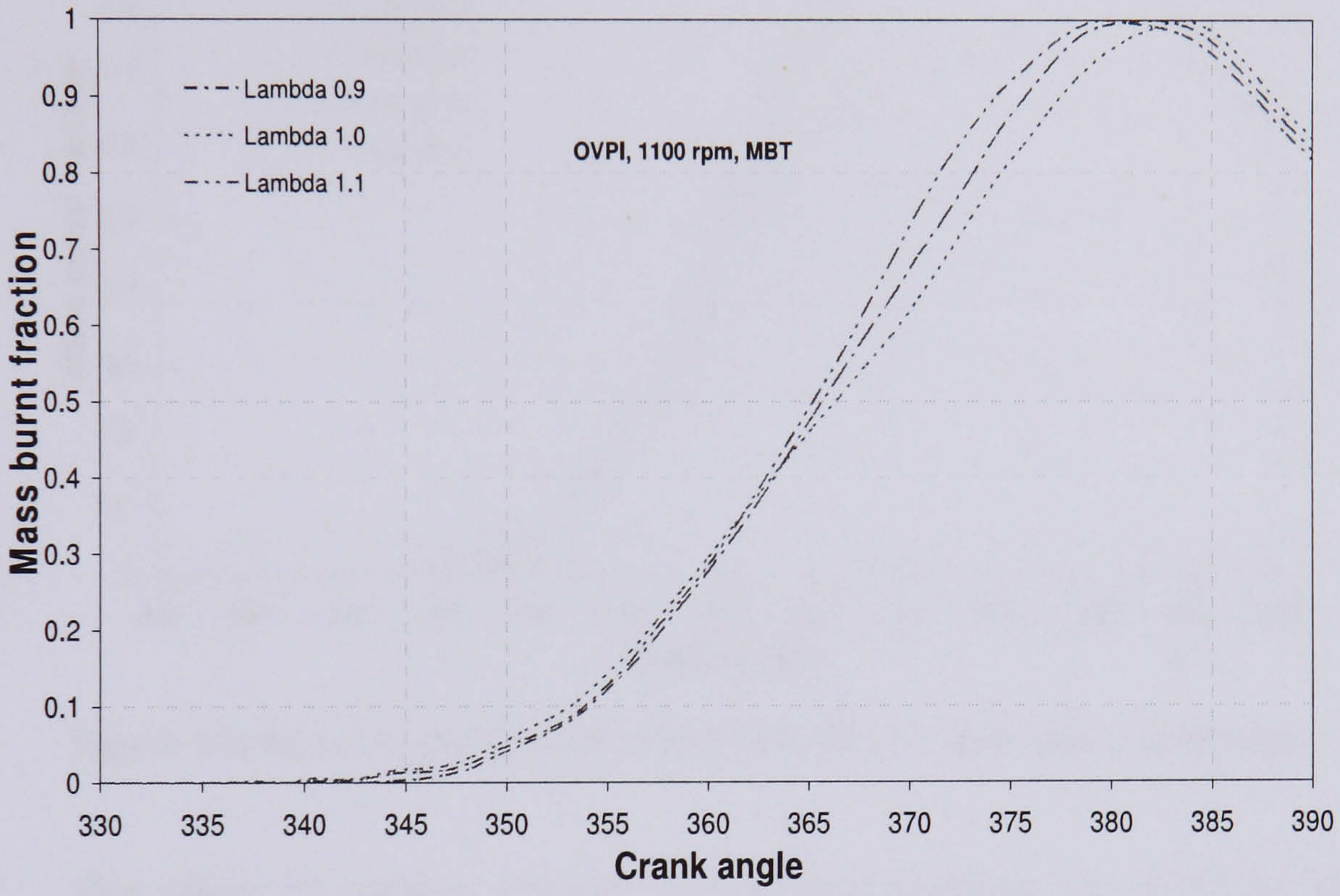

Figure 5.71 Mass burnt fraction for OVPI at various air-fuel ratios

5.7.4.2 SPFI direct injection

Combustion analyses for SPFI CH_4 direct injection were done by repeating the same procedures used in the port injection mode. However, two more parameters were tested and varied; engine loads and fuel path length. The data presented in this section are also subjected to the effect different ambient conditions during engine testing because the inhaled air were not pre-conditioned to certain temperature and pressure.

The effects of different injection timings with respect to crank angle are shown on Figure 5.72. As mentioned earlier, the optimal performance was achieved with injection at 190° ATDC where the MBF curve is the steepest. The combustions at earlier injection show longer combustion periods but shorter ignition delay, and the later injections result in shorter combustion durations and relatively longer ignition delay, which agree with the findings by Huang [2003].

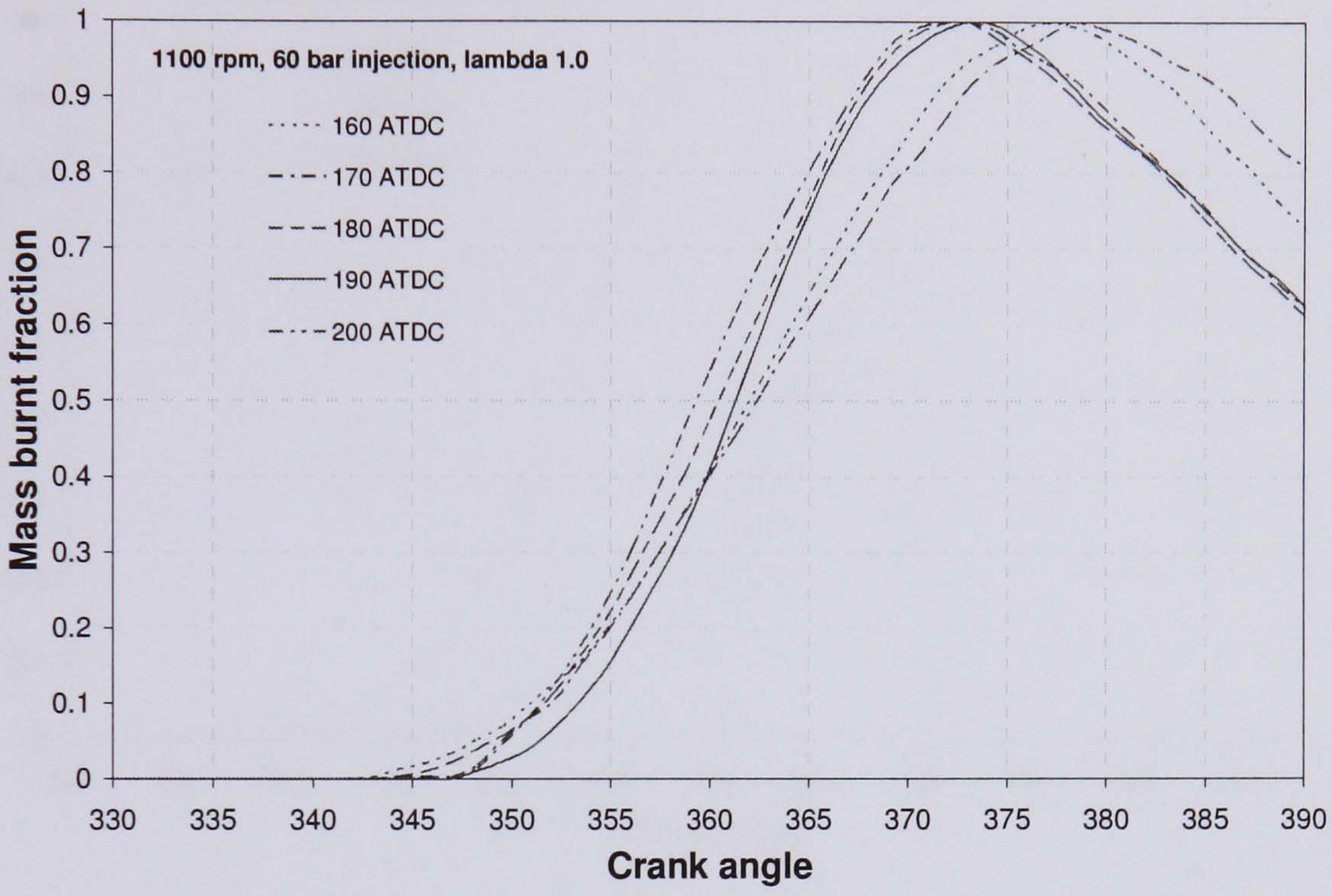

Figure 5.72 Mass burnt fraction for SPFI CH_4 DI at various injection timings

The effect of ignition advance is presented in Figure 5.73. Three ignition advances were selected for this purpose; 20°, 25° and 30° BTDC. The most significant effect of advancing spark ignitions is reduction of combustion duration. MBT performance was achieved at 25° BTDC ignition, and this corresponds to 50% mass burnt or the phasing angle of 2° ATDC. The effect of ignition timing is more significant in the direct injection mode than in port injection. As ignition is retarded, both combustion duration and ignition delay increase. The combustion duration patterns follow the normal combustion behavior but the ignition delay do not. It is expected that ignition delay is increased as spark is advanced [Harrison, 2002]

The effects of injection pressure on SPFI CH_4 DI MBF are shown in Figure 5.74. Injection pressure has significant effect on the combustion behaviour. The ignition delays are well distinguished with 60 bar injection yielding the shortest delay and 50 bar results in the longest. The ignition time for all injection pressures is 25°BTDC (345° CA on the graph). Combustion duration remain the same for all injection pressures, but the 80 bar injection shows faster early burning stage and slower later stage. At this particular operational set up, the 60 bar injection yields best performance which was discussed in section 5.7.2.2.

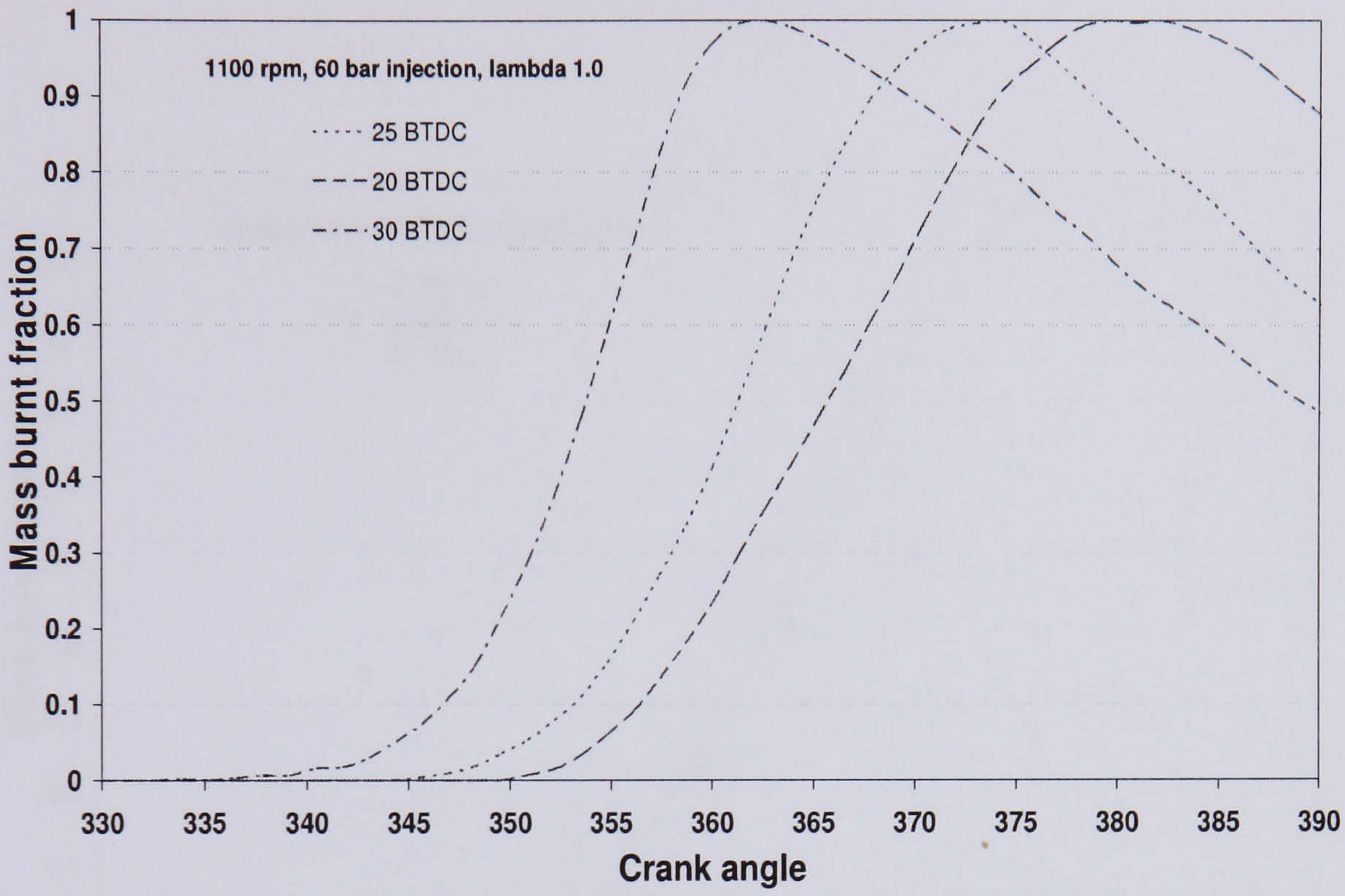

Figure 5.73 Mass burnt fraction for DI at various ignition times

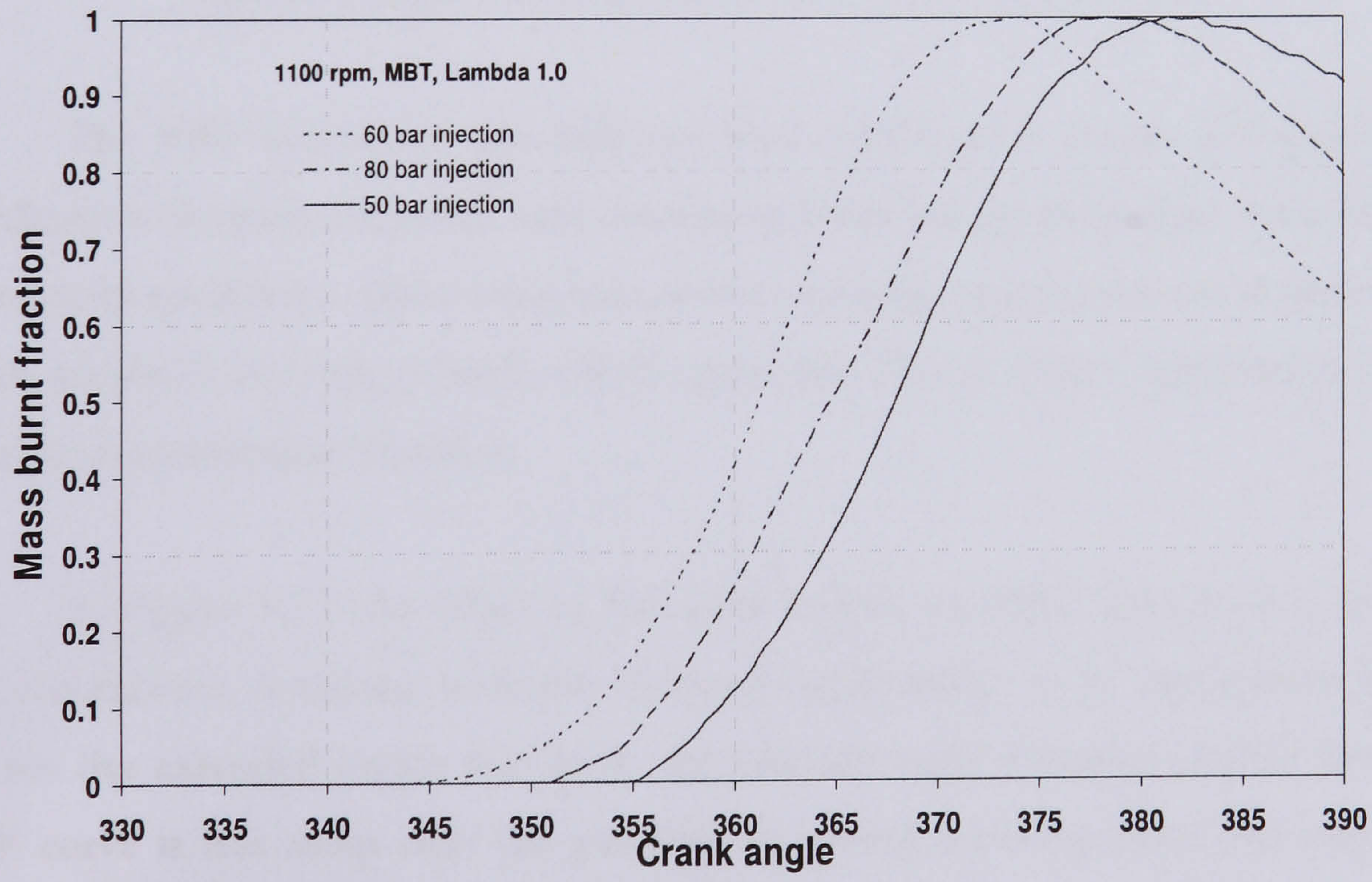

Figure 5.74 Mass burnt fraction for DI at various injection pressures

The effect of mixture stoichiometry is shown in Figure 5.75. At lambda 1.1, combustion duration is the longest, and it decreases as mixtures get richer. However, ignition delay trend indicates inconsistency with lambda values showing values of 10°, 15° and 18° CA for lambda 1.1, 0.9 and 1.0 respectively.

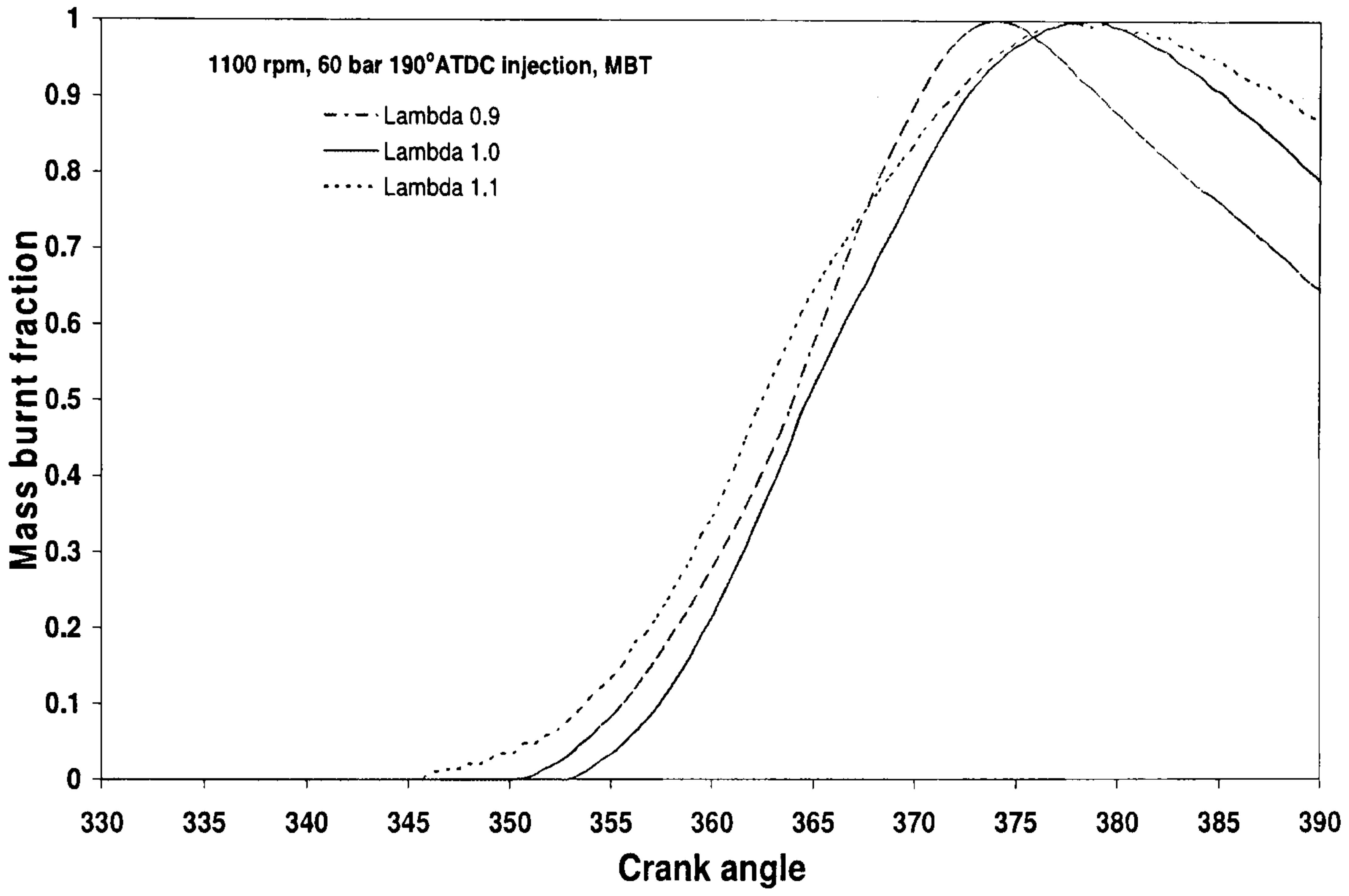

Figure 5.75 Mass burnt fraction for DI at various air-fuel ratios

The MBF behaviour with different load conditions is shown in Figure 5.76. Combustion duration increases with decreasing loads but ignition delay is shortest at lowest load conditions. Decreasing load means reducing charge amount in each cycle which results in lowering overall cylinder pressure. This in return contributes to the increase in combustion duration.

In Figure 5.77, the effect of fuel path lengths on MBF behaviour is shown. The combustion durations were not changed significantly, so as the ignition delay, but for the extended length fuel path, the phasing angle happened earlier and the MBF curve is less steep after the combustion period resulting from fuel existence due to its delayed arrival in combustion chamber.

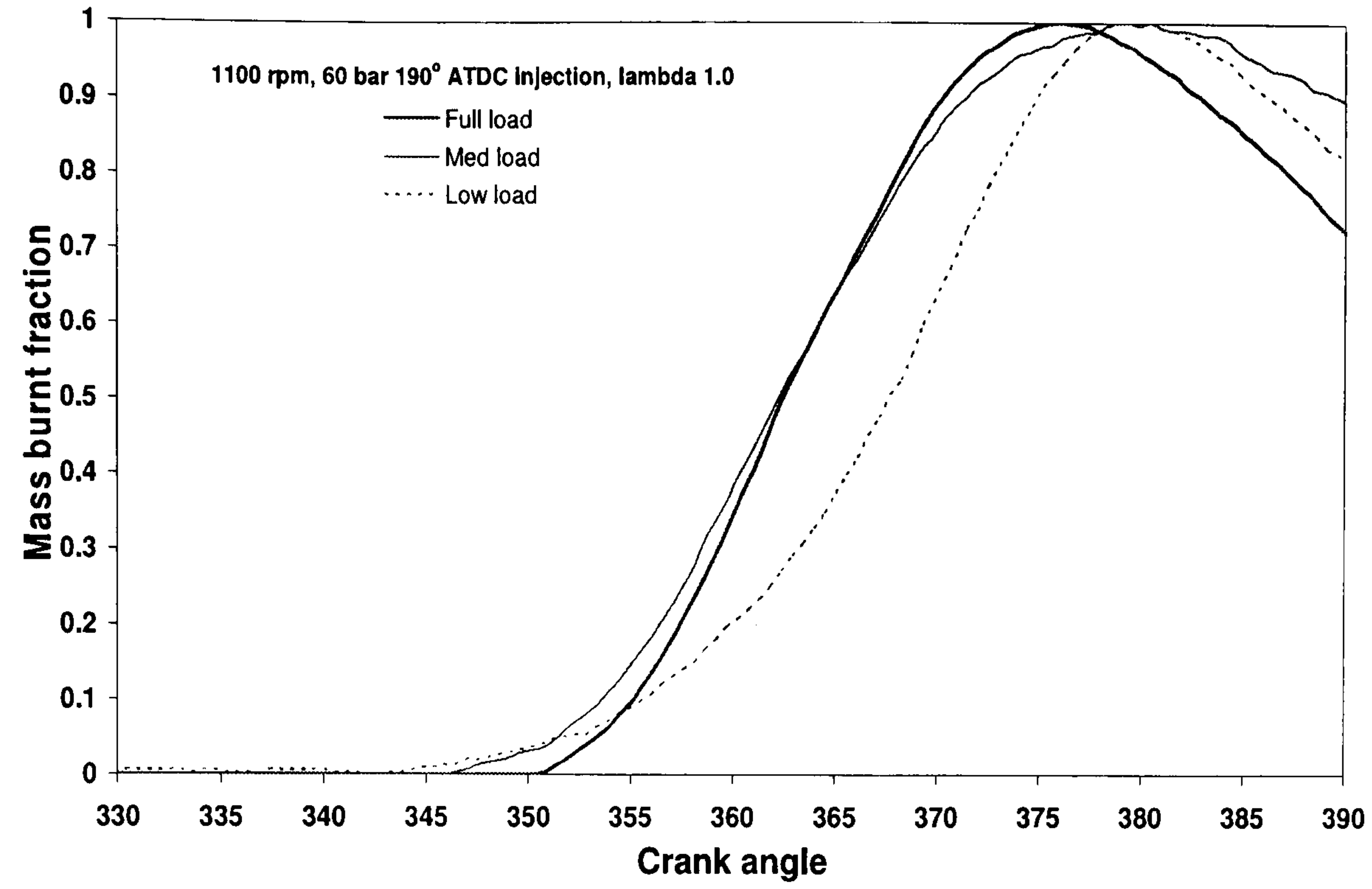

Figure 5.76 Mass burnt fraction for DI at various engine loads

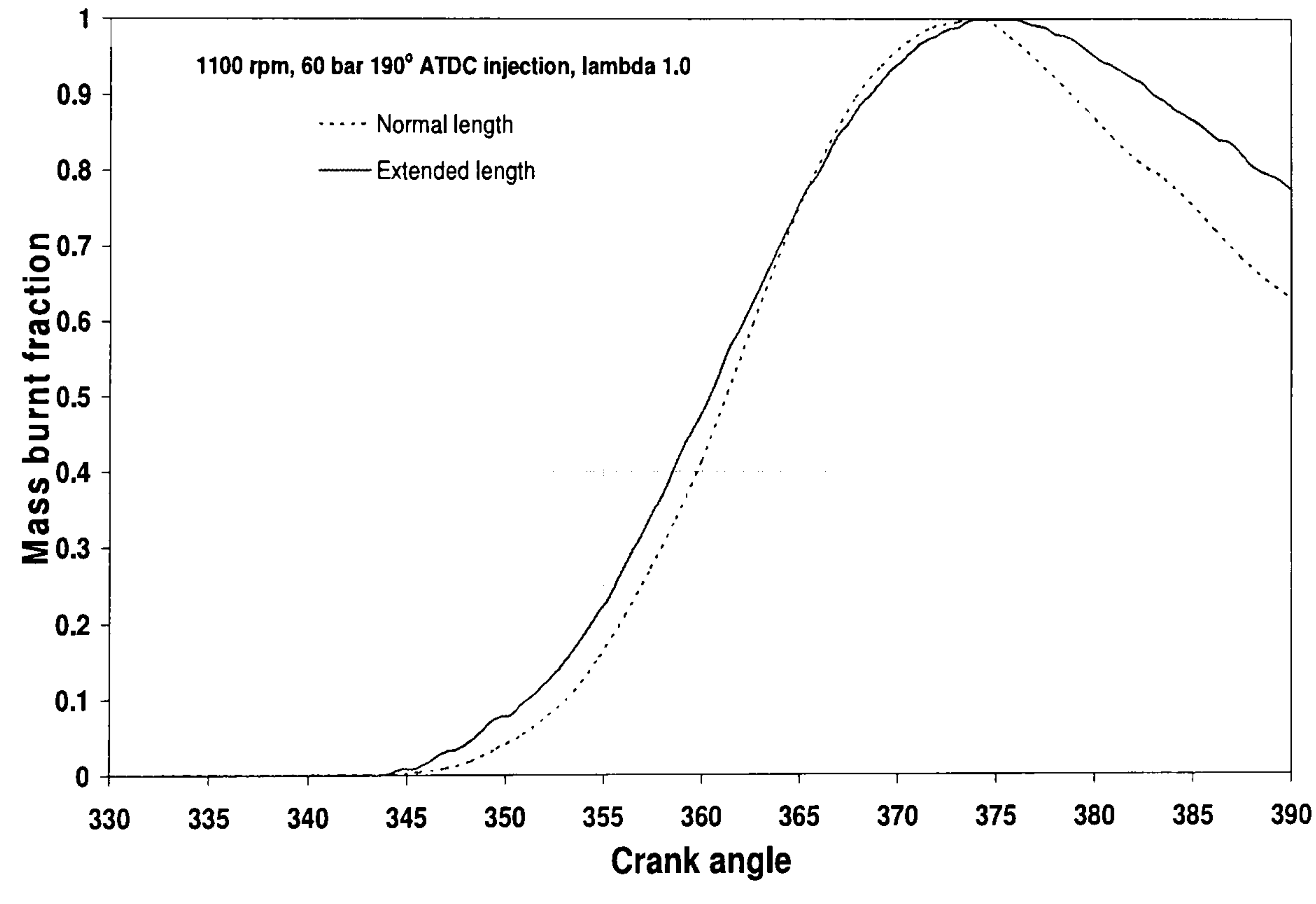

Figure 5.77 Mass burnt fraction for DI without and with fuel path extension

5.7.4.3 Port injection vs. direct injection methods

In this section, comparison of the combustion characteristics between the optimal settings of port injection and SPFI direct injection are presented in the form of MBF and cycle-to-cycle pressure variation. Figure 5.78 shows the MBF behaviours of the two methods. The first observation is that the ignition delay is shorter in the case of port injection compared to direct injection. However, the combustion duration in DI method is significantly shorter. The 50% mass burnt fraction or the phasing angle correspond to 2° and 7° ATDC for direct injection and port injection respectively. In the direct injection mode, a greater amount of cylinder charge causes higher pre-combustion pressure, thus sped up the combustion process. The difference in ignition delays on the other hand is due to the longer time taken to develop initial flame kernel in the more dense charge if direct injection.

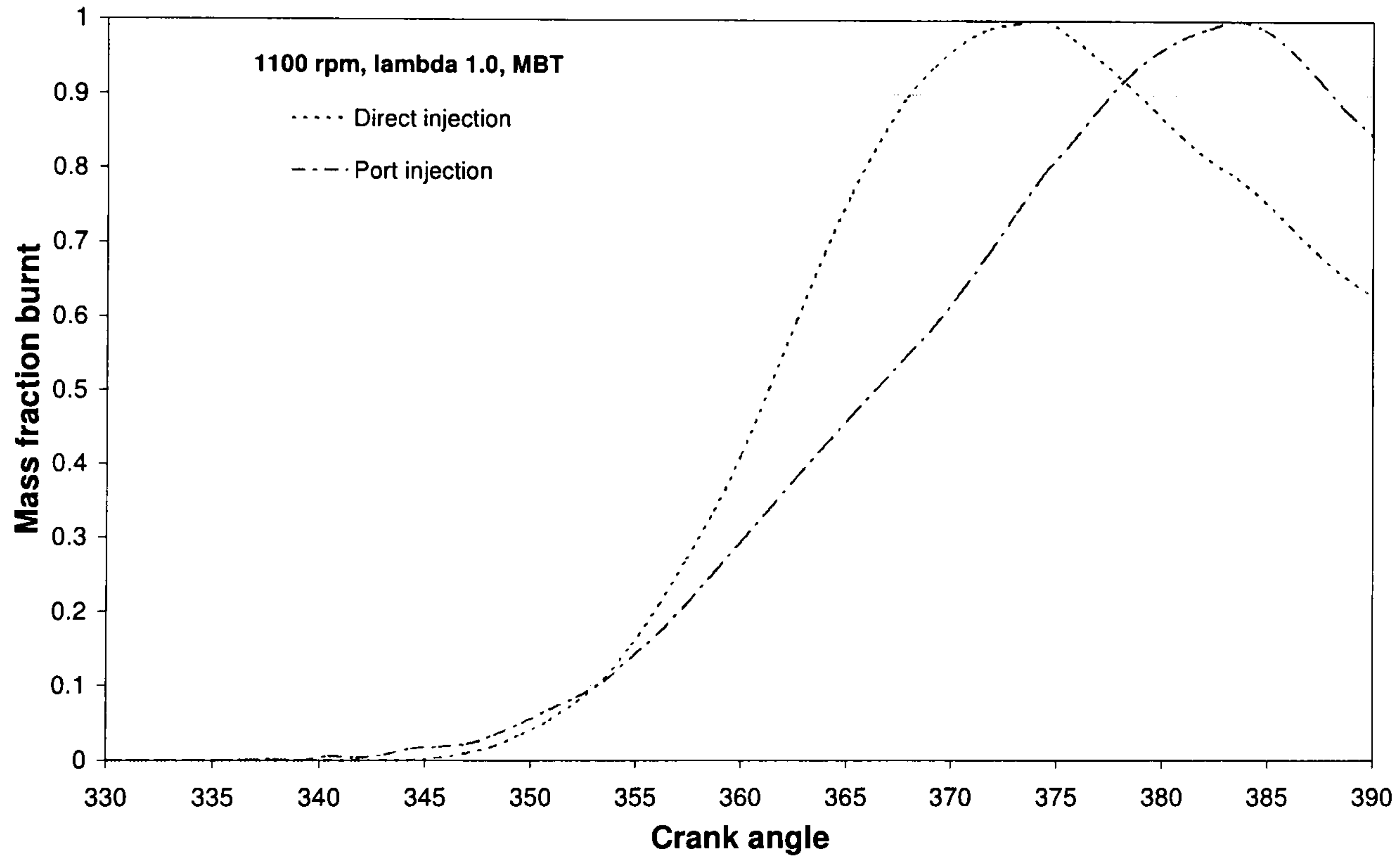

Figure 5.78 Mass burnt fractions of methane port injection and SPFI direct injection

Figure 5.79 and 5.80 show the cycle-to-cycle variation in cylinder pressures for port injection and direct injection modes respectively. The engine was run at 1100 rev/min, wide open throttle, stoichiometric AFR and spark advanced for MBT. At this optimal operational setup, two main differences can be observed. First is that the peak firing pressures in direct injection mode are higher than the ones in port injection mode. The second is the locations of peak pressures where the direct injection method results in the earlier peak pressure (~10° ATDC) compared to the port injection (~18° ATDC). The first observation was due to the fact that charge density is higher in the direct injection mode, thus the absolute heating value increases. This results in more intense combustions for the same cylinder capacity and engine speed. The second observation was due to the more rapid combustion process in the direct injection method. However, these do not give direct injection method much advantage in terms of its performance because the main measure for better output is the optimal offset between positive work and negative work measured from cylinder pressure behaviour. The offset can be described as the ratio of positive work to the negative work as shown in the cylinder work vs. crank angle curves in Figure 5.67. In this regard, the pressure curves in port injection method show a higher fraction of positive work compared to ones of direct injection method.

Another important observation from these figures is the variation in cylinder pressures from five consecutive cycles. Even though variations in both methods were not significant in magnitude, a more uniform peak pressures are observed in the direct injection combustion.

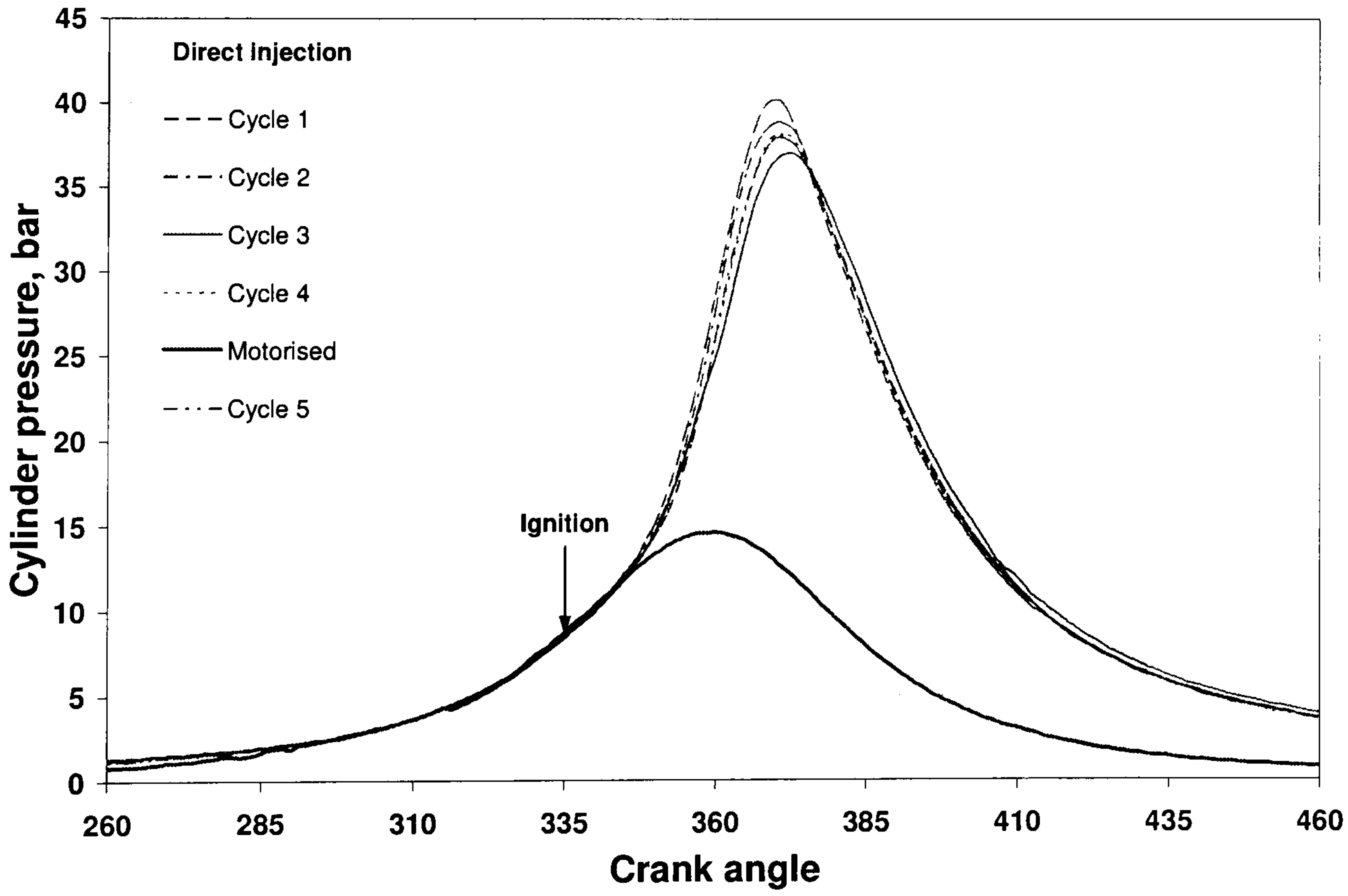

Figure 5.79 Cylinder pressures of SPFI methane direct injection for five consecutive cycles

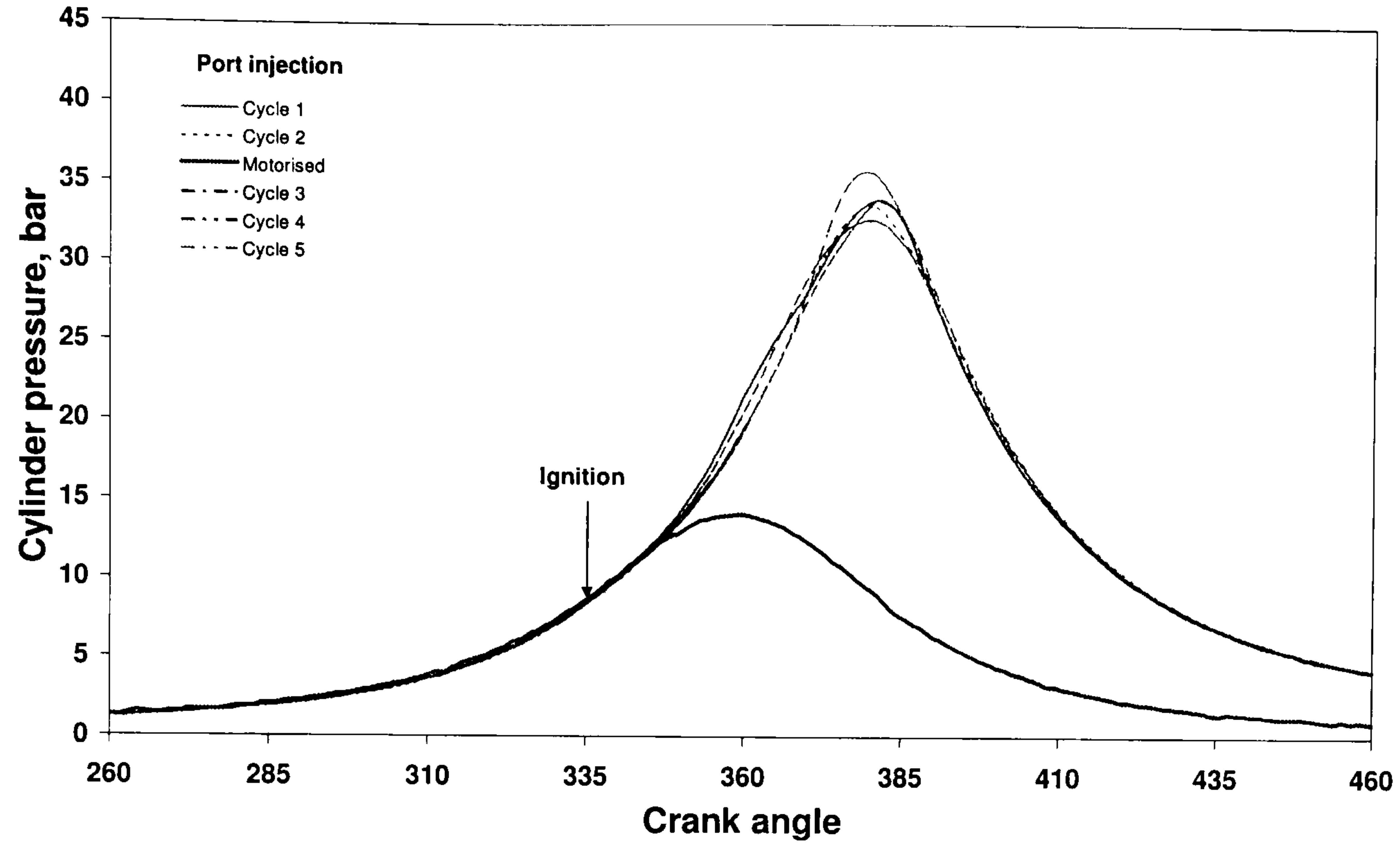

Figure 5.80 Cylinder pressures of methane port injection for five consecutive cycles

5.8 DISCUSSION

Data for both port injection and direct injection have been presented. The effects of changing operational and physical parameters have been described and followed by causing factors where applicable. When comparing the performance of port injection with SPFI direct injection, the improvement through direct injection method expected from the simulation results in Chapter 3 was not achieved. The factors that contribute to the suppression of the potential improvement by direct injection method must be discovered. This can be done by analysing the behaviour of SPFI CH_4 DI in Ricardo E6 engine that can lead to formulation of appropriate improvement measures.

5.8.1 Compression ratio and air fuel mixing

One reason for lower DI performance was due to the fact that the SPFI design, particularly the fuel path volume has caused reduction in actual compression ratio from 10.5:1 to 10.07:1, which was described in Chapter 4. It is a known fact that thermal efficiency and indicated performance are directly proportional to compression ratio. Thermal efficiency, η_{th} and compression ratio, CR is related by the following equation, where γ is the specific heat ratio of the related gas. From this equation alone, the expected reduction of thermal efficiency is calculated to be in the order of 0.7%.

$$\eta_{th} = 1 - \frac{1}{CR^{\gamma-1}} \qquad \text{(Equation 5.19)}$$

Another reason for the disadvantage of SPFI DI performance over PI performance was suspected to be due to poor air-fuel mixing in SPFI DI. In the PI method, air and fuel were premixed before entering the combustion chamber. The optimal performance was achieved with open valve operation because methane was injected into a flowing air, after some amount of air has already induced, giving the premixing process more effectiveness. In the case of closed valve injection where methane was injected while the inlet valve was still closed, methane will be the majority part of mixture to first enter the combustion chamber followed by the bulk of air behind it. This means most part of mixing process happened inside the combustion chamber. In the open valve port injection, as the mixing process continued within the cylinder, shorter time was required for a more complete mixing. The overall available mixing time for PI method was relatively longer than in the DI method.

Because the mixing process has more time and space, the combustion chamber shape has less effect on the mixing process of the PI method. This was not the case with the DI method where air-fuel mixing only happened after fuel arrival inside combustion chamber. The SPFI design has caused delay in fuel arrival and total duration of fuel delivery, which further shorten the available mixing time prior to spark ignition. Ideally, the cylinder shape should assist the mixing process in the direct injection method but because in this project, a disk-shaped cylinder was used, this mixing enhancing cylinder geometry was not available.

Another factor for poor mixing is due to the location of fuel injection nozzle as shown in Figure 5.9. During injection process, methane is sprayed out of and away from the spark plug. With the swirl and tumble air motion from the opposing inlet valve, the mixing charge would be swept away from and then return to the ignition point. In the typical direct injection engine, fuel injector and spark plug almost point to each other and the fuel spray is guided by cylinder geometry towards ignition point as soon as injection occurs. SPFI design contradicts this practice by spraying methane away from the ignition point, and spray was not guided back to the spark plug. It was concluded that due to the shape and orientation of the intake manifold, during the last part of intake stroke and the initial part of compression stroke where fuel injection takes place, intake air and the partially mixed charge was swirled and tumbled away from the spark ignition location. Since the time between fuel injection and ignition was relatively short, at the time and vicinity of ignition, it seems probable that proper mixing has not completed yet.

5.8.2 Effect of injection timing

Injection timing with respect to crank angle is one of the most important parameters in the SPFI direct injection method because it determines volumetric efficiency and it affects the mixing process. For 60 bar injection pressure, the best injection timing was at 190° ATDC which yield the highest IMEP and thermal efficiency as in Figure 5.80. However, when injection pressure was increased to 80 bar, the best injection timing was shifted to an earlier timing of 145° ATDC, but the highest IMEP at this injection pressure were less than the ones in 60 bar injection. The trend of performance curves show that at higher injection pressure, variation of injection timing has less effect on the performance. Figure 5.80 also suggest that more mixture stoichiometry control was obtained at higher injection pressure because combustion at lambda 1.0 was achieved at crank angle earlier than 160° ATDC which was the limit for 60 bar injection.

With the 80 bar injection pressure, methane travels further with more momentum than the 60 bar injection. The injection duration is relatively shorter and initial methane volume occupies less space in the cylinder. Therefore, more air can be induced even when injection happens earlier than in the case of 60 bar injection pressure. Thus the mixing process is better over a wider range of injection timing.

The difference of maximum IMEP shown in Figure 5.81 however, is believed to be due to the relative in-cylinder fluid movement which causes difference mixture stratification or local stoichiometric value.

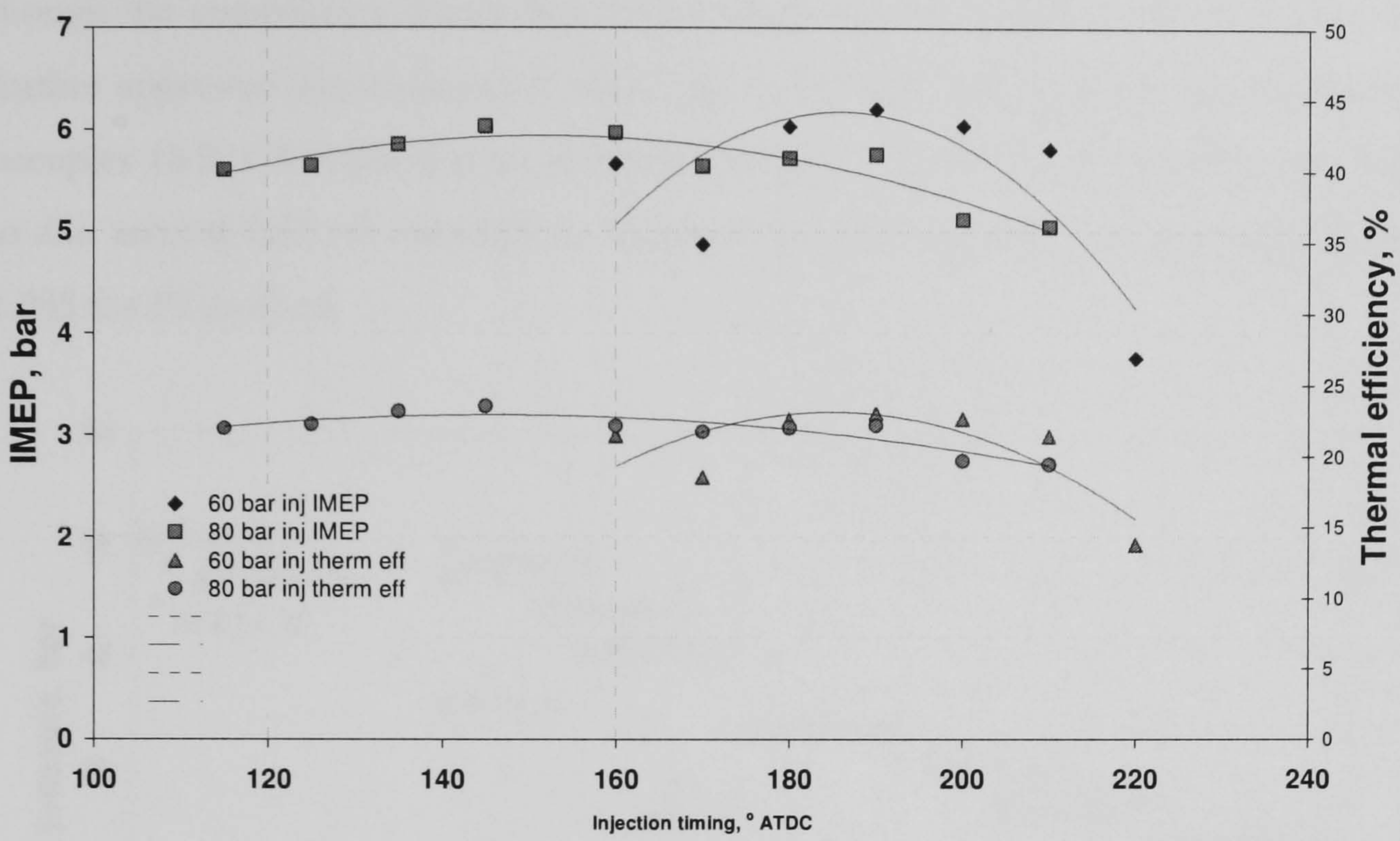

Figure 5.81 Effect of fuel injection timing on SPFI CH_4 DI performance

5.8.3 Effect of ignition advance

It was observed that spark advance for MBT in majority part of the experiment were barely unchanged. The values range near 25° BTDC for all speeds, mixture stoichiometries, engine loads, injection pressures, and fuel path lengths in direct injection method. For the DI method, spark advance of 25° ATDC resulted in peak pressure around 10° ATDC while in the PI method, the same spark advance resulted in peak pressure at the vicinity of 18° ATDC. This was mainly due to the difference in combustion duration between the two methods. Figure 5.82 shows the values and locations of peak pressures corresponding to spark advances. Even though the locations of peak pressures to obtain best torque differ by 10° CA, the reason for better IMEP by PI method was due to the combustion characteristics which combine the value of peak pressure and the timing at which it is achieved. Typical timing of peak pressure for best torque happening between 15-20° BTDC was achieved by the PI method. For the DI method, to achieve peak pressure at the above-mentioned range, the spark must be retarded and this has the consequence of reduced peak pressure. Furthermore, when spark was retarded to 15° BTDC, the peak pressure occurred at an earlier crank angle. It can be concluded that this happened because the earlier part of direct injection is slower that later part even though the combustion duration is shorter than the one of PI method. Figure 5.74 further approved this conclusion, which shows the first half of combustion duration occupies 16.5° CA while the second half occupies 12° CA. The ratio of the first half to the second half of combustion duration for DI method is 1.375 compared to 1.285 for PI method.

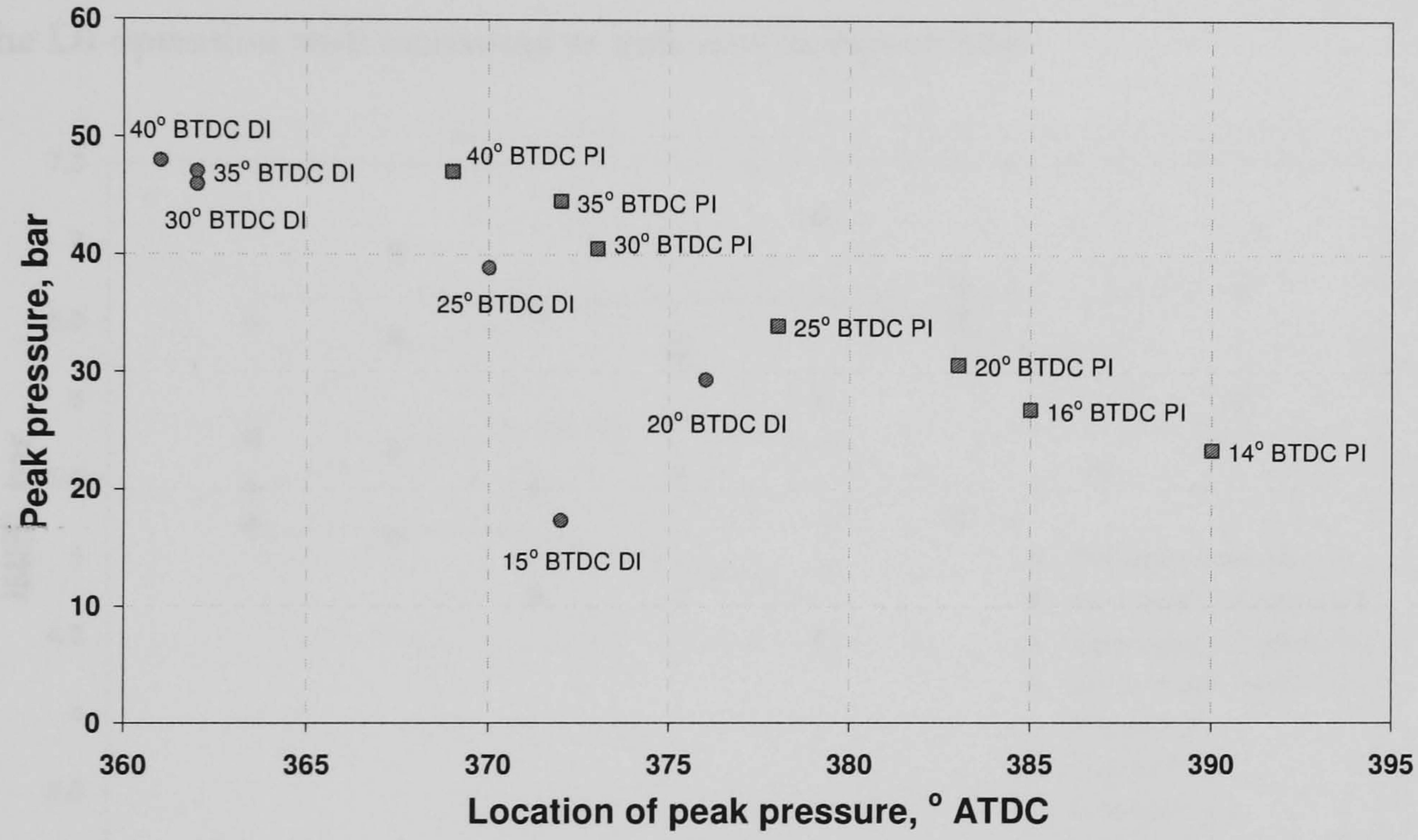

Figure 5.82 Optimum peak cylinder pressure timing for SPFI CH_4 DI and OVPI

5.8.4 Effect of injection pressure

Injection pressure variation has little effect on the port injection method but very significant consequence in the direct injection method. This is due to the fluid motion and mixing process it induces in the cylinder. In Figure 5.81, at injection pressure of 80 bar, a more stable engine performance was achieved over a wider range of injection timings compared to the 60 bar injection. For the same fuel injection nozzle, higher injection pressure requires less injection time, but produces higher jet velocity and longer jet penetration which is the key factor for enhancing air-fuel mixing. However, for each injection pressure, a proper adjustment to injection timing must be made for achieving optimal output. This can be concluded due to different in-cylinder flow induced by each injection pressure which can be studied by flow visualization as shown in Chapter 6.

5.8.5 Effect of speed

Increasing speed causes adverse effect on the performance of SPFI direct injection which was mainly due to the problem with fuel arrival delay into combustion chamber. The operation of PI methane shows more consistency than the DI operation with increasing as indicated in Figure 5.83.

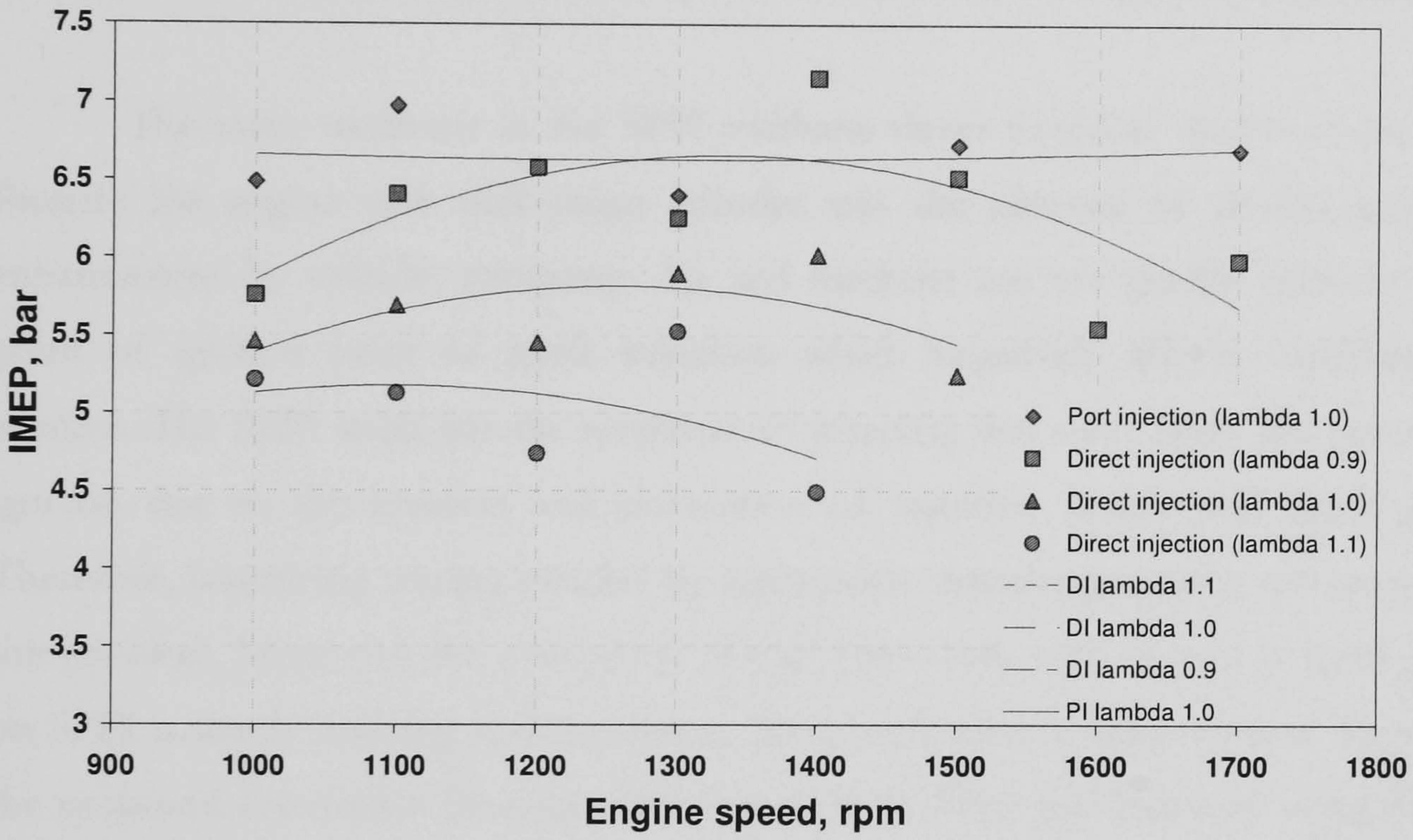

Figure 5.83 Effect of engine speeds on IMEP for OVPI and SPFI CH_4 DI.

For the speed range between 1000 and 1700 rev/min, the PI operation maintains its IMEP almost at constant values. In the DI operation, IMEP increases with speed up to 1300 rev/min but reduces at higher speed. The main reason for this is because at certain injection pressure, the fuel arrival delay time into the combustion chamber was offset by the reduction of mixing time with increasing engine speed. Therefore, in order to maintain engine performance, proper adjustment of fuel injection pressure and/or timing of fuel injection must be made at each speed.

5.8.6 Effect of fuel path length

Another main factor that has significant effect on the performance of SPFI direct injection is the fuel path length because it determines the degree of fuel arrival delay. The longer the pipe, the more time it takes for methane to arrive in the combustion chamber. Moreover, the longer the fuel path, the more pressure is lost at the SPFI injection nozzle. By increasing injection pressure, the negative effects of fuel path length can be reduced. This was shown in the fuel delay measurement described in Chapter 4 on the development of SPFI where delay time of fuel arrival to combustion chamber was shorten exponentially with increasing injection pressure.

The main weakness in the SPFI methane direct injection operation on the Ricardo E6 engine with disk-shape cylinder was the absence of air-fuel mixing enhancement by cylinder geometry. Air and methane are not guided towards the point of ignition prior to spark initiation which negatively affects combustion process. The SPFI itself has the weakness of injecting fuel away from the point of ignition due to the location and orientation of injection nozzle and spark gap. Therefore, improving mixing process by appropriate cylinder geometry can mitigate this problem. Moreover, the orientation of injection nozzle with respect to spark gap on SPFI is worth studying and improving. Thus performance improvement through the proposed conversion from gasoline operation to direct fuel injection using SPFI can be accomplished.

All the contributing factors in the operation of SPFI methane direct injection suggested that engine performance is significantly sensitive to the change of the operational parameters of the engine and the physical parameter of the SPFI. These call for the need to understand, develop and optimised a more detailed engine mapping in order to closely match SPFI operating parameters with each engine operating conditions. In addition, a more effective and optimised design of fuel path within the SPFI must be undertaken to reduce the dependence and sensitivity of SPFI to the operational parameters.

5.8.7 Consideration for gasoline-to-methane conversion

The attraction of methane as gasoline replacement in spark ignition engine is due to its cleaner emissions and cheaper price. Most natural gas (i.e. methane) conversion engines work by incorporating a natural gas fuel system with the gasoline system. In the port injection operation, fuel is injected in the intake manifold. Injecting natural gas causes air displacement and consequently reduced charge energy and output power. The main aim of developing SPFI system is to enable conversion of gasoline operation to methane direct injection in any engine. By doing so, the problems of displaced air in intake manifold and lower performance due to liquid-to-gaseous fuel conversion in port injection engine can be reduced. The comparison of engine performance can be seen in Table 5.13 based on results from this work and the work done by Simms [1994] with the very same Ricardo E6 engine. In his work however, Simms ran the engine with gasoline (carburettor) and natural gas (mixing chamber) at compression ratio of10:1 which is slightly lower than and an advantage to the ratio of 10.5:1 used in this project.

Operation	**Gasoline Carburettor [Simms, 1994]**	**Natural gas Gas mixer [Simms, 1994]**	**Methane port injection**	**Methane SPFI DI**
MEP, bar	7.60_b	5.52_b	6.63_i	6.20_i
η_v, %	88	82.5	72.35	83.43
$\eta_{f,\ indicated}$, %	24.8	21.3	26.94	21.84
SFC, g/kWh	344_b	340_b	267.28_i	329.67_i

Table 5.13 Engine performance of gasoline and natural gas/methane operations (subscript i and b are indicated and brake data respectively)

This table however shows that for the same engine cylinder geometry, using methane as gasoline replacement has great potential for retaining fuel conversion efficiency and lowering specific fuel consumption. In addition, the volumetric efficiency was regained with direct injection method.

A typical gasoline engine has fuel conversion efficiency of probably 28-30% at 1100 rpm. With this engine, carburetted gasoline fuel efficiency was around 25%. Methane efficiency ranges between 21% and 26%. Considering the best range of gasoline engine with 32% efficiency, converting to methane causes engine to be 6-11% less efficient. However, from the emissions point of view, burning a unit mass of methane releases ~11% less CO_2 than a unit mass of gasoline as shown in the correlation below. This gives a good balance of advantage and loss when considering methane as gasoline replacement in IC engines.

Methane combustion

$$CH_4 + 2O_2 \rightarrow CO_2 + 2H_2O$$

$$16 \text{ gram } CH_4 \rightarrow 44 \text{ gram } CO_2$$

$$1 \text{ gram } CH_4 \rightarrow 2.75 \text{ gram } CO_2$$

Gasoline combustion

$$C_7H_{17} + 11.75O_2 \rightarrow 7CO_2 + 8.5H_2O$$

$$101 \text{ gram } C_7H_{17} \rightarrow 308 \text{ gram } CO_2$$

$$1 \text{ gram } C_7H_{17} \rightarrow 3.05 \text{ gram } CO_2$$

$$((3.05 - 2.75)/2.75) \times 100\% = 10.89\%$$

It is important to note that the consideration for methane/natural gas utilization as conventional fuel replacement is not only for the power requirement, but more importantly the environmental and economic ones. Even though the engine output was less than those of port injection, direct injection improves the volumetric efficiency, thus absolute mixture heating value. This gives the basis for engine power increase per cycle if the air-fuel mixing is improved. The advantage of SPFI methane direct injection can be discussed in three main aspects; technological, economics and environmental

Technological

If direct conversion from gasoline port injection or carburetion spark ignition engine to natural gas direct injection is considered, the SPFI design is probably one of the easiest and the cheapest options. Most kits for natural gas conversion turns an engine into a bi-fuel operation, where a fuel selector determines the fuel usage, either gasoline or natural gas. Natural gas is delivered to the combustion chamber via gas mixer or fuel injector. In these methods, the high pressure natural gas passes through a regulator where its pressure is reduced to near atmospheric or a low pressure considering the structural strength of the intake manifold. Thus, at these pressures, natural gas density is relatively high and it will displace some air causing reduction of volumetric efficiency and subsequently absolute air-fuel mixture heating value. If natural gas is to be injected at higher pressures with shorter injection period, thus allowing more air to be induced to the cylinder, the structural strength of the intake manifold must be increased to accommodate the injection momentum. Also, gas injection into a plastic manifold is not wise.

Economic

In the countries where the natural gas resources and production are abundant and the price is relatively cheap, converting car engines to natural gas operation is advantageous. Fuel economy is significantly improved with natural gas utilization. In addition, the engine life and service interval are prolonged because natural gas combustion produces less soot particle and other pollutant gases. The unit price of natural gas has always been less than gasoline.

Environmental

Utilizing natural gas with optimal calibration reduces most polluting exhaust gases. In many parts of the world where ageing vehicles are used with minimal maintenance and coupled with the lack of emission regulations, harmful gases are being disposed to the environment. Using natural gas use the road vehicle has direct impact to the quality of air by reducing oxides of carbon and particulate emissions. The problem with smog formation in cities due to particulate emissions from road vehicle can be reduced as well.

5.9 Conclusions

In conclusion, the results and findings from the engine experiment data can be described as follows.

1. The performance of SPFI direct injection at its optimal operational set up on the Ricardo E6 engine was not superior to the performance of open valve port injection.

2. Mixture formation in the direct injection was probably poor due to limited time for completion. Moreover, the combustion chamber shape provides very minor assistance to this process. The design of SPFI itself has the weakness of spraying methane away from the point of injection, which is in contradiction of direct fuel injection normal practice where fuel is promoted towards spark plug. Since the shape of SPFI will remain basically the same, this problem must be solved by developing a proper mixing enhancing geometry of cylinder.

3. At relatively low injection pressure (60 bars) in DI method, mixture stoichiometry control was less achievable at injection timing earlier than 145° ATDC due to premature air rejection by expanding methane in cylinder. However, increasing injection pressure reduced this problem.

4. The performance of SPFI direct injection is significantly affected by the change in injection pressures and engine speeds. While higher injection pressures result in a more stable performance over wider range of injection timing, increased speed has negative effect on engine performance. These require a proper and more detailed operational mapping to maintain engine performance.

5. The delay of fuel arrival to the combustion chamber associated with the SPFI fuel path has significant effect on engine performance at higher speed. This can be corrected by optimising the length of fuel path and reducing pressure

loss within it. Another measure for maintaining engine performance at higher speed is by increasing injection pressure accordingly and/or advancing fuel injection timing as the speed increase.

6. Combustion duration in SPFI CH_4 DI operation is shorter than the one of OVPI. However, combustion in DI injection is slower at the earlier part and faster at the later part of combustion duration compared to PI.

7. Combustion durations were shortened by advancing spark ignition. In addition, by spark advancing, the ratio of the first half to the second half combustion duration is increased resulted in a less uniform burning rate.

8. Combustion durations were not changed with different injection pressures but ignition delay was affected by this variation. However, there is no direct correlation between injection pressure and ignition delay which is most probably due to the effect of charge flow difference.

9. Changing mixture stoichiometry affects the magnitude of ignition delay. Combustion duration, on the other hand increases with leaner mixture.

10. Different load conditions have significant effect on combustion process, Lower loads tend to increase combustion duration but shorten ignition delay.

Chapter 6

SPRAY VISUALIZATION

6.1 Introduction

The flow patterns of air and fuel in an internal combustion engine play an important role in determining many operating characteristics such as air-fuel mixing, combustion, fuel economy, performance and emissions. The absence of detailed knowledge of the flow will lead to engine development based mainly on empiricism and intuition rather than well established scientific principles [Cole, 1979]. The objective of this study is to investigate the shape and depth of penetration of methane jet in the SPFI direct injection. This was done by planar laser-induce fluorescent (PLIF) flow visualization in a confined chamber or so-called bomb. The results of this study can also be used to back the suspicion that mixing was bad, which was one of the main reason for poor engine performance with SPFI methane direct injection.

Methane substitute, acetone-doped nitrogen, was directly injected into a pressurised chamber (bomb) at pressures of 50, 60 and 80 bar. The bomb pressures were set to be 1 bar, 3 bar and 10 bar, which were based on the cylinder pressures during injection process in the Ricardo E6 engine with compression ratio 10.5:1. The depth of jet penetration and the shape can give a qualitative insight into the performance of SPFI methane direct injection in the Ricardo E6 engine. Planar Laser-Induced Fluorescent (PLIF) method with acetone as the gas tracer was used to visualize the fluid flow. A high speed CCD camera captured the images of gas plumes at various times during the injection process. The study, however, does not intend to quantify the fuel concentration distribution in the flow.

6.2 Fuel spray imaging methods

Optical diagnostic methods for visualizing fluid flows have been widely used in many areas including medical, automotive and industrial applications [Halliwell &

Hargrave, 2003]. In the automotive application, the measurements of interests are mainly fuel injection and in-cylinder flows. The most popular fuel injection visualization techniques are based on the monochromatic laser light sheet. The major advantage of these techniques is the opportunity to obtain quantitative information of fluid flow with high temporal and spatial resolution.

The Mie scattering technique is based on light and surface interaction where the scattering response is proportional to the total surface area of scattered particles. This technique is widely used to measure spray pattern and spray penetration. The laser-induced fluorescent (LIF) method is used to measure fuel vapour distribution, spray penetration and fuel vaporization. The technique is based on the conversion of the wavelength of a LIF active molecule. A tracer component is added to the measured fluid flow to give fluorescent effect when excited by absorbing photons from the laser sheet. The tracer should have properties close to the measured fluid. The Laser Sheet Dropsizing (LSD) method combines Mie and LIF imaging by acquiring both signals simultaneously, to provide information on mean droplet sizes [Jermy & Greenhalgh, 2000].

The Laser Doppler Anemometry (LDA) or Phase Doppler Anemometry (PDA) or Laser Doppler Velocimetry (LDV) is a single point optical measuring technique which enables the velocity of the seeded particles conveyed by a fluid flow to be measured in a non-intrusive manner. By analysing the Doppler-equivalent frequency of the laser light scattered (intensity modulations within the crossed-beam probe volume) by the seeded particles within the flow, the local velocity of the fluid can be determined. The area of interest within the flow field is sampled by a crossed-beam in a point by point manner. The PDA method has been successfully used in measurement of fluid flow for direct injection of liquid spray [Hargrave, 2000].

The schlieren and shadowgraph techniques are also used in fuel spray imaging. Image or shadowgrams are formed using a white light source for illumination, In some cases, a laser can be used for the schlieren technique. The techniques are based on observing density or refractive index gradient in inhomogeneous media. While a schlieren image displays the light deflection angle caused by a refractive index gradient, a shadowgraph image displays the ray obscuration resulting from the scattering and refraction.

All these methods were considered for visualizing methane flow from the SPFI injection nozzle. The selection of method was influenced by the objective to visualize the jet penetration and the shape of gas plume at different injection and cylinder pressures. Because compressed nitrogen is injected into nitrogen, the imaging method must be able to differentiate the injection and surrounding gas when injection takes place. Therefore, the method with a tracer element included is advantageous. The planar-LIF method was chosen over all other methods due to this and also due to its simplicity and local availability of equipment. Furthermore, it is advantageous to the author because of his experience with LIF measurement during the design stage of the SPFI.

6.3 Basic concept of Laser-Induced Fluorescent (LIF) method

The concept of PLIF imaging is described in Figure 6.1. A pulsed laser is transformed into a laser sheet by a set of optic lenses. The laser sheet passes through the measured fluid flow which is seeded by a flow tracer (acetone for instance). The tracer element in the flow is excited by the laser and emitted a fluorescent light within 1 to 100 ns when a high speed digital camera captures the image. The image is transferred to appropriate image processing software where it is saved in any desired format.

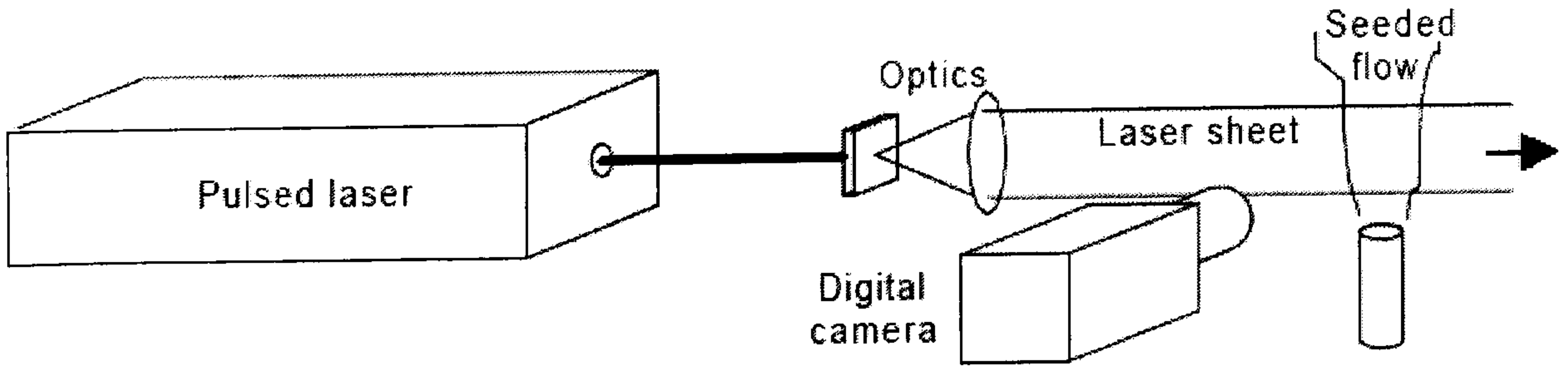

Figure 6.1 PLIF concept

Selection of the tracer must be based on the properties of the tracer material itself, which must not significantly alter the properties of flowing fluid that is being measured. In other word, its saturation properties must be equivalent to the fluid. The tracer also must be able to produce some kind of visible effect when excited by the laser sheet. A number of tracer materials have been used in PLIF imaging including acetone, pentanone-3, NO_2 [Hayashida, 1999], and rhodamine [Yamakawa, 2001]. As the tracer absorbs the light from the laser, it fluoresces at a certain wavelength and a selective filter then sends the filtered wavelength light to the CCD chip in the camera as imaging takes place. Acetone was chosen to be the LIF gas tracer as it has been successfully utilised in gaseous flow measurement as reported by a number of sources [Lozano, 1992, Olsen, 2002, Choi, 2002].

6.4 Experimental setup

The main components involved in the setup of this experiment can be categorised into four sub-groups;

- *A laser and optical lenses system*
  - An excimer laser source produces pulses of laser light at a set time interval. Then a laser sheet is formed by a set of optical lenses. The laser sheet passes through bomb windows along the vertical plane of fuel spray.
- *An imaging system*
  - The main component is the high speed CCD camera and focusing lenses. An image intensifier on the lenses is controlled externally in order to enhance the illumination on the images. The camera is controlled by an external driver, which is this case is the laser pulse, so that shutter opening is synchronised with laser pulse. The images are sent to a processing software on a computer.
- *A fuel supply system*
  - Nitrogen acts as methane substitute in this experiment. It is supplied to the injector through a pressure regulator, and an acetone threshold bottle, where it is bubbled through and doped. The fuel injector is controlled by a driver circuit which consists of a power supply unit (12V and 2 A), a pulse generator and a Mosfet. The pulse generator set the injection length and frequency and is

connected to the Mosfet. The Mosfet then act as a gate between the power supply and the fuel injector.

- A fuel injection chamber
  - A confined chamber (bomb) is filled with pressurised nitrogen to a specified pressure from a regulator-controlled high pressure nitrogen bottle.

An image of in-laboratory settings is shown in Figure 6.2. Details of the complete components are listed in Table 6.1 and shown schematically in Figure 6.3. The fuel injection driver circuit was synchronized with the camera and laser systems. A Mosfet, acted as a gate/bridge between a power supply unit and the SPFI, and was excited by the output of a pulse generator which functioned as the main driver to the experiment. At the same time, the pulse generator output was connected to another pulse/delay generator where its signal was sent to the laser source. The laser simultaneously sent a signal to the camera so laser pulse was synchronised with the opening of the shutter. An oscilloscope was connected to both pulse/delay generator to measure the delay between initiation of fuel injection and image capturing.

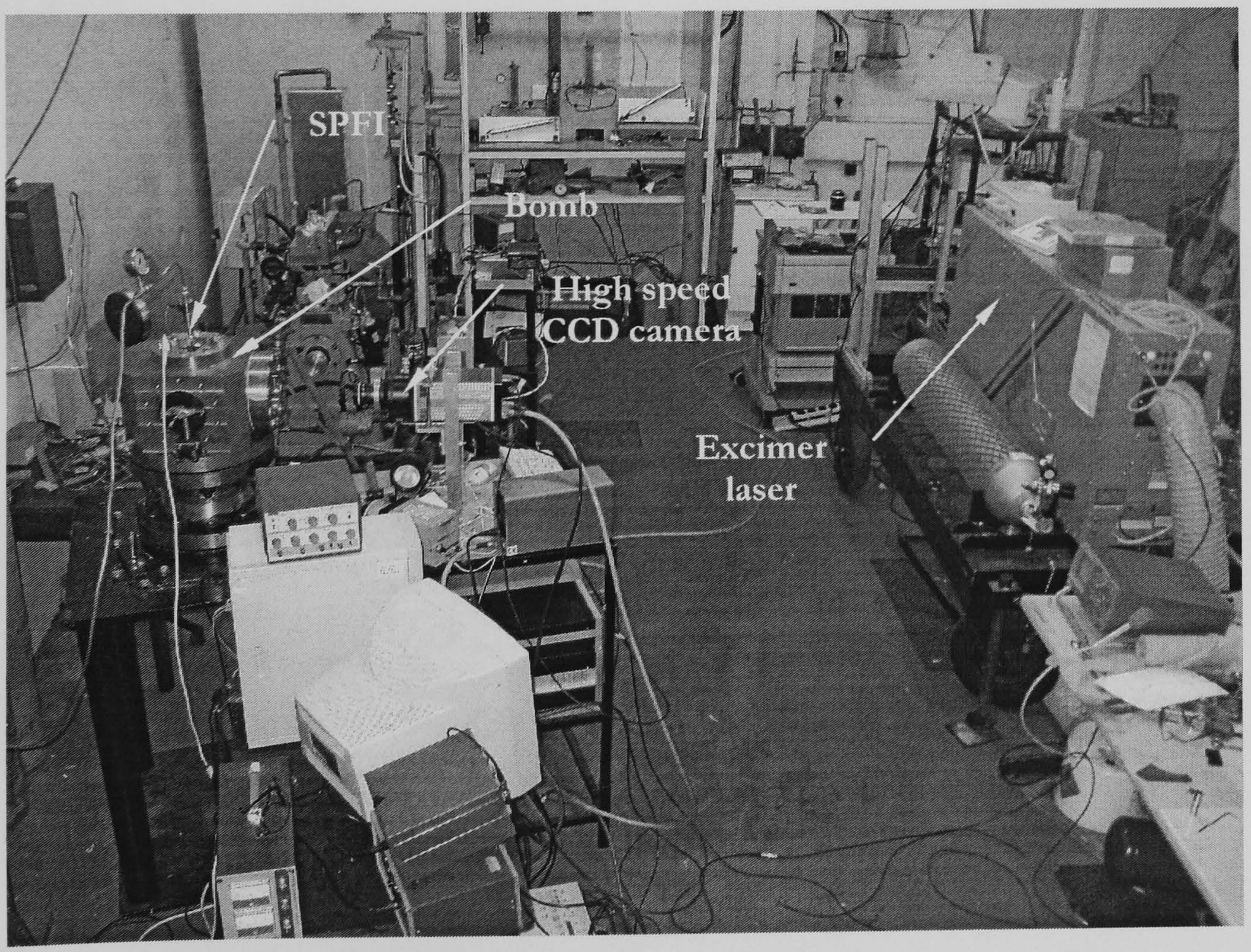

Figure 6.2 Laboratory set up for PLIF imaging of SPFI injection flow visualization

Item	Equipment	Manufacturer	Model
1	Excimer Laser	Lambda Physik	CompexPro
2	Camera High speed CCD	Princeton Instrument	PI-MAX
3	Camera temperature control	Princeton Instrument	
4	Image intensifier controller	Princeton Instrument	IIC-100
5	Programmable pulse generator	Princeton Instrument	PG-200
6	Pulse/delay generator		
7	Mosfet		
8	Power supply unit		
9	Oscilloscope		
10	Bomb		
11	SPFI		
12	Nitrogen bottles		
13	Acetone threshold bottle		
14	Pressure regulators and gauges		

Table 6.1 List of equipments for the PLIF imaging

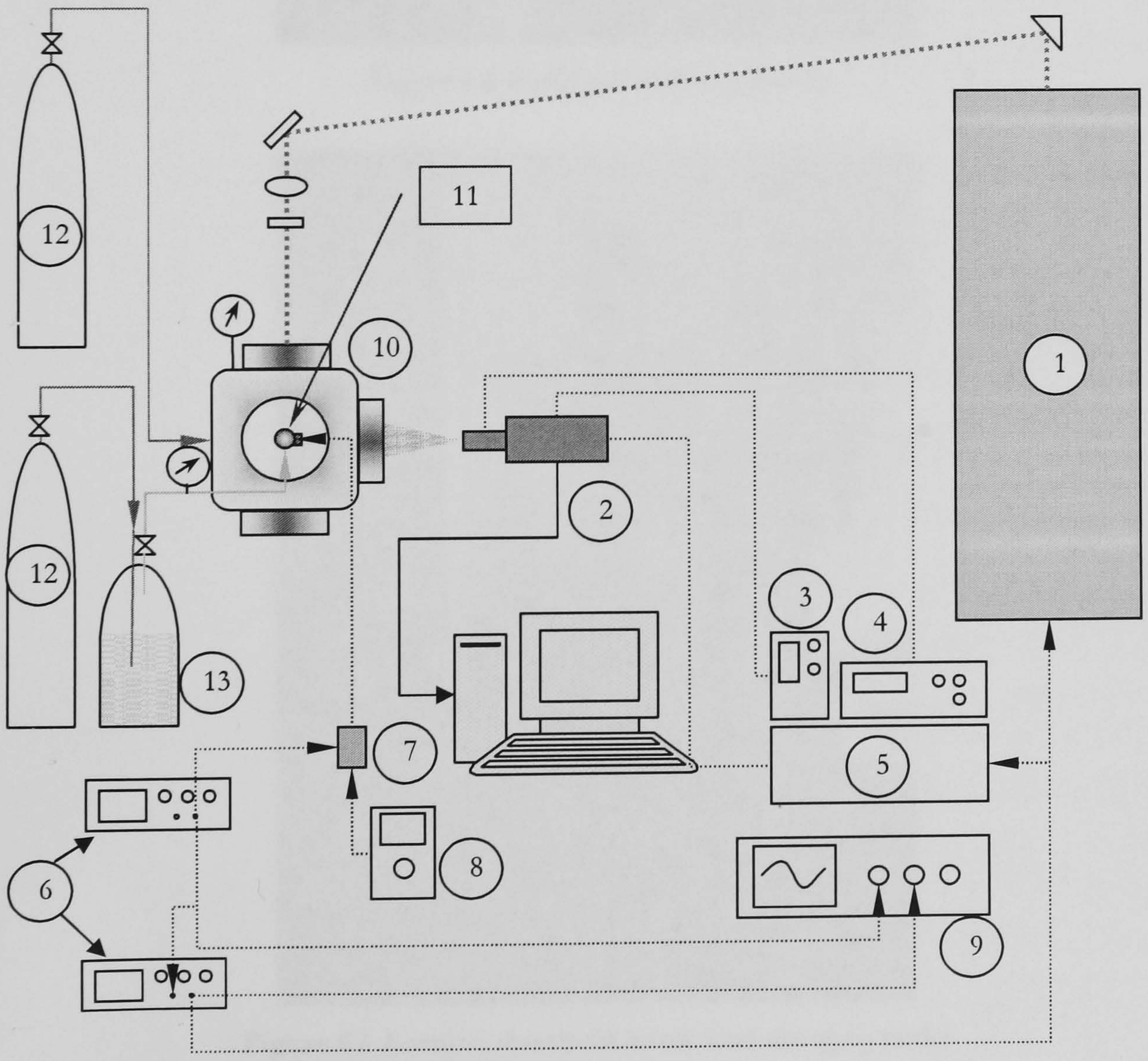

Figure 6.3 Schematic of the PLIF imaging of SPFI injection flow visualization (correspond to numbered components in Table 6.1)

Figure 6.4 shows the bomb arrangement with a pressurised nitrogen supply to pressurise the bomb and to act as injection gas. In order to pressurise the bomb, air must be displaced so that mainly nitrogen is left pressurised. This was done by repeatedly flushing out the bomb with pressurised nitrogen. Flushing was also done from time to time when the bomb is saturated by acetone after repeatedly injecting acetone-doped nitrogen into it.

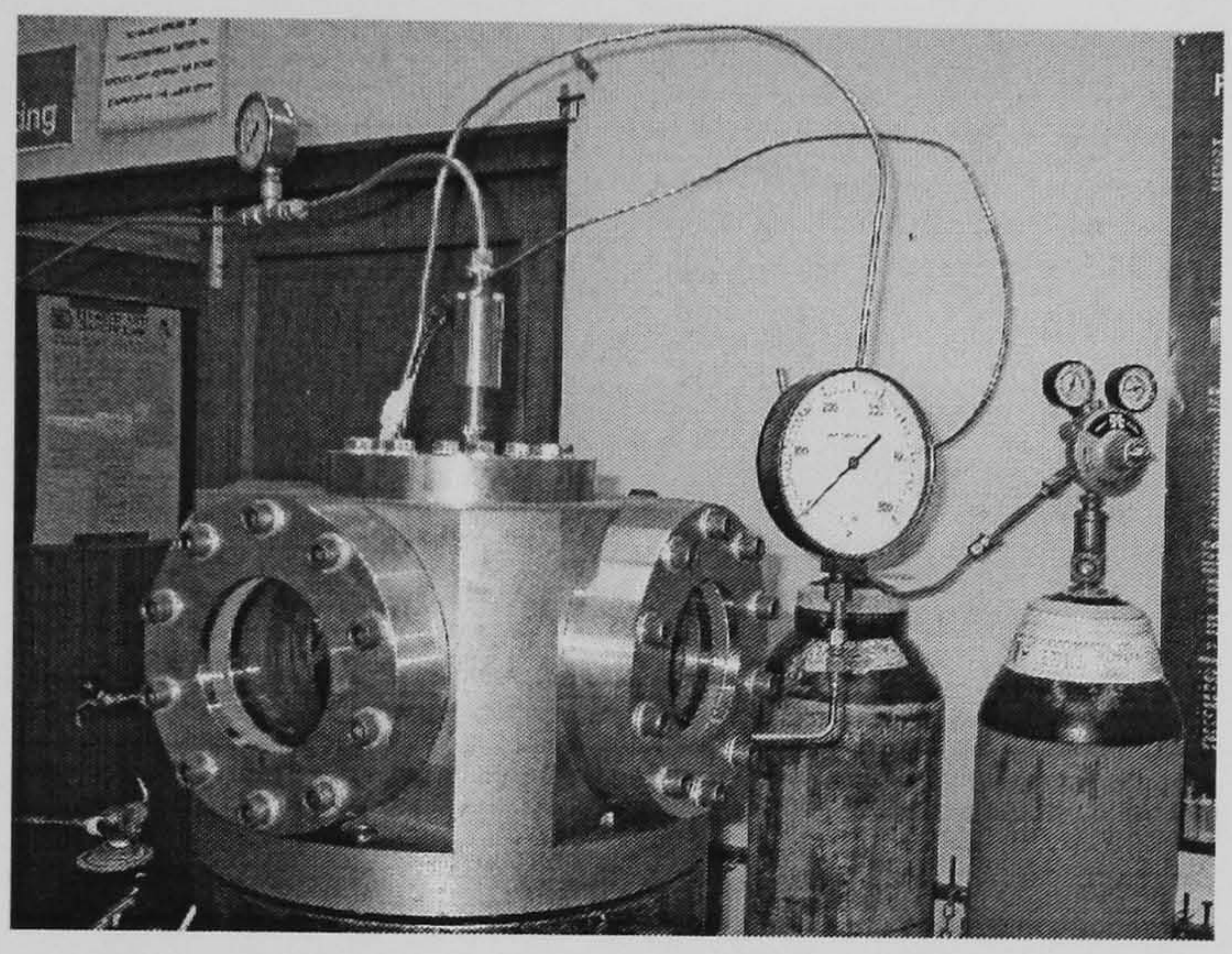

Figure 6.4 Fuel injection and Bomb

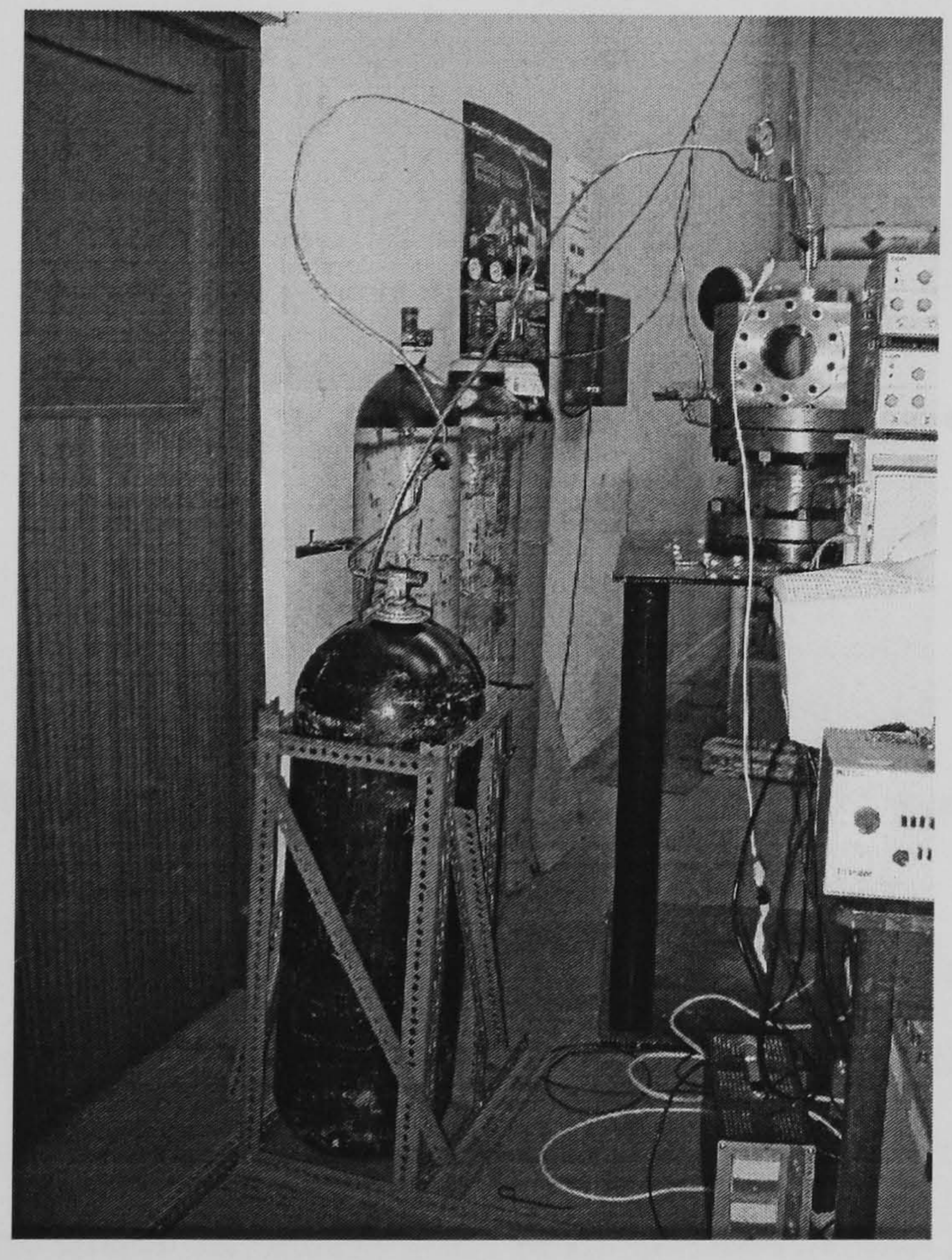

Figure 6.5 Acetone threshold bottle and nitrogen tanks

Figure 6.5 shows the acetone threshold bottle where nitrogen is bubbled through 15 litres of liquid acetone and pressurised to the desired injection pressure. The supply nitrogen is bubbled through the acetone and trapped in the upper part of the threshold bottle. As bubbling progresses, the trapped gas increases its pressure and as it reaches the desired injection pressures, the supply valve is closed. An outlet gas pipe is attached to the bottle positioned above the surface of acetone, thus only acetone-saturated gas is delivered to the SPFI. The pressure gauge on the gas pipe near SPFI was used to determine the injection pressures. Figure 6.6 shows the nitrogen acetone doping mechanism.

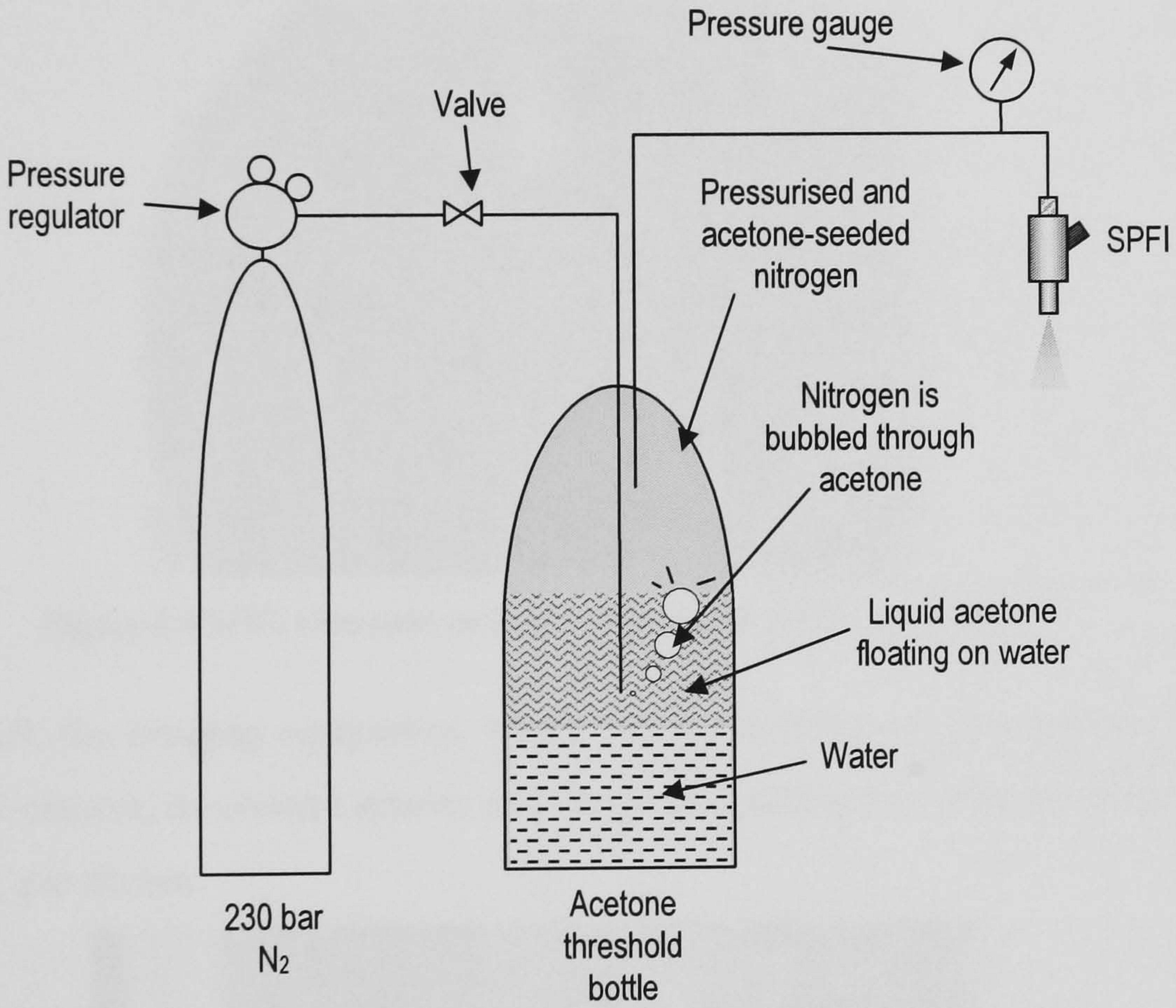

Figure 6.6 Nitrogen acetone doping mechanisms for SPFI spray imaging.

In Figure 6.7, the SPFI attachment to the bomb is shown. A specially made window adaptor was made to accommodate the SPFI with the pre-existing top window of the bomb which is mainly to hold a fuel injector the imaging purposes. Figure 6.8 shows the inside of bomb with SPFI electrodes and injection nozzle on the surface of the window adaptor.

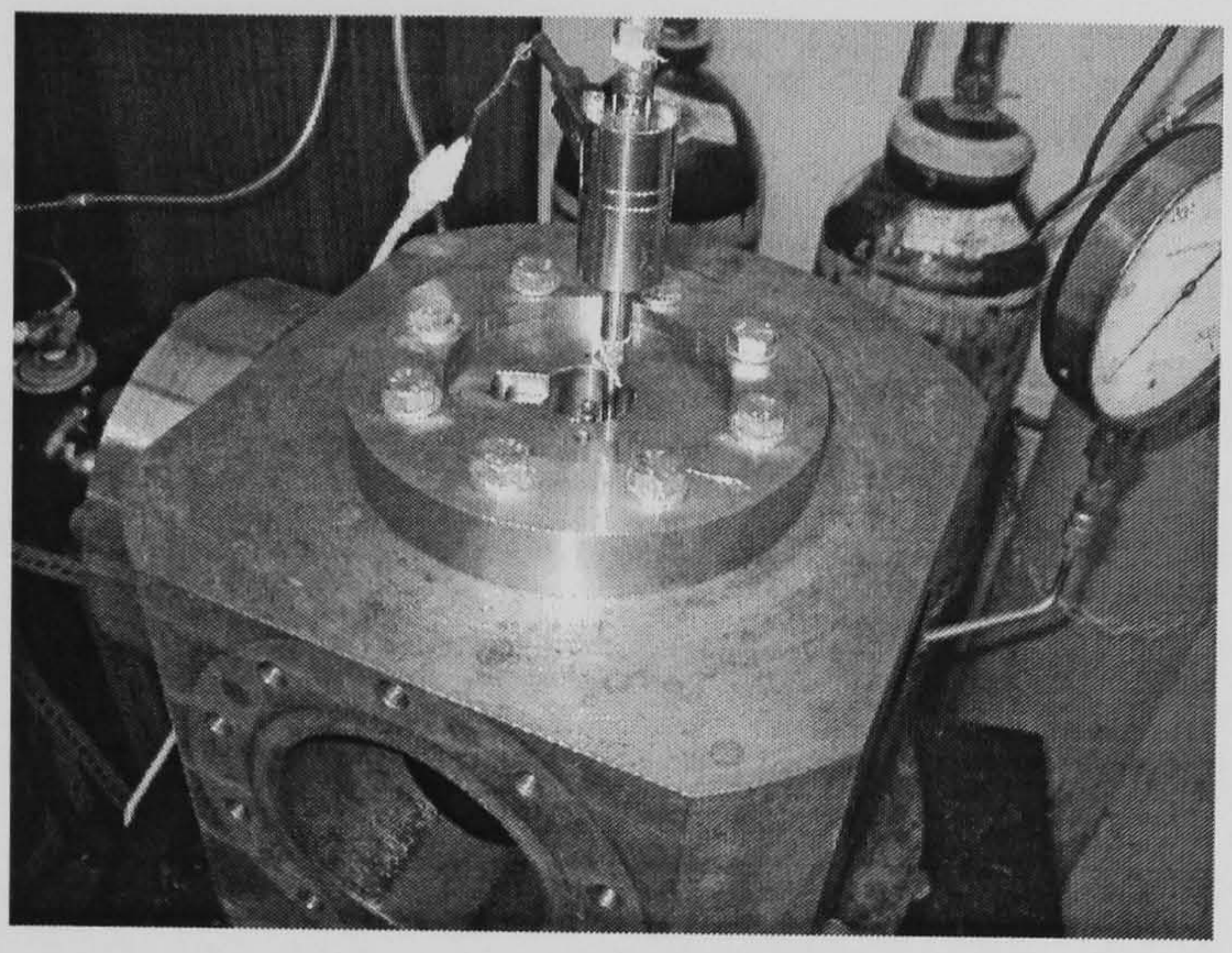

Figure 6.7 SPFI attachment to Bomb

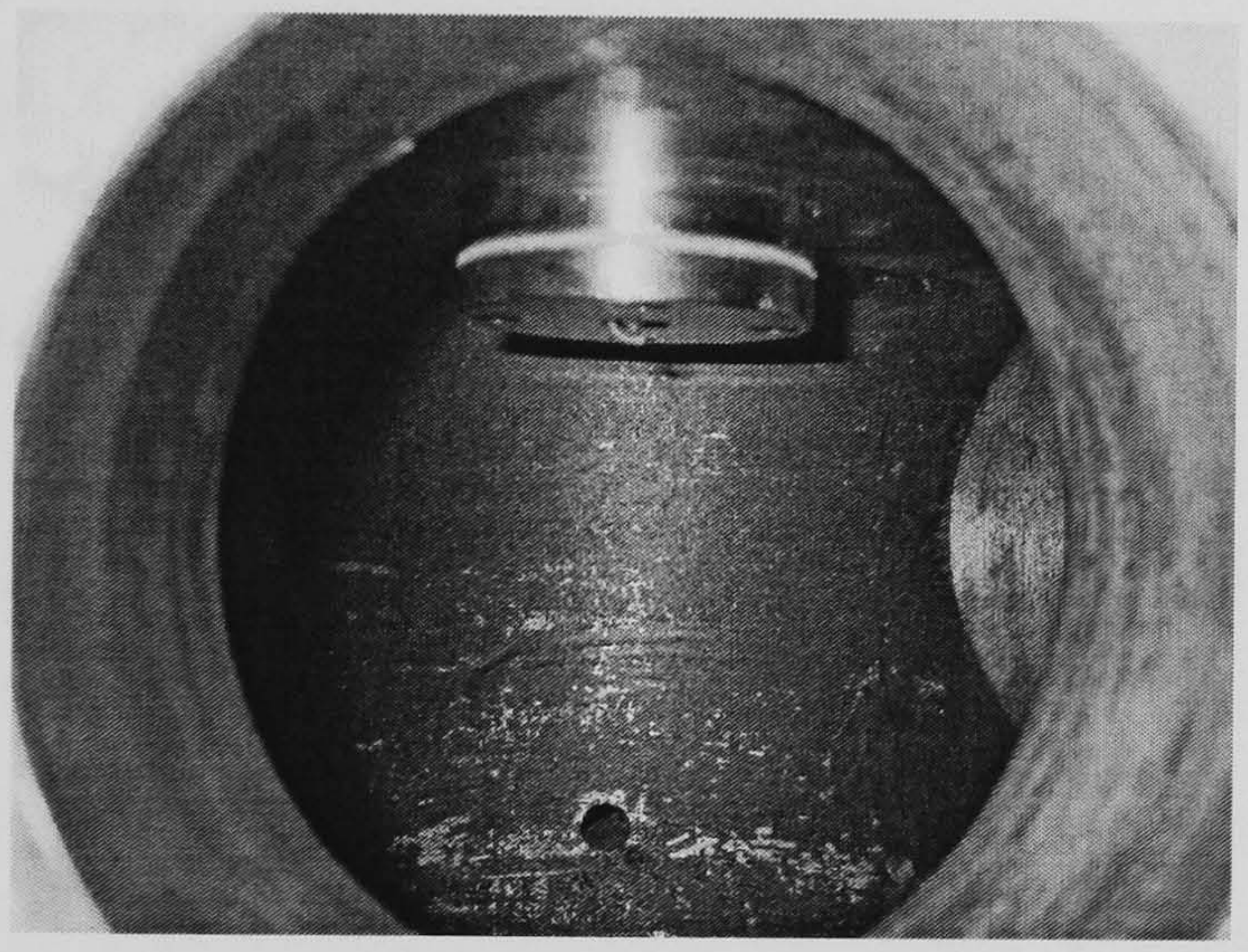

Figure 6.8 SPFI electrode and injection nozzle inside the Bomb

In Figure 6.9, the imaging equipment, which include a Princeton Instruments High Speed CCD camera, its control system and image processing software (WinView) on a computer, are shown.

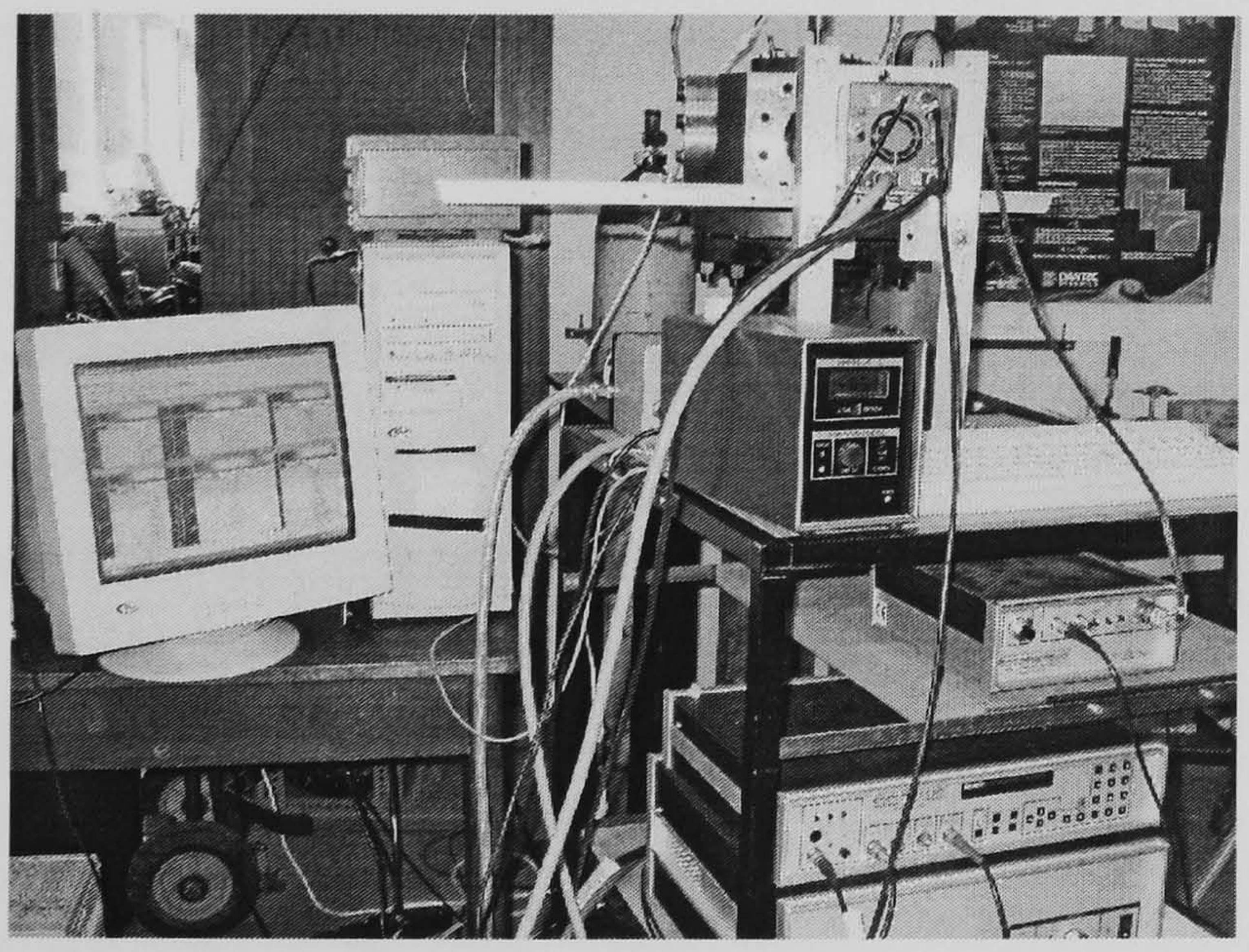

Figure 6.9 Imaging equipments

6.5 Method

The experiments were carried out by referencing the cylinder pressure of the Ricardo E6 engine motorised without injecting fuel. Figure 6.10 shows the cylinder pressure during the compression stroke and the injection locations where optimal calibrations for stoichiometric air-fuel ratio operations were achieved. For 80 bar injection pressure, the optimal injection time is at 215° BTDC (compression). For 50 bar and 60 bar injections, the optimal injections were at 170° BTDC (compression). The fuel injections were relatively early considering the normal practice of direct fuel injection where injection happens at a later stage of compression stroke.

Even though the injection starts mostly at pressure near to 1 bar cylinder pressure, as shown in Figure 6.9, due to the lengths of injection durations, fuel delivery stops at some higher cylinder pressures. Fuel injection durations are 6 ms, 10 ms and 12 ms for 80 bar, 60 bar and 50bar injection pressures respectively. At 1100 rpm, these injections cover 40°CA, 66°CA and 79°CA respectively, as shown in the figure. Taking into account the fuel delivery delay due to the lengthy fuel path in the SPFI, it was decided to perform injections at three bomb pressures: 1 bar, 3 bar and 10 bar. The 1 and 3 bar pressure represent the range of actual injection cylinder pressure, while the 10 bar pressure was chosen to investigate the effect of gas jet if injection is delayed at later stage of compression stroke, which can be the pressure during injection at higher engine speed.

At each injection pressure, images were captured at every 2 ms time intervals starting from 2 ms after the initiation of injection signals. Images at 2.5 ms have also been recorded which show clear first appearances of injected gas. The imaging continued until the time reached twice the injection duration; 12 ms, 20 ms and 24 ms for 80 bar, 60 bar and 50 bar respectively. For each shown image, a set of 10 images were captured and averaged.

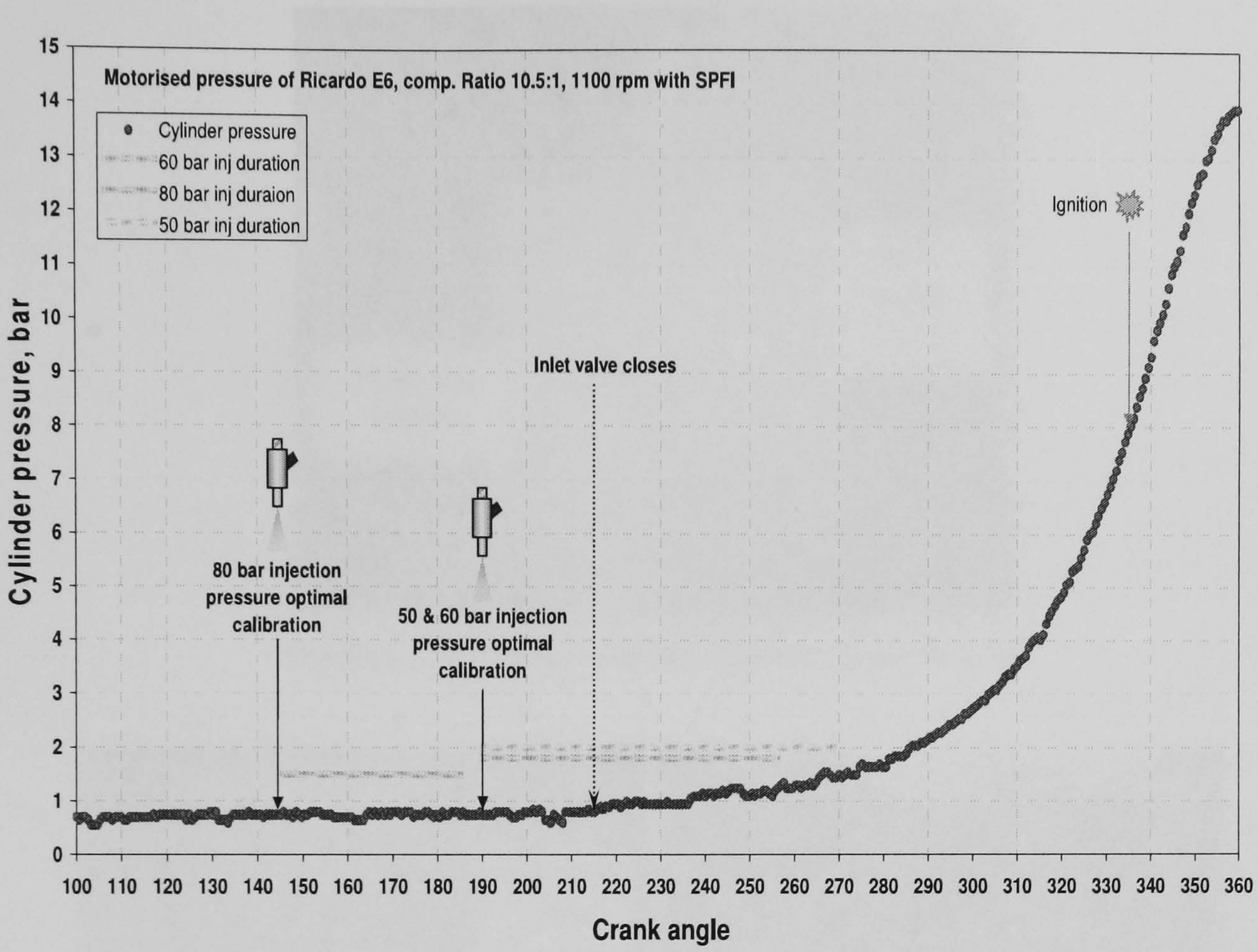

Figure 6.10 Motorised cylinder pressure and fuel injection timings

6.6 Calibration

It is important to quantify the injection penetration and the width of gas plume from the images. The bomb viewing window allows 110 mm circular diameter visual access to the injection gas flow. Calibration of gas jet dimensions was achieved by taking of a scaled image attached to the fuel injection vertical plane as shown in Figure 6.11. Figure 6.12 shows a calibration image captured by the CCD camera and compared with a PLIF image with no gas injection. The bright spots on the PLIF image are the unsolved scattering from the injector holder, which could not be avoided. Figure 6.12 also shows a grainy texture to the PLIF image. Much effort was applied to avoiding this background noise and improvements were made. However, the need to pick out the very slight fluorescent caused by the light doping (stronger doping proved impossible) also means picking out this background noise. The design of the doping system was limited by a need to operate it at high pressures (up to 80 bar) and limited supply of acetone (hence the depth of bubbling was limited).

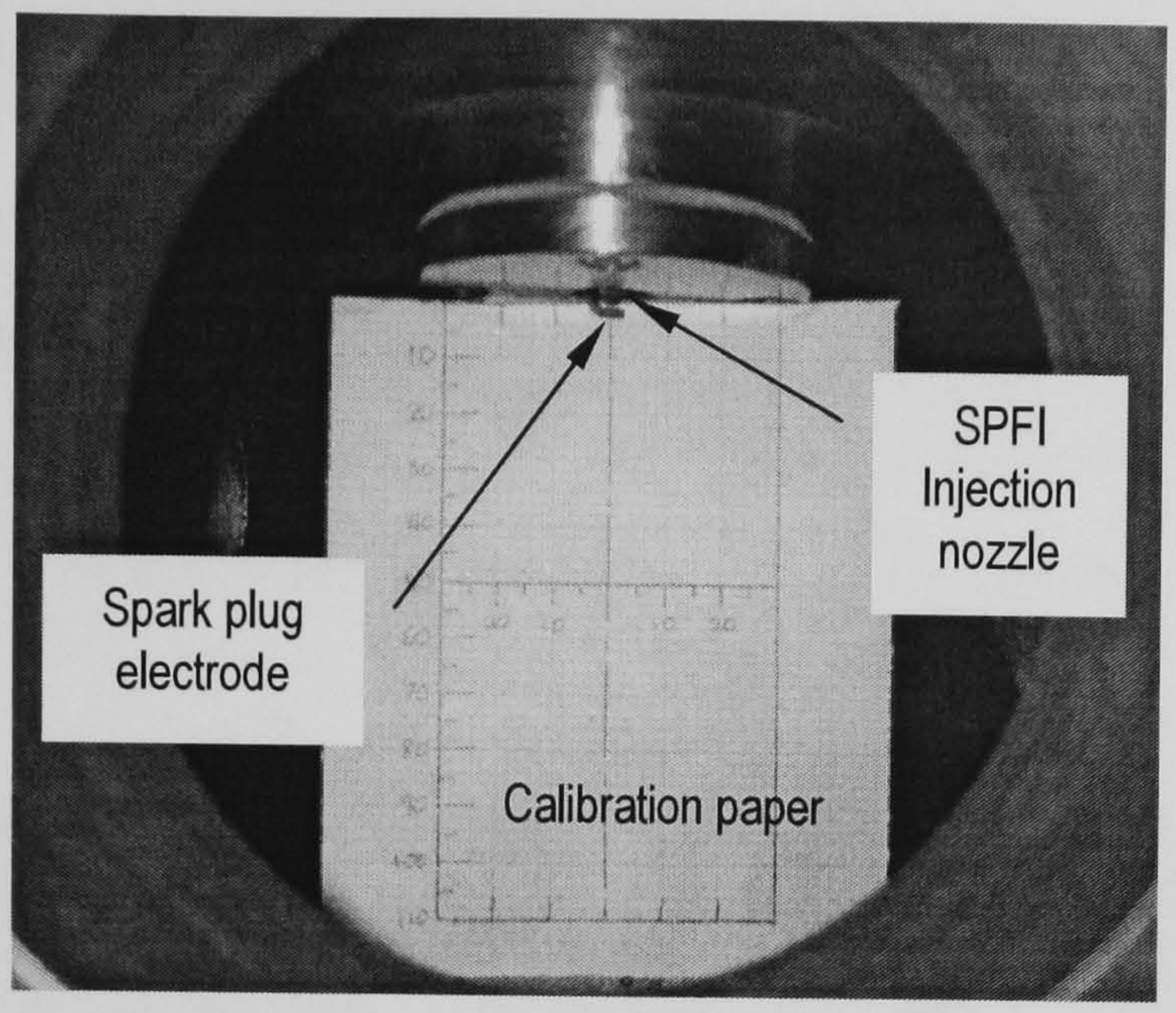

Figure 6.11 Calibration of fuel injection measurement

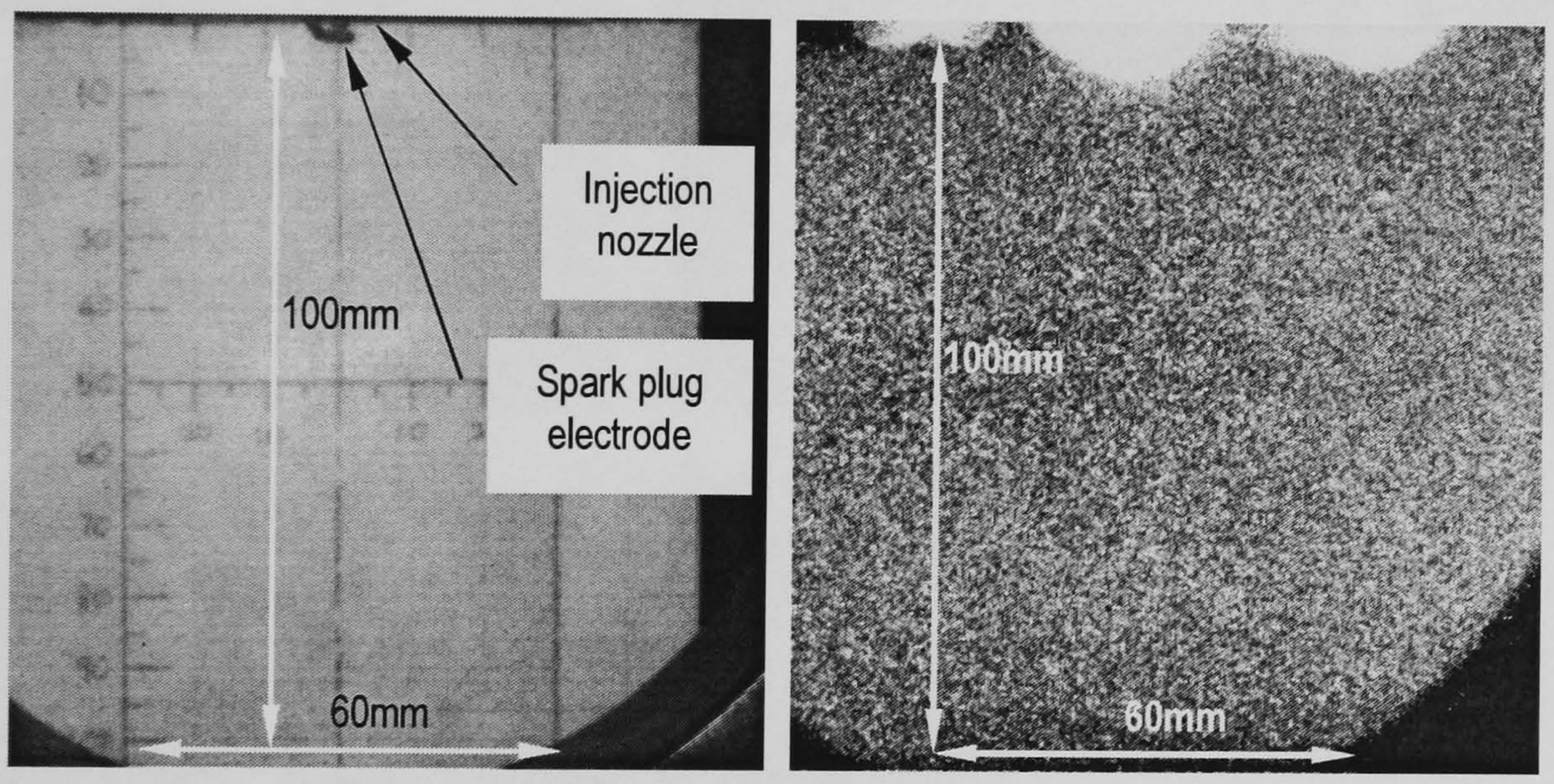

Figure 6.12 Calibration image (left) and PLIF image with no gas injection (right)

6.7 Results

The images showed in all the figures indicate some interesting observation of jet penetration and jet width relation with injection pressures. The bright white areas penetrating from the top of each image indicates the injected gas presence. The intensities of brightness can be used to describe qualitatively the gas concentration. It is important to note that because the acetone-doped nitrogen stayed almost statically inside the injection fuel line due to slow rate of injection in this experiment (once in every 1 second), it was possible that some of the acetone settled or condensed to the pipe walls. This can also be a cause of the background noise problem.

6.7.1 Injection into 1 bar bomb pressure

Figure 6.13 shows the consecutive images from a 50 bar injection pressures into 1 bar bomb pressure. Injection duration was 12 ms and the images were taken within 24 ms. The first appearance of gas jet can be seen at 2.5 ms, and gas plume fully developed by 10.0 ms. Detachment of gas jet from injection nozzle can be seen at 22.0 ms.

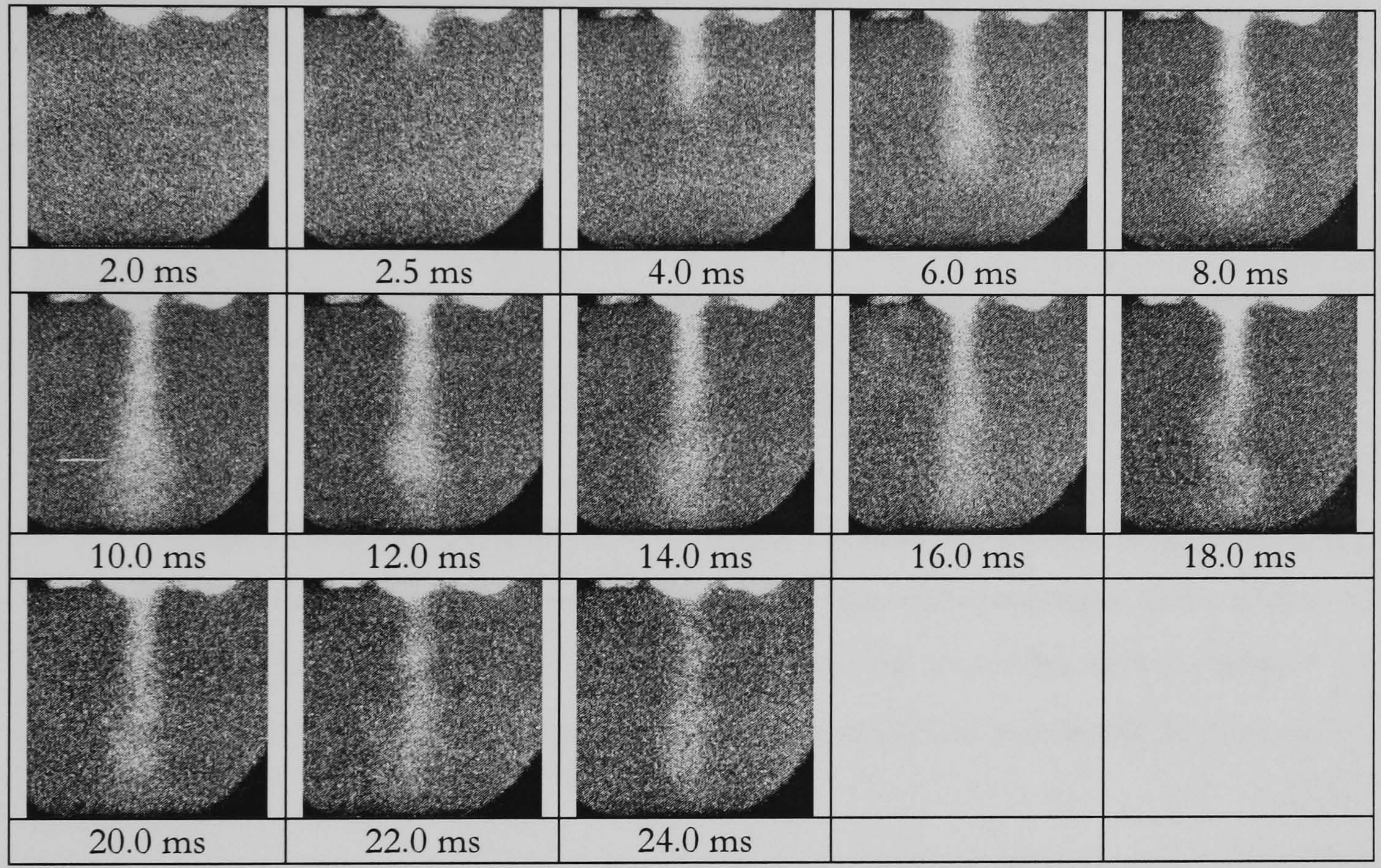
2.0 ms 2.5 ms 4.0 ms 6.0 ms 8.0 ms
10.0 ms 12.0 ms 14.0 ms 16.0 ms 18.0 ms
20.0 ms 22.0 ms 24.0 ms

Figure 6.13 Consecutive images of 50 bar fuel injection into 1 bar bomb pressure

Figure 6.14 shows the consecutive images from a 60 bar injection pressures into 1 bar bomb pressure. Injection duration was 10 ms and the images were taken within 20 ms. The first appearance of gas jet can be seen at 2.5 ms, and gas plume fully developed by 10.0 ms. Detachment of gas jet from injection nozzle can be seen at 18.0 ms.

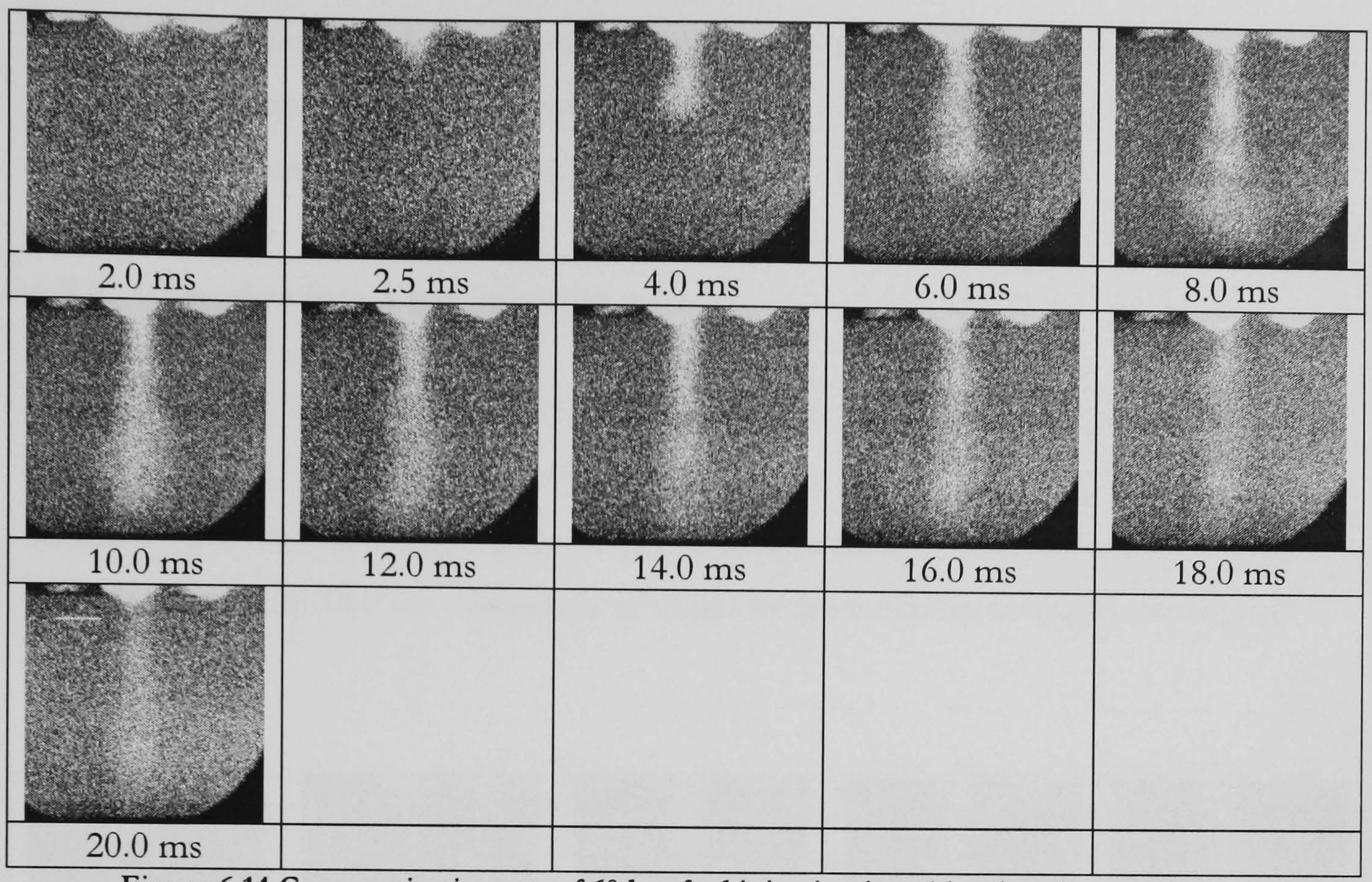

2.0 ms 2.5 ms 4.0 ms 6.0 ms 8.0 ms

10.0 ms 12.0 ms 14.0 ms 16.0 ms 18.0 ms

20.0 ms

Figure 6.14 Consecutive images of 60 bar fuel injection into 1 bar bomb pressure

Figure 6.15 shows the consecutive images from an 80 bar injection pressure into 1 bar bomb pressure. Injection duration was 6 ms and the images were taken within 12 ms. The first appearance of gas jet can be seen at 2.5 ms, and gas plume fully developed by 8 ms. Detachment of gas jet from injection nozzle can be seen at 12.0 ms.

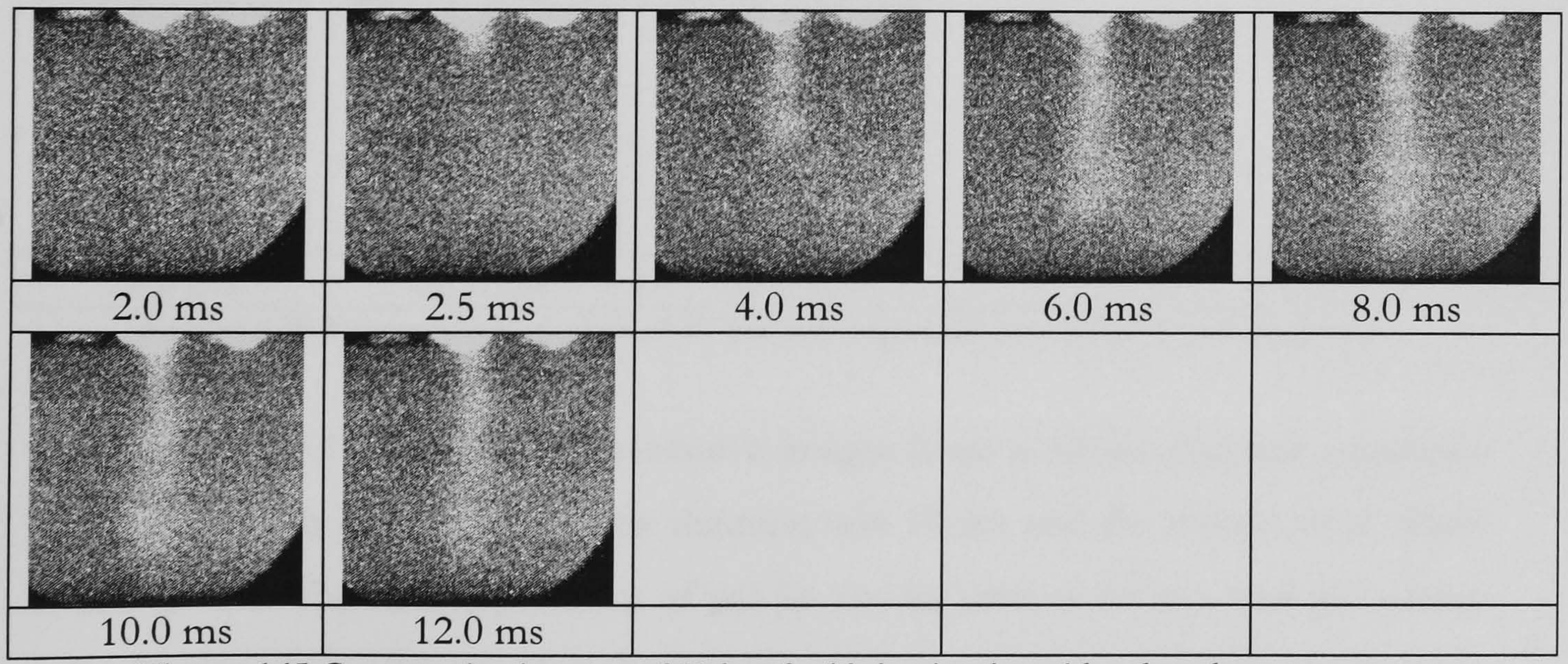

2.0 ms 2.5 ms 4.0 ms 6.0 ms 8.0 ms

10.0 ms 12.0 ms

Figure 6.15 Consecutive images of 80 bar fuel injection into 1 bar bomb pressure

In all injection pressures, the first appearance of gas jet occurs at 2.5 ms but fully developed at different times. Higher injection pressure produce earlier fully-developed gas plume. Injection pressures also have strong influence on the effective fuel delivery time which can be implied from the time of detachment of gas plume from the injection nozzle. Higher injection produces less delivery time.

6.7.2 Injection into 3 bar injection pressure

Figure 6.16 shows the consecutive images from a 50 bar injection pressures into 3 bar bomb pressure. Injection duration was 12 ms and the images were taken within 24 ms. The first appearance of gas jet can be seen at 2.5 ms, and gas plume fully developed by 14.0 ms. Detachment of gas jet from injection nozzle can be seen at 20.0 ms.

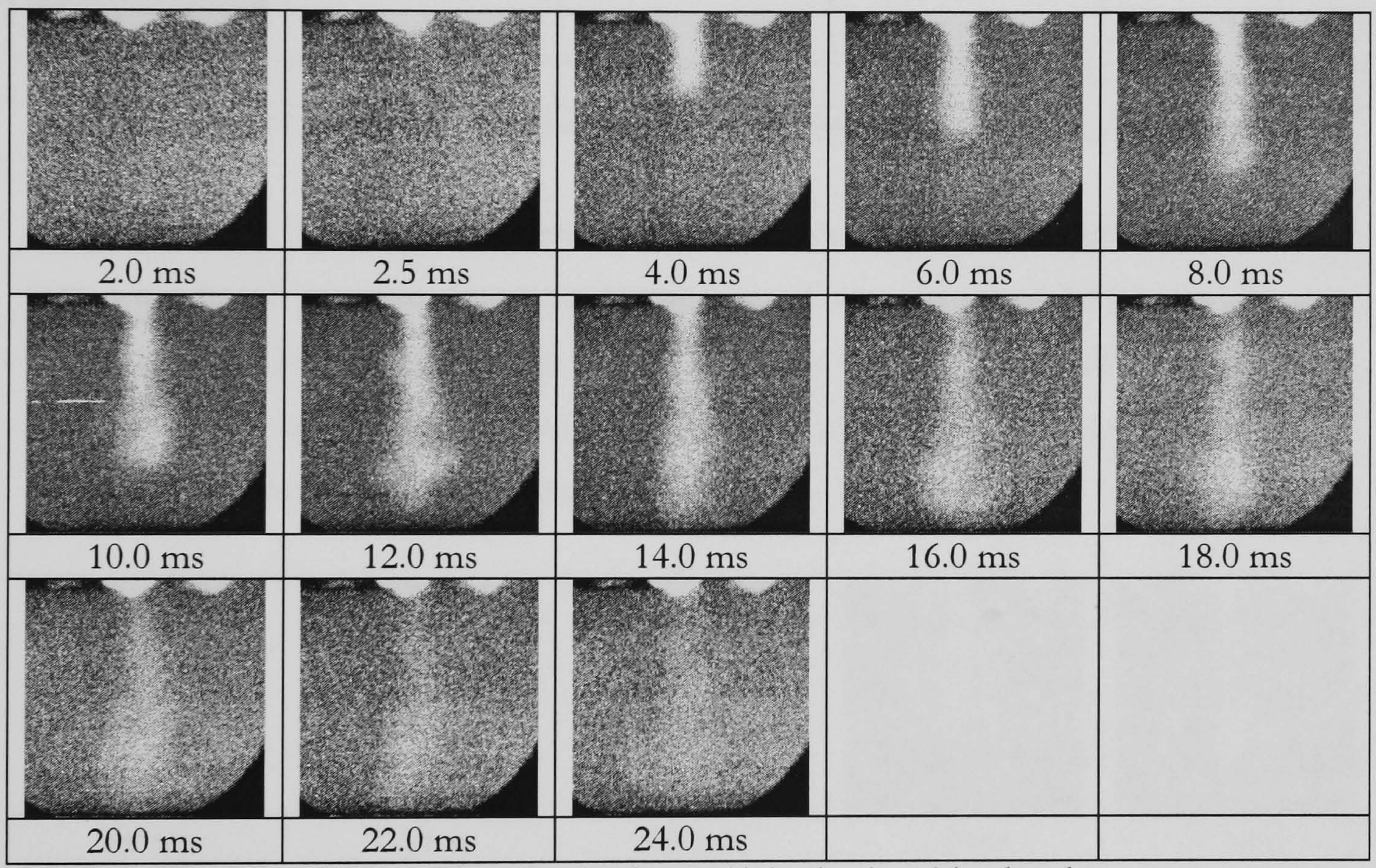
2.0 ms
2.5 ms
4.0 ms
6.0 ms
8.0 ms
10.0 ms
12.0 ms
14.0 ms
16.0 ms
18.0 ms
20.0 ms
22.0 ms
24.0 ms

Figure 6.16 Consecutive images of 50 bar fuel injection into 3 bar bomb pressure

Figure 6.17 shows the consecutive images from a 60 bar injection pressures into 3 bar bomb pressure. Injection duration was 10 ms and the images were taken within 20 ms. The first appearance of gas jet can be seen at 2.5 ms, and gas plume fully developed by 12.0 ms. Detachment of gas jet from injection nozzle can be seen at 18.0 ms.

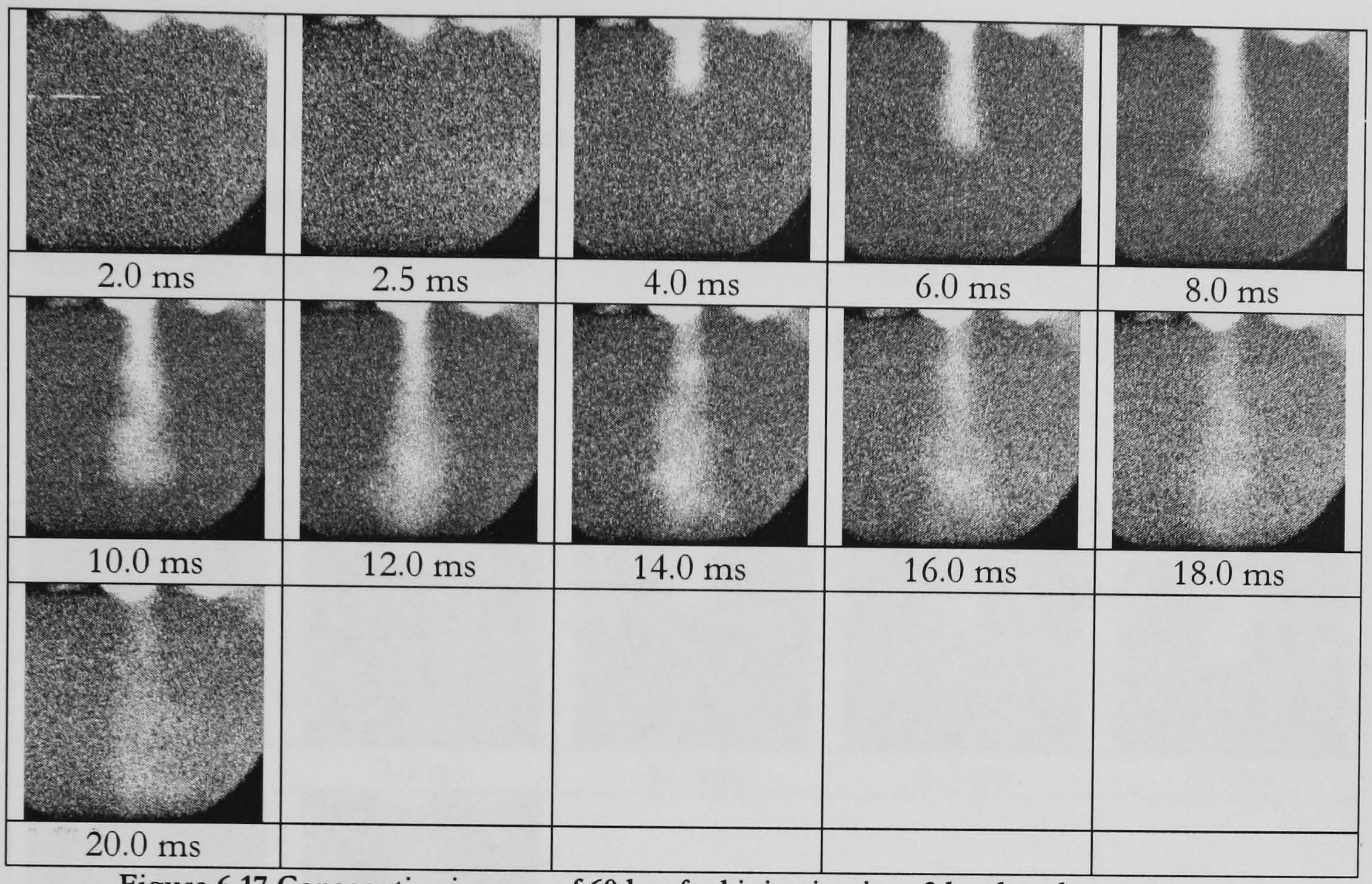

Figure 6.17 Consecutive images of 60 bar fuel injection into 3 bar bomb pressure

Figure 6.18 shows the consecutive images from an 80 bar injection pressures into 3 bar bomb pressure. Injection duration was 6 ms and the images were taken within 12 ms. The first appearance of gas jet can be seen at 2.5 ms, and gas plume fully developed by 10.0 ms. Detachment of gas jet from injection nozzle can be concluded at some time after 12.0 ms.

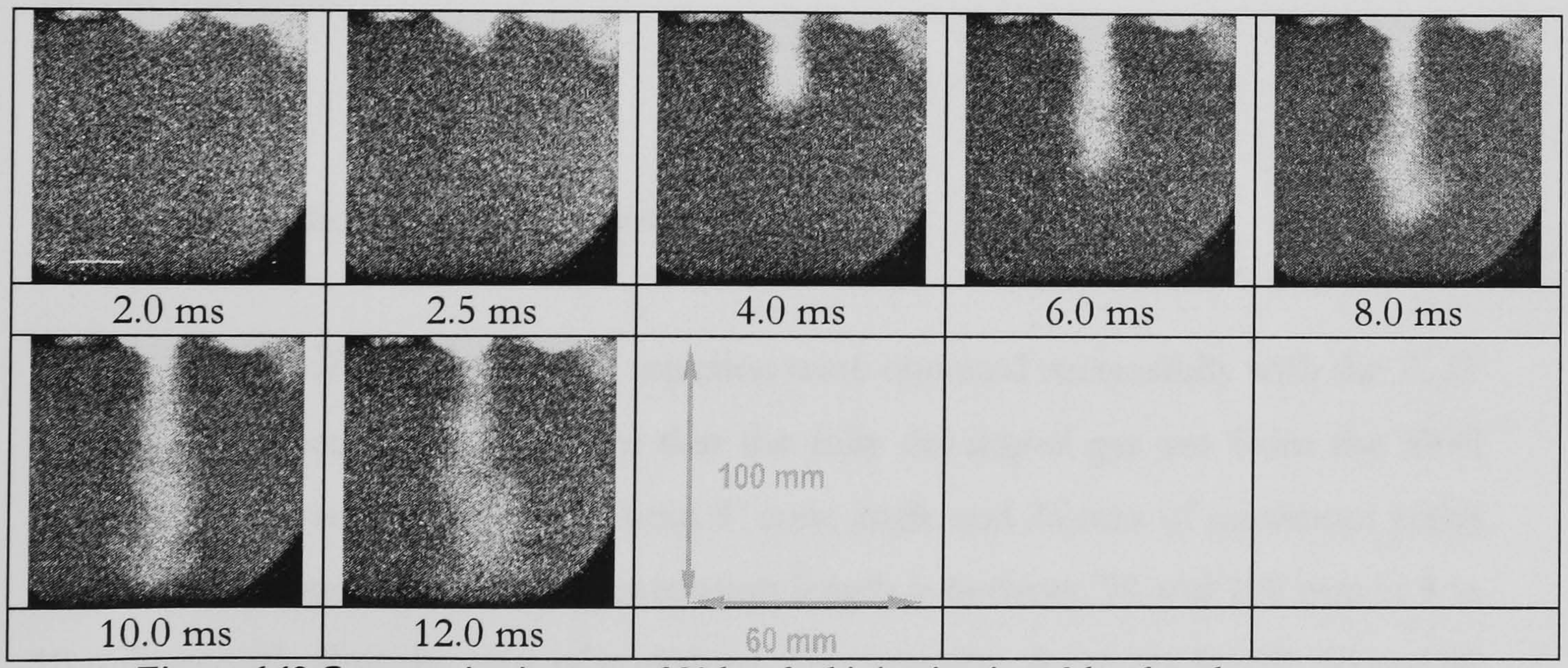

Figure 6.18 Consecutive images of 80 bar fuel injection into 3 bar bomb pressure

Increasing bomb pressure from 1 to 3 bar results in shorter jet penetration and slower effective delivery time.

6.7.3 Injection into 10 bar injection pressure

Figure 6.19 shows the consecutive images from a 80 bar injection pressures into 10 bar bomb pressure. Injection duration was 6 ms and the images were taken within 12 ms. The first appearance of gas jet can be seen at 2.5 ms, and gas plume fully developed by 12.0 ms. Detachment of gas jet from injection nozzle cannot be seen.

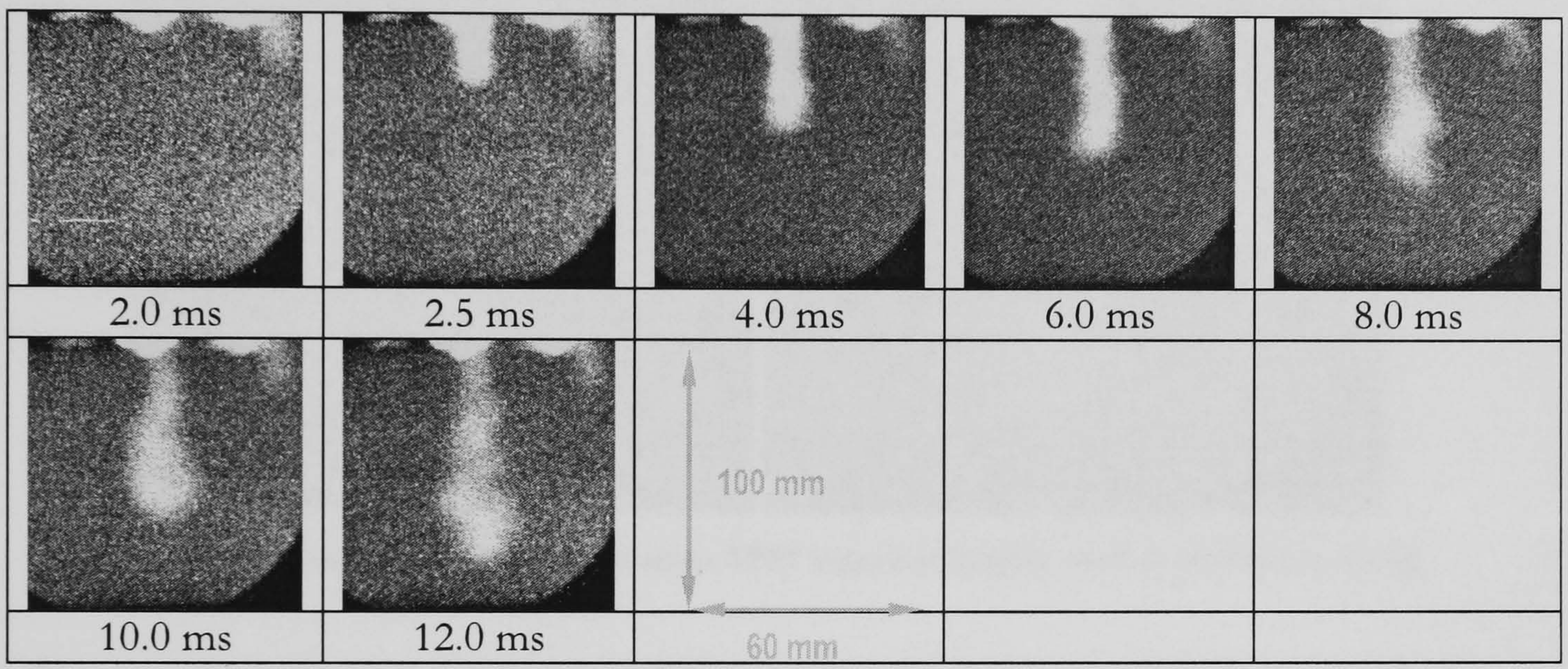

2.0 ms 2.5 ms 4.0 ms 6.0 ms 8.0 ms

10.0 ms 12.0 ms

Figure 6.19 Consecutive images of 80 bar fuel injection into 10 bar bomb pressure

The effect of increasing bomb pressure is further enhanced with 10 bar bomb pressure, where jet penetration is cut by about 30% and effective delivery time is further increased.

6.8 Discussion and conclusion

Images of flow from SPFI injection were obtained successfully with the PLIF method. In general, it can be seen that the fully developed gas jets from the SPFI injection were very narrow, with about 9° cone angle and 25 mm of maximum width in a fully developed gas jet. The penetration length is between 90 and 100 mm at 8 to 10 milliseconds after the start of injections. The injection durations for 50, 60 and 80 bars fuel pressures on the Ricardo E6 engine were 12 ms, 10 ms and 6 ms respectively. A fully developed gas jet is shown in Figure 6.20. Considering the stroke length of Ricardo E6 (111.125 mm) and the injections occur during compression stroke where piston is moving towards to injector, the jet penetration lengths indicates that sufficient vertical distance would be achieved for air-fuel mixing. However, due to the fact that the cone angle is narrow, the mixing process would be poor because horizontal distribution of the injected gas failed to cover most part of the cylinder.

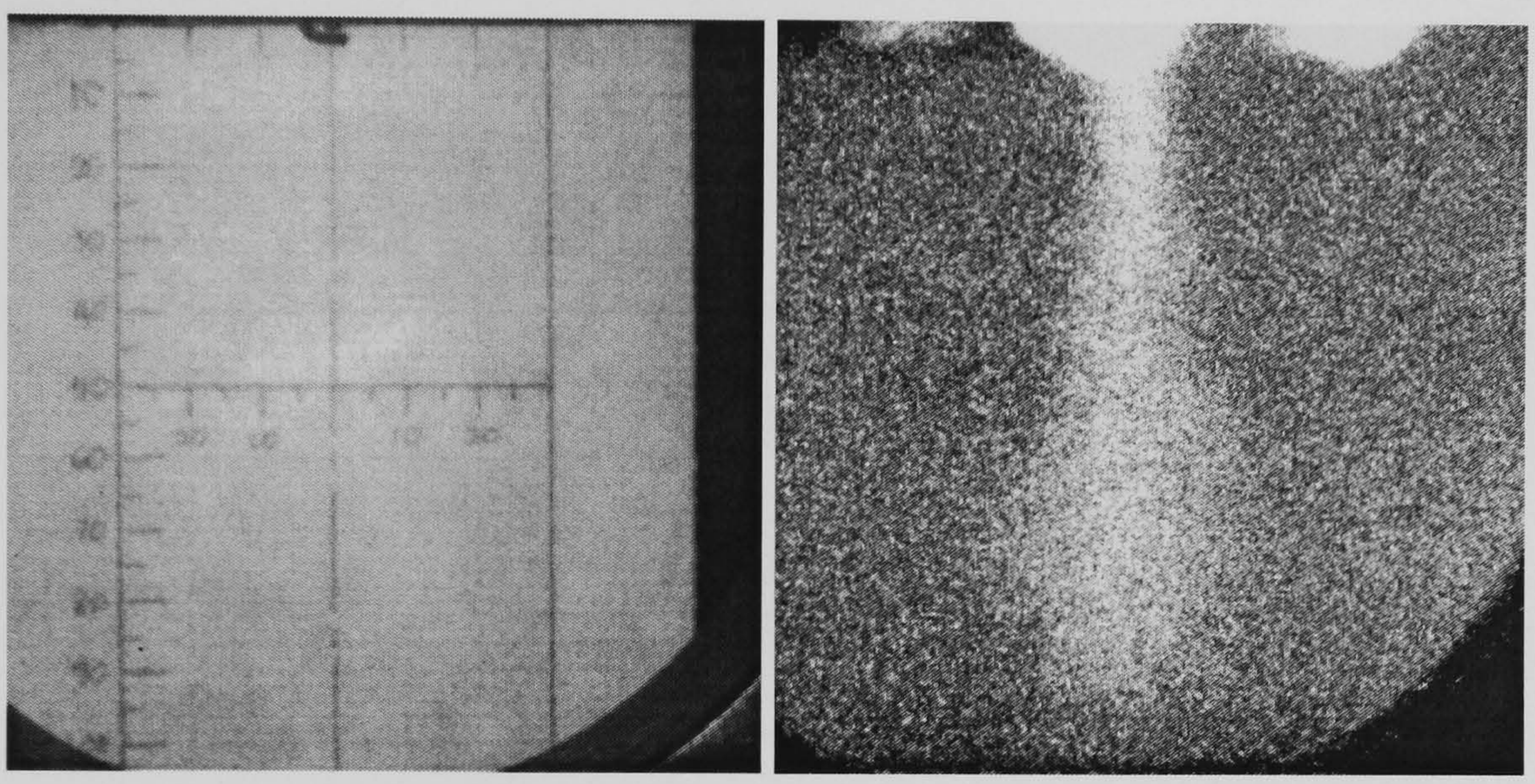

Figure 6.20 Fully developed gas jet from SPFI injection (right) with scaled frame (left)

The image on the right of Figure 6.20 shows a fully developed gas jet. A significant amount of background scattering on the image can be seen. The scattering was believed to be the result of minor illumination of the background gas in the bomb by the laser sheet. It was made worse by the need to pick out slight fluorescent from a lightly doped injection gas. This however, did not prevent the visualization of gas jet development and qualitative determination of penetration length and plume width.

Bomb pressure has a noticeable effect on jet penetration. As the pressure increases, jet penetration becomes shorter, as shown in Figure 6.22. However, for the same bomb pressure, the differences between jet penetration lengths with changing fuel pressure are relatively small. This is because fluid flows exiting the SPFI injection nozzle were at sonic conditions for all injection pressures. For gas flow through an orifice, as shown in Figure 6.21, there exists a condition where gas velocity reaches sonic conditions. This occurs when the downstream absolute pressure is less than or equal to 52.8% the upstream absolute pressure. In this experiment, the downstream absolute pressure, P_2 is the bomb pressure and the upstream absolute pressure, P_1 is the injection pressure. Therefore, the absolute pressure ratio (P_2/P_1) for all tested injection pressures are all in sonic conditions for the given bomb pressures ($P_2/P_1 \leq 0.528$). Sonic conditions cause the flow to be choked, which means the gas velocity remains constant except when flow temperature increases. However, the mass flow rate at the sonic conditions not only depends on flow temperature but also depends on the injection densities which are proportional to pressures. Therefore mass flow rate determines the length of injection duration and in certain degree affected the length of jet penetration.

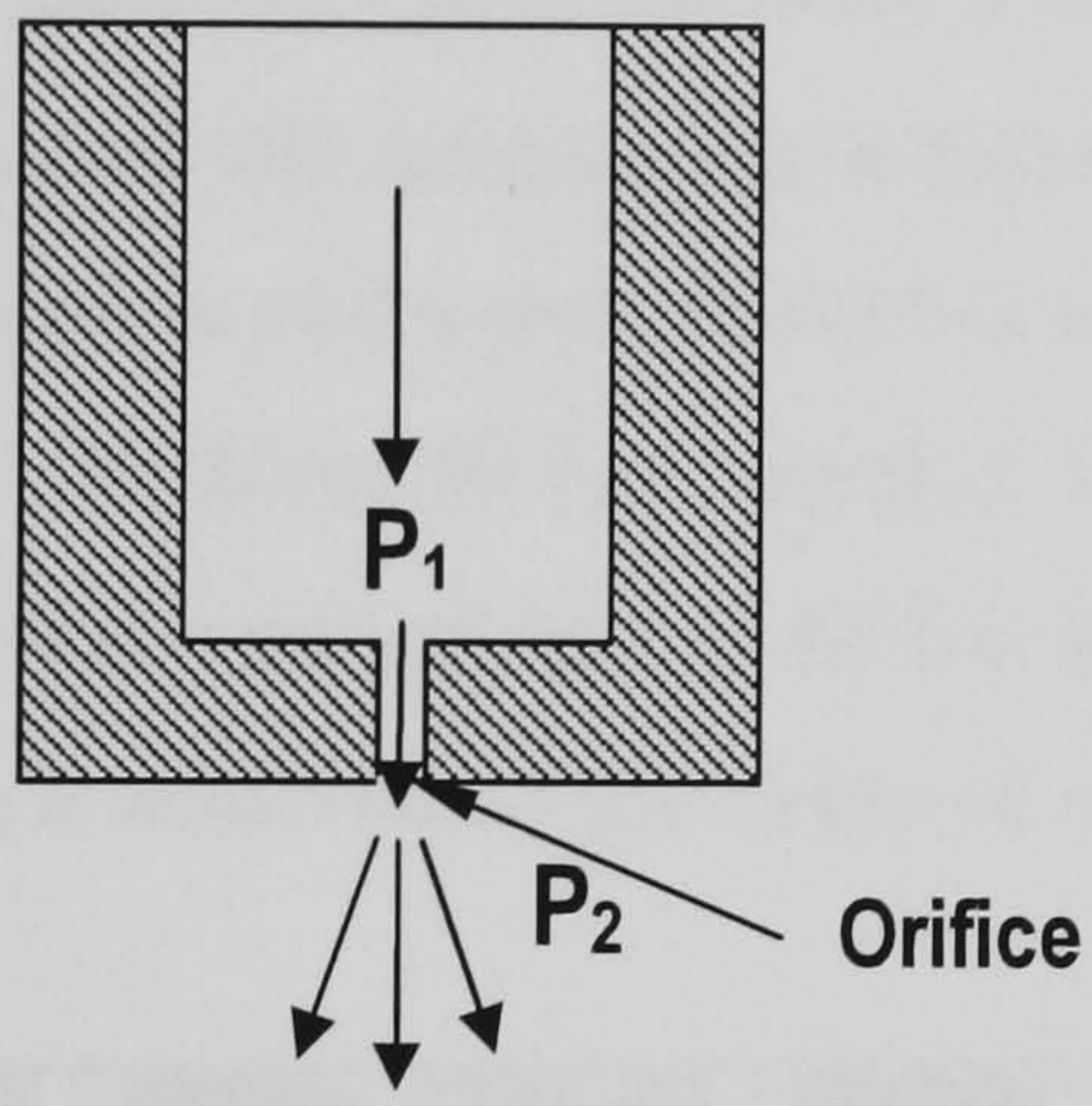

Figure 6.21 Flow through an orifice

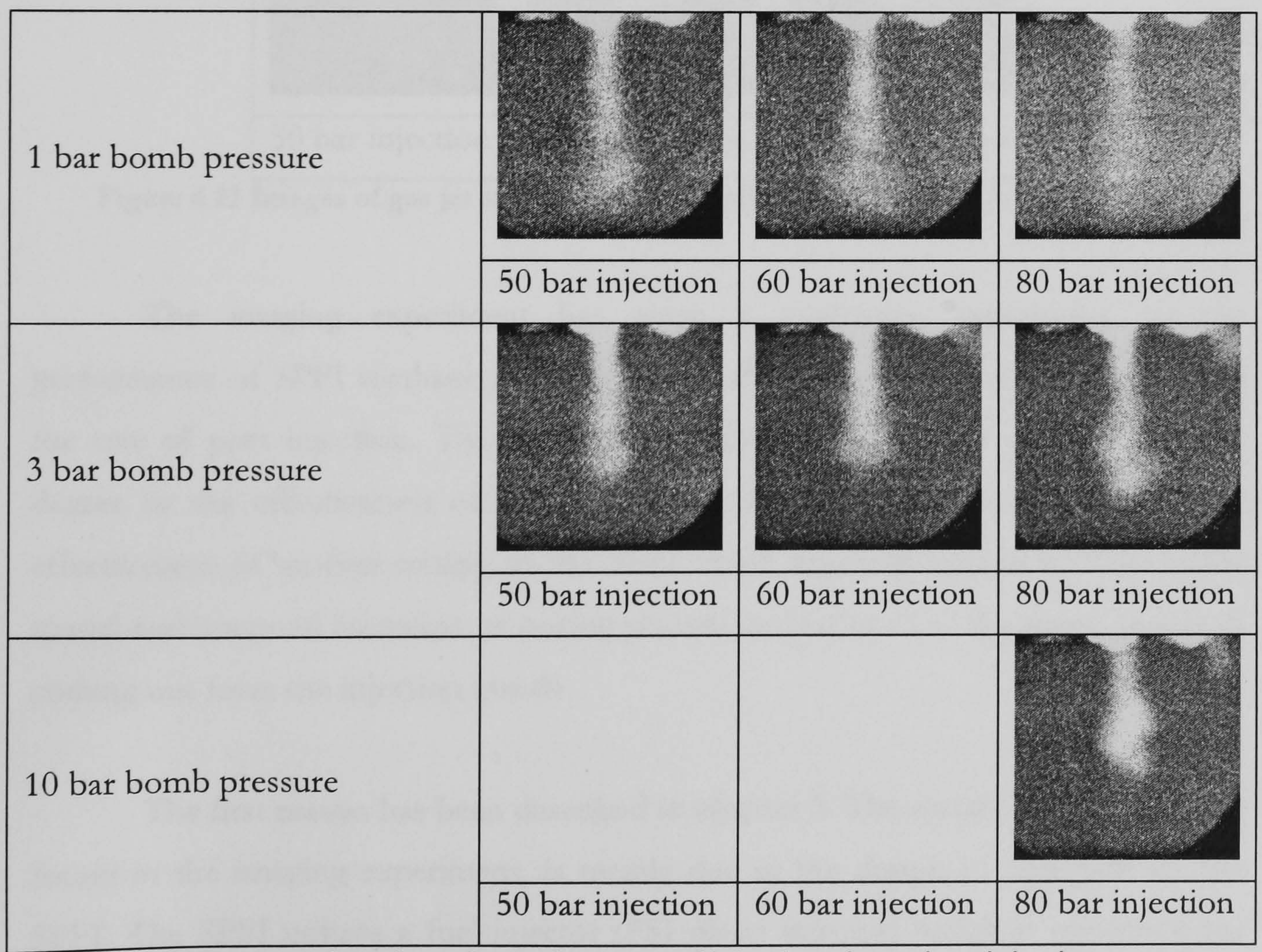

Figure 6.22 Images of gas jet at 8 ms after starts of injections for various injection pressure and bomb pressure

At a fixed injection pressure, as the bomb pressure increases, the absolute pressure ratio decreases, thus flow velocity is reduced. This is the reason for the reduction of penetration length when bomb pressure is increased, at any given duration time from ignition starts.

Varying injection pressure has little effect on the jet penetration for any given bomb pressure. As shown in Figure 6.23, at 8 ms, with 3 bar bomb pressure where gas jets were sufficiently developed, the penetration lengths are almost similar with the highest shown by 80 bar injection and lowest by 60 bar injection. The jet from 60 bar injection is wider than the one from 50 bar injection even though it is slightly shorter. This could explain why the performance of 60 bar injection is better than of 50 bar injection; a better mixing is achieved by the shape of the gas jet.

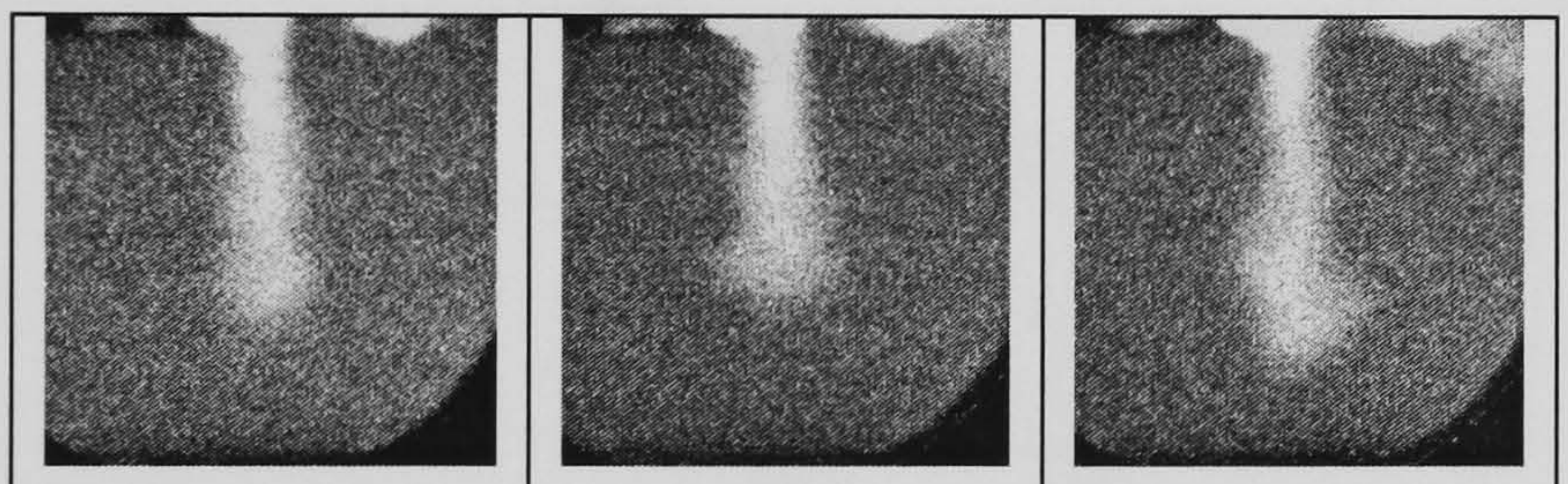

50 bar injection | 60 bar injection | 80 bar injection

Figure 6.23 Images of gas jet at 8 ms after starts of injections at 3 bar bomb pressure

The imaging experiment has given a qualitative explanation to the performance of SPFI methane direct injection which was found to be poorer than the one of port injection. The key factor which determines this difference is the degree or the effectiveness of air-fuel mixing. There are two factors limiting the effectiveness of air-fuel mixing in the SPFI direct injection operation. One is the spatial and temporal limitation of mixing process and secondly is the shape of fuel jet coming out from the injection nozzle.

The first reason has been described in chapter 5. The second reason, which is found in the imaging experiment, is mainly due to the design of fuel path on the SPFI. The SPFI utilizes a fuel injector (FSI direct injector) which is optimised for direct injection and stratified charge operations. However, the optimization of nozzle design and orientation to give best effect on stratified charge direct injection was not taken as an advantage when used as a part of SPFI. As a result, the effective fuel injection behaviour is determined mainly by the injection nozzle as well as the fuel path. Figure 6.24 shows the representation of a projected fully developed gas jet inside the Ricardo E6 combustion chamber with piston at BDC. As it can be seen, because the gas jet is narrow and the injection is directed diagonally, a significant proportion of area is not covered by the gas plume. Furthermore, because injection is directed away from the point of ignition (i.e. spark plug electrodes) the mixture at that point could be lean and unstable during ignition, which is undesirable for initiation of combustion flame. Thus mixing will not be sufficiently enough to maximize the potential of higher output as a result of greater charge absolute heating value achieved by direct fuel injection.

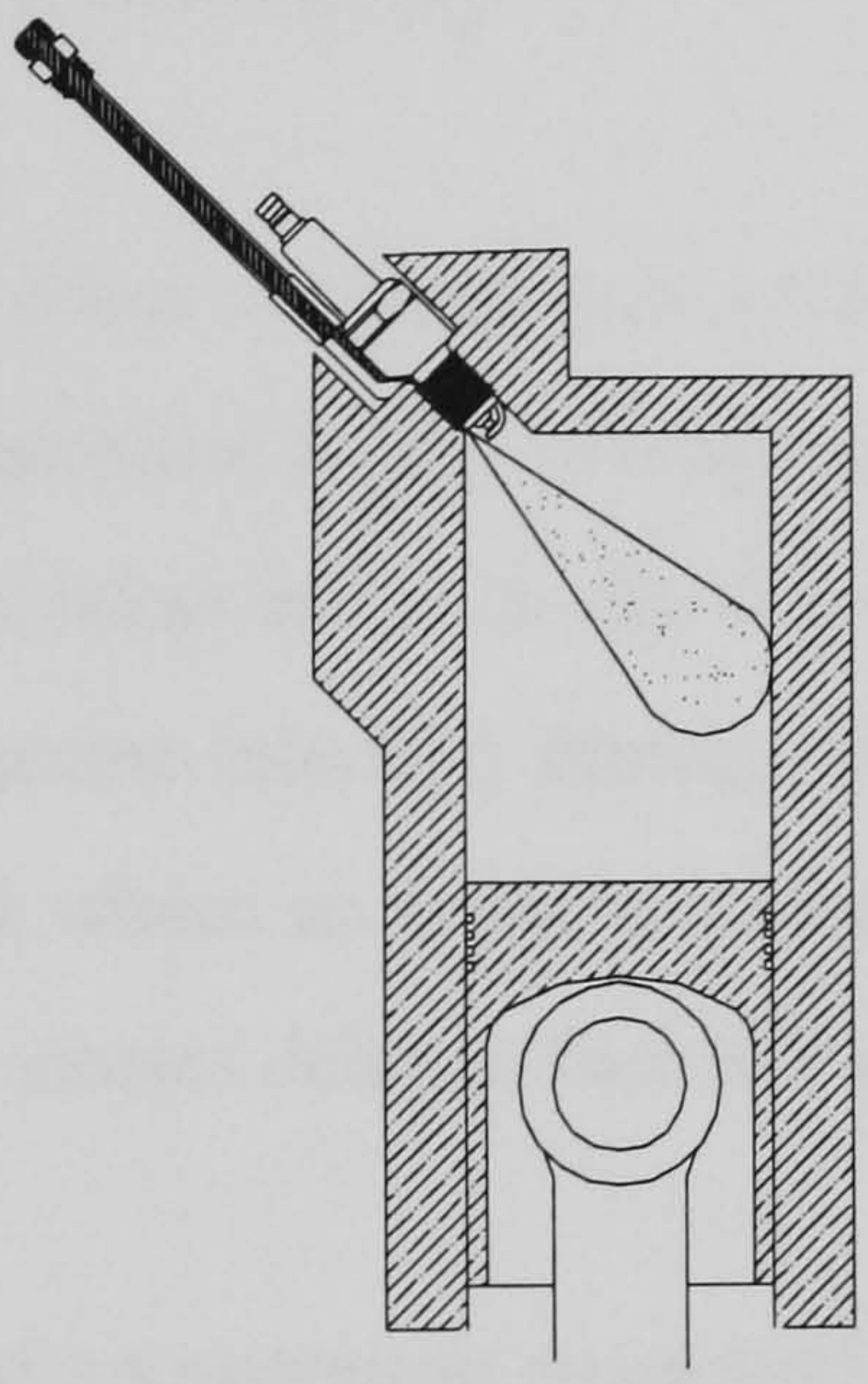

Figure 6.24 A fully developed gas jet inside Ricardo E6 combustion chamber with piston at BDC (compression ratio 10.5:1)

In conclusion, the inferior performance of SPFI methane direct injection to the port injection in this work is mainly due to poor mixing of air and fuel. The gas jet visualization from PLIF imaging implies that with a narrow spray cone, the degree of mixing is lower. The absence of air-fuel-mixing enhancer due to the flat piston crown further elevated this problem. Moreover, because fuel is injected away from the point of ignition, the mixture strength can be lean or unstable during start of ignition. In order to avoid any change to the original structure of the engine, the SPFI design needs optimization to produce a wider gas jet for an improved in-cylinder mixing.

Chapter 7

CONCLUSION, RECOMMENDATION AND FUTURE WORK

7.1 Conclusion

The objective of this work was to develop a conversion system for direct injection of CNG/methane in spark ignition engines. The system, which is called SPFI, is a combination of a fuel injector and a spark plug. A GDI fuel injector is embedded into spark plug body so that there is no modification to the structure of the converted engine. A prototype of the SPFI was developed through a number of design processes before it properly and reliably works on the Ricardo E6 engine. The work described in this thesis can be concluded as the following:

1. The most immediate effect of installation of SPFI on the Ricardo E6 engine is the reduction of motorised engine cylinder peak pressure due to decrease in compression ratio. Another effect is the delay in fuel arrival to the cylinder relative to the fuel injector injection timing. The two behaviours were due to the fuel path of SPFI where its volume increases the effective total cylinder volume and its length causes delay in fuel delivery to the cylinder.

2. Preliminary theoretical investigation suggested that complete combustion and ignition reliability can be achieved within normal range of engine speed. These were referred to the calculated turbulent Reynolds number and turbulent flame speed.

3. The initial investigation also suggest that a minimum fuel injection pressure of 50 bar is required to achieve close-valve injection operation for engine speed up to 2000 rpm for the purpose the engine experiments.

4. AVL boost computer simulation based on the Ricardo E6 single cylinder spark ignition engine models for gasoline and methane operation was developed and compared. Results show that when methane replaces gasoline

in a port injection engine, volumetric efficiency decreases and power is reduced. Direct injection of methane partly recovered the lost performance due to the conversion which mainly due to improved volumetric efficiency. However, results from engine experiments showed that methane direct injection performance was poorer than those of methane port injection which was suspected due to poor air-fuel mixing.

5. Engine experiments were carried out to measure the indicated performance of SPFI methane direct injection. The engine was run at 1100 rpm and various other operating parameters were varied. The results were compared to the ones from optimally calibrated methane port injection. At the specified speed, results show that SPFI methane direct injection performance is lower than those of port injection even though volumetric efficiency is increased. This was mainly because of spatial and temporal limitations in direct injection operation which lead to poor mixing. This was also due to the absence of mixing enhancing geometry within the disk-shaped cylinder. Furthermore, because methane is injected away from spark plug electrode, at the time of ignition, the stoichiometry of cylinder charge at the vicinity of spark plug and other areas may not be at optimal conditions.

6. Combustion of methane direct injection has been shown to be faster than of port injection. However, the initial part of combustion is relatively slower in direct injection. This implies the presence of charge stratification. The combustion behaviour and indicated performance show that combustion of SPFI methane direct injection is easily controlled and in good agreement with the data from available literature.

7. Images from PLIF flow visualisation from SPFI injection nozzle show narrow gas jets with 9° cone angle and a depth of penetration of 90-100 mm. This further proves that air-fuel mixing is relatively poor which leads to inferior performance than ideally expected. Injection pressure has small effect on jet penetration length because all injection flows were at sonic condition.

At sonic condition, gas velocity is 'choked' while only mass flow rate is affected by injection pressure.

8. SPFI methane direct injection is practical, viable and easy way for natural gas conversion but further improvement on its design is required particularly to improve fuel spray to achieve better air-fuel mixing.

9. The operation of SPFI methane direct injection is significantly affected by engine speed due to fuel arrival delay. There is a need to keep adjusting the injection timing to get optimal performance from the changing speed

7.2 Recommendation

Improvement of SPFI design

The natural continuation of this work is to improve the SPFI design, particularly to produce a more effective gas jet for better air-fuel mixing. These can be done by having multiple nozzles so that the area covered by the gas jet would be wider and covering more volume in the cylinder. If a better gas spray is achieved, not only the engine performance can be improved, but also the required injection pressure can be lowered.). This means for a normal CNG on-board storage pressure (200 bar) the engine operation is less dependent to an auxiliary compressing mechanism or limited driving distance when supply fuel is running low.

Adaptable injection control

From this work, it was obvious that operation of SPFI methane direct injection is significantly affected by engine speed due to the problem with fuel arrival delay. There is a need to keep adjusting the injection timing to get optimal performance from the changing speed. Therefore, the injection timing should be able to change during engine transient operation. This requires continuous crank angle encoding and externally controlled injection timing.

Full-scale engine testing

The reliability of SPFI must be investigated with full-scale engine testing which can be done by installing SPFI system in a car. First the design of SPFI must be adapted to the engine geometry, taking into account the placement and position of spark plugs attachment to the engine. However, the optimized geometry from this experiment must not be altered significantly to avoid additional requirement for calibration and optimization. In addition, there is a need to measure the fuel consumption alongside emission testing to quantify the emission levels.

7.3 Future work

Development of natural gas fuel injector

High pressure injection of natural gas requires more current flow in the solenoid-operated injector which is subjected to high temperature during long and continuous engine operations. While in the liquid fuel injector (like the GDI injector used in this work) some of the cooling is done by the flowing fluid, less cooling effect is achieved when natural gas is used with the same injector. Therefore, a specially developed solenoid injector is needed for reliable continuous operation with high pressure natural gas, with less dependency on fuel cooling. Durability testing is hence required on a full scale engine experiments. This will enable understanding of the effects of engine operational conditions on the reliability of the fuel injector.

Development of ECU for methane/NG operation

Since the combustion and operation of natural gas/methane is not identical to gasoline, a dedicatedly developed ECU for methane operation is desirable. This will optimise the engine operation and realised the advantage of this cleaner fuel. An extensive engine testing is needed to develop the ECU which must base on the converted engine itself.

Fuel storage and delivery

One of the fundamental problems with natural gas vehicle is the fuel storage. Natural gas occupies a larger amount of volume for the same energy content compared to liquid fuels it replaces. This causes limited vehicle driving distance which is not suitable for long journey and the absence of extensive refuelling stations. A new technology for NG storage is needed to increase storage capacity thus the potential driving distance with each fuelling.

REFERENCES

Abraham, J., Magi, V., MacInnes, J., and Bracco, F.V., (1994), *Gas Versus Spray Injection: Which Mixes Faster?*, SAE Paper 940895.

Abraham, J., and Bracco, F.V. (1995) *Effects of Combustion on In-cylinder Mixing of Gaseous and Liquid Jets*, SAE paper 950467.

Ahmed, F.M., Andrews, G., Aviss, N.J., and Jones, D., (1997), A Comparison of SI Engine Paticulate Emissions for Gasoline and Natural Gas, S496/004/97, in *IMechE Seminar Publication: Automotive Fuels for the 21st Century*, IMechE Publication Ltd, London, pp. 59-76.

Akansu, S.O., Dulger, Z., Kahraman, N. and Nejat Veziroglu, T, (2004) Internal combustion engines fueled by natural gas-hydrogen mixture, *International Journal of Hydrogen Energy*, vol. 29, no. 14, pp. 1527–1539.

Arcoumanis, C., Godwin, S.N. and Kim, J.W (1998) *Effect of Tumble Strength on Combustion and Exhaust Emissions in a Single-cylinder, Four-valve, Spark-Ignition Engine*, SAE 981044.

Aslam, M.U., Masjuki, H.H., Kalam, M.A., Abdesselam, H., Mahlia, T.M.I. and Amalina, M.A., (2006) An Experimental investigation of CNG as an alternative fuel for a retrofitted gasoline engine, *Fuel*, vol. 85, pp. 717-724.

AVL Boost User's Guide, version 4.0, AVL GmbH, May 2002.

Beck, Johnson and Peterson (1991) Optimized E.F.I for Natural gas Fuelled Engines, *SAE Paper 911650*, SAE Transaction.

Ben, L., Raud-Ducros, N, Truquet, R., and Cahrnay, G., (1999), Influence of Air/Fuel Ratio on Cyclic variation and Exhaust Emission in Natural Gas Engine, *SAE Paper 1999-02-2901*.

Bosschaart, K.J., and de Goey, L.P.H., (2004) The laminar burning velocity of flame propagating in mixtures of hydrocarbons and air measured with the heat flux method, *Combustion and Flame*, 136, pp. 261-269.

Boyan, x and Furuyama, M. (1998) *Jet Characteristics of CNG Injector with MPI system*, JSAE Review, 19, pp. 229-234.

Bradley, D., Lau, A.K.C. and Lawes, M., (1992), Flame Stretch Rate as a Determinant of Turbulent Burning Velocity, *Phil. Trans. R. Soc.*, London, A338, pp. 357-387.

Bradley, D., Gaskell, P.H. and Gu, X.J., (1996) Burning Velocities, Markstein Lengths, and Flame Quenching for Spherical Methane-Air Flames: A Computational Study, *Combustion and Flame*, vol. 104, pp. 176-198.

Bradley, D., Lawes, M., Sheppard, C.G.W., and Woolley, R., (1996) *Methane as an engine fuel*, in Using Natural Gas in Engines, I Mech E Seminar Publication, S410/002/96, IMechE, pp. 9-15.

Brunt, M.F.J., Rai, H., Emtage, A.L. (1998) The Calculation of Heat Release from Engine Cylinder Pressure Data, *SAE Technical Paper Series*, 981052.

Carter, S., J. Heenann and B. Williamson (1992), The GFI Prototype to Product, in the *3rd International Conference on Natural Gas Vehicles*, Goteborg.

Chen, S.K., and Beck, N.J., (2001), Gas Engine Combustion Principles and Applications, *SAE Paper 2001-01-2489.*

Choi, H.J., Ko, Y.S, Chung, S.H. (2002), Visualization of Concentration Field in a Vortex Ring Using Acetone PLIF, *Journal of Visualization* Vol. 5, No. 2, pp.145 - 152

Chun, K.M., and Heywood, J.B., (1987) Estimating Heat-Released and Mass of Mixture Burned from Spark-Ignition Engine Pressure Data, *Combustion Science and Technology*, vol. 54, pp. 133-143.

Cole, J.B., and Swords, M.D., (1979), Laser Doppler anemometry measurements in an engine, *Applied Optics*, Vol. 18, no. 10.

Cox, G.B., DelVecchio, Hays, W.J., Hiltner, J.D., Nagaraj, R. and Emmer, C. (2000) *Development of a Direct-Injected Natural Gas Engine System for Heavy-Duty Vehicles*, NREL/SR-540-27501.

Egnell, R., (1998) Combustion diagnostics by means of multizone heat release analysis and NO calculation, *SAE Technical Paper Series*, 981424.

Erdil, A., Kodal, A., and Aydin, K., (2002) Decomposition of Turbulent Velocity Fields in an SI Engine, *Flow, Turbulence and Combustion*, Vol. 68, pp. 91-110.

Eriksson, L., (1998) Requirements for and a symmetric method for identifying heat release model parameters, *SAE Technical Paper Series*, 980626.

Evans, R. L. and Blaszczyk, J. (1997), *A comparative study of the performance and exhaust emissions of a spark ignition engine fuelled by natural gas and gasoline*, Proceeding, Institute of Mechanical Engineers, 211, part D, pp. 39- 47.

Ferguson, C.R. and Kirkpatrick, A.T. (2001), *Internal Combustion Engines: Applied Thermosciences*, 2nd Edition, John Wiley and Sons, New York.

Gatowski, J.A., Balles, E.N., Chun, K.M., Nelson, F.E., Ekchian, J.A., Heywood, J.B., (1984) Heat release analysis of engine pressure data, *SAE Technical Paper Series*, 841359.

Goodger, E.M. (2000), *Transport Fuels Technology,* Landfall Press, Norwich, pp. 146-147.

Goodger, E.M., (1982), *Alternative Fuel Technology Series, Volume 2: Comparative Properties of Conventional and Alternative Fuels*, Cranfield Press, Cranfield Institute of Technology, Cranfield, Bedfordshire, England.

Goto, Y. and Sato, Y., (2001), *Combustion Improvement and Exhaust Emissions Characteristics in a Direct Injection Natural Gas Engine by Throttling and Exhaust Recirculation*, SAE Paper 2001-01-0737, pp. 31-37.

Geuzennec, Y.G. and Hamama, W., (1999) Two-zone heat release analysis of combustion data and calibration of heat transfer correlation is an IC engine, *SAE Technical Paper Series*, 1999-01-0218.

Guibert, J.C., (1999), *Fuels and Engines: Technology, Energy, Environment*, Institut Francais du Petrole Publication, Paris, p.p. 548-572.

Halliwell, N.A., Hargrave, G.K., (2003) Optical engineering: diagnostics for industrial applications, Proc. Institute of mechanical Engineers, *Journal of Mechanical Engineering Science*, vol. 217, part C:.

Hargrave, G.K., (2000), Optical diagnostics and direct injection of liquid fuel sprays, *Journal of Visualization*, v 2, n 3-4, pp. 293-300

Harrison, M., (2002), *Notes to Accompany CPD course: Cosworth Technology Limited*, Cranfield University.

Hassaneen, A.E., Varde, K.S., Bawady, A.H. and Morgan, A.A., (1998), A Study of The Flame Development and Rapid Burn Durations in a Lean-Burn Fuel Injected Natural Gas S.I. Engine, *SAE Technical Paper 981384.*

Hayashida, M., Yamato, T., Sekino, H. and Sugahara, K. [1999] *Investigation of Performance and Fuel Distribution of a Direct Injection Gas engine using LIF Measurement*, SAE technical paper 1999-01-3291.

Heywood, J.B. (1988), *Internal Combustion Engines Fundamentals,* McGraw Hill, New York.

Huang, Z., Shiga, S., Ueda, T., Nakamura, H., Ishima, T., Obokata, T., Tsue, M. and Kono, M., (2003), Combustion Characteristics of Natural-gas Direct-injection Combustion under Various Fuel Injection timings, *Proceeding Institute of Mechanical Engineers, Vol 21, Part D, Journal of Automobile Engineering*, pp. 393 – 401.

Ishida, M., Tagai, T., and Ueki, H., (2003) Effect of EGR and Preheating on Natural Gas Combustion Assisted with Gas-Oil in a Diesel Engine, *JSME International Journal*, Series B, Vol. 46, No. 1, pp. 124-130.

Ishii, M., Ishizawa, S., Inada, E. Idoguchi, R. and Sekiba, T., (1994) *Experimental Studies on Natural Gas Vehicle*, SAE Paper 942005.

Iwamoto, Y., Noma, K., Nakayama, O., Yamuchi, T. and Ando, H. (1997) *Development of Gasoline Direct Injection Engine*, SAE 970541.

Jääskeläinen, H. E. and Wallace, J. S. (1993) Performance and Emissions of a Natural Gas-Fueled 16 Valve DOHC Four Cylinder Engine, *SAE Technical Paper 930380*, SAE International, Michigan.

Jermy, M.J., Greenhalgh, D., (2000), Planar dropsizing by elastic and fluorescent scattering in sprays too dense fir phase Doppler measurement, *Applied Physics B: Laser and Optics*, vol. 71, no. 5, pp. 703-710.

Jones, A. L. and Evans, R. L., (1985), Comparison of Burning Rates in Natural-Gas-Fuelled spark Ignition Engine, *Journal of Engineering for Gas Turbines and Power*, vol. 107, pp. 908 – 913.

Kalam, M.A., Masjuki, H.H., Amalina, M.A., Abdesselam, H., Mahlia, T.M.I., Aslam, M.U., Varman, M., Halim, K., Chuah, L., Fuad, A., Fadzil, A.H., and Zulkiflee, B, (2005) *Performance, Combustion and Emissions Studies of A Natural Gas Engine*, in the Proceedings of ACTi 2005, Conference on Automotive Technology, Dec 6-8, 2005, Putrajaya, Malaysia.

Kim, J.W., (2000) *Flow, Combustion and Emissions in a Four-Valve Spark Ignition Engine Fuelled by Compressed Natural Gas*, PhD Thesis, Imperial College, London.

Knowles, D. (1984) *Alternative Fuels*, Reston Publication, USA.

Kubesh, J.T. (2002) *Development of a Throttleless Natural Gas Engine*, NREL/SR-540-31141.

Liou, T.M., M., Hall, D.A. Santavicca and F.N., Bracco, (1984), *Laser Doppler Velocimetry Measurements in Valved and Ported Engines*, SAE Paper 840375.

Lozano, A., Yip, B., and Hanson, R.K., (1992) Acetone: a tracer for concentration measurements in gaseous flows by planar laser-induced fluorescent, *Experiments in Fluids*, 13, pp. 369-376.

MacLean, H. L. and Lave, L. B., (2003), Evaluating Automobile Fuel/Propulsion System Technologies, *Progress in Energy and Combustion Science*, Vol. 29, pp. 1 – 69.

Masahisa Yamakawa, Seiji Isshiki, Takuo Yoshizaki and Keiya Nishida, (2001), *Measurement of Ambient Air Motion of D.I. Gasoline Spray by LIF-PIV*, in the Proceedings of The Fifth International Symposium on Diagnostics and Modeling of Combustion in Internal Combustion Engines (COMODIA 2001), July 1~4, 2001, Nagoya, Japan.

Mattavi, J.N., Groff, E.G., Liensesch, J.H., Matekunas, F.A., and Noyes, R.N., (1980), Engine Improvements Through Combustion Modeling, *Combustion Modeling in Reciprocating Engines*, Plenum Press, New York.

Mohamad, T.I, Jermy, M and Harrison, M (2003), *Direct Injection of Compressed Natural Gas in Spark Ignition Engine*, in the Proceedings of the International Conference of Advanced and Strategies Technologies (ICAST 2003), 12-14 August 2003, Kuala Lumpur, Malaysia.

Mohamad, T.I., Harrison, M., Jermy, M., Theodoridis, E., and Dolinar, A., [2005] *Preliminary Investigation of the Combustion and Performance of Methane Direct Injection in a Single-Cylinder Engine Using Spark Plug Fuel Injector (SPFI) for Low Cost Conversion*, in the proceedings of the ATCi 2005, Conference on Automotive Technology, Dec 6-8, Putrajaya, Malaysia.

Morita, K., (2003), Automotive power source in 21st century, *JSAE Review*, Vol. 24, pp. 3-7.

Olsen, D.B., and Willson, B.D., (2002), The impact of cylinder pressure on fuel jet penetration and mixing, *ICE*, vol. 39, pp233-239.

Ove Sviden, EKI, University of Linkoping, "*Sustainable Mobility: A Systems Approach to Determining The Role of Electric Vehicles*," paper contained in OECD document on proceedings of an international conference, Stockholm, Sweden, "The Urban Electric Vehicle," ISBN 92-64-13752-1 (1992).

Papagiannakis, R.G. and Hountalas, D.T., (2003), Experimental Investigation concerning the effect of natural gas percentage on performance and emissions of a DI dual fuel diesel engine, *Applied Thermal Engineering*, 23, pp. 353-365.

Papagiannakis, R.G., and Hountalas, D.T., (2004) Combustion and Exhaust Emission Characteristics of a Dual Fuel Compression Ignition Engine operated with Pilot Disel Fuel and Natural Gas, *Energy Conversion and Management*, vol. 45, pp. 2971-2987.

Pirouzpanah, V., and Kashani, B.O., (1999), Prediction of Major Pollutants Emission in Direct-Injection Duel-Fuel Diesel and natural Gas Engines, *SAE Paper 1999-01-0841.*

Potter, A.E. and Berlad, A.L., (1956) A Relation Between Burning Velocity and Quenching Distance, NACA Technical Note 3882, National Advisory Committee for Aeronautics, Cleveland, Ohio.

Pulkrabek, W.W., (1997), *Engineering Fundamentals of The Internal Combustion Engine*, Prentice Hall, London.

Rassweiler,G.M., and Withrow, L., (1938) Motion Pictures of Engines Flames Corelated with Pressure Cards, *SAE Transaction*, vol. 42, no. 5, pp. 85-204

Reynolds, A., (1974), *Turbulent Flows in Engineering*, John Wiley and Sons, New York.

Reynolds, C.C.O.B, and Evans, R.L., (2003) Improving emissions and performance characteristics of lean burn natural gas engines through partial stratification, *Int. Journal of Engine Research*, vol. 5, no. 1, pp. 105-114.

Risi, A.D., Gajdeczko, B.F., and Bracco, F.V., (1997) *A study of* H_2, CH_4, C_2H_6 *mixing and combustion in a Direct-injection Stratified-Charge engine*, SAE Paper 971710.

Ricardo, S.H.R, (1953), *The High Speed Internal Combustion Engine*, Blackie & Son Limited, London & Glasgow.

Roethlisberger, R.P., and Favrat, D. (2002), Comparison between direct and indirect (prechamber) spark ignition in the case of a cogeneration natural gas engine, part I: engine geometrical parameters, *Applied Thermal Engineering*, vol. 22, pp 1217-1229.

Rubas, P.J. et.al. (1998) Methane Jet Penetration in a Direct-Injection Natural Gas Engine, *SAE Paper 980143*, pp. 1-13.

Shiga, S. et al. (2002). A Study of the Combustion and Emission Characteristics of Compressed-Natural-Gas Direct-Injected Stratified Combustion Using a Rapid-Compression-Machine. *Combustion and Flame*, 129, 1-10.

Shiga, S., Ozone, S., Machacon, H.T.C., Karasawa, T. and Nakamura, H., (2002), A Study of the Combustion and Emission Characteristics of a Compressed-Natural-Gas Direct-Injection Stratified Combustion Using a Rapid-Compression-Machine, *Combustion and Flame*, 129: 1-10.

Shudo, T., Shimamura, K., and Nakajima, Y., (2000), Combustion and Emissions in a Methane DI stratified charge engine with hydrogen pre-mixing, *JSAE Review*, 21,1, pp. 3-7.

Simmie, J.M., (2003) Detailed chemical kinetic models for the combustion of hydrocarbon fuels, *Progress in Energy and Combustion Science*, vol. 29, pp. 599-634.

Simms, A.R., (1994) *Natural gas fuelled spark ignition engine performance and emissions*, M.Sc. Thesis, Cranfield University.

Smith, J.R., (1982) *Turbulent Flame Structure in Homogeneous-Charge Engine*, SAE Paper 820043.

Soriano, B., (1982), *The Role of Flow Characteristics on Fire Spread with Streams of Fuel-Air Mixtures*, M.Sc. Thesis, Department of Mechanical Engineering, The University of Calgary.

Stan, C., (2002), *Direct Injection Systems: The Next Decade in Engine Technology*, SAE International, Society of Automotive Engineers, Warrendale, PA.

Stone, C.R., and Green-Armytage, D.I., (1987) Comparison of Methods for the Calculation of Mass Fraction Burnt from Engine Pressure-Time Diagrams, *Proc. Institute of Mechanical Engineers*, vol. 201, no. D1.

Tanabe, H. et. al. (1985) Trans. JSME (B), vol. 51, no. 467, pp. 2235.

Theodoridis, E, (2003), *Diesel/LPG Combustion Studies*, MSc. Thesis, Cranfield University, Cranfield.

Thomas, J.R. (1991) *Low Emission Gas Engines for Stationary of Vehicle Uses: Lean-burn, 3-way Catalysts or any other techniques?* In Proceedings, First ENSERV Gas Engine Symposium, 9-10 April 1991, Arnhem, Netherlands.

Turner, J.S. (1962) The 'Starting Plume' in Neutral Surroundings, *Journal of Fluid Mechanics*, vol. 13, pp. 356-369.

Unich, A., Bata, R.M. and Lyons, D.W. (1993), *Natural Gas: A Promising Fuel for I.C. Engines*, SAE Paper 930929, Pennsylvania, pp. 291-301.

Vourenkoski, A.K., (2004) *Development of a Liquid-phase LPG MPI Conversion System*, PhD Thesis, Cranfield University, Cranfield.

Wyszynski, L.P., Stone, C.R., and Kalghatgi, G.T. (2002), *The Volumetric Efficiency of Direct and Port Injection Gasoline Engine with Different Fuels*, SAE Paper 2002-01-0839.

Yamakawa, M., Isshiki, S., Yoshizaki, T. and Nishida, K., (2001), *Measurement of Ambient Air Motion of D.I. Gasoline Spray by LIF-PIV*, in the proceedings of the Fifth International Symposium on Diagnostics and Modeling of Combustion in Internal Combustion Engines, (COMODIA 2001), July 1-4, Nagoya.

Yuan, K.Y., and Chen, S.C., (1990) A New Algorithm for Coupled Solutions of Electric, Magnetics, and Mechanical Systems in Dynamic Simulation of Solenoid Actuators, *IEEE Transactions on Magnetics*, vol. 26, no.3, pp.1189-1197.

Zeng, K., Huang, Z., Liu, B., Liu, L., Jiang, D., Ren, Y., and Wang, J. (2006) Combustion Characteristics of a Direct Injection Natural Gas Engine under various Fuel Injection Timings, *Applied Thermal Engineering*, vol. 26, pp. 806-813.

Zhao, F. et al. (1999), Automotive spark-ignited direct injection gasoline engines. *Progress in Energy and Combustion Science*, 25, 437-562.

Zhao, F., Harrington, D.L., and Lai, M.C., (2002), *Automotive Gasoline Direct-Injection Engines*, SAE International, Warrendale, PA.

International Association for Natural Gas Vehicles (IANGV) website: http://www.ngvglobal.com/

Green Car Congress website: http://www.greencarcongress.com/

Volvo Car Corporation website: http://www.volvocars.com/

Proton Car Corporation, Malaysia website: http://www.proton.com.my/

World Meteorological Organization website: http://www.wmo.ch/

BIBLIOGRAPHY

Abramovich, G.N. (1963), *The Theory of Turbulent Jets*, MIT Press, Cambridge.

Abramovich, S. and Solan, A., (1973) The Initial development of A Submerged Laminar Round Jet, *Journal of Fluid Mechanics*, vol. 59, part 4, pp. 791-801.

Aleiferis, P.G., Taylor, A.M.K.P., Ishii, K. and Urata, Y. (2004) The nature of early flame development in a lean-burn stratified-charge spark ignition engine, *Combustion and Flame*, 136, pp.283-302.

Arici, M.E., and Maxwell, T. (2003) Analysis of mixing distribution in an engine-like configuration, *International Journal of Energy Research*, 27, pp. 1039-1050.

Bechtold, R.L. (1997), *Alternative Fuels Guidebook: Properties, Storage, Dispensing and Vehicle Facility Modifications,* SAE International, Warrendale, PA.

Brasoveanu, D. and Gupta, A.K., (2000), Maximum mixing times for methane and air, *Journal of Propulsion and Power*, vol. 16, no 6. pp. 956-963.

Brasoveanu, D. and Gupta, A.K., (2003), Enhancement of Methane-air Mixing Using Shock and Expansion waves, *Transaction of ASME*, vol. 125, pp.332-335.

Crangle, J. (1977), *The Magnetic Properties of Solids*, Edward Arnold, London.

Chen, R. and Lucas, G.C., (1996) *An Investigation into a use of Piezo-Fluidic Combined Units as Fuel Injectors for Natural Gas Engines*, SAE Technical Paper 961987.

Duan, S.Y. (1996), *Laboratory experience with the use of natural gas fuel in IC engines,* in Using Natural Gas in Engines, I Mech E Seminar Publication, London, pp. 39-48.

Evans, R. L. and Blaszczyk, J. (1992), Low-*emission Combustion Chamber Design*, 25th ISATA International Symposium on Automotive Technology and Automation, Florence, Italy, 1 – 5 June, Paper 920420.

Evans, R. L., Jones, A. L. and Lorghese, R. (1986), *A Comparison of Natural Gas and Gasoline in a Spark Ignition Engine*, Proceedings, Gaseous Fuels for Transportation I, Vancouver, British Columbia, Canada, pp. 713 – 726.

Hong, H., Krepec, T. and Cheng, R.M.H., (1997) Computer Aided Design Optimization of Fast Operating Electronically Controlled Fuel Injectors, in *Road Vehicle Automation II* ed. C. Nwagboro, Wiley, New York, pp236-245.

Hong, S., Assanis, D., and Wooldridge, M, (2002) *Multi-Dimensional Modeling of NO and Soot Emissions with Detailed Chemistry and Mixing in a Direct Injection Natural Gas Engine*, SAE Technical Paper 2002-01-1112.

Hountalas, D.T., and Papagiannakis, R.G., (2001) *A Simulation Model for the Combustion Process of Natural Gas Engines with Pilot Diesel Fuel as an Ignition Source*, SAE Technical Paper 2001-01-1245.

Jaafar, M.Z., Kheng, W.H., and Kamaruddin, N, (2003) Greener energy solutions for sustainable future: issues and challenges for Malaysia, *Energy Policy*, 31, pp. 1061-1072.

Jennings, M.J., and Jeske, F.R. (1994) Analysis of the Injection Process in Direct Injected Natural Gas Engines: Part I – Study of Unconfined and In-Cylinder Plume Behavior, *Journal of Engineering for Gas Turbines and Power*, vol. 116, pp. 799-805.

Jennings, M.J., and Jeske, F.R. (1994) Analysis of the Injection Process in Direct Injected Natural Gas Engines: Part II – Effects of Injector and Combustion Chamber Design, *Journal of Engineering for Gas Turbines and Power*, vol. 116, pp. 806-813.

Jones, I.P. (2001), *Materials Science for Electrical and Electronic* Engineers, Oxford University Press, Oxford, pp. 259-283.

King, R.P. (2002), *Introduction to Practical Fluid Flow*, Butterworth-Heinemann, Oxford, pp. 9-31.

Kleinstein, G. (1964), Mixing in Turbulent Axially Symmetric Free Jets, *Journal of Spacecraft*, vol.1, no. 4, July-August, pp. 403-408.

Klimstra, J. (1987), Catalytic Converter for Natural Gas Fuelled Engines – A Measurement and Control Problem, *SAE Paper 872165.*

Lave, L., Maclean, H., Hendrickson, C., and Lankey, R., (2000), Life-Cycle Analysis of Alternative Automobile Fuel/Propulsion Technologies, *Environmental Science and Technology*, vol. 34, no. 17, pp. 3598-3605.

Malheiro, S., Lacoste, D., Bellenoue, M., and Kageyama, T. (2002) *Combustion of Methane Directly Injected in Quiescent Air in a Constant Volume Chamber*, in the Proceedings of the 29th International Symposium on Combustion, 21-26 July 2002, Sapporo, Japan.

Mason, J. L., (1990), Energy and Transportation, SAE *Paper No. SP-869.*

Miles, R.B. (2000) *Planar Laser Imaging* in *Flow Visualization; Techniques and Examples*, Smits, A.J. and Lim, T.T. ed, Imperial College Press, London, p.p. 93-118.

OECD/IEA (1990), *Substitute Fuels for Road Transport: A technology Assessment.*

Owen, K. and Coley, T, (1995*), Automotive Fuels Reference Book, 2nd Ed.*, SAE INC. PA, U.S.A.

Papageorgakis, G., and Assanis, D., (1998), *Optimizing Gaseous Fuel-Air Mixing in Direct Injection Engines using an RNG Based k-ε Model*, SAE Paper 980135.

Schulz, C., and Sick, V., (2005), Tracer-LIF diagnostics: quantitative measurement of fuel concentration, temperature and fuel/air ratio in practical combustion systems, *Progress in Energy and Combustion Science*, 31, pp. 75-121.

Stan, C., (2000), *Direct Injection Systems for Spark Ignition and Compression Engines*, SAE International, Society of Automotive Engineers, Warrendale, PA.

Sviden, O., (1992), Sustainable Mobility: *A Systems Approach to Determining The Role of Electric Vehicles*, paper contained in OECD document on proceedings of an international conference, Stockholm, Sweden, "The Urban Electric Vehicle," ISBN 92-64-13752-1.

Tabaczynski, R.J., Trinker, F.H. and Shannon, B.A. (1980). Further Refinement and Validation of Turbulent Flame Propagation Model for Spark Ignition Engines. *Combustion and Flames.* 39, 111-121.

Umierski, M., and Stmmel, P., (2000), Fuel Efficient Natural Gas Engine with Common-Rail Micro Pilot Injection, *SAE Paper 2000-01-3080.*

Uspenskii, V.A., Letyuk, A.I., Vivdenko, O., Kh., Sharapov, V.A., and Zaitsev, V.N., (1975), translated from *Teoreticheskie Osnovy Khimicheskoi Tekhnologii*, vol. 9, no. 1, pp. 142-148.

Wang, D.E., and Watson, H.C., (2000), *Direct Injection Compressed Natural Gas Combustion and Visualisation*, SAE Paper 2000-01-1838.

Wang, S.M., Miyano, T., and Hubbard, M., (1992), *Personal Computer Design Software for magnetic Analysis and Dynamic Simulation of a two-valve Solenoid Actuator*, SAE Paper 921086.

Yamasawa, K., Suzuki, S., and Biringer, P.P., (1990) A Proposal for a Finite-Element Force Approximation of an Automotive Magnetic Actuator, *IEEE Transactions on Magnetics*, vol. 26, no.4, pp. 1270-1273.

APPENDIX

Technical drawing of SPFI

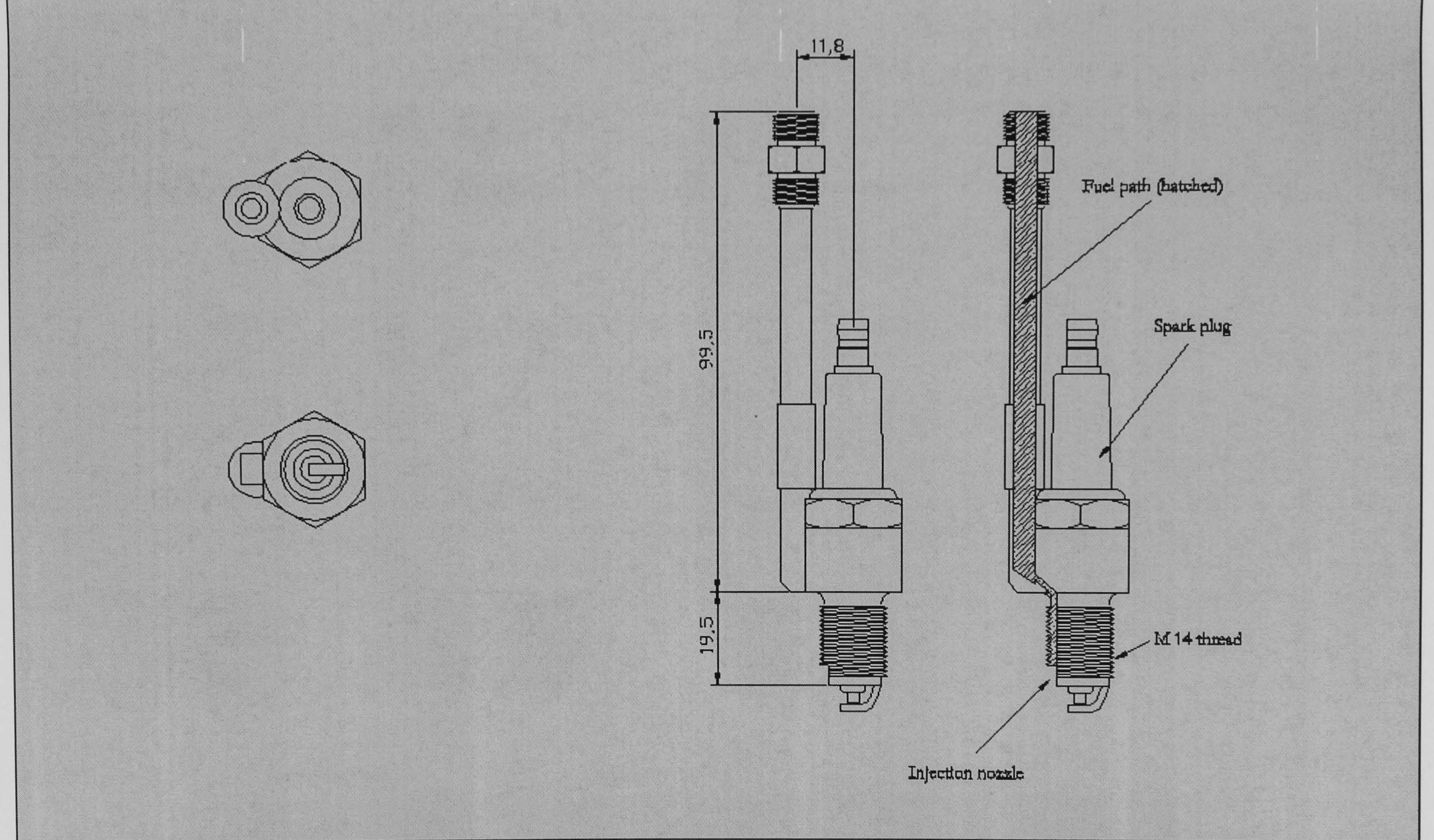

SPFI v.2	Part name :		Material :
TAIB I MOHAMAD	January 2005		All dimensions in mm